Bio-orthogonal Catalysts for the Activation of Fluoroquinolone Prodrugs within Bacterial Cells

James W. Southwell

PhD

University of York

Chemistry

September 2021

Abstract

Iron is an essential metal in biology. Siderophores are low molecular-weight compounds excreted by bacteria to bind and retrieve iron. These systems have been exploited by bacteria for the design of antibacterial-siderophore conjugates called sideromycins. Disguised as useful iron sources these conjugates are internalised and release the active component to kill the competing bacteria.

This project investigates siderophore-conjugated bio-orthogonal catalysts for the activation of prodrugs within bacteria. The selected transformation for activation was the deprotection of an allyl ester-protected carboxylic acid of the fluoroquinolone antibacterial moxifloxacin performed by an organometallic ruthenium complex. As kinetics assays for prodrug activation identified catalyst decomposition by molecular oxygen, enteric pathogens were targeted due to the low oxygen atmosphere at parts of the gastrointestinal tract. Antibacterial activity assays showed the synthesised moxifloxacin prodrug was 300-fold less toxic than its active form against gut-relevant bacteria *E. coli* K12 (BW25113) grown under micro-aerobic (2% O_2) and iron-limited conditions to mimic the environment of the intestines. Subsequent bacterial uptake studies suggested that the prodrug is internalised.

A variety of siderophores with different denticities were covalently attached to the catalyst core *via* glycine linkage to the hydroxyquinoline ligand, such as bidentate catechols, azotochelin, desferrioxamine and pyranone. Positively, prodrug activation kinetics were not significantly impeded by these catalyst decorations. The catechol and azotochelin conjugates improved the growth of iron-starved *E. coli* 2-fold and 9-fold respectively, implying their facilitation of iron-uptake. Moreover, co-addition experiments for each conjugate with prodrug at their upper, non-toxic concentrations gave antibacterial activity attributed to moxifloxacin formation. The growth recovery of a siderophore biosynthesis deficient strain of *E. coli* K12 (BW25113) suggested that the catechol and azotochelin conjugates act as weak siderophores. Prodrug incubation experiments mirrored these results, as the catechol conjugate gave the most significantly diminished bacterial growth (~40%) after their prior loading with prodrug.

Table of Contents

Table of Figures, Tables and Equations

Accompanying Material

A compact disk containing an electronic copy of this thesis, data for the characterisation of synthesised compounds, prodrug-activation kinetics and bacterial uptake studies by HPLC, and bacterial growth studies is attached at the back of this thesis.

Acknowledgments

First, I thank the University of York, Department of Chemistry for a Teaching Studentship that funded my PhD research and the excellent facilities and support they provided throughout. This includes the hard work of technicians including Heather, Karl, Graeme, Scott and Emma.

I would like to thank my supervisors Prof. Anne-Kathrin Duhme-Klair and Prof. Keith Wilson. Without Anne's guidance and support, I would still be aimlessly synthesising compounds. It is because of her direction and teachings I can now efficiently manage a research project, and have the confidence for the next chapter of my career. I also thank Keith for his wisdom and patience even as I delivered meaningless kinetics and bacterial growth plots. Although not strictly my supervisor, I would also like to acknowledge the support from, and kindness of Prof. Gavin Thomas, as he welcomed me into his research laboratories.

Without the help of colleagues including members and ex-members of the AKDK and GHT research groups, the project in this capacity would not have been possible. Firstly, I thank Reyme for his patience, kindness, and trainings in the now not-so-daunting world of microbiology. Thorsten, I thank for his friendship and efforts running what felt like hundreds of NMRs for me. I thank Conor for his help with research and publications but more importantly the hours of time we spent debating fantasy football. I would also like to highlight the help and support I received from Lisa, as she gave me the confidence and courage to do fearless research. Furthermore, I thank the talented undergraduate students I supervised, some of which have contributed to my work. To this end, I thank Marvin, Sophie, Tammy, Isabelle and Tom.

I must thank my incredible family, as their love and guidance inspired me to become a scientist and moulded me into the person I am today. Moreover, I thank them for their support, which included hosting me whilst I wrote this thesis. Finally, I thank my amazing girlfriend Emily, for her love and support as we both battled through our masters and PhD research together.

Declaration

I declare that the work presented within this thesis is, to the best of my knowledge, original and my own. This research was executed under the supervision of Prof. Anne-Kathrin Duhme-Klair and Prof. Keith Wilson at the University of York, between October 2017 and September 2021. No part of this work has been submitted for any other qualification at this, or any other university. Any publications that resulted from this work are outlined below and stated in the text they correspond to. All sources are acknowledged as References. The following work was carried out by, or with the assistance of other researchers:

Chapter 2:

- The conditions for the synthesis of compounds ***C*-cipro** and ***N*-cipro** were established by Dr. D. Raines
- Some of the Kitamura-type catalyst stability investigations were performed with the assistance of Miss. I. Böswald[1]
- The iron-limited minimal, modified MOPS medium used for the aerobic bacterial growth of *E. coli* K12 (BW25113) is published (1)
- The ICP-MS results for the iron concentration of supplemented iron-limited MHII is published (1)

Chapter 3:

- The precursor for the synthesis of compound **18** was supplied by Mr. C. Black
- The jobs plot for compound **18** and the auto-uncaging kinetics of compound **17** were obtained by Miss. S. Gutenthaler[2]

Experimental:

- Mass spectrometry was performed by Mr. K. Heaton, Dr. R. Cercola and Mr. A. Lopez
- NMR spectroscopy on 500 MHz and 600 MHz instruments were performed by Ms. H. Fish, Dr. A. Heyam and Mr. T. Dreher
- Elemental analysis was performed by Dr. G. McAllister

Citations for Publication of Results:

1. Sanderson, T. J.; Black, C. M.; Southwell, J. W.; Wilde, E. J.; Pandey, A.; Herman, R.; Thomas, G. H.; Boros, E.; Duhme-Klair, A.-K.; Routledge, A. *ACS Infect. Dis.* **2020**, 6(9), 2532–2541

James W. Southwell

Chapter 1 : Introduction

1.1 Prodrugs and Methods for their Activation

A prodrug is an inactive form of a drug, typically activated *in vivo* by the metabolism of the host or targeted microorganism, to release the active component (drug). This approach to drug delivery is usually aimed at overcoming pharmacokinetic or pharmacodynamic barriers, such as solubility and stability, passive permeability, bioavailability and unwanted toxicity.[3] If the target tissue of a drug possesses unique metabolic processes, they can be targeted for localised prodrug activation. This method of rational drug design is useful for combatting pharmaceutical inadequacies such as poor bio-distribution and off-site toxicity. Methods for localised prodrug activation include the enrichment of target tissue or targeting of specific transporters, cell-surface antigens, and enzymes.[4]

1.1.1 Localised Prodrug Activation by Environmental Factors

An example of a blockbuster drug derived by rational prodrug design for specific tissue targeting is omeprazole, Figure 1. Omeprazole is administered to combat stomach ulcer formation caused by gastroesophageal reflux disease. The active sulfenamide component is selectively released in acidic environments, such as the stomach, resulting in the inhibition of proton-pumps *via* covalent disulfide linkage to their cysteine residues.[5, 6]

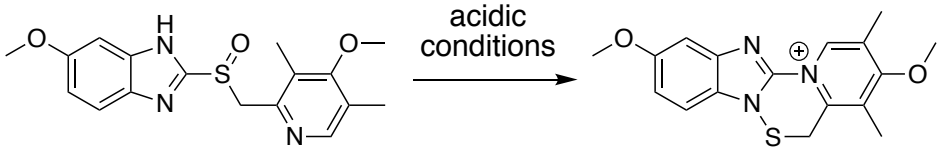

omeprazole
= prodrug

sulfenamide
= drug

Figure 1 Omeprazole prodrug activation under acidic conditions to release the sulfenamide active component.

1.1.2 Localised Prodrug Activation by Metabolism

In the development of anticancer therapies, the selective delivery of cytotoxic drugs is especially important for preventing damage to healthy tissue. Tumour cells behave quite differently to healthy tissue; these differences are highlighted by 'The

Hallmarks of Cancer'.[7] Tumour-specific metabolism has provided methods for the localised accumulation and/or release of anticancer prodrugs, such as upregulated enzymes or over-expressed cell-surface antigens. Capecitabine is an anticancer prodrug that is activated *via* tumour-specific enzymes, Figure 2.[8] This is a particularly elegant prodrug strategy as each activation step targets the tumour tissue selectively. This is a three-step process:

i) Carboxylesterase-mediated hydrolysis in the liver
ii) Cytidine deaminase-mediated deamination in the liver and tumour cells
iii) Release of the active 5-fluorouracil (5-FU) drug by thymidine phosphorylase in tumour cells

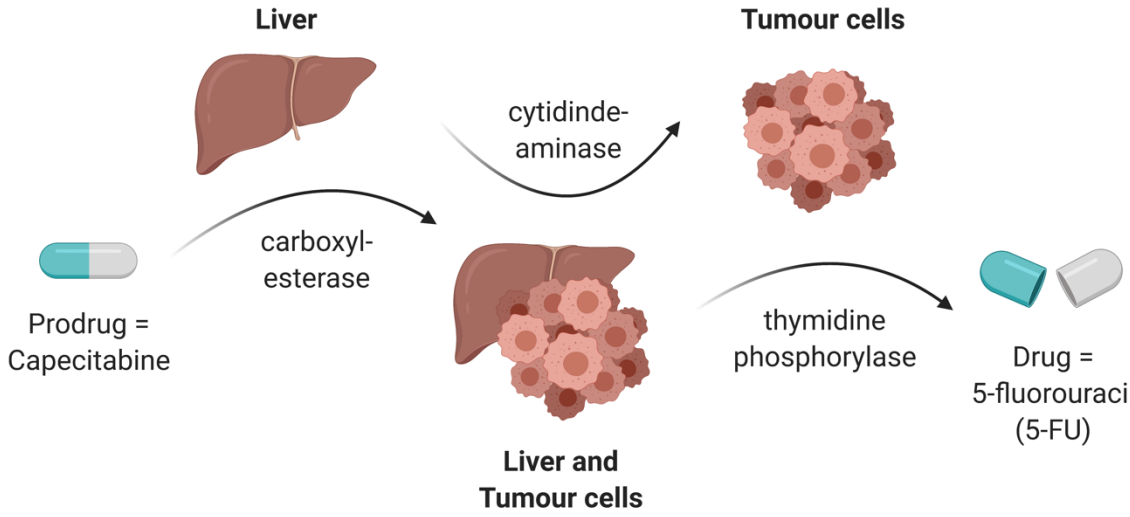

Figure 2 Schematic representation of the three-step activation of prodrug capecitabine by enzymes present in the liver and / or tumour cells, to release active 5-FU. Created with BioRender.com.

1.1.3 Localised Prodrug Activation by Artificially Introduced Systems

A more elaborate form of localised prodrug activation utilises co-administered systems that activate the prodrug *in vivo*. Such systems are appended to moieties that target specific tissue. A well-known example of such a strategy is directed enzyme prodrug therapy (DEPT) used in the treatment of cancer. Antibody-directed enzyme prodrug therapy (ADEPT), a type of DEPT, is a more elaborate type of antigen-targeting therapy, where the drug is not simply bound to a tumour specific

antibody but selectively activated by a co-administered antibody-enzyme conjugate that accumulates at the site of the tumour, Figure 3.[9]

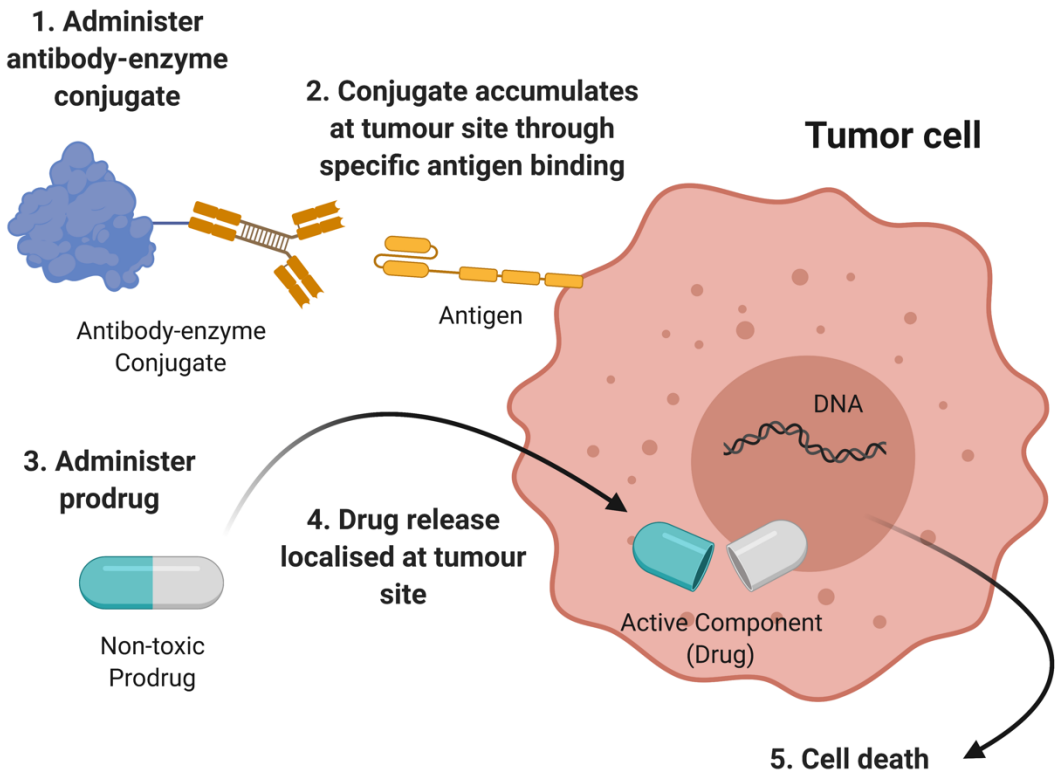

Figure 3 Schematic representation of antibody-directed enzyme prodrug therapy (ADEPT). Created with BioRender.com.

Treatment using ADEPT first involves administration of the antibody-enzyme conjugate allowing for tumour-site accumulation followed by the non-toxic prodrug. The prodrug is more homogenously distributed throughout the host but crucially is only activated within tumour tissue. ADEPT is a developing field with no current use in the clinic. Significant efforts towards such systems are largely based on monoclonal antibody-carboxypeptidase G2 enzyme conjugates for the prodrug activation of aniline mustard compounds.[10] An example of a prodrug candidate investigated is 4-[bis(2-chloroethyl)amino]benzoyl L-glutamic acid, Figure 4.[11] A more early-stage example of prodrug activation by artificially introduced systems involves the use of bio-orthogonal inorganic complexes. This strategy is reviewed in section 1.2.

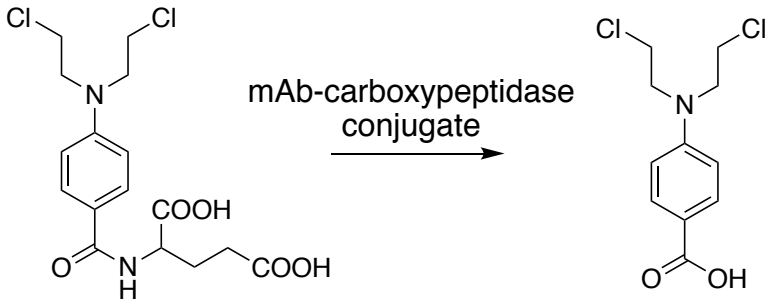

Figure 4 Monoclonal antibody carboxypeptidase-mediated prodrug activation of the anticancer prodrug 4-[bis(2-chloroethyl)amino]benzoyl *L*-glutamic acid, to give 4-[bis(2-chloroethyl)amino]benzoic acid.

1.2 Bio-orthogonal Catalysis

Bio-orthogonal chemistry is a term coined by Carolyn Bertozzi in 2003 meaning 'any non-biological chemical reaction that can occur inside living systems without interfering with native biochemical processes'.[12] Whilst there has been much development in the field of stoichiometric transformations, far fewer catalytic processes have been reported.

The integration of abiotic inorganic catalysts into living cells and organisms is a relatively new concept. The metals used for such catalysis are typically either Ru, Ir, Pd or Au and their inherent toxicity, as well as the complexity of biological solutions presents a number of challenges, rendering the majority of established laboratory catalysts incompatible. Cells contain numerous potential catalyst poisons such as glutathione (GSH) meaning that even if cell-penetration is achieved, catalysts are often readily inactivated. Despite such problems, numerous advances have been reported and for reviews see references.[13-18] A collection of notable advances and applications is summarised in Figure 5. Ultimately, the development of bio-orthogonal catalyst systems would allow for numerous therapeutic applications. Significant advances in the last decade could potentiate a revolutionary inclusion of inorganic complexes into medicinal chemistry.

An example of a bio-orthogonal catalyst is the ruthenium complex developed by Soldevila-Barreda *et al.* in 2012, which induces reductive stress in cells, Figure 8.[19, 20] Nicotinamide adenine dinucleotide (NAD) is an essential coenzyme found in all

living cells that participate in redox chemistry, allowing the transfer of electrons between molecules. It is commonly found in two oxidations states (NAD = oxidised and NADH = reduced) and is extensively involved in metabolic processes including transcription, DNA repair, and cell death. These ruthenium complexes are thought to significantly reduce NAD levels when co-administered with sodium formate and are proposed to have potential applications in the treatment of cancer.

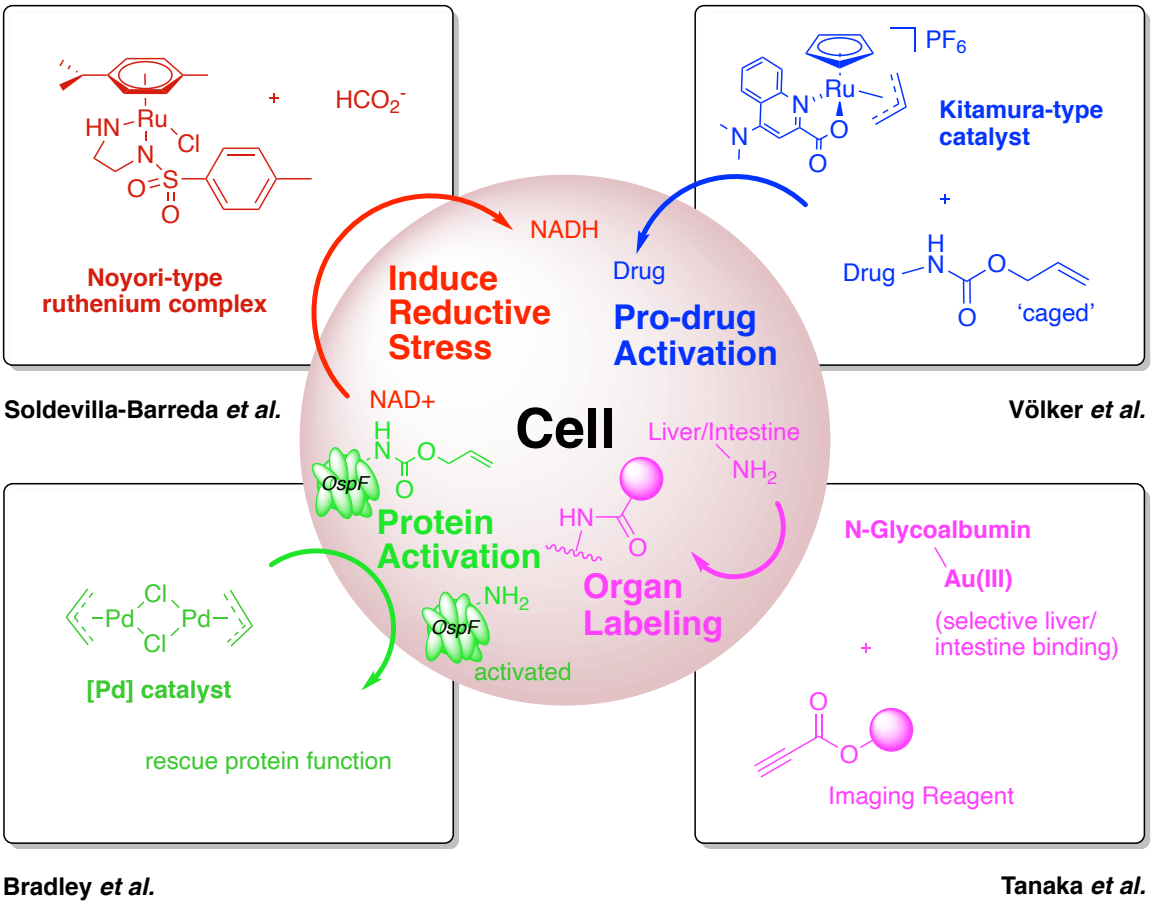

Figure 5 Examples of bio-orthogonal inorganic complexes and their biological applications. Red = Soldevila-Barreda *et al.*[20], Blue = Völker *et al.*[21], Green = Bradley *et al.*[22] and Pink = Tanaka *et al.*[23]

Similar to enzymes in DEPT and ADEPT, the utilisation of inorganic complexes can offer advantages if such systems are catalytic, due to lower dosage requirements. Over the last decade, significant progress has been made towards stable small molecule inorganic catalysts that can perform chemical reactions inside living systems, such as prodrug activation. Notably, in 2014 Völker *et al.*[21] described the use of a organometallic ruthenium catalyst for the deprotection of allyl carbamate-

protected amines under biologically-relevant conditions previously reported by Tanaka *et al.*[24], Figure 5. After the principal researcher responsible for the development of these catalysts, this catalyst and its derivatives are referred to as 'Kitamura-type catalysts'.[24, 25] Detailed information regarding the development of these catalysts and their applications can be found in section 1.2.1.

1.2.1 The Kitamura-type Catalysts

1.2.1.1 The Development of the Kitamura-type Catalysts

In 2002, Tanaka *et al.* reported the development of a Ru(II) catalyst **Ru-1** for the deprotection of allyl esters, Figure 6.[25] This reaction was achieved in a variety of solvents such as isopropanol, MeOH and MeOH mixtures with acetonitrile, THF, dichloromethane and water under an argon atmosphere at room temperature, giving the corresponding carboxylic acid in quantitative yields.

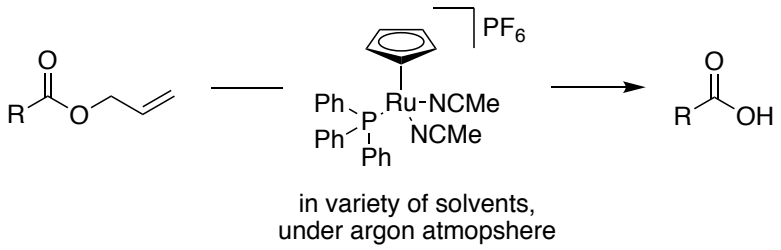

Figure 6 Allyl ester deprotection using catalyst **Ru-1** under an argon atmosphere in a variety of solvents (isopropanol, MeOH, and MeOH mixtures), reported by Tanaka *et al.*[25]

Two years later, the same researchers reported a structurally-similar catalyst, generated *in situ* by the mixing of $[RuCp(MeCN)_3]PF_6$ and quinaldic acid for the reversible deprotection of allyl ethers, Figure 7.[24] In the presence of excess nucleophile (e.g. MeOH) the reaction is driven in favour of the de-allylated product.

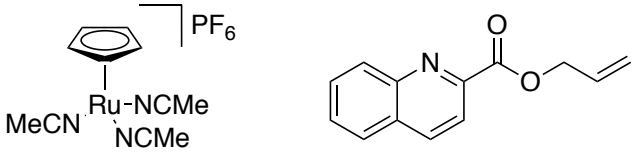

Figure 7 The precursors for the *in situ* formation of a quinaldic acid Ru(IV) catalyst for the deprotection of allyl ether-protected alcohols reported by Tanaka *et al.*[24]

By studying changes in catalyst activity brought about by various bidentate ligands, the importance of a synergistic effect between the ligand's sp^2 hybridised *N*-atom and adjacent pyridine carboxylic acid, producing a 5-membered chelate ring was realised. It was suggested that whilst the strong σ-donor *N*-atom of the quinaldic acid ligand increases ruthenium nucleophilicity, the same ligand's carboxylic acid hydrogen-bonds to the allyl alcohol ligand increases allyl electrophilicity, forming the transition state shown in Figure 8. This suggested the +2 oxidation state was the active species. In 2010, Kiesewetter *et al.* reported the use of a derivative of this catalyst for the de-allylation of carbonates in water, with enhanced catalyst stability compared to reactions in MeOH.[26]

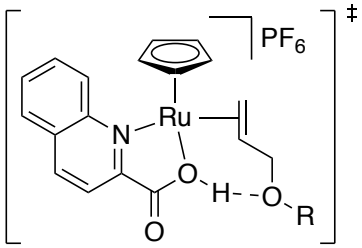

Figure 8 Catalyst transition state for **Ru-2**-mediated deprotection of allyl ethers proposed by Tanaka *et al*.[24]

In 2006, Streu and Meggers reported a different Ru(IV) catalyst **Ru-3** for the deprotection of allyl carbamate protected amines inside cells, Figure 9.[27] In these studies, the addition of strong nucleophiles (thiophenol) was essential for conversion, while physiological temperatures gave improved yields. This consistent requirement for nucleophiles potentiated the catalyst's applications for reactions in living cells, as nucleophiles such as GSH are present at higher concentrations in the cytoplasm of mammalian cells.[28]

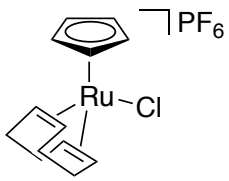

Figure 9 Chemical structure of **Ru-3**.

To evaluate the activity of **Ru-3** inside cells, the allyl carbamate deprotection of a bis allyl carbamate-protected rhodamine 110 pro-fluorophore (Rho-allyl$_2$) was tracked using confocal microscopy, Figure 10. A HeLa cell line was incubated with the catalyst for 30 min, then washed with PBS to remove catalyst that was not inside the cells, and then supplemented with Rho-allyl$_2$. Subsequent florescence yields provide a quantitative value for the cellular uptake of both components. Results showed a disappointing 6% fluorescence yield with 20 mol% catalyst loading in cell extract with GSH. However, with the addition of thiophenol an 80% yield was observed. Impressively, these experiments suggested **Ru-3** is taken up into HeLa cells, but the limiting aspect of this strategy was the requirement of exogenous nucleophiles.

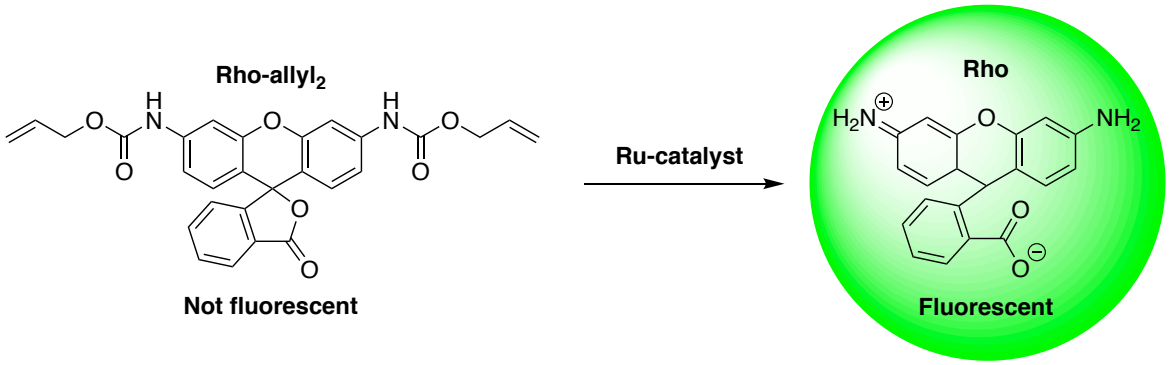

Figure 10 Kitamura-type catalyst-mediated activation of the allyl carbamate-protected rhodamine 110 dye (Rho-allyl$_2$) to form the fluorophore rhodamine 110 dye (Rho).

In 2014 Völker *et al.* reported the optimisation of the Kitamura-type catalyst previously reported by Tanaka *et al.*[24] **Ru-2** for the deprotection of allyl carbamate-protected amines under non-buffered biologically-relevant conditions, with excess GSH.[21] By investigating how changing the electron-withdrawing abilities of different ligated quinaldic acids influenced catalyst activity, an optimised analogue **Ru-5** was obtained, Figure 11. The reasoning given for the activity trend was reduced π-backbonding of the bidentate ligand. This observation was in line with the hypothesis made by Tanaka *et al.* in 2004, as it was believed increased electron donating strength of the *para*-substituent to the *N*-donor atom increases catalyst activity due to increased ruthenium electron density.[24] However Tanaka *et al.* reported the opposite trend in 2009.[29]

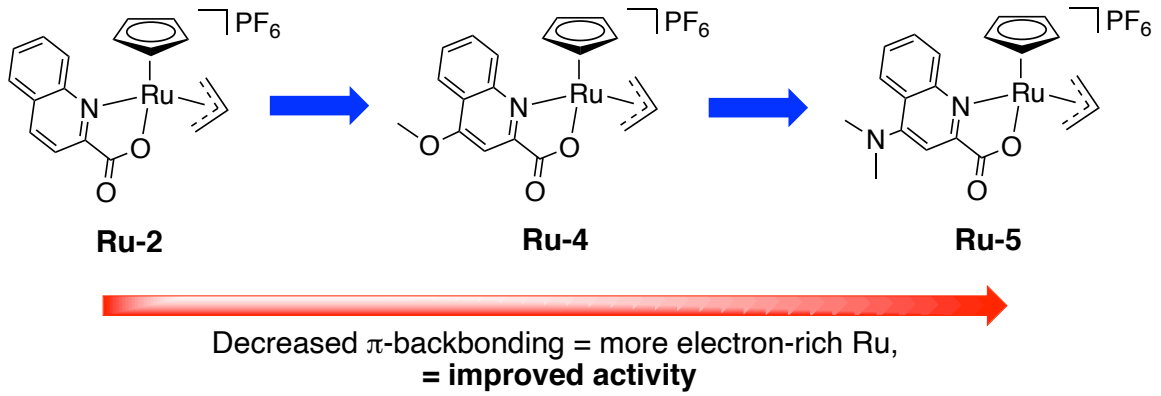

Figure 11 Electron-withdrawing effect of quinaldic acid ligand on catalyst activity.

The generally agreed upon catalytic mechanism was reported by Völker *et al.* in 2014 and is separated into two steps named catalyst priming (blue) and substrate activation (red), Figure 12.[21] Catalyst priming involves reaction of the Ru(IV) precursor species with a nucleophile to form the active Ru(II) intermediate species during step 2. In the absence of strong nucleophiles that facilitate fast η^3–allyl group loss (e.g. GSH), catalyst priming tends to be the rate limiting step. This conclusion is similar to that made by Kiesewetter *et al.* as better nucleophiles gave enhanced reaction kinetics (MeOH > water).[26] Substrate activation first involves occupation of the vacant co-ordination sphere of the active Ru(II) intermediate species by the allyl motif of the substrate, in step 3. In line with the transition state proposed by Tanaka *et al.*[24], it is believed a hydrogen bond forms between the carboxylic acid of the quinaldic acid ligand and the oxygen atom within the carbamate of the substrate. This then induces a hydrogen transfer, releasing the free-amine of the substrate, carbon dioxide and in turn, oxidises the ruthenium metal centre to regenerate the Ru(IV) catalyst precursor species in step 4. If strong nucleophiles are present, the reaction kinetics are more dependent on substrate.

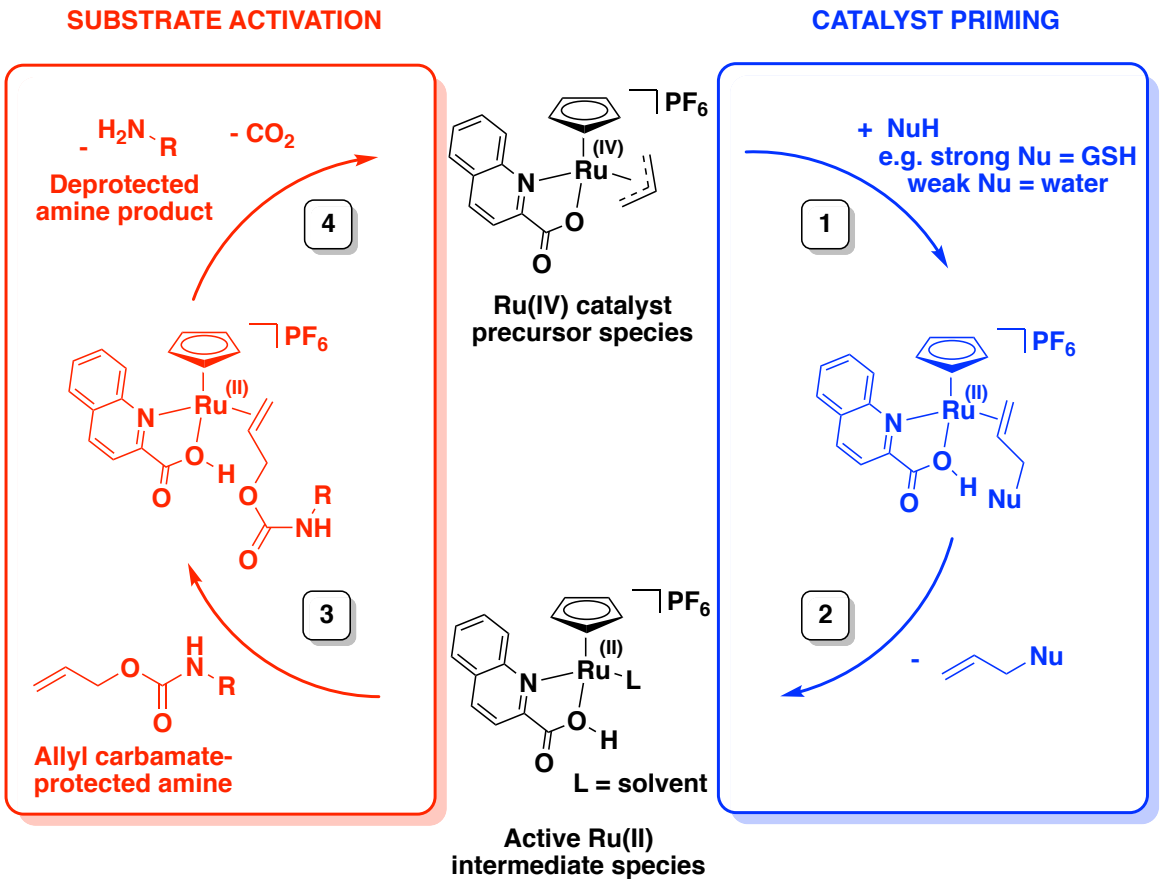

Figure 12 Mechanism for the catalyst-mediated allyl carbamate deprotection proposed by Völker *et al.* in 2014.[21] Catalyst Priming = blue, Substrate Activation = red.

To evaluate the cellular-uptake of these Kitamura-type catalysts, Völker *et al.* again employed Rho-allyl$_2$ pro-fluorophore incubation experiments. In comparison to negative 'no catalyst' controls, fluorescence increased 17-fold indicating the catalysts are readily taken up by human cells. However, this finding is contradicted in work by Hsu *et al.*[30] as these catalysts were evaluated for intracellular reactions utilising a fluorescence based luciferase reporter system. Results from these studies suggested the requirement for cell-permeable moieties, such as nanoparticle encapsulation and phosphine attachment for selective mitochondrial uptake.[31, 32]

Ru-5 was used to activate the anticancer drug doxorubicin. Doxorubicin's mode of action is binding to DNA causing strand damage, resulting in cell death. Masking of the amine (positively charged at physiological pH) lowers its affinity for the negatively charged DNA backbone thus decreasing drug activity. Incubation assays of a HeLa cell line suggested that the doxorubicin prodrug at 100 μM was

successfully activated by **Ru-5** at 20 μM with cells, resulting in their significantly decreased survival rates, Figure 13.

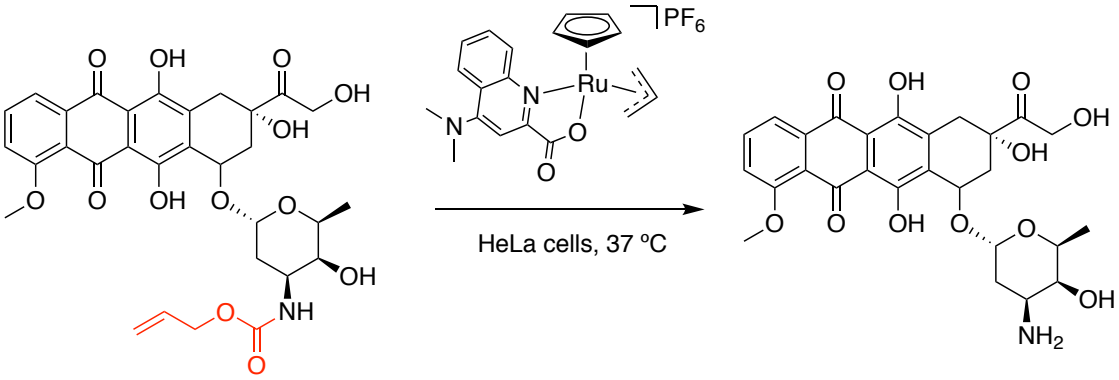

Figure 13 Activation of allyl carbamate-protected doxorubicin by **Ru-5** in HeLa cells.

More recently in 2017, Völker and Meggers further optimised catalyst activity.[33] Previous structure activity relationship (SAR) studies suggested that increasing electron density at the ruthenium-centre gave improved activity. However, the limited number of substituents that could be added to the quinaldic acid limited its further optimisation. Consequently, alternative ligands were explored, where 8-hydroxyquinoline gave enhanced catalyst activity, **Ru-6**, Figure 14.

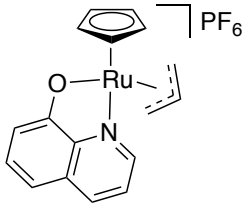

Figure 14 Chemical structure of **Ru-6**.

The overall emission yields improved compared to those of catalysts **Ru-2** (12%) and **Ru-5** (30%) reported by Völker *et al.* in 2014.[21] By iterative alteration of the substituent *para*- to the *N*-donor atom of the hydroxyquinoline ligand, an optimised catalyst was found in **Ru-8** with overall yields of 89% in aqueous phosphate buffer (pH 7.4) at room temperature with 10 mol% catalyst loading, Figure 15. Impressively, a 30% yield was achieved in blood serum at the same loading. Blood serum activity is more challenging considering its millimolar protein and high salt concentrations. Furthermore, **Ru-8** was again utilised for the activation of the doxorubicin prodrug in a HeLa cell line, where significant reductions in cell survival

rates were achieved with prodrug concentrations of 2 μM using non-toxic concentrations of **Ru-8** (1 μM).

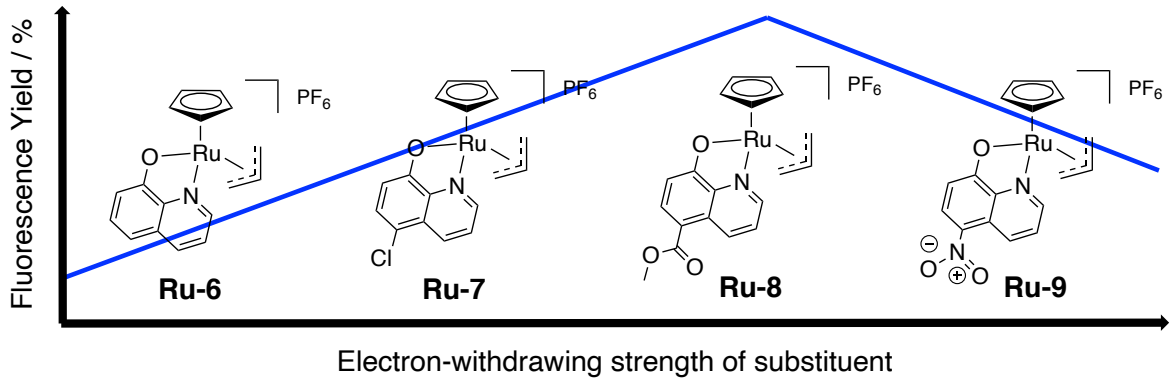

Figure 15 Relationship between electron withdrawing potential of 8-hydroxyquinoline *para*-substituents to *N*-donor atom and the corresponding Ru-catalysts allyl carbamate uncaging fluorescence yields for **Ru-6**, **Ru-7**, **Ru-8** and **Ru-9**.

In 2019, Rubini *et al.* reported a screening platform to identify and tailor the bio-compatibility of the Kitamura-type catalysts, Figure 16.[34] Each catalyst was tested at various concentrations and equivalents to substrate. Catalytic conversion and turnover number (TON) were quantified by a fluorescence readout corresponding to the formation of a green fluorescent protein (GFP) that is produced within the transformed *E. coli* bacteria. During these assays, the tested catalyst is added exogenously to the bacterial culture to activate a non-canonical amino acid (ncAA) which induces a cascade of biological processes which ultimately results in GFP production. Impressively, this assay also informs on bacterial fitness, as ncAA incorporation relies on several critical biological pathways.

Results from these experiments suggested that the quinaldic acid-ligated Kitamura-type catalysts are better tolerated by the *E. coli* bacteria as they remain non-toxic at 100 μM. In contrast, the hydroxyquinoline-ligated Kitamura-type catalysts were toxic at concentrations above 12.5 μM. Despite this, **Ru-6** provides similar overall conversions for the same substrate concentration and improved TONs at these catalyst concentrations. However, it was found that a quinaldic acid-ligated catalyst reported by Völker *et al.* in 2014 **Ru-4** gave the best compromise between toxicity and performance.

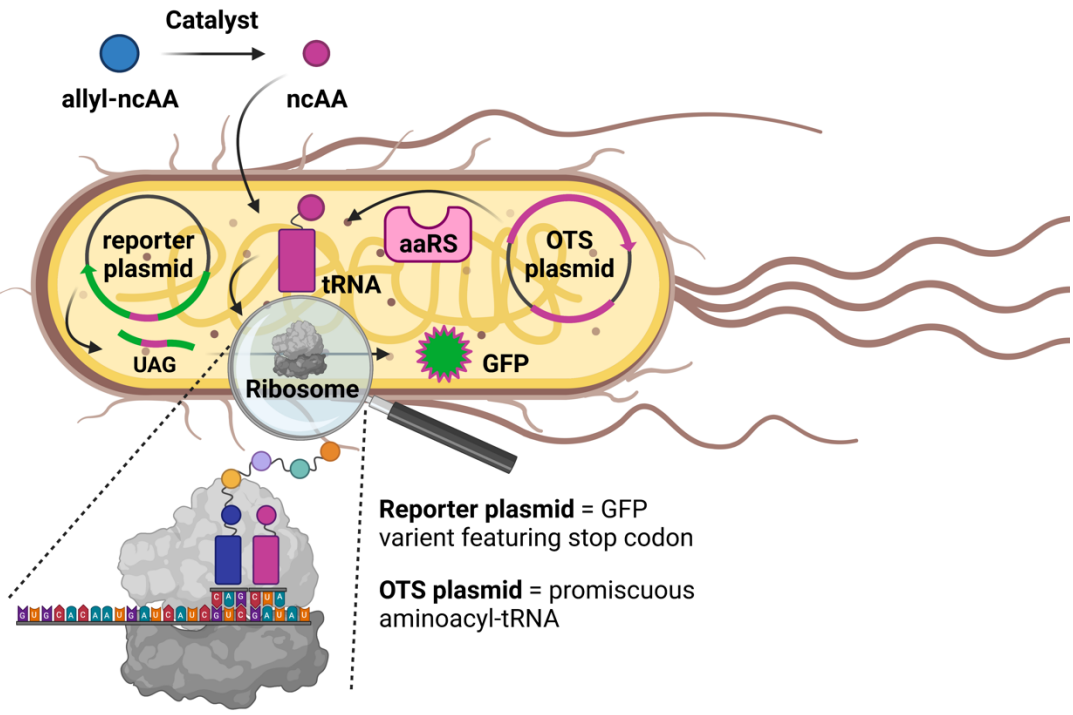

Figure 16 Schematic for the screening platform reported by Rubini *et al.*[34] (i) the tested catalyst releases a non-canonical amino acid (ncAA) from its allyl carbamate-protected version (inside or outside cells) (ii) ncAA is loaded onto tRNA aminoacyl-tRNA synthetase (aaRS) which is produced *via* transcription of the transformed orthogonal translation system (OTS) plasmid (iii) a tRNA that contains in-frame stop codon is incorporated by the ribosome into the GFP variant which is produced *via* transcription of the transformed reporter plasmid. Created with Biorender.com.

1.2.1.2 Biological Applications of the Kitamura-type Catalysts

Since their discovery, Kitamura-type catalysts have been investigated for uses in artificial metalloenzymes as well as prodrug activation strategies.[31, 32, 35, 36] Their major uses however have been for prodrug activation where examples are limited to eukaryotic cells such as cervical cancer cells (HeLa cell line).

Catalysis within the Mitochondria of Living Cells

In 2016, Tomás-Gamasa *et al.*[31] reported the development of Kitamura-type catalyst conjugates for reactions within the mitochondria of HeLa cells, Figure 17. This was achieved by catalyst conjugations to triphenylphosphonium (TPP) cations, as these motifs possess hydrophobicity and a resonance-stabilised cationic charge which

enables their uptake across the mitochondrial inner membrane, and subsequent accumulation.

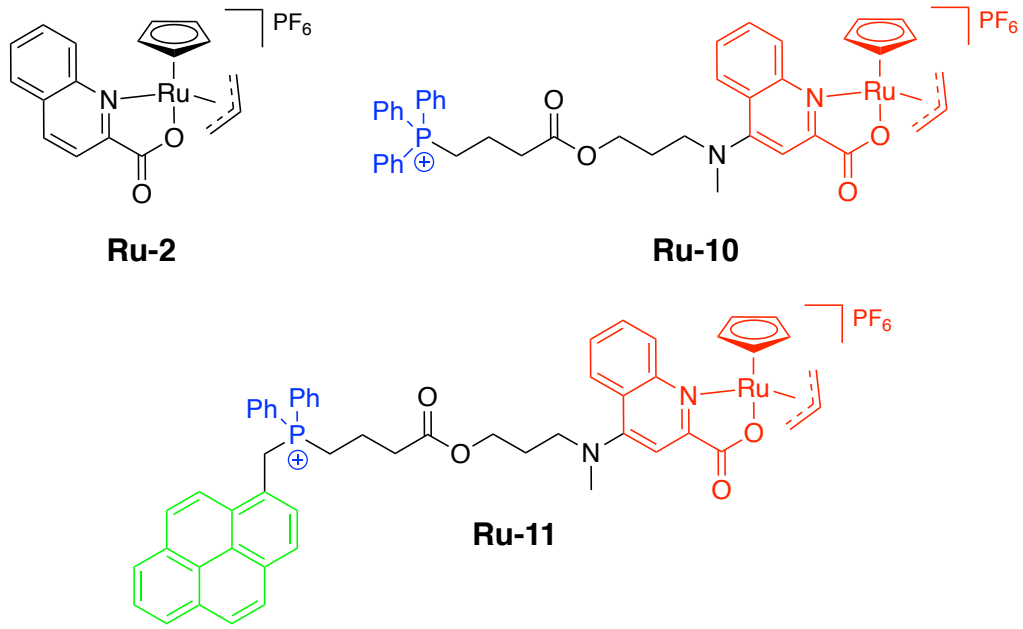

Ru-2 **Ru-10**

Ru-11

Figure 17 Chemical structures of trisphosphonium (TTP) cation conjugates with the Kitamura-type catalysts reported by Tomás-Gamasa *et al.*[31] For the conjugates: catalyst = red, TTP cation = blue, fluorescent probe = green.

Utilising incubation experiments similar to those initially reported by Streu and Meggers in 2006, the uptake and activity of **Ru-10** were measured using a Rho-allyl$_2$ pro-fluorophore and confocal microscopy. The results suggested improved cellular uptake relative to the 'no TPP' control catalyst **Ru-2**. Moreover, by synthesising a pyrene-phosphonium conjugate **Ru-11** they were able to track the catalyst within the cell which further supported good internalisation, Figure 18A. This same catalyst then showed the localised activation of protonophore 2,4-dinitrophenol (DNP) within mitochondria, which is known to perturb ATP production. These studies were the first reported examples of conjugates of the Kitamura-type catalysts and showed that their derivatisation did not diminish catalyst performance.

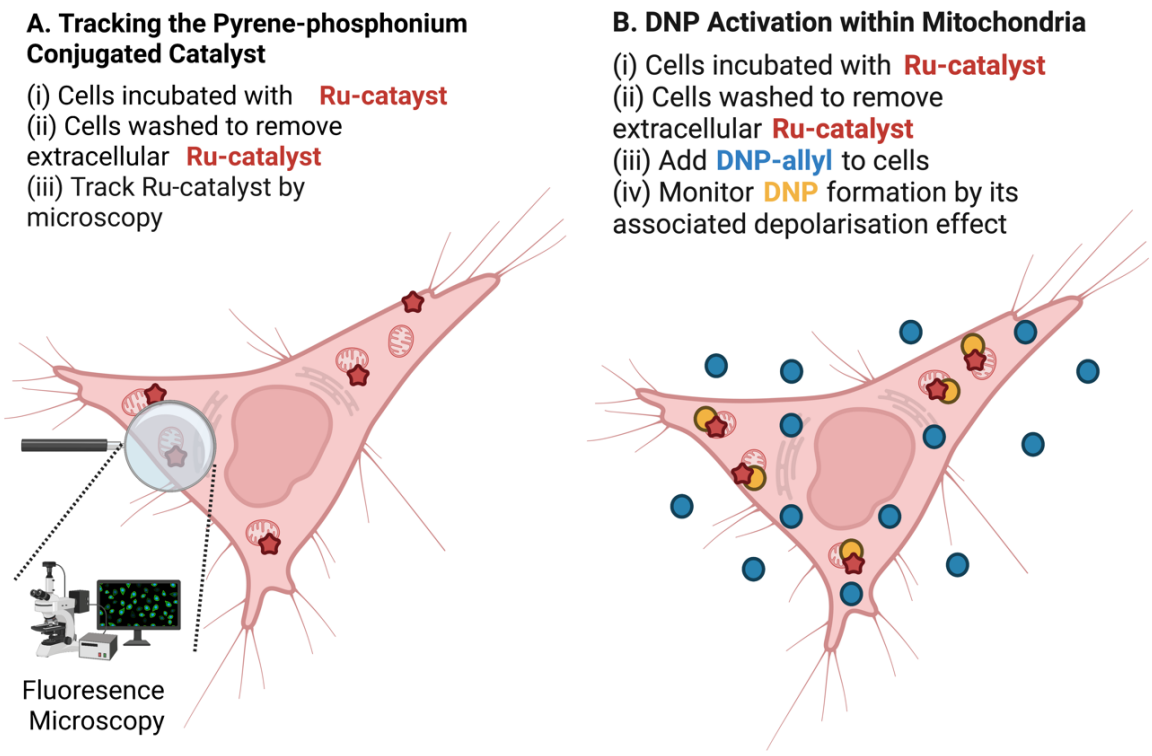

Figure 18 Schematics to illustrate experiments reported by Tomás-Gamasa *et al.*[31] for (A) the cellular tracking of the pyrene-phosphonium conjugated catalyst **Ru-11** within HeLa cells (B) the confined activation of 2,4-dinitrophenol (DNP) within the mitochondria of HeLa cells using **Ru-11**. Created with Biorender.com.

Controlling Intracellular *versus* Extracellular Bio-orthogonal Reactions using Nanozymes

In 2019, Das *et al.*[32] reported so called 'nanozymes' for targeted intracellular or extracellular bio-orthogonal reactions. These nanozymes were composed of the Kitamura-type catalyst reported by Streu and Meggers in 2006 encapsulated in a gold-centred nanoparticle.[27] By modifying the interacting unit on the outside of the nanoparticle, they could control uptake into HeLa cells. Where decoration with a zwitterionic motif provided selective extracellular reactions, decoration with positively charged motifs provided uptake and therefore intracellular reactions. The location of these nanozymes within a HeLa cell line was visualised utilising a combination of cell permeable and cell impermeable fluorescent dyes and confocal microscopy.

Considering the successful application of the Kitamura-type catalysts for bio-orthogonal reactions within human cell lines, especially for the activation of

prodrugs, it is surprising this strategy has not yet been applied to the activation of antibacterial prodrugs for the treatment of bacterial infections.

1.3 Antibacterials

1.3.1 The Antibacterial Pipeline

Antibacterials are drugs used in the treatment of bacterial infections to kill (bactericidal) or inhibit the growth of (bacteriostatic) pathogenic bacteria, where those derived from natural products are called antibiotics. Antibacterials are commonly classified by their mode of action, chemical structure, or spectrum of activity. Since the discovery of the first antibacterial, penicillin in 1928 by Sir Alexander Fleming, a wide range of antibacterial classes have been developed; most of these between 1940 – 1960, a time period hailed as the 'Golden Age' of natural product drug discovery, Figure 19.[37, 38] Since this era, few novel antibiotic classes have been discovered.

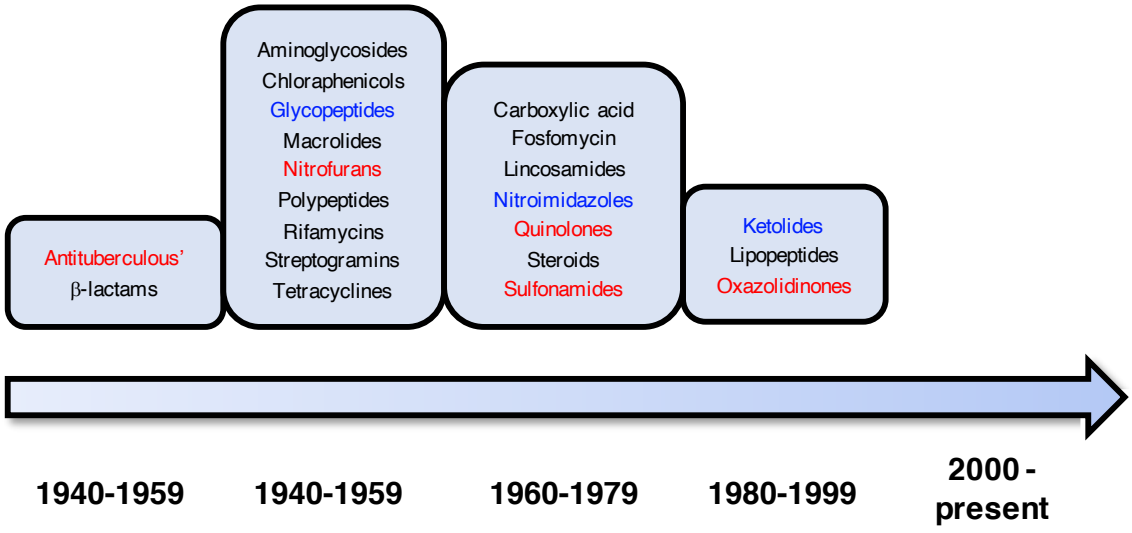

Figure 19 Timeline indicating the year of discovery for antibacterial classes.[37] Colour of text indicates derivation, black = natural product, red = synthetic, blue = semi-synthetic.

1.3.2 Antibacterial Resistance

Bacterial strains exposed to antibacterials can be intrinsically resistant or acquire resistance through natural selection by either chromosomal mutations or horizontal gene transfer (e.g. plasmids). Bacteria with a selective advantage then replicate and

distribute this information, resulting in resistant strains.[37] The various resistance mechanisms to clinically available antibiotics, some of which are depicted in Figure 20.[39-41], have been reviewed.[41, 42] For example, the primary method for β-lactam antibiotic resistance is the bacterial production of β-lactamase enzymes that inactivate the drug; this is an example of resistance mechanism 3, in Figure 20. In contrast, resistance mechanisms to fluoroquinolone antibacterials mainly involve chromosomal mutations in the protein target (mechanism 4) as well as the overproduction of efflux pumps (mechanism 1) and the reduced expression of porins that facilitate uptake (mechanism 5).

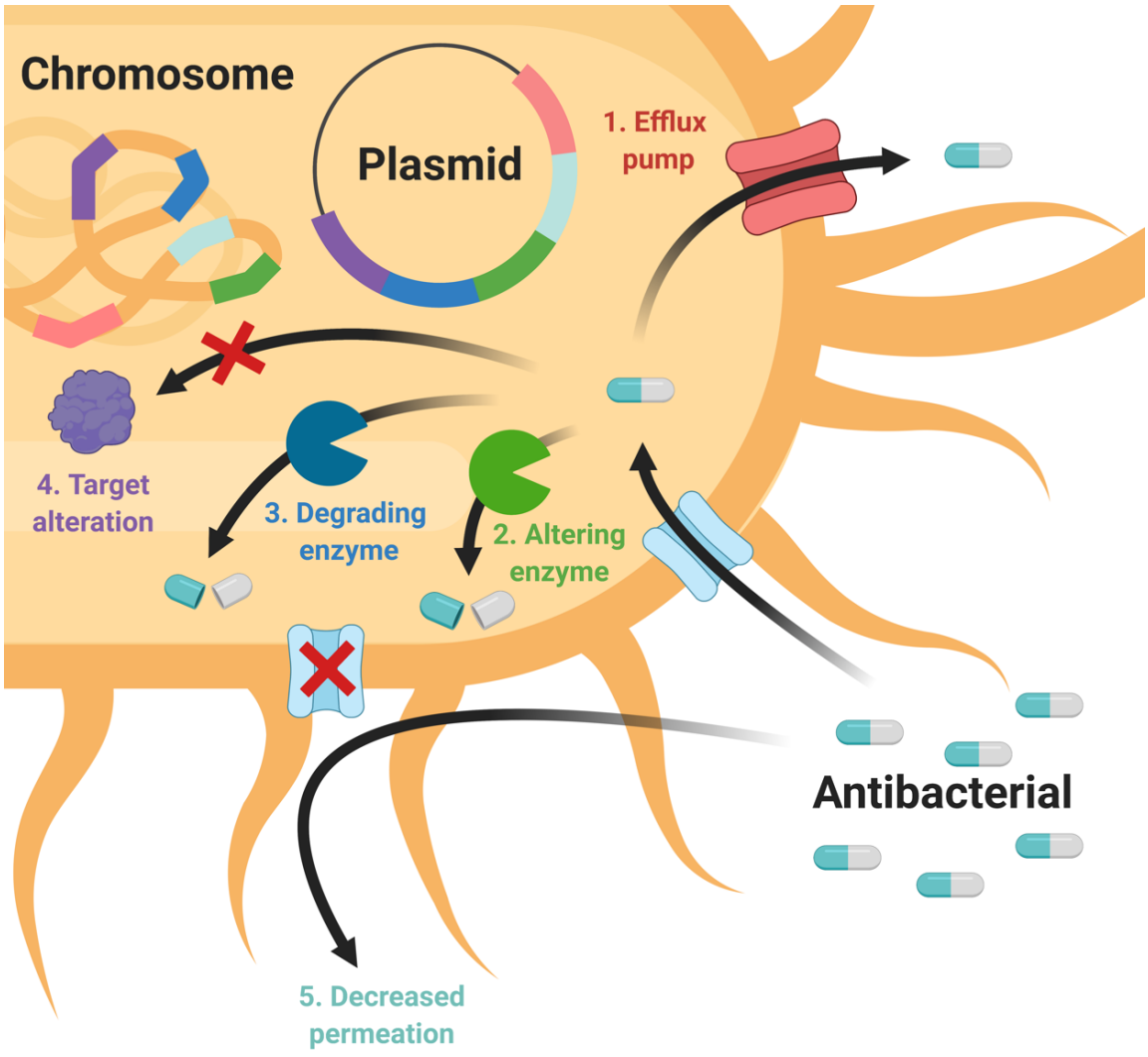

Figure 20 Antibacterial resistance mechanisms. Created with BioRender.com.[39]

If a bacterial strain becomes resistant to multiple antibiotics, it is labelled multi-drug resistant (MDR) and an increasing prevalence of such pathogens has been reported in recent years.[43] In 2015, an MDR bacterial strain was found to be resistant to the

'antibiotic of last resort' colistin and the first infection in human was reported in the United States of America in 2016. The gene believed to be responsible for this resistance development is called mcr-1 (Mobilised Colistin Resistance), an example of a gene that is rapidly shared *via* horizontal transfer.[44] This gene codes for a protein that modifies the lipid A present on the outer-membrane of Gram-negative bacteria resulting in lower colistin affinities and thus reduced potencies.

Due to the increased prevalence of resistant and MDR bacterial strains, the fight against bacterial infections is becoming increasingly important. The World Health Organisation (WHO) regularly assesses the condition of the antibiotic pipeline and its ability to combat the current rate of resistance.[45] Their recent study concluded that current antibiotic development is 'insufficient to mitigate the threat of antimicrobial resistance'. This document outlines the need for antibiotics with novel modes of action or the modification of existing antibiotics to bypass resistance mechanisms. One example of the latter method includes the attachment of antibacterials to compounds called siderophores for the generation of Trojan-Horse antibacterials.[46-48] Siderophores are compounds produced by bacteria to scavenge and internalise iron from their surrounding environment, see section 1.4.

1.4 Iron-uptake in Bacteria

1.4.1 Iron in Biology

Iron is an essential resource for most living organisms and in aqueous media, commonly exists in its +2 and +3 oxidation states. Due to iron's specific redox chemistries and high affinity for oxygen, it has been exploited by organisms for various biological processes, including the electron transport chain for the synthesis of ATP. Despite its biological merit, iron is toxic in excess due to its ability to create radical oxygen species (ROS) and therefore organisms have developed regulatory systems to maintain levels within an ideal range.[49-51] During the earth's oxygenation event, the predominant oxidation state of iron was shifted towards Fe(III). This caused a dramatic decrease in iron bioavailability due to the decreased solubility of Fe(III), and microorganisms adapted accordingly.

1.4.2 Siderophores

Siderophores are low molecular-weight compounds that possess a high affinity and selectivity for Fe(III).[49-51] These compounds are biosynthesised and secreted by bacteria, fungi and some plants, into their surrounding medium, to bind to and solubilise Fe(III), facilitating its cellular uptake. The Fe(III) is then released from the siderophore intracellularly.

The high selectivity of siderophores for Fe(III) can be attributed to their well-matched coordination geometries and donor atom 'hardness'. Fe(III) is a 'hard' ion according to Hard-Soft Acid Base (HSAB) theory with a d^5 electronic configuration and thus, favours coordination to charge dense, negatively charged donor atoms, in an octahedral geometry.[52, 53] To satisfy these preferences, siderophores are typically made up of bidentate chelator motifs composed of negatively charged oxygen donor atoms. Although they vary in denticity and backbone structure, the iron-binding components of siderophores are mainly limited to three types of bidentate chelator: catecholates, hydroxamates, and α-hydroxycarboxylates, Figure 21, where the most thermodynamically stable iron-complexes employ hexadentate ligands.

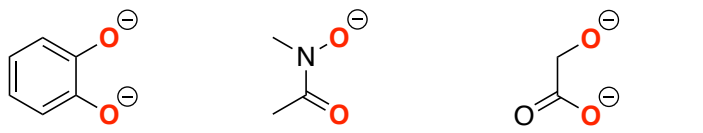

Catecholate (13.0, 9.2) **Hydroxymate** (9.0) **α-Hydroxycarboxylate** (3.0, 14.5)

Figure 21 Chemical structure of the most common chelator motifs in siderophores, with donor atoms in red and pKa values in brackets.

The discovery of the first siderophore dates back to the late 1940s and since then over 500 additional siderophores have been identified.[51, 54] The chemical structure of exemplar siderophores are shown in Figure 22. There are few other biologically-important trivalent metals and therefore there is little competition for iron-siderophore binding in nature. Although Al(III) is present in several biological settings, its smaller ionic radius (Al(III) = 0.54 Å, Fe(III) = 0.65 Å) renders siderophore binding weaker. For example, the log affinity constants for desferrioxamine B (DFO) with Fe(III) and Al(III) are 30.5 and 21.4, respectively.[51]

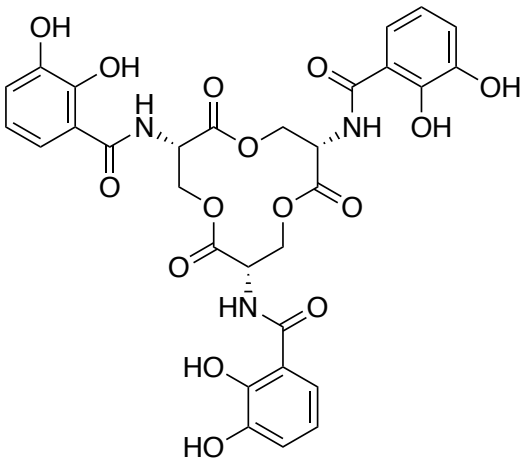

enterobactin

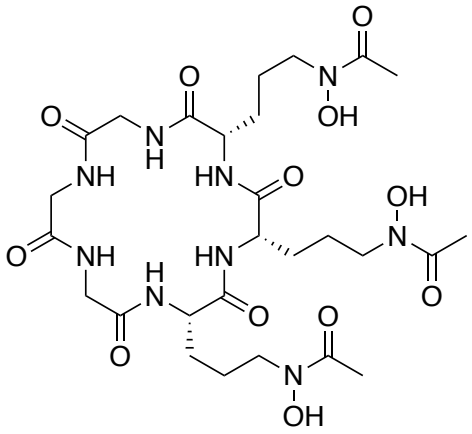

desferrichrome

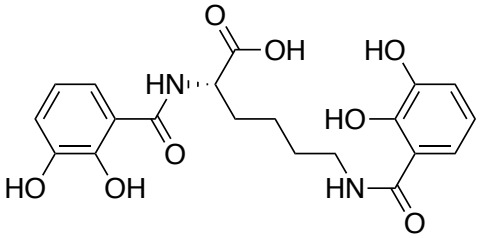

azotochelin

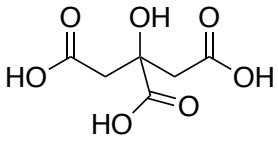

citrate

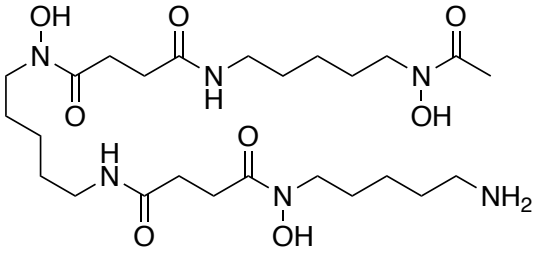

desferrioxamine B

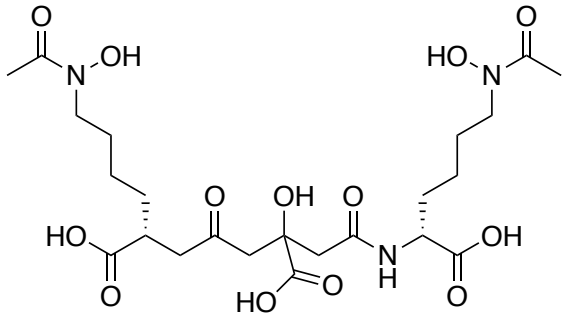

aerobactin

Figure 22 Chemical structures of siderophores enterobactin, desferrichrome, azotochelin, citrate, desferrioxamine B (DFO), and aerobactin.

The iron-binding strength of siderophores varies and cannot be simply interpreted using a formation constant (K_f). This is because siderophore iron-binding motifs require deprotonation prior to iron-complexation. Instead, siderophore iron affinities are typically quantified using pFe(III) at a known pH (commonly physiological pH 7.4), which accounts for the proton competition in aqueous media, where larger pKa values give stronger competition, Equation 1.[51] Larger pFe(III) values correspond to stronger iron-binding. The pFe(III) constants for exemplar siderophores are shown in Table 1, alongside their corresponding denticities.

$$pFe(III) = -\log[Fe(III)]_{unbound}$$

Equation 1 pFe(III) definition. $[Fe]_{total}$ = 1 mM, $[siderophore]_{total}$ = 10 mM.

A favourable entropic contribution arises from displacing the bound hydroxide ligands of $Fe(OH)_3$ to release water molecules. As previously stated, larger iron-affinities are observed for higher denticity siderophores, up to hexadentate complexes. This phenomenon can be attributed to the chelate effect, as the iron-binding motifs are predisposed for complexation to iron.

Table 1 Denticity and pFe(III) binding constants for siderophores and controls (EDTA, DHBA and hydroxide). DHBA = 2,3-dihydroxy-*N,N'*-dimethylbenzamide, EDTA = ethylenediaminetetraacetic acid.

Siderophore	Denticity	pFe(III)	Reference
Enterobactin	6	35.5	[55]
Desferrioxamine B	6	30.5	[56]
Aerobactin	6	23.4	[57]
EDTA	6	23.4	[51]
Citrate	3	17.7	[58]
DHBA	2	15	[59]
Hydroxide ions	1	14.6	[51]

1.4.3 Iron Homeostasis in Bacteria

In Gram-negative bacteria, iron-uptake pathways are regulated by an iron-dependent repressor protein called Fur.[51] This protein acts at a transcriptional level and when bound to intracellular Fe(II), binds to specific DNA regulatory sequences, to prevent their transcription.[60, 61] The Fur regulon includes genes that are responsible for the biosynthesis of siderophores and their translocation inside bacteria (e.g. cell-surface receptors).[62] When bacteria experience iron-limiting conditions, intracellular levels of Fe(II) are depleted which leads to iron's dissociation from Fur and thus the induction of gene expression. Consequently, the

utilisation of siderophore-mediated iron-uptake pathways is upregulated under iron-limited conditions. Similar regulatory proteins exist for Gram-positive bacteria, examples include DrxR.[51]

1.4.4 Siderophore-mediated Iron-uptake in Bacteria

Siderophores that have acquired Fe(III) from the bacteria's extracellular environment are then recognised and bound to specific, complementary cell-surface receptors, which are typically β-barrels. In Gram-negative bacteria, a protein complex, TonB, anchored to the inner-membrane by ExbB and ExbD, mediates the transferal of iron-siderophore complexes across the outer-membrane into the periplasm.[63] Inside the periplasm, the siderophore complex binds to cognate periplasmic proteins and is transported across the inner-membrane to the cytoplasm *via* ABC transporters, Figure 23A. In contrast, as Gram-positive bacteria only possess the one membrane, specific cell-surface receptors on this membrane bind to and transfer the siderophore-iron complexes across the membrane *via* ABC transporters directly into the cytoplasm, Figure 23B.[64]

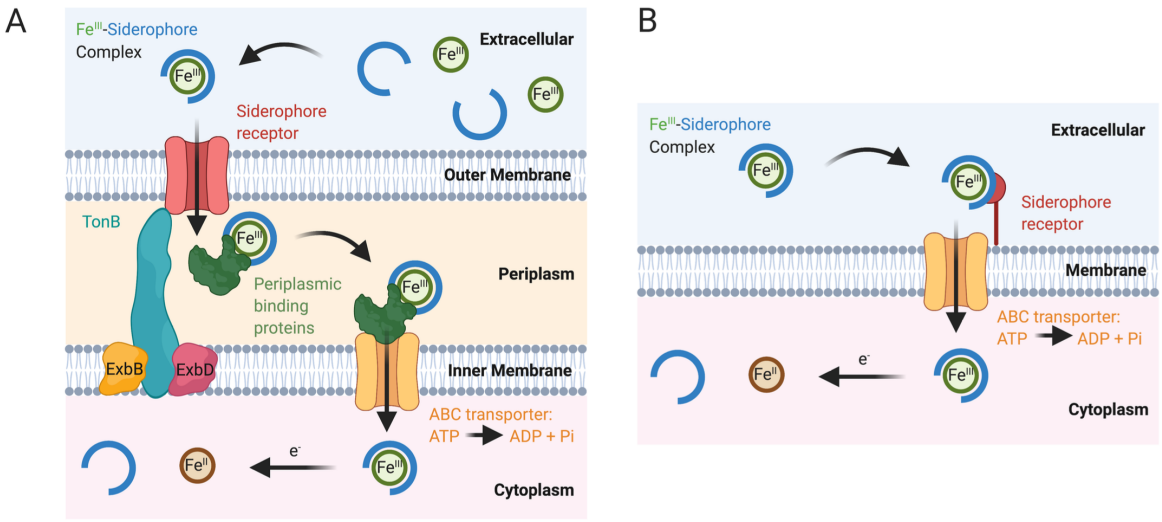

Figure 23 Schematic of siderophore-mediated iron-uptake into a (A) Gram-negative and (B) Gram-positive bacterial cell (peptidoglycan omitted for brevity). Reprinted from Southwell, J. W.; Black, C. M.; Duhme-Klair, A.-K., *ChemMedChem* **2021**, 16, 1063.[65]

1.4.4.1 Siderophore-mediated Iron-uptake in *E. coli*

The major siderophore for *E. coli* is enterobactin and was simultaneously isolated and characterised in the 1970s from cultures of *Salmonella typhimurium* and *E. coli*, Figure 22.[66, 67] Enterobactin is a hexadentate siderophore composed of three catecholate iron-binding motifs. Each catecholate is attached to an *L*-serine amino acid *via* an amide bond to give three 2,3-dihydroxybenzoylserine (DHBS) units which are bonded together to form a cyclic trilactone. This backbone forms an ideally suited cavity size for Fe(III) as the intramolecular hydrogen bonds that form between the amide nitrogen and *ortho*-phenolate in the structure impose rigidity thus pre-disposing it for Fe(III)-binding; this provides an entropic contribution to the stability of the resulting complex, Figure 24. Consequently, enterobactin possesses an extremely high affinity for Fe(III) ($\log K_f$ = 49.0, pFe^{III} = 35.5) at physiological pH 7.4.[59, 68] Moreover, the intramolecular hydrogen bonding significantly lowers the pKa of the *ortho*-phenolates to 7.2, reducing proton competition thereby enhancing Fe(III)-complex stability.

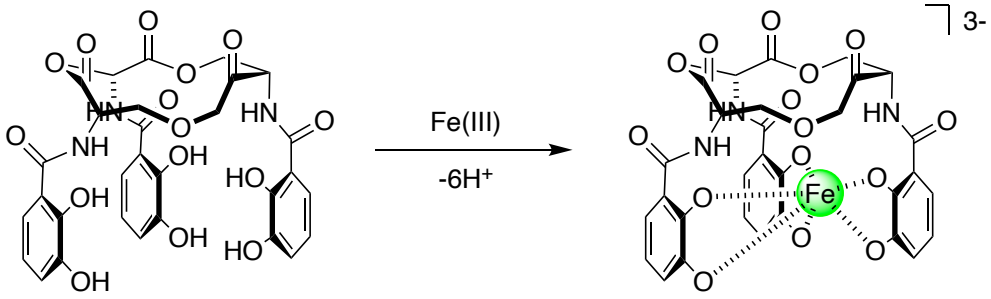

Figure 24 Schematic to show enterobactin's pre-disposed geometry for Fe(III) coordination.

When enterobactin captures extracellular Fe(III), the resulting complex is taken up across the outer-membrane by cell-surface receptor FepA into the periplasm where it binds periplasmic protein FepB Figure 25. The iron-siderophore complex is then internalised *via* the ABC transporter FepCDG across the inner-membrane.[63, 69, 70] On entry to the bacterial cytoplasm, the cyclic trilactone of the enterobactin-Fe(III) complex is hydrolysed by the Fes esterase to release the reduced Fe(II) oxidation state.[71]

The ester backbone of enterobactin is prone to hydrolysis and leads to the formation of the H_6-linear trimer, H_4-linear dimer, and the H_2-monomer of DHBS, Figure 26. The loss of pre-disposition of the H_6-linear trimer compared to enterobactin is reflected in their respective $\log_{10}K_f$ values of 43 and 49.[72] Each of these hydrolysis products have been shown to promote bacterial growth, demonstrating their function as 'secondary' siderophores. This is the case for the enteric (bacteria that infect the gastrointestinal tract) pathogens *E. coli* [73, 74] and *Campylobacter jejuni (C. jejuni).*[75] In contrast, *C. jejuni* do not themselves produce enterobactin and therefore these hydrolysis products are termed xenosiderophores.[76] For *E. coli*, it is believed the enterobactin hydrolysis product DHBS is internalised through the outer-membrane transporters FepA, Fiu and Cir, Figure 25.[73] It is not certain whether these hydrolysis products are exported by *E. coli* after hydrolysis by Fes, or utilised after extracellular hydrolysis.

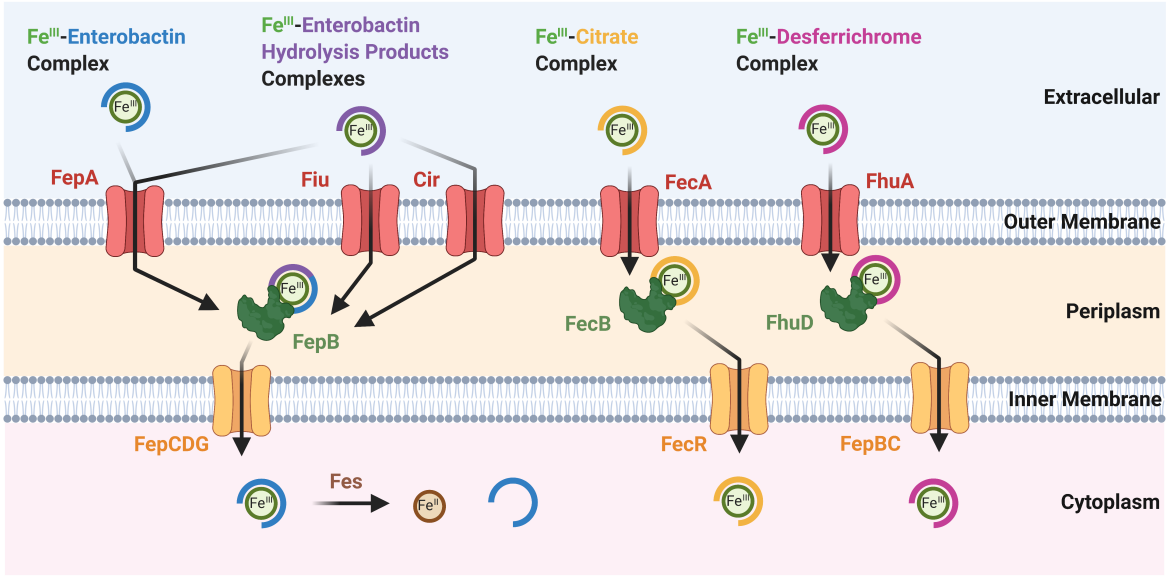

Figure 25 The uptake mechanisms in *E. coli* for Fe(III) complexes with enterobactin, enterobactin hydrolysis products, citrate and desferrichrome. Created with BioRender.com.

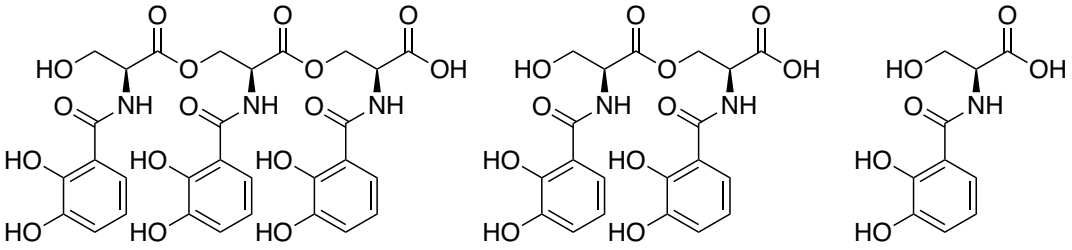

H_6-linear trimer **H_4-linear dimer** **H_2-DHBS**

Figure 26 Chemical structures of enterobactin's hydrolysis products.

In 1977, Hancock *et al.* investigated the 2,3-dihydroxybenzoic acid (DHB)-mediated uptake of Fe(III) into *E. coli* bacteria.[77] From this work, it was concluded DHB did indeed facilitate iron-uptake *via* diffusion across the outer-membrane followed by transfer to enterobactin or its hydrolysis products in the periplasm where translocation into the cytoplasm occurred *via* ABC transporters. This conclusion is made due to the enterobactin-dependent growth enhancement of mutants of *E. coli* deficient in DHB biosynthesis, supplemented with DHB under iron-limited conditions. These results are reinforced by growth response assays by Winkelmann *et al.* in 1991.[78]

There also exist siderophores for *E. coli* that are not catechol-based, such as citrate and desferrichrome, Figure 22. Iron-uptake pathways that utilise citrate are believed to be induced in its presence, where citrate-Fe(III) complexes are taken up into the periplasm by cell-surface receptor FecA, subsequently bound to periplasmic protein FecB and translocated in the cytoplasm by FecR, Figure 25.[51, 79-81] Citrate-mediated iron-uptake pathways in *E. coli* are significantly less important than those of enterobactin.

Desferrichrome is a cyclic hexapeptide composed of glycine and ornithine amino acids. The side chains of the latter are *N*-acetylated and *N*-hydroxylated to give three hydroxamate motifs, where each provides two donor atoms to form a hexadentate Fe(III) complex. When bound to Fe(III), these complexes are taken up into the periplasm of *E. coli via* the cell-surface receptor FhuA and bound to the periplasmic binding protein FhuD.[73, 82] It is believed all hydroxamate-based siderophores are translocated across the cytosolic membrane by the same transport

systems; the aforementioned periplasmic binding protein FhuD and an inner-membrane transporter composed of FhuB and FhuC, Figure 25.[83]

1.4.5 Antibacterial-Siderophore Conjugates

Siderophores have also been exploited by some bacteria, in the form of antibacterial-siderophore conjugates termed sideromycins. An example of which is produced by *Streptomyces sp.* called albomycin, Figure 27.[84] Disguised as innocent siderophores, sideromycins are internalised by bacteria as their Fe(III)-complex *via* siderophore pathways, where the antibacterial component is then released, resulting in cell death. In fact, the discovery of sideromycins pre-dates that of siderophores. These conjugates have since inspired synthetic analogues which are commonly referred to as 'Trojan-Horse' antibacterials due to analogies made with the wooden horse utilised to conquer the city of Troy in Greek mythology.[47, 48] To date, several Trojan-Horse antibacterials have been investigated for potential pharmaceutical applications however only cefiderocol (FETROJA®) has made it to the clinic, for the treatment of urinary tract infections, Figure 27.[85-87]

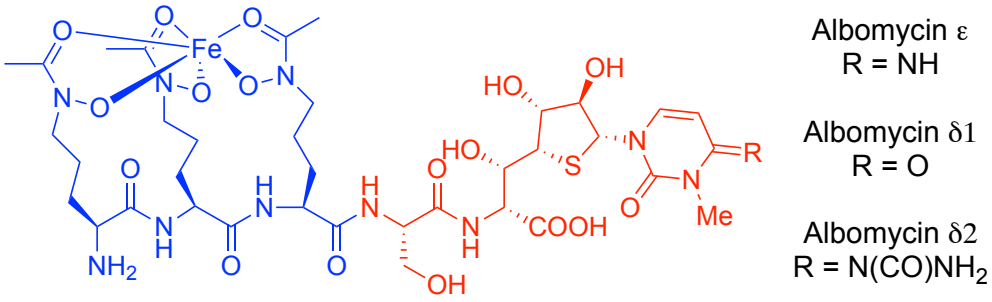

albomycin

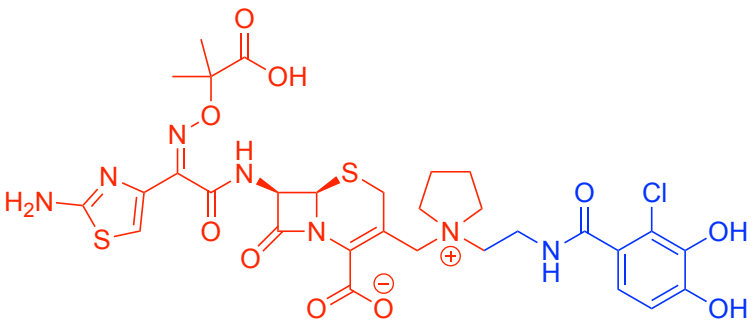

cefiderocol

Figure 27 Chemical structures of sideromycin albomycin and Trojan-Horse antibacterial, cefiderocol. Antibacterial warhead = red, siderophore mimic = blue.[65]

1.4.5.1 Targeting Enteric Pathogens

The relative amounts of Fe(III) and Fe(II) within the gastrointestinal (GI) tract are difficult to predict. The species distribution varies significantly throughout the GI tract mainly due to changes in oxygen partial pressure and pH. Under atmospheric conditions, iron is mostly in its +3 oxidation state, however, at lower pH and oxygen levels its +2 oxidation state becomes increasingly prevalent. Uptake pathways for Fe(II) differ to those for Fe(III), and bacteria possess mechanisms that detect the form of iron available and alter iron uptake pathways accordingly.[88] In *E. coli*, Fumarate and Nitrate Reductase (FNR) is the global regulator that controls transcription of genes whose functions facilitate adaptation to growth under O_2 limiting conditions such as that in the intestines.[89, 90] When low oxygen conditions are detected, iron-uptake pathways for *E. coli* typically result in decreased iron-uptake *via* siderophores.[91] Furthermore, the repressor protein Fur repsonsible for iron-homeostasis is upregulated in response to decreased oxygen levels.[92, 93] Despite this, significant amounts of iron in the intestine are present in the +3 oxidation state, as studies have reported the production of siderophores by bacteria in this enviroment.[94] These findings suggest siderophores are commonly utilised by enteric pathogens in the colonic lumen to outcompete the resident microbiota, especially when the intestine is inflamed. Furthermore, studies by Pi *et al*. have reported the requirement for the catechol-mediated iron-uptake into *E. coli* that reside in the GI tract, as ΔtonB deletion mutants showed impaired colonisation in the intestinal lumen of mice.[95] Therefore, the targeting of pathogenic *E. coli* in the intestine using siderophores is promising, be this by their attachment to antibacterials or alternative compounds that facilitate intracellular reactions such as those outlined in section 1.2 for the activation of prodrugs.[96-98]

1.5 Project Aims

The overall aim of this project is to develop siderophore-conjugated Kitamura-type catalysts for the activation of antibacterial prodrugs within bacterial cells. Individual objectives are:

1. The design and synthesis of a suitable antibacterial prodrug for activation by the bio-orthogonal Kitamura-type catalysts.
2. The measurement of catalyst-mediated prodrug activation kinetics under biologically-relevant conditions.
3. The investigation of catalyst stabilities and thus, the identification of a suitable medicinal application.
4. The determination of prodrug antibacterial activity compared to their active form against relevant bacteria under conditions that mimic the targeted host environment.
5. The synthesis of catalyst-siderophore conjugates and the measurement of their activity for prodrug activation under biologically-relevant conditions.
6. The determination of conjugate toxicities to bacteria and their enhanced antibacterial action following prodrug co-addition.
7. The evaluation of catalyst-siderophore conjugate uptake into bacteria.

Chapter 2 : The Design, Synthesis, and Biological Activity of Antibacterial Prodrugs

2.1 Introduction

2.1.1 Fluoroquinolones

Quinolones are an important class of broad-spectrum antibacterial agent, active against Gram-negative, Gram-positive, mycobacteria, and anaerobic bacteria, commonly used in the clinic for the treatment of respiratory and urinary tract infections.[42] The first quinolone is generally believed to be nalidixic acid, Figure 28, and was discovered in the early 1960s.[99] Since then, extensive SAR studies have produced numerous improved analogues, with expanded spectrum-activity and higher efficacy.[100] This development has proceeded through chemical modification of the bicyclic core structure related to 4-quinolone, Figure 29. This includes fluoroquinolones, as they are now more commonly known, a sub-category of quinolone antibiotics, fluorinated on the bicyclic core.

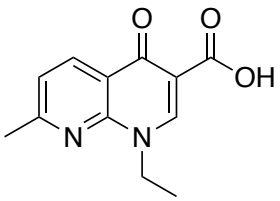

Figure 28 Chemical structure of nalidixic acid.

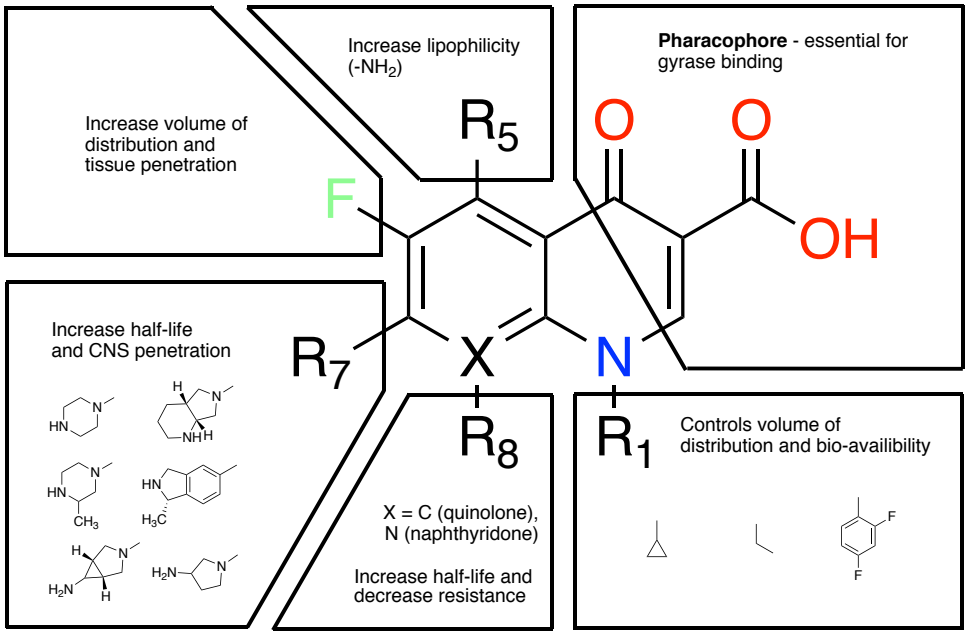

Figure 29 Core structure of quinolone antibacterials. The X atom and R groups represent functional motifs that have been varied between quinolone analogues.

2.1.2 Mode of Action

The antibacterial action of fluoroquinolones can be attributed to their targeted inhibition of topoisomerase type IIA enzymes in bacteria: DNA gyrase and topoisomerase IV, generally for Gram-negative and Gram-positive bacteria respectively.[101] Topoisomerases are essential and ubiquitous A_2B_2 heterotetrameric enzymes that regulate DNA topology. They act by forming a double-stranded DNA break stabilised by forming covalent bonds between the catalytic tyrosines and 5'-phosphates of the DNA, passing another DNA duplex through this breakage followed by re-annealing. Fluoroquinolones intercalate DNA at nicks introduced by topoisomerases, located in the α-helix near the active-site tyrosine that induces the breakage. A crystal structure depicting these interactions is shown in Figure 30, for the fourth generation quinolone moxifloxacin complexed with topoisomerase IV from *Acinetobacter baumannii*.[102] The most significant quinolone-enzyme interaction is the contribution of the water-mediated β-keto acid motif binding to the magnesium co-factor, alongside serine and aspartic/glutamic acid residues of the enzyme.[103] This motif is conserved in all fluoroquinolone antibacterials.

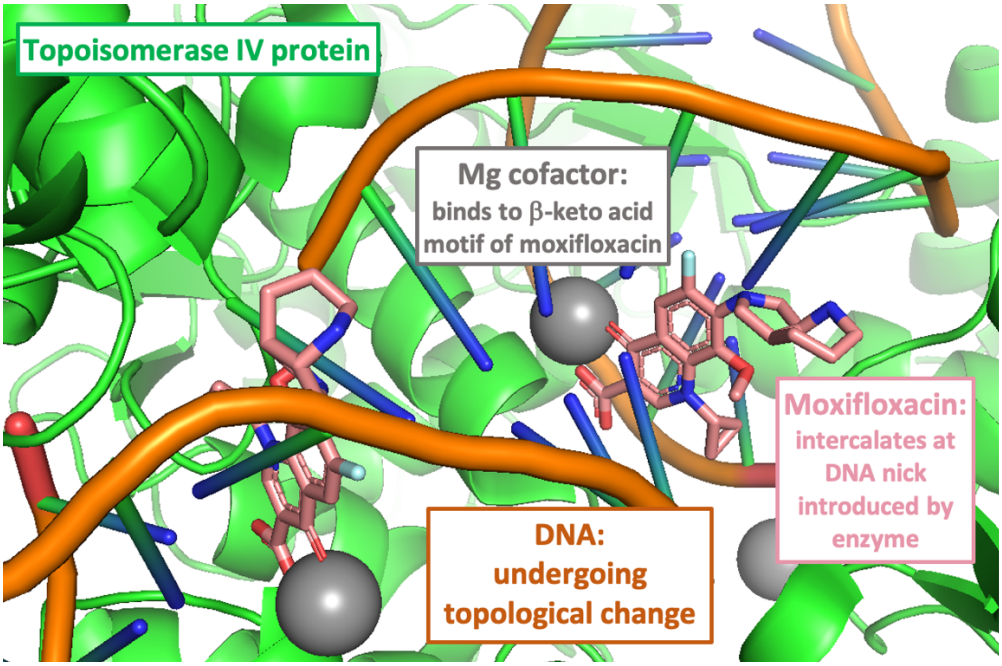

Figure 30 Crystal structure (PDB 2XKK) of moxifloxacin, with topoisomerase IV and DNA (in *Acinetobacter baumannii*), made with PyMOL.[102] Pale pink = moxifloxacin (fluoroquinolone), grey sphere = magnesium co-factor, orange = DNA backbone, green = topoisomerase IV.

2.1.3 Side Effects

Fluoroquinolones are known to have several side effects, the most common being gastrointestinal (nausea, dyspepsia, vomiting) and/or effects on the central nervous system (dizziness, insomnia, headache).[104, 105] More rare serious side effects can include tendon rupture and phototoxicity.[105, 106] Ciprofloxacin and moxifloxacin are known to possess a degree of UV-associated genotoxicity (phototoxicity) and cytochrome P450 inhibition.[107] In 2016, the US Food and Drug Administration (FDA) released an update on fluoroquinolone antibiotics, stating: *'FDA safety review found that both oral and injectable fluoroquinolones are associated with disabling side effects involving tendons, muscles, joints, nerves and the central nervous system'*.[108]

2.1.4 Resistance Mechanisms

In 2019, the World Health Organisation (WHO) labelled *Mycobacterium tuberculosis* as the global priority pathogen, whilst *Salmonella,* and *Campylobacter* species and *Neisseria gonorrhoeae* were labelled high priority and *Shigella* species as medium priority, partly due to their fluoroquinolone resistance.[45] Fluoroquinolones are known to enter bacterial cells predominantly *via* porins and lipid-mediated pathways. Several resistance mechanisms are thought to occur for quinolones, outlined in section 1.3.2, such as reduction in the expression of outer-membrane porins of bacteria, preventing cellular uptake.[109-111]

2.1.5 Chapter Aims

The primary aim of the work in this Chapter is to identify an antibacterial candidate and synthesise its prodrug *via* chemical modifications with suitable abiotic motifs for catalyst-mediated activation inside bacterial cells. Limiting the exposure of human cells to fluoroquinolones *via* a prodrug strategy is promising for the mitigation of side effects. Furthermore, chemical modification to form fluoroquinolone prodrugs should significantly alter bacterial uptake pathways, which could combat resistance mechanisms such as decreased levels in outer-membrane porins.

The selected catalysts for prodrug activation are the optimised Kitamura-type catalysts first utilised for prodrug activation by Völker and Meggers in 2017.[33] These catalysts can cleave allyl carbamates and allyl esters to release the free amine and carboxylic acid, respectively. Several fluoroquinolone antibiotics possess both amine and carboxylic acid functionalities, and therefore fluoroquinolones were chosen as the model antibacterial for these studies. After their design and synthesis, their compatibility for prodrug activation with the selected catalyst will be measured under biologically-relevant conditions to evaluate their suitability for medicinal application. Following this, their antibacterial activity will be measured *versus* the parent antibiotic under conditions that mimic those imposed by an infected host organism. After an upper, non-toxic concentration has been determined for the prodrugs, their bacterial uptake will be evaluated.

2.2 The Design and Synthesis of Antibacterial Prodrugs

In order to begin investigations into catalyst-mediated prodrug activation, a suitable antibacterial must first be identified. The ideal fluoroquinolone candidate will possess broad-scope antibacterial potency against medicinally relevant bacteria. During their design, reported fluoroquinolone SAR studies and observed prodrug physical properties will be considered to predict their target inhibition and bacterial uptake mechanisms. Moreover, the synthesis of the prodrug targets will exploit pre-existing synthetic conditions for similar compounds, so that an efficient synthetic pathway can be found.

2.2.1 Fluoroquinolone Prodrugs

Ciprofloxacin is a broad-spectrum, second-generation quinolone antibacterial that targets Gram-negative bacteria and some atypical pathogens such as *Mycoplasma pneumonia* and *Chlamydia pneumonia*, Figure 31. Moxifloxacin is a broad-spectrum, fourth-generation quinolone antibacterial. Whilst retaining the excellent antibacterial potencies against Gram-negative bacteria that earlier generations such as ciprofloxacin possess, moxifloxacin provides expanded Gram-positive coverage and improved activity against atypical pathogens and under anaerobic conditions.[107]

Similar to many quinolones, ciprofloxacin and moxifloxacin both possess the essential β-keto acid motif (*C*-terminus) and a secondary amine (*N*-terminus); these functional groups provide means for chemical modification to form allyl ester and allyl carbamate-modified versions, respectively, which should be compatible for catalyst-mediated cleavage.

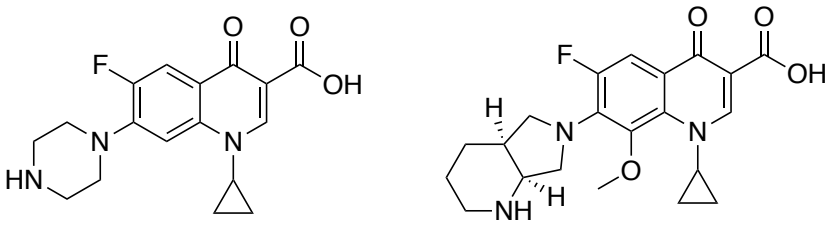

ciprofloxacin **moxifloxacin**

Figure 31 Chemical structures of fluoroquinolones ciprofloxacin and moxifloxacin.

2.2.1.1 *O*-Allyl carbamate-protected Fluoroquinolones

As previously described in section 1.2.1, Kitamura-type catalysts have been used for the cleavage of allyl carbamate-protected amines. As ciprofloxacin and moxifloxacin possess secondary amines, their respective allyl carbamate prodrugs ***N*-cipro** and ***N*-moxi**, can be synthesised, Figure 32. SAR studies for quinolones have led to numerous examples of clinically-approved drugs through modifications at the *N*-terminus, Figure 29.[107] Therefore, it is proposed that these prodrugs might retain substantial antibacterial potency, thereby yielding a poor toxicity window. Nevertheless, similar prodrugs of these antibacterials have recently been studied by Rotello *et al.* in 2020 for the treatment of biofilms utilising polymer-based bio-orthogonal nanocatalysts.[112, 113]

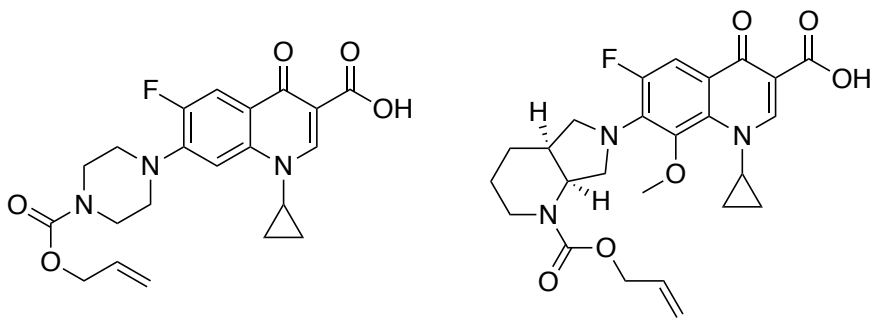

***N*-cipro** ***N*-moxi**

Figure 32 Chemical structure of *O*-allyl carbamate fluoroquinolone prodrugs of ciprofloxacin (***N*-cipro**) and moxifloxacin (***N*-moxi**).

Another consideration during prodrug design concerns bacterial uptake; it is important that the prodrugs of ciprofloxacin and moxifloxacin are still up-taken so that their catalyst-mediated activation can take place inside the bacteria. The major pathways for the uptake of quinolones by Gram-negative bacteria such as *E. coli*, utilise a combination of outer-membrane porins (in particular OmpF) and lipid-mediated pathways.[111] The relative contribution of these two pathways correlates with the lipophilicity of the specific quinolone, which includes the effect of the protonation state at physiological pH.[114, 115] A positive correlation has been established between the increased hydrophilicity of quinolone antibiotics, and their uptake *via* OmpF porins.[116] In addition, studies by Chapman and Georgopapadakou in 1988 suggested that increased quinolone hydrophobicity leads to greater uptake *via* lipid-mediated pathways.[114] The calculated octanol-water partition coefficients, $cLogD_{7.4}$, of ciprofloxacin and moxifloxacin are -1.24 and -1.11, respectively.[117] For details regarding these calculations, see section 6.4. Due to the hydrophilic nature of ciprofloxacin and moxifloxacin, bacterial uptake is predominantly *via* porins.[118] Therefore, it is hypothesised that the increased lipophilicity of ***N*-cipro** ($cLogD_{7.4}$ = 1.05) and ***N*-moxi** ($cLogD_{7.4}$ = 1.27), compared to their corresponding parent antibiotic, might preferentiate lipid-mediated uptake, in turn mitigating porin-deficiency type resistance mechanisms. The preservation of the β-keto acid motifs in ***N*-cipro** and ***N*-moxi** might enable additional uptake pathways; quinolones are known to bind to metals through this functionality and it is hypothesised that such complexes can utilise self-promoted uptake pathways, as well as porins, for crossing

the outer-membrane of Gram-negative bacteria.[114, 119-122] The syntheses of ***N*-cipro** and ***N*-moxi** are shown in Figure 33 and Figure 34, respectively.

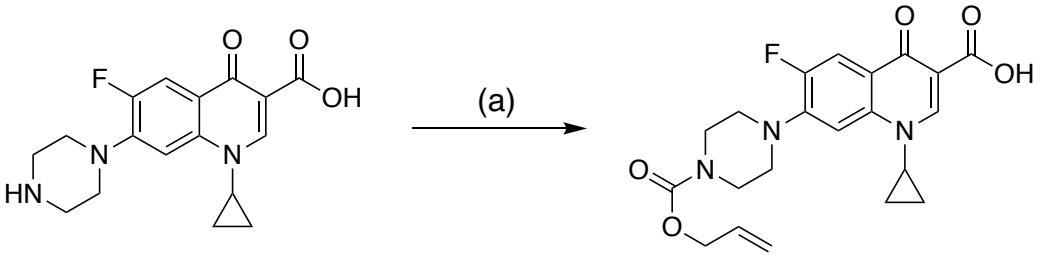

ciprofloxacin ***N*-cipro**

Figure 33 Synthesis of ***N*-cipro**. (a) allyl chloroformate, 1,8-bis(dimethyl)naphthalene, DIPEA, dry DCM, rt, 20 h, 91%.

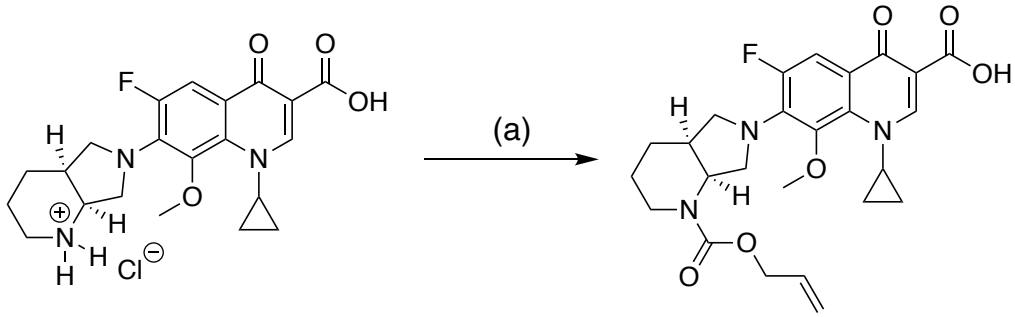

moxifloxacin.HCl ***N*-moxi**

Figure 34 Synthesis of ***N*-moxi**. (a) allyl chloroformate, 1,8-bis(dimethyl)naphthalene, DIPEA, dry DCM, rt, 18 h, 97%.

***N*-cipro** and ***N*-moxi** were obtained *via* one-step reactions from the readily available, inexpensive ciprofloxacin and hydrochloride salt of moxifloxacin, respectively. These reactions used basic conditions generated by a combination of *N,N'*-diisopropylethylamine (DIPEA) and 'proton sponge' to generate the free-bases of the secondary amines in ciprofloxacin and moxifloxacin, which then reacts with the electrophile allyl chloroformate to give ***N*-cipro** and ***N*-moxi** in 91% and 97% yields, respectively. The identity and purity of these novel, final compounds were confirmed by a combination of ^{1}H, ^{19}F and ^{13}C NMR spectroscopy, HRMS, IR spectroscopy and elemental analysis. ***N*-moxi** was also characterised by UV-vis spectroscopy.

2.2.1.2 Allyl ester-protected Fluoroquinolones

To the best of our knowledge, catalyst-mediated prodrug activation has not yet been utilised for allyl ester prodrugs. Compared to modification of the *N*-terminus, that of the *C*-terminus is expected to provide a more significant toxicity window, as the β-keto acid motif constitutes part of the quinolone pharmacophore. Therefore its chemical modification should perturb crucial interactions within the enzymatic targets, significantly decreasing the resulting prodrug's antibacterial activity compared to the parent antibiotic.[123, 124]

Similar to ***N*-cipro** and ***N*-moxi**, it is hypothesised that the increased lipophilicity of ***C*-cipro** ($cLogD_{7.4}$ = 1.66) and ***C*-moxi** ($cLogD_{7.4}$ = 1.22) compared to their parent antibiotics, might increase bacterial uptake *via* lipid-mediated pathways, in turn mitigating porin-deficiency type resistance mechanisms. In contrast to modification at the *N*-terminus, these prodrugs still possess their secondary amines that would be protonated under physiological conditions. Studies by Hergenrother *et al.* in 2017 and 2019 outline the importance of positively charged amines for uptake of rigid, small molecule drugs in Gram-negative bacteria and therefore it is hoped significant bacterial uptake is retained.[125, 126] The syntheses of ***C*-cipro** and ***C*-moxi** are shown below in Figure 35 and Figure 36, respectively.

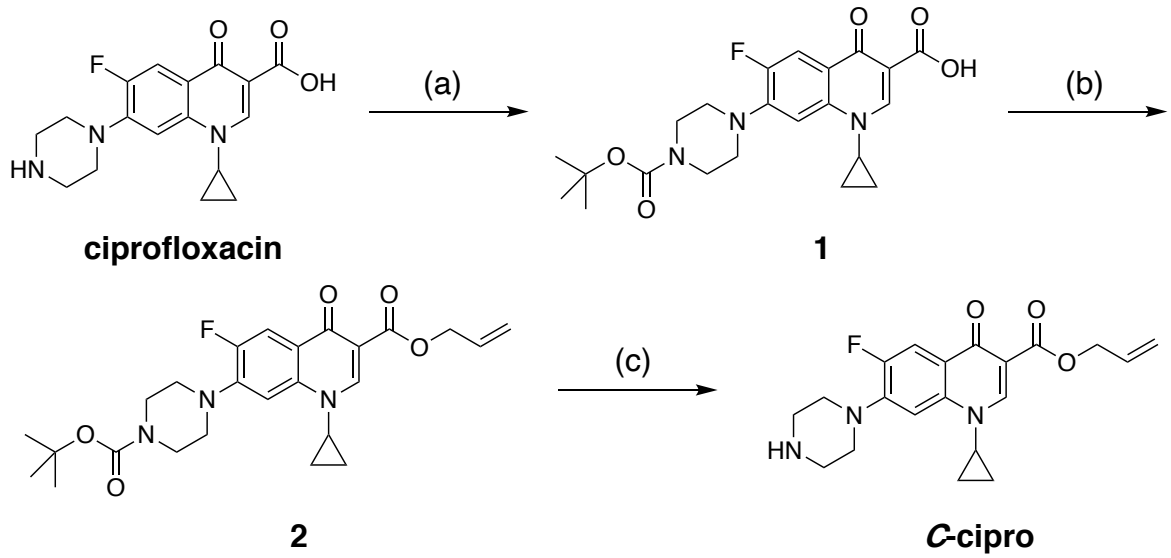

Figure 35 Synthesis of ***C*-cipro**. (a) NaOH (aq), Boc_2O, dioxane:water (1:1), rt, 2 h, 78% (b) allyl bromide, K_2CO_3, dry DMF, 80 °C, 18 h, 90% (c) TFA, rt, 2 h, 53%.

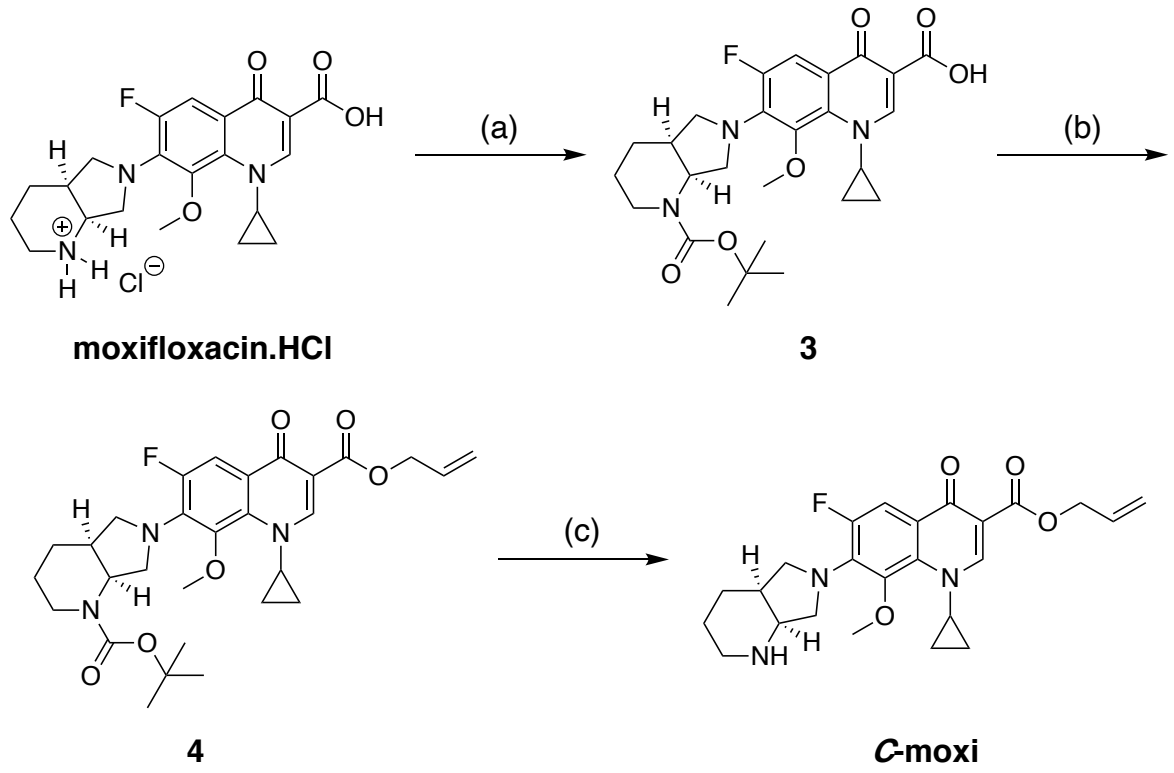

Figure 36 Synthesis of ***C*-moxi**. (a) NaOH (aq), Boc_2O, dioxane:water (1:1), rt, 3 d, 96% (b) allyl bromide, K_2CO_3, dry DMF, 80 °C, 18 h, 94% (c) TFA, rt, 18 h, 98%.

The synthesis of ***C*-cipro** and ***C*-moxi** was more challenging, as the secondary amines of ciprofloxacin and moxifloxacin require protection prior to allyl ester formation. Therefore, step (a) involves boc-protection of the secondary amine, using boc anhydride and sodium hydroxide in a dioxane:water solvent mixture. The presence of aqueous base whilst using boc anhydride is atypical due to a competing anhydride hydrolysis reaction to form tertbutyl carboxylic acid, however due to the poor organic solubility of ciprofloxacin and moxifloxacin such conditions were required; boc-protected ciprofloxacin, **1** and moxifloxacin, **3** were formed with 78% and 97% yields, respectively. The identity and purity of these literature compounds were confirmed by ^{1}H and ^{19}F NMR spectroscopy and HRMS compared to those reported by Tanaka *et al.* for the same compounds.[127]

In step (b), the electrophile allyl bromide in dry DMF at 80 ºC was used under basic conditions to react with the weakly nucleophilic carboxylic acids of ciprofloxacin and moxifloxacin, to form the *N*-boc-protected allyl esters of each, to give **2** and **4** in 90% and 94% yields, respectively. The identity and purity of novel compound **2** was confirmed by a combination of ^{1}H, ^{19}F and ^{13}C NMR spectroscopy, HRMS, IR

spectroscopy, and elemental analysis. Whereas that of literature compound **4**, was confirmed by ^{1}H and ^{19}F NMR, and HRMS compared to those reported by Houghton *et al.* for the same compound.[128]

Finally, ***C*-cipro** and ***C*-moxi** were formed in 53% and 98% yields respectively, using trifluoroacetic acid (TFA) in DCM at room temperature to remove the *N*-boc protection, with overall yields of 37% and 88%, respectively. The identity and purity of novel, final product ***C*-cipro** was confirmed by a combination of ^{1}H, ^{19}F and ^{13}C NMR spectroscopy, HRMS and IR spectroscopy. That of literature known compound ***C*-moxi**, was by ^{1}H and HRMS compared to those reported by Houghton *et al.* for the same compound, as well as IR spectroscopy, elemental analysis, and UV-vis spectroscopy.[128]

2.2.1.3 Doubly-protected Fluoroquinolones

Thus far, the prodrugs synthesised have possessed one allyl motif, and therefore only one cleavage reaction is required to release the active, parent antibiotic. A doubly-protected prodrug of ciprofloxacin was also synthesised, modified at both the *N*- and *C*-termini, named ***NC*-cipro**, Figure 37. Due to the presence of two hydrophobic motifs, it is hypothesised that ***NC*-cipro** possesses significantly increased hydrophobicity compared to all the previously synthesised prodrugs and active drug forms ($cLogD_{7.4} = 4.05$). ***NC*-cipro** was synthesised from ***N*-cipro**, using conditions like those for the formation of the allyl ester motifs in ***C*-cipro** and ***C*-moxi**, with a 90% yield, Figure 37. The identity and purity of this novel, final product was confirmed by a combination of ^{1}H, ^{19}F and ^{13}C NMR spectroscopy, HRMS, IR spectroscopy and elemental analysis.

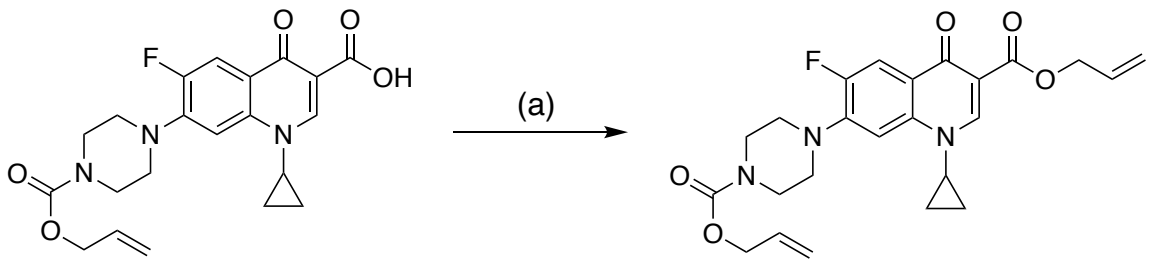

***N*-cipro** ***NC*-cipro**

Figure 37 Synthesis of ***NC*-cipro**. (a) allyl bromide, K_2CO_3, dry DMF, 60 °C, 24 h, 90%.

2.2.1.4 Fluoroquinolone Solubility

Generally, the aqueous solubility of fluoroquinolones at physiological pH is poor but due to their significant potency, this is more than sufficient for their medicinal application.[129] This solubility profile is attributed to the formation of zwitterions within this pH range, where the carboxylic acid is deprotonated and the amine protonated simultaneously. However, their solubility is drastically improved at low pH, where the positively charged species dominates.[129] The improved solubility of the prodrugs is advantageous, so that significantly higher concentrations can be added to bacteria to improve their cellular uptake, and thus the likelihood of reaction with catalyst at the same location.

The solubility of each synthesised prodrug was tested under biologically-relevant conditions that will be used to measure reaction kinetics for their catalyst-mediated activation: 10% DMSO in aqueous 3-morpholinopropane-1-sulfonic acid (MOPS) buffer (pH 7.4). The solubility of the prodrugs under these conditions respective to one another is as follows:

***C*-moxi** > ***N*-moxi** > moxifloxacin > ***C*-cipro** > ***N*-cipro** > ciprofloxacin >> ***NC*-cipro**

It was found that the prodrugs of moxifloxacin possessed superior solubility to those of ciprofloxacin. Interestingly, modification of just the *C*- or *N*-terminus of both antibacterials improved their solubility; this might be due to the prevented formation of the zwitterion species. Moreover, modification at the *C*-terminus alone increased solubility the most, which was attributed to formation of the favourable +1 protonation state observed at low pH for both parent antibacterials. ***NC*-cipro** possessed the worst solubility under these conditions, as expected, since modification at both termini prevents the two key hydrogen bonding interactions with solvent, and significantly increases $cLogD_{7.4}$.

2.2.2 Summary

To conclude, five prodrugs of the antibacterials ciprofloxacin and moxifloxacin were successfully synthesised, by either modification of their *N*-terminus, *C*-terminus, or both. These prodrugs were specifically designed for Kitamura-type catalyst-mediated activation, with additional aims to alter their bacterial uptake pathways to

mitigate existing antibiotic resistance mechanisms in bacteria. Considering its favourable solubility profile and moxifloxacin's improved antibiotic scope (including *versus* anaerobes) compared to ciprofloxacin, ***C*-moxi** was selected as the preferred candidate to take forward in these studies. However, its compatibility for catalyst-mediated activation must first be confirmed as well as its reduced antibacterial activity under medicinally-relevant conditions.

2.3 Catalyst-mediated Prodrug Activation

The next step was to measure catalyst-mediated prodrug activation kinetics. This kinetic data should be measured under biologically-relevant conditions to mimic the environment inside bacterial cells, so that data can be utilised to infer *in vivo* activity.

2.3.1 Catalyst-mediated Activation Kinetics

The optimised hydroxyquinoline-ligated Kitamura-type catalysts disclosed by Völker and Meggers in 2017 were chosen for investigation because of their reported faster reaction kinetics compared to the previous catalyst generations and precedented applications for intracellular prodrug activation *via* the cleavage of allyl carbamate-protected amines in biological media, such as blood plasma. The specific catalyst **Ru-control** (referred to as **Ru-6** in 1.2.1) was selected to measure prodrug activation kinetics due to its synthetic tractability, and was synthesised following a two-step procedure reported by Völker and Meggers in 2017, Figure 38.[33]

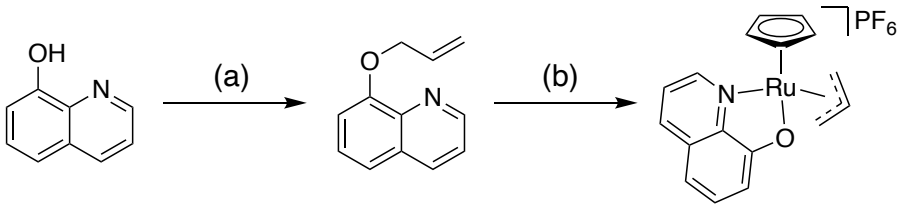

8-hydroxyquinoline **5** **Ru-control**

Figure 38 Synthesis of **Ru-control**: (a) allyl bromide, sodium hydride, dry DMF, rt, 48 h, 74% (b) tris(acetonitrile)cyclopentadienylruthneium hexafluorophosphate, dry DCM, rt, N_2, 56%.

A high-performance liquid chromatography (HPLC) assay was employed to measure **Ru-control**-mediated prodrug activation kinetics. At specific time-points

after the addition of **Ru-control** to the prodrug-containing reaction mixture, aliquots were taken and injected onto a HPLC column. The subsequent UV-traces for each corresponding time-point were analysed to calculate prodrug (***N*-moxi** or ***C*-moxi**) and drug (moxifloxacin) concentrations, using calibration curves obtained using known concentrations of these components. By plotting the changing concentration of the prodrug and drug at specific time-points, kinetic information is obtained. For procedural details (including calibration curves) see section 6.3. To ensure the kinetic data obtained are a realistic estimate for *in vivo* activity, the experiments were conducted under biologically-relevant conditions that mimic those inside of bacterial cells. The components of the selected reaction conditions are detailed and explained below.

Buffered aqueous media: aqueous M9 (70 mM) buffer with 10% DMSO, at pH 7.0.

Excess nucleophiles: with and without excess GSH (5 mM) to approximate the predominant environment for prodrug activation (extracellular or intracellular). Intracellular levels of GSH in Gram-negative bacteria are significantly higher than that in the extracellular environment and can exceed a concentration of 10 mM.[130-132] As explained in section 1.2.1, strong nucleophiles such as GSH lead to faster catalyst activation and subsequent prodrug activation. Therefore, if prodrug activation kinetics are enhanced with excess GSH, it is likely intracellular prodrug activation will be faster. Although this serves as an additional selectivity mechanism to facilitate intracellular catalyst-mediated prodrug activation, this would not select bacterial cells over mammalian cells due to their similar intracellular millimolar levels of GSH.[28, 133]

Dosage relevant concentrations: as reaction kinetics can be influenced by the concentration of reagents, prodrug concentrations were used at similar levels to those that would be used for bacterial growth assays (100 μM), to best approximate rates of reaction for *in vitro* studies.

The measured catalyst-mediated prodrug activation kinetics of ***N*-moxi** and ***C*-moxi** (100 μM) using **Ru-control** (10 mol% catalyst loading) was tested under biologically-relevant conditions with and without GSH at 5 mM, Figure 39.

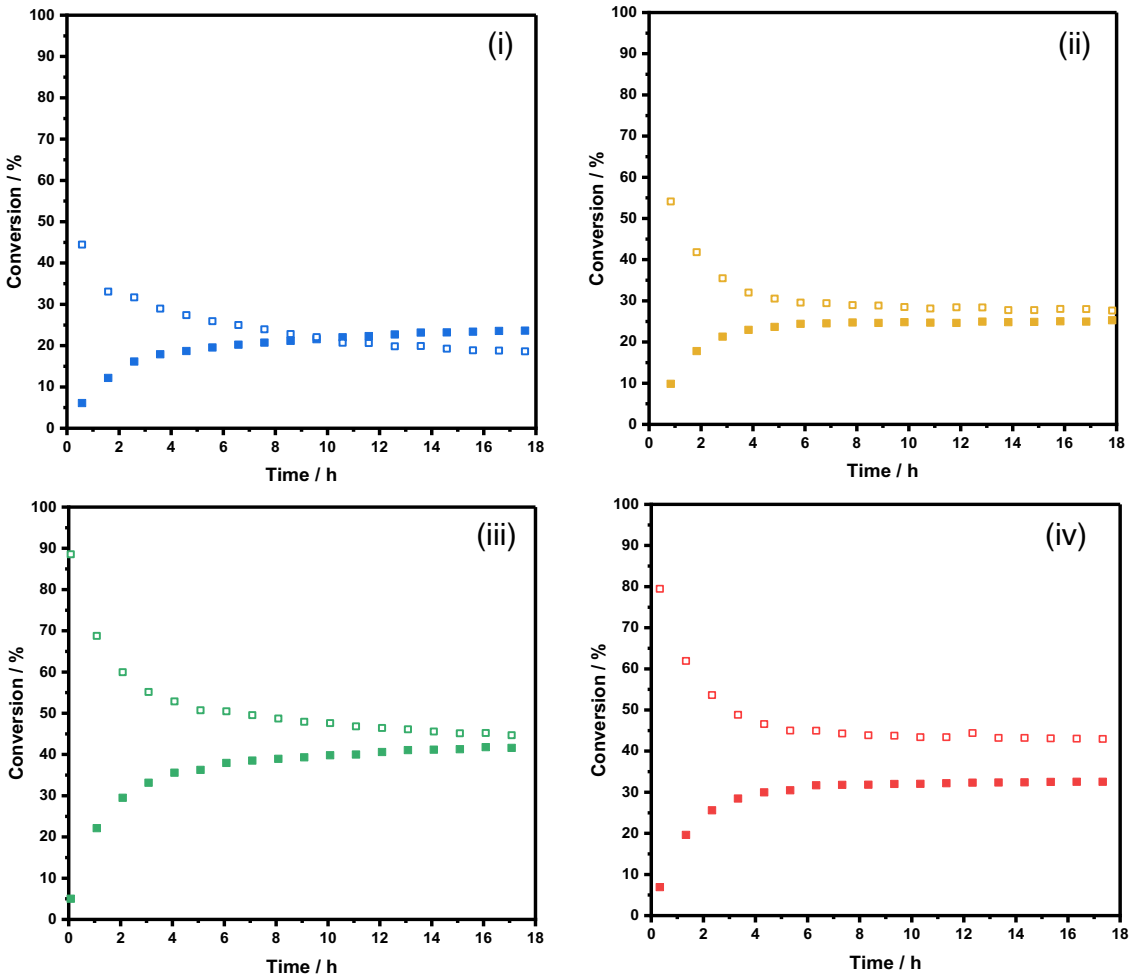

Figure 39 Catalyst-mediated prodrug activation kinetics using **Ru-control** (10 mol%) in 10% DMSO in aqueous M9 buffer at pH 7.0 at room temperature, under an aerobic atmosphere, showing prodrug (100 μM) consumption (empty squares) and moxifloxacin formation (solid squares) for: (i) ***N*-moxi** + GSH (blue), (ii) ***N*-moxi** (yellow), (iii) ***C*-moxi** + GSH (green) and (iv) ***C*-moxi** (red) over 18 h.

This data shows that **Ru-control** activates both ***N*-moxi** and ***C*-moxi** under these conditions, with and without GSH, but the kinetic profile in each case shows poor activity. For ***N*-moxi** activation, similar reaction profiles are observed irrespective of GSH, with overall moxifloxacin yields of 25%. Typically, reaction rates for the Kitamura-type catalysts increase in the presence of excess GSH where this phenomenon is explained by referring to the catalyst mechanism postulated by Völker and Meggers in 2014, section 1.2.1, Figure 12.[21] The observed 25% moxifloxacin formed corresponds to 80% ***N*-moxi** consumed. The 55% unaccounted for can be partly attributed to a competing reaction for by-product formation, especially in the absence of GSH. Under such conditions, the free amine of

moxifloxacin competes with water for catalyst priming, resulting in the formation of the by-product, *N*-allyl moxifloxacin, Figure 40 where labelled HPLC chromatograms of the reaction mixtures at 18 h are shown in Figure 41 (i) and (ii). However, a more complete explanation includes precipitation of ***N*-moxi** over time.

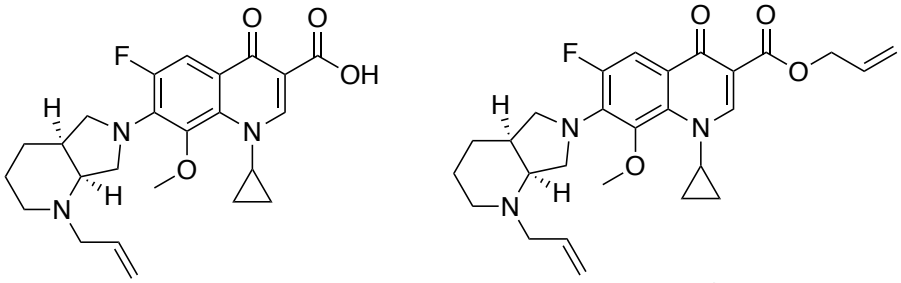

***N*-allyl moxifloxacin** ***N*-allyl *C*-moxi**

Figure 40 Chemical structure of by-products: *N*-allyl moxifloxacin and *N*-allyl *C*-moxi.

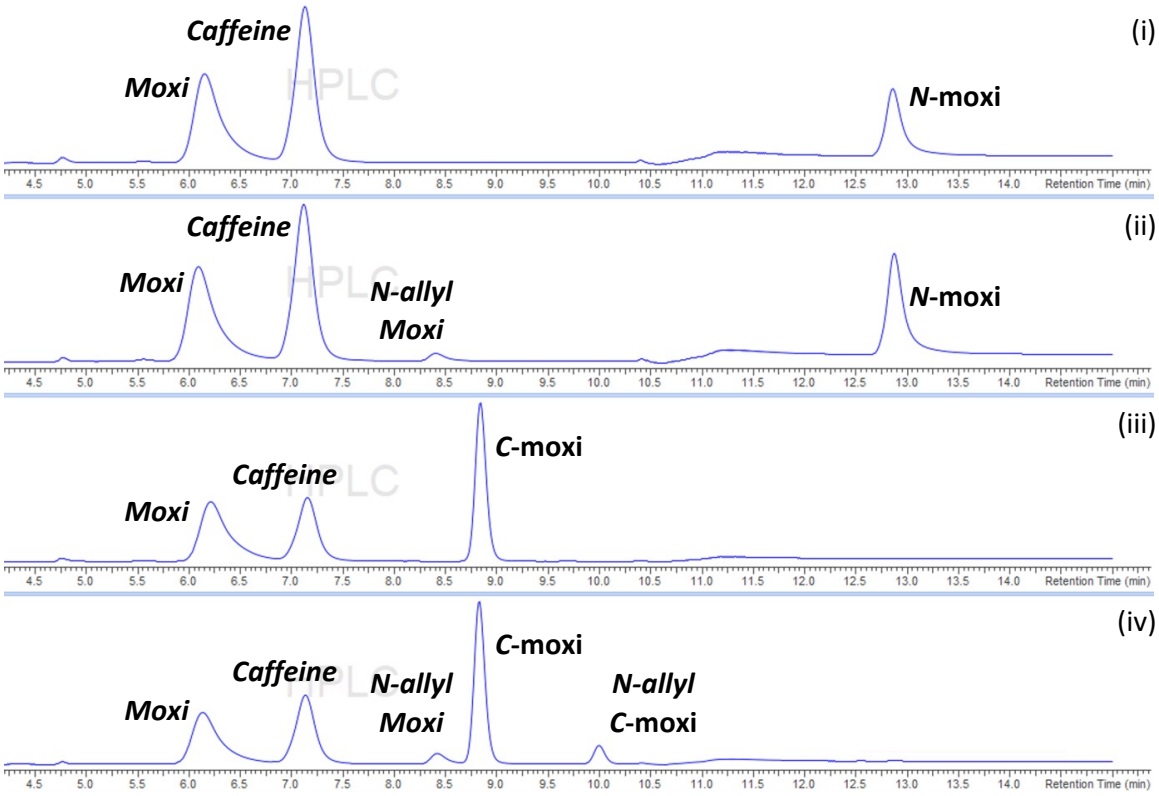

Figure 41 HPLC chromatograms that correspond to catalyst-mediated prodrug activation using **Ru-control** (10 mol%) at 18 h, in 10% DMSO in aqueous M9 buffer at pH 7.0 at room temperature, under an aerobic atmosphere, with caffeine internal standard for: (i) ***N*-moxi** + GSH, (ii) ***N*-moxi**, (iii) ***C*-moxi** + GSH and (iv) ***C*-moxi**. With peaks labelled with the reaction component they correspond to. *N*-allyl moxifloxacin = *N*-allyl Moxi.

For ***C*-moxi** activation, faster reaction kinetics and greater overall yields are observed. However as expected, improved yields are observed in the presence of excess GSH. Overall yields for moxifloxacin formation were 40% and 30%, in the presence and absence of GSH, respectively. This suggests prodrug activation inside bacteria would be faster than that in the extracellular medium. Similar to ***N*-moxi** activation, that of ***C*-moxi** also produces by-products, but since ***C*-moxi** also bears the secondary amine, an additional by-product is formed, *N*-allyl *C*-moxi. However, this is converted to the *N*-allyl moxifloxacin following activation, Figure 40 where labelled HPLC chromatograms of the reaction mixtures at 18 h are shown in Figure 41 (iii) and (iv). Importantly, during ***C*-moxi** activation kinetic experiments, substrate precipitation is not observed. This is in-line with the solubility properties outlined in section 2.2.1.4.

A more general observation made for all experiments shows catalyst activity is high within the first 2 h after catalyst addition, with a quick drop off and complete loss of activity after 8 h. This suggests either one or a combination of product-inhibition of the catalyst, catalyst/substrate precipitation and/or catalyst degradation, where the first two rationales were disproved by ERASMUS placement student Isabelle Böswald in 2019 through reaction kinetic analysis using HPLC.[134]

2.3.2 Investigating Catalyst Stability

The synthesised prodrugs (***N*-moxi** and ***C*-moxi**) are activated by the catalyst, **Ru-control**. Although this activation occurs at an acceptable initial rate, the catalyst's activity quickly decreases and is completely lost after 8 h under biologically-relevant conditions. To assess whether the Kitamura-type catalysts are suitable for prodrug activation, the reason for this loss of catalyst activity needs identification. If suitable adjustments to the catalyst or reaction conditions can be made that significantly improve catalyst activity whilst maintaining applicability to its intended medicinal setting, the use of this catalyst can be justified.

In 2010, Kiesewetter and Waymouth reported kinetic data for catalyst-mediated cleavage of an allyl carbonate-protected allyl alcohol in methanolic and aqueous solutions under an argon atmosphere, using the quinaldic-ligated Kitamura catalyst **Ru-4**, Figure 38. They concluded that the catalyst activity was faster in methanol

than water due its superior nucleophilicity. However, when these same reactions were performed under air, decreased conversions were observed in methanol with apparent negligible changes in water. Although these investigations did not unambiguously determine the cause for the low conversions for the methanolysis in air, they proposed oxidative decomposition of the active Ru(II) intermediate species was the likely cause due to the long-shelf life of the Ru(IV) catalyst precursor species, Figure 42. They subsequently reasoned the greater oxygen solubility in methanol compared to water gave more significant decreases in conversion under air. This proposed catalyst decomposition pathway could also be responsible for the loss of catalyst activity observed during the **Ru-control**-mediated prodrug activation kinetics experiments undertaken in section 2.3.1.

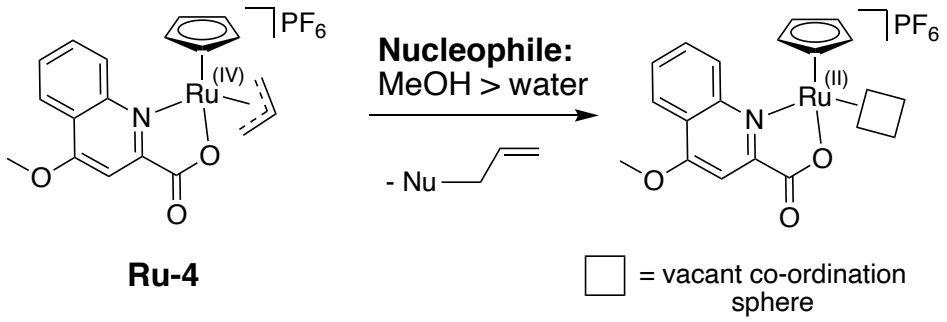

Figure 42 Chemical structure and catalyst priming of **Ru-4** (catalyst precursor species) to form the active Ru(II) intermediate species.

To identify whether the loss of catalyst activity observed for **Ru-control** was due its decomposition by molecular oxygen, the catalyst's activity for ***C*-moxi** activation under an aerobic atmosphere was compared to that under an anaerobic atmosphere. For thoroughness the biologically-relevant media was degassed by backfilling the reaction mixture on a Schlenk line using nitrogen gas prior to kinetic runs. The measured catalyst-mediated prodrug activation kinetics of ***C*-moxi** (100 μM) using **Ru-control** at a 10 mol% catalyst loading under biologically relevant conditions with GSH under an anaerobic atmosphere *versus* an aerobic atmosphere, Figure 43. The procedural detail (including calibration curves) can be found in section 6.3.

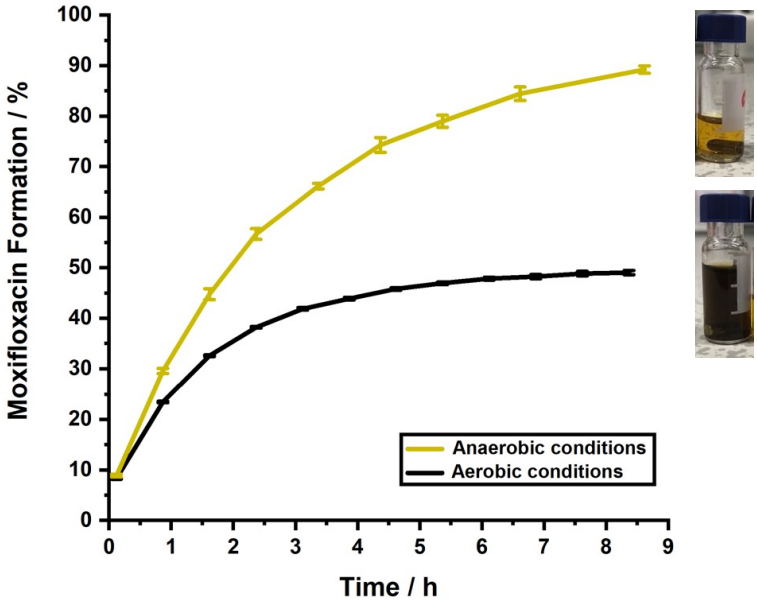

Figure 43 Catalyst-mediated prodrug activation kinetics using **Ru-control** (10 mol%) for ***C*-moxi** (100 μM) in 10% DMSO in aqueous MOPS buffer, pH 7.4 at room temperature, with 5 mM GSH under an aerobic atmosphere (black) and an anaerobic atmosphere (yellow), with corresponding final solution appearances shown next to their corresponding endpoints.

From these results, it is clear that **Ru-control**-mediated ***C*-moxi** activation kinetics are greatly improved in the absence of molecular oxygen; 90% moxifloxacin formation is achieved after only 8 h whereas after the same time period under an aerobic atmosphere, only 45% conversion is observed. Moreover, **Ru-control** remains active for the entire reaction time. Collectively, these results suggest the poor catalyst activity observed in section 2.3.1 was due to O_2-mediated catalyst decomposition.

To the best of our knowledge, there have been no investigations into the mechanism for the oxidative decomposition of Kitamura-type catalysts. In fact, the only published mentions of their stability issues were by Kiesewetter *et al.* in 2010, four years prior to its debuted application in bio-orthogonal approaches for prodrug activation.[21, 26] It is possible that the lack of mechanistic understanding for catalyst oxidative decomposition might have limited their uses under physiological conditions. Consequently, investigations were undertaken into the mechanism for the catalyst decomposition of **Ru-control**. It is hoped that understanding how the

catalyst decomposes in the presence of molecular oxygen and what species are formed as a result, might assist the discovery of more stable catalysts.

As proposed by Kiesewetter *et al.* in 2010, it is likely the catalyst species sensitive to molecular oxygen is the active Ru(II) intermediate species shown in Figure 42. To rule out decomposition of the Ru(IV) catalyst precursor species, **Ru-control** was dissolved in DMSO-d_6 at 10 mM and ^{1}H NMR spectra were recorded at intervals over 2 weeks, Figure 44. Due to the absence of strong nucleophiles (such as GSH) there should be limited formation of the active Ru(II) intermediate species and therefore significant changes at a similar rate to the loss of catalyst activity observed in sections 2.3.1 indicate the sensitivity of the Ru(IV) catalyst precursor species to molecular oxygen.

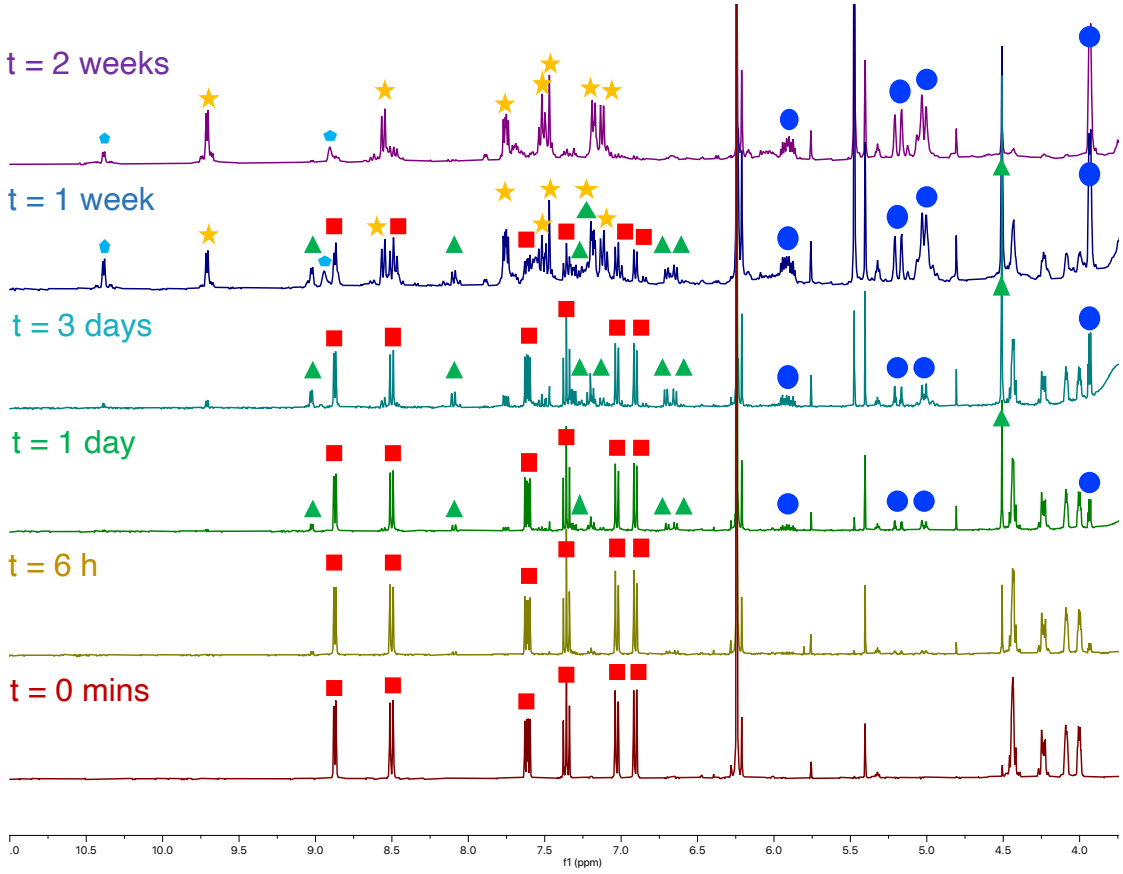

Figure 44 ^{1}H NMR spectra of **Ru-control** in DMSO-d_6, after different time points after catalyst addition. **Key:** red square = **Ru-control**, Ru(IV) catalyst precursor species, blue circle = allyl alcohol, green triangle = active Ru(II) intermediate species, cyan pentagon = unknown product 1, yellow star = unknown product 2.

This data suggests that the reason for the loss of catalyst activity is not the oxygen-mediated decomposition of the Ru(IV) catalyst precursor (red square) as it remains the major species after 3 d in DMSO-d_6 under an aerobic atmosphere, with small amounts of the active Ru(II) intermediate species (green triangle) formed through the catalyst priming mechanism by water. Moreover, significant amounts of the Ru(IV) catalyst precursor species remain after one week. The formation of the active Ru(II) intermediate species is identified by the characteristic chemical shift corresponding to the cyclopentadienyl ligand at 4.5 ppm and generation of equimolar, allyl alcohol (blue circle).[135] After one week in solution, two subsequent unknown species are observed (yellow star and cyan pentagon) and one might assume these species are formed *via* the active Ru(II) intermediate species, as it is consumed over the same time period. These species appear to be in equilibrium, with one more thermodynamically stable (yellow star). Neither of the unknown species is uncomplexed ligand (8-allyloxyquinoline or 8-hydroxyquinoline, Figure 45), as confirmed by ^{1}H NMR spectroscopy and therefore are likely quinolate-complexed ruthenium complexes. Due to disappearance the singlet peak corresponding to the cyclopentadienyl ligand, it can be assumed that the formed ruthenium complex is not coordinated to this motif. A schematic representing the dynamics of **Ru-control** in DMSO-d_6 (10 mM) under air is shown in Figure 46.

8-allyloxyquinoline **8-hydroxyquinoline**

Figure 45 Chemical structure of 8-allyloxyquinoline and 8-hydroxyquinoline.

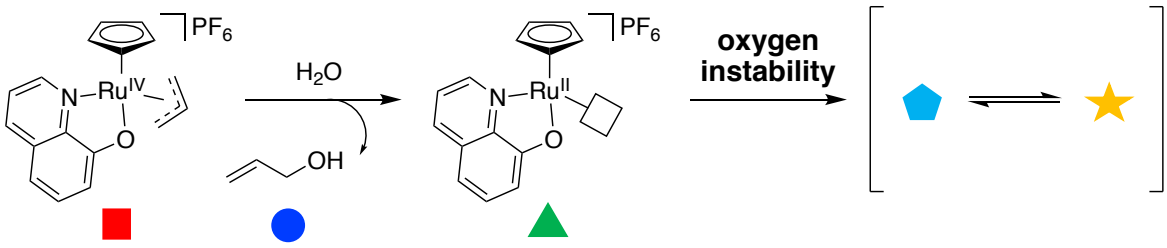

Figure 46 Proposed solution dynamics of **Ru-control**, with water as nucleophile for catalyst priming.

After stability of the Ru(IV) catalyst precursor species to molecular oxygen was confirmed, that of the active Ru(II) intermediate species was investigated. In buffered media or the presence of millimolar concentrations of strong nucleophiles (such as GSH), **Ru-control** is rapidly converted to the active Ru(II) intermediate species. If catalyst decomposition is observed under these conditions at a similar rate to loss of activity displayed in the kinetic assays, this suggests that the active Ru(II) catalyst species is in fact sensitive to molecular oxygen. To test this, **Ru-control** was dissolved at 2 mM in aqueous MOPS buffer (pH 7.4) using deuterated water with 10% DMSO-d_6, where spectra were recorded at t = 15 min and t = 18 h, under an aerobic and anaerobic atmosphere, Figure 47.

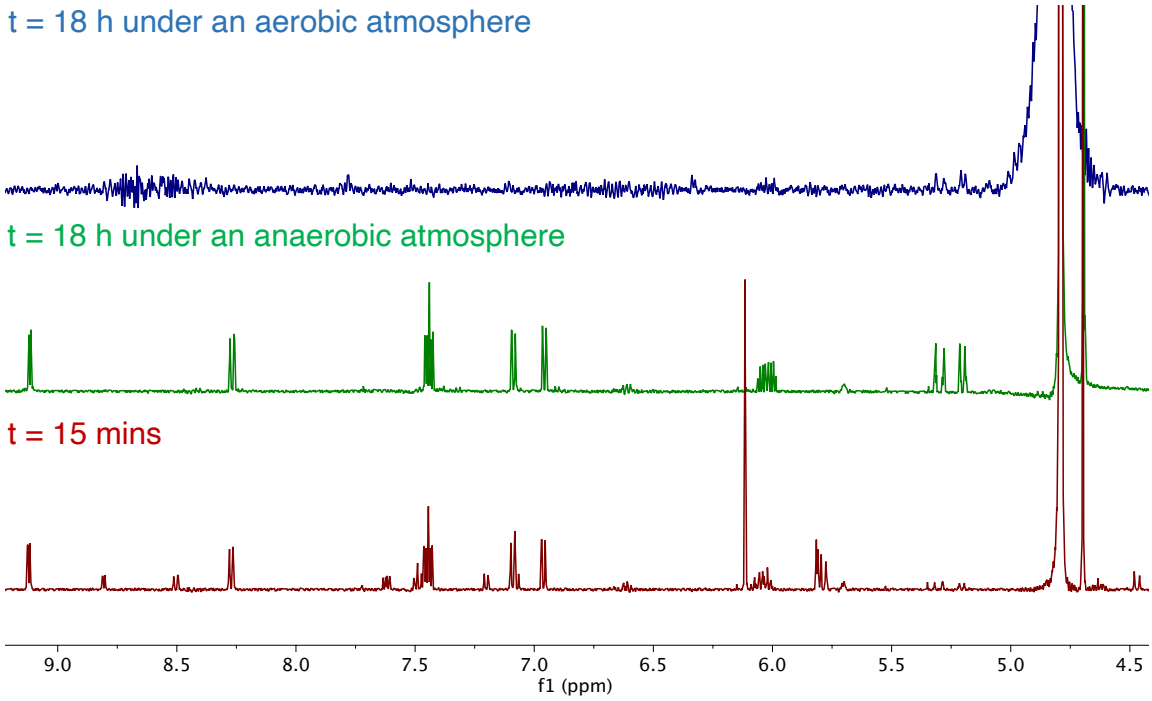

Figure 47 ^{1}H NMR spectra of **Ru-control** (2 mM) in aqueous MOPS buffer (pH 7.4, 40 mM) using D_2O with 10% DMSO-d_6, at t = 15 min (red) and 18 h under an anaerobic (green) and aerobic (blue) atmosphere. A single ^{1}H NMR spectrum is shown for t = 15 min, as they are identical regardless of atmosphere.

These data show that in after only 15 min solution, **Ru-control** has already mostly been primed by the nucleophilic water in the buffer solution, to form the active Ru(II) intermediate species and under an anaerobic atmosphere, this remains after 18 h as a yellow solution. However, under an aerobic atmosphere, it decomposes and precipitates to form a dark coloured suspension, similar to the images in Figure 43.

These experiments indicate that it is indeed the active Ru(II) intermediate species that is sensitive to molecular oxygen, as suggested earlier by Kiesewetter and Waymouth in 2010.[26]

2.3.3 Summary

To conclude, it was found that the synthesised ***C*-moxi** and ***N*-moxi** prodrugs were activated under biologically-relevant conditions by the Kitamura-type catalyst, **Ru-control**. However, the ***N*-moxi** prodrug precipitated under these conditions and poor conversion was observed for both prodrugs under an aerobic atmosphere. It was confirmed that this poor activity was due to decomposition of the active Ru(II) intermediate species by molecular oxygen. Unfortunately, attempts to identify the degraded species were unsuccessful. Despite this, there remains promise for the use of these catalysts for prodrug activation, for the treatment of bacterial infections in host environments where the levels of molecular oxygen are low. If such an application is identified, it should lead to prolonged catalyst lifetimes and therefore improved prodrug conversion kinetics and overall yield.

2.4 The Antibacterial Activity of Moxifloxacin Prodrugs

An essential property of prodrugs is their limited antibacterial activity prior to activation. Therefore, to establish the suitability of the synthesised prodrugs of moxifloxacin (***N*-moxi** and ***C*-moxi**) their antibacterial activity must be determined against medicinally relevant bacteria, under physiologically-relevant conditions.

As established in section 2.3.2, the Kitamura-type catalysts decompose in the presence of oxygen and therefore their application site *in vivo* should possess a low oxygen environment to prolong catalyst lifetimes. This considered, the treatment of intestinal infections was identified due to its reduced oxygen atmosphere. The antibacterial activity of ***N*-moxi**, ***C*-moxi** and moxifloxacin should therefore be tested against relevant bacteria. Moreover, such experimental conditions should mimic those of the intestine which includes (i) a reduced oxygen atmosphere concentration and (ii) low iron conditions. Even though some food compounds may be a source of

iron, it is generally believed that there is a limited access to iron in the gut and therefore iron-acquisition is competitive.[94]

2.4.1 Methods for Achieving Iron-limited Bacterial Growth

During the infection of a host by bacteria, there is an ongoing fight for resources such as iron. In humans, native proteins such as transferrin and ferritin, sequester and store iron respectively, thereby creating an iron-limited environment with iron concentrations as low as 10^{-24} M.[136] To combat this, bacteria release iron chelators called siderophores into the surrounding medium to scavenge for Fe(III). Subsequent iron-siderophore complexes are then translocated into bacterial cells through specific transporters. These siderophore iron-uptake pathways are upregulated under iron-limited conditions. Consequently, the antibacterial activity of moxifloxacin and its prodrugs (***N*-moxi** and ***C*-moxi**) must be determined under iron-limited conditions.

It is proposed that the iron concentration of a bacterial medium that is required to cause iron-limitation is < 1 μM.[51] Typical iron-limited conditions utilise defined minimal media, such as minimal M9 media[137, 138] and tris-minimal succinate (TMS) media[139-141] for *E. coli* and *Staphylococcus aureus (S. aureus)*, respectively. Additionally, there are numerous examples of the use of desferrated broths such as lysogeny broth (LB)[137, 142], tryptic soy broth (TSB)[143, 144] and Müller-Hinton broth II (MHII)[137, 142, 145, 146]. However, the levels of concomitant iron in such media often remain too high to impede bacterial growth hence additional measures are taken.

It is common to acid-treat any glassware used for bacterial growth under iron-limited conditions since glassware is often iron contaminated. Acid treatment involves stirring concentrated acid in the glassware, followed by decanting and rinses with organic solvent. Chelex treatment is a method of removing concomitant iron from stock solutions for minimal media components or to create desferrated broths. Prior to use, media are stirred with a chelating resin called Chelex, which binds the iron present in solution. Subsequently, the Chelex resin (with the bound iron) can be removed by filtration.[147] However, this method does not always completely remove iron from solutions.[148]

In some applications, synthetic chelators such as bipyridin (bpy), Figure 48, have been added to media during bacterial growth assays to sequester iron thereby reducing iron availability.[149] Unlike previously discussed experiments, this technique does not lower the iron content of the media but introduces a greater kinetic and thermodynamic barrier for siderophore binding *via* the formation of iron-synthetic chelator complexes in solution. Importantly, the chosen synthetic chelators are weak iron binders and therefore outcompeted by siderophores produced in response. The cumulative Fe(III) log formation constant (K_f) for bpy is 16.3, whereas those of principal siderophores such as enterobactin and DFO are far greater, with values of 30.6 and 49.0, respectively.[50, 51] There are several literature examples of chelator addition to media in attempts to impose iron-limited conditions on bacteria but unless these chelators possess iron-selectivity, debilitated bacterial growth cannot be solely attributed to iron limitation.[150] Therefore, it is important to employ adequate control assays (i.e. chelate + excess iron *versus* just chelate) to ensure iron-starvation is the primary source of perturbed bacterial growth. The extent of iron limitation is reflected by the disparity in bacterial growth between iron-limited and iron-supplemented conditions. Despite this, many literature articles fail to report such experiments.

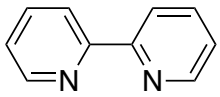

Figure 48 Chemical structure of bpy.

2.4.2 Iron-limited Growth of *E. coli*

Enterobacteriaceae are a family of bacteria labelled a ‘critical priority’ by the World Health Organisation due to antibiotic resistance.[151] *E. coli* is a member of this family and commonly regarded as the most well-characterised bacterial strain and as a result, its iron-uptake pathways are well-undertsood.[151] *E. coli* is a facultative anaerobe, which means it can adapt its metabolism for growth in low levels of or the absence of oxygen. GI tract infections caused by enteric pathogens affect over 1.7 billion individuals annually, with approximately 2.2 million cases ending in death.[152] Among the leading causes of these infections are Gram-negative bacteria such as

E. coli, *Salmonella sp.* and *C. jejuni*. For these reasons, the common *E. coli* laboratory strain K12 (BW25113) was chosen as a bacteria model system.

2.4.2.1 Iron-limited *E. coli* Growth using a Modified, Minimal MOPS media

Initial iron-limiting bacterial growth conditions were obtained using a modified, minimal MOPS media based on a study reported for *Enterobacteriaceae* by Neidhardt *et al.* in 1974.[153] This media was pursued after unsuccessful attempts to impose iron-limited growth using minimal M9 media (data not shown). A description of the minimal, modified MOPS media components and why they were chosen follows, and a detailed procedure for its making can be found in section 6.5.1.

Buffer component: MOPS, pH 7.4. Bacteria growth assays were initially investigated using a phosphate-buffered minimal M9 media[154] however insufficient growth differences were observed between iron-limited (no added iron) and iron-supplemented (+100 μM $FeCl_3$) conditions. It was hypothesised that M9 possessed high levels of concomitant iron due to its high phosphate content thereby providing a hidden, sufficient iron-source for bacteria. This was confirmed by ICP-MS measurements, Table 2.

Carbon-source: sodium acetate. Neidhardt *et al.* suggested that an acetate carbon-source inflicts a higher iron requirement on bacteria compared to glucose due to the iron-containing proteins involved in acetate metabolism.[153]

Phosphorus-source: potassium phosphate. In minimal M9 media, the buffer component is also the phosphorus source therefore when using MOPS-buffered media, a separate source is required. The phosphorus demand is much lower than the levels present in minimal M9 media therefore lower concentrations can be used in order to mitigate iron contamination. Potassium phosphate was used at the same concentrations reported in the MOPS medium from the studies by Neidhart *et al*.[153]

Nitrogen-source: ammonium chloride. This is the same nitrogen-source used in minimal M9 media. This was added at the same concentration as in minima M9 media.

Bivalent metals and sodium chloride: magnesium sulfate, calcium chloride and sodium chloride were added at the same concentrations as in minimal M9 media.

Chelate ligand: tricine, Figure 49. Neidhart *et al.*[153] reported the use of tricine to help solubilise Fe(III) but not for iron sequestering, as they reported its addition does not impede growth.

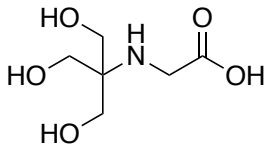

Figure 49 Chemical structure of tricine.

Table 2 Iron content of media determined using ICP-MS by Sanderson *et al.*[155]

Medium	[^{56}Fe] / ppb	[^{56}Fe] / μM
Minimal, modified MOPS Media	<LLOQ*	<LLOQ
Minimal, modified MOPS Media (+100 μM)	5331	95
Minimal M9 Media	8234	147
MHII	2967	53

* Lowest limit of quantification = 36.2 ppb; detection limit = 12.05 ppb.

The suitability of the minimal, modified MOPS media for the iron-limited growth of *E. coli* was assessed using growth curve assays, and this data is reported by Sanderson *et al.*[155] As previously described in section 2.4.1, if restricted bacterial growth under certain conditions is rescued on the sole addition of an iron-source, said conditions can be deemed iron-limited. Bacteria stocks were 'iron starved' prior to all growth assays to deplete their intracellular iron stores and for procedural details regarding this, see section 6.5.4. These bacterial stocks were grown overnight in chelexed, minimal M9 media supplemented with casamino acids and diluted (to 0.01 OD_{600}) in the minimal, modified MOPS media (pH 7.4) where subsequent growth was measured under iron-limited (no added iron) and iron-supplemented (+100 μM $FeCl_3$) conditions over 48 h, Figure 50. Growth is approximated by measuring the scattering of light at 600 nm.

These results show a clear distinction between iron-limited and iron-supplemented conditions, indicating minimal, modified MOPS media is suitable for the iron-limited growth of 'iron starved' bacterial stocks of *E. coli* K12 (BW25113). These media and conditions were utilised to measure the antibacterial activity of Trojan Horse antibacterials *versus E. coli* K12 and Nissle strains, with Sanderson *et al.* in 2020.[155] This antibacterial activity data was measured under iron-limited and iron-supplemented conditions, as differences in the obtained data can be used the infer the uptake of Trojan Horse antibacterials *via* iron-uptake pathways, as outlined by Southwell, Black and Duhme-Klair in 2021.[65]

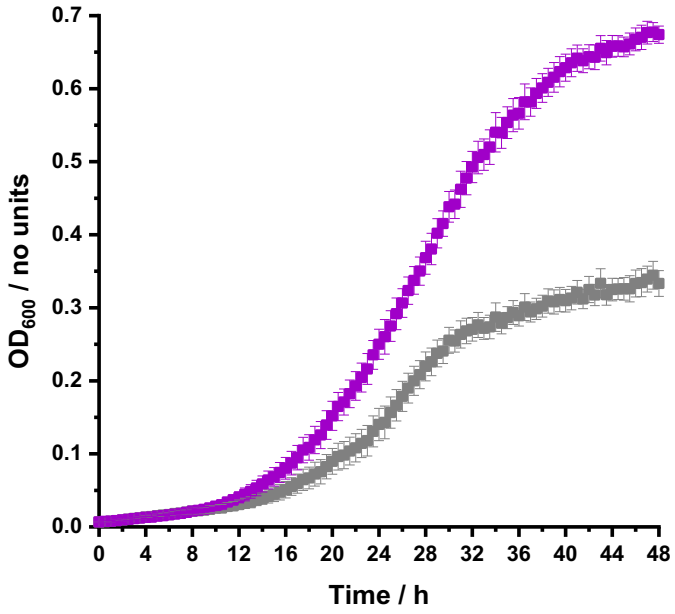

Figure 50 Aerobic growth of *E. coli* K12 (BW25113) in minimal, modified MOPS media (pH 7.4) in iron-limited (no added $FeCl_3$, grey) and iron-supplemented (100 μM $FeCl_3$, purple) conditions, at 37 ºC for 48 h.[155]

As concluded from the catalyst stability investigations in section 2.3.2, the Kitamura-type catalysts decompose in the presence of molecular oxygen over a period of approximately 8 h under biologically-relevant conditions. Therefore, their uses in a medicinal setting are limited to physiological environments where the oxygen content is low. The mammalian intestine are significantly de-oxygenated, as gut microbiota undergo transformation from aerobic and facultatively anaerobic bacteria to obligate anaerobes early in life.[156] This generation of an anaerobic environment is consistent with the rapid consumption of oxygen by aerotolerant organisms. Moreover, it has been recently discovered that there exist additional mechanisms

responsible for oxygen consumption other than microbe respiration, as germ-free GI models exhibit anaerobic conditions.[157] As a result, the percentage oxygen in intestinal tissue at different parts of the intestine range between approx. 9 - 0%.[156] The decreased oxygen atmosphere and increased competition for bacterial pathogens in the intestine potentiates the suitability of catalyst-mediated prodrug activation, as the environment should prolong catalyst lifetimes resulting in faster and better sustained prodrug activation.

Intial studies involved measuring the growth of *E. coli* in iron-limited *versus* iron-supplemented conditions under a micro-aerobic environment. The difference between the level of bacterial growth depending on iron concentration is indicate of the bacteria's reliance on iron. The chosen oxygen percentage for these growth experiments was 2% as, apart from the duodenum region of the colon, most other intestinal regions possess oxygen percentages of 2% or lower.[156] The growth of *E. coli* in iron-limited *versus* iron-supplemented conditions under a micro-aerobic atmosphere is shown in Figure 51, compared to the previously reported aerobic growth.

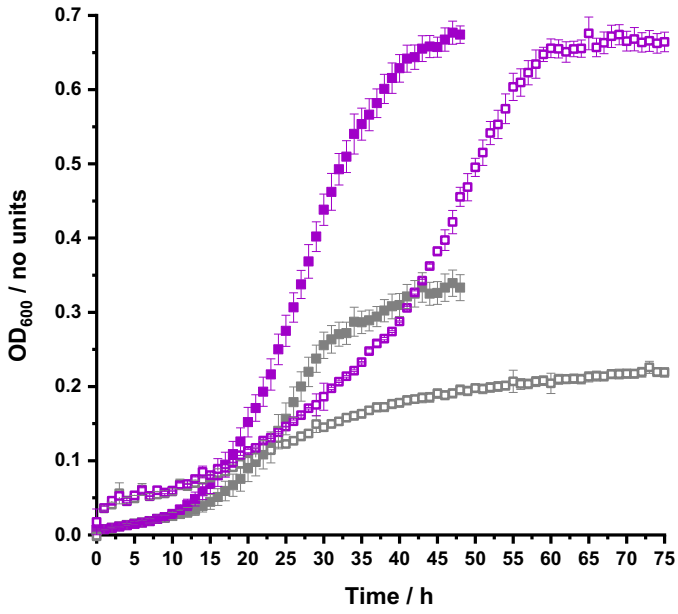

Figure 51 Aerobic (solid squares) and micro-aerobic (2% O_2) (empty squares) growth of *E. coli* K12 (BW25113) in modified-MOPS media (pH 7.4) in iron-limited (no added $FeCl_3$, grey) and iron-supplemented (100 μM $FeCl_3$, purple) conditions, at 37 ºC for 48 and 75 h respectively.

The growth rates under a micro-aerobic atmosphere relative to those grown aerobically are consistent with the fact that *E. coli* is a facultative anaerobe and known to grow more slowly with less oxygen present, due to less efficient ATP synthesis.[158] Under iron-supplemented conditions, similar final OD_{600} values are reached under each atmosphere, showing that overall bacterial growth is similar, despite varied oxygen availability. An approximate, quantitative value for the iron-associated growth difference for micro-aerobically and aerobically grown bacteria can be obtained by subtracting the stationary phase OD_{600} value in iron-supplemented conditions (which is similar for each atmosphere) from that of iron-limited conditions, to give ΔOD_{600}(Fe) values of ~ 0.5 and ~ 0.4, respectively. The larger ΔOD_{600}(Fe) value for *E. coli* grown under a micro-aerobic atmosphere, indicate a higher iron-requirement is imposed by these conditions. This was expected considering the well-known increased demand for iron-containing proteins utilised in micro-aerobic and anaerobic metabolism.[159]

2.4.2.2 Iron-limited *E. coli* Growth using Müller-Hinton Broth II

Despite previous successes in the determination of iron-limited media using the minimal, modified MOPS media, it was decided MHII should be pursued for use in antibacterial activity assays. This is because MHII is more commonly used in the literature for such biological experiments, especially for iron-limited growth.[137, 142, 145, 146] For the iron-limited growth of *E. coli*, this broth is commonly used with the synthetic chelator bpy at 200 μM. The suitability of MHII supplemented with 200 μM bpy for the iron-limited growth of *E. coli* was assessed using growth curve assays, like those used for the validation of the minimal, modified MOPS media. This time, absorbance was measured at 800 nm, as the Kitamura-type catalysts which will be used in future experiments absorb at 600 nm. These experiments were initially trialled under aerobic conditions, Figure 52.

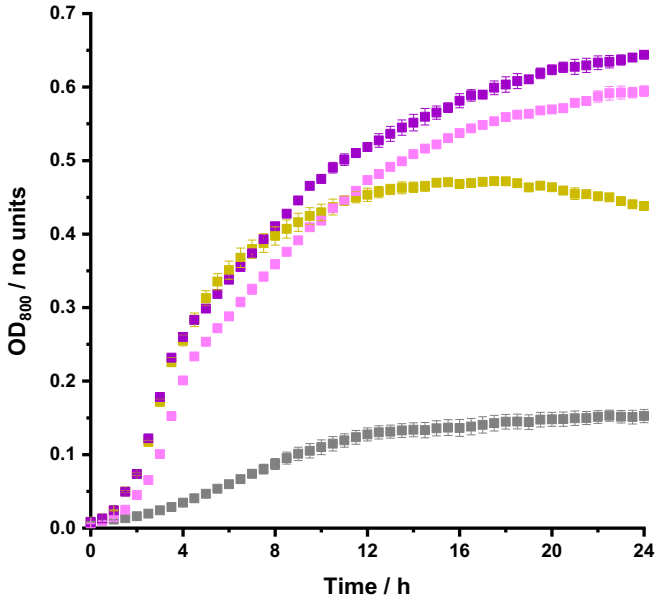

Figure 52 Aerobic growth of *E. coli* K12 (BW25113) in MHII (pH 7.4) supplemented with: no addition (yellow), 200 μM bpy (grey), 100 μM $FeCl_3$ (purple), and 200 μM bpy + 100 μM $FeCl_3$ (pink), at 37 ºC for 24 h.

These data show that MHII supplemented with 200 μM bpy does indeed impose significant iron-limitation, with overall growth decreased 4-fold compared to both iron-supplemented controls, which are very similar. In fact, plain MHII imposed some iron-limitation, as overall growth is approximately 70% of the iron-supplemented controls. This difference is simply due to the amount of iron-available in solution which suggests the residual amount of iron that remains after Chelex treatment is still nearly optimal for growth. Whereas the difference in growth between the plain MHII and MHII supplemented with 200 μM bpy conditions reflects the iron-sequestering ability of the bpy in solution. As with the growth of *E. coli* in minimal, modified-MOPS media, that in MHII was also measured under a micro-aerobic atmosphere (2% O_2), compared to its previously reported aerobic growth, Figure 53.

Importantly, these data show iron-limited conditions have also been obtained for the micro-aerobic growth of *E. coli*. Growth under these iron-limited conditions is very similar to that under an aerobic atmosphere. However unexpectedly, overall growth for all non-iron-limited conditions under a micro-aerobic atmosphere are 3-fold higher than their equivalents under an aerobic atmosphere. Despite this, iron-limited growth under aerobic and anaerobic conditions was very similar.

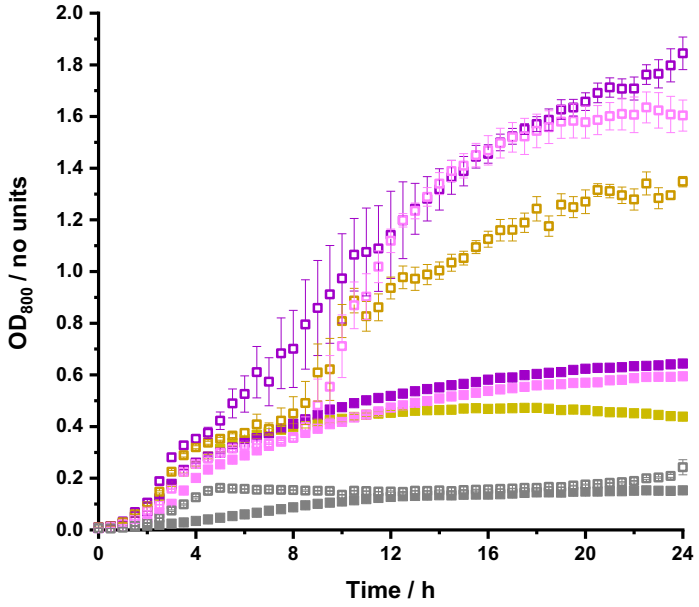

Figure 53 Aerobic (solid squares) and micro-aerobic (2% O_2) (empty squares) of *E. coli* K12 (BW25113) in MHII (pH 7.4) supplemented with: no addition (yellow), 200 μM bpy (grey), 100 μM $FeCl_3$ (purple), and 200 μM bpy + 100 μM $FeCl_3$ (pink), at 37 ºC for 24 h.

The iron content of the minimal, modified-MOPS media and the MHII was also investigated during these studies, measured with Sanderson *et al*. using ICP-MS, Table 2.[155] The iron content of the minimal, modified MOPS media was significantly lower than that of the other media, especially the minimal M9 media. This result strengthens the argument that high phosphate concentrations in this media prevent successful Chelex treatment, as it competes for iron binding. The iron content of MHII was low but still in the micro-molar range. This explains why MHII alone was insufficient to impose iron-limited growth. The addition of 200 μM bpy successfully imposes iron limitation and it can be assumed that this is due to the excess bpy co-ordinating to this residual iron and with-holding it from the bacteria.

2.4.3 Antibacterial Activity of Moxifloxacin and Prodrugs

Suitable conditions that mimic the iron- and oxygen-limited environment of the intestine have been identified in Chelex-treated MHII supplemented with 200 μM bpy under a 2% O_2 atmosphere, for the growth of relevant bacteria *E. coli* K12 (BW25113), as detailed in section 2.4.2.2. The antibacterial activity of moxifloxacin and its prodrugs (***N*-moxi** and ***C*-moxi**) was measured under these conditions.

These data are represented as dosage-response curves, which show how the overall growth after 24 h compares to 'no addition' controls (normalised OD_{800}) at the various concentrations of added substrate. The dosage-response curves for moxifloxacin, ***N*-moxi** and ***C*-moxi** are shown in Figure 54. The procedural detail for these experiments can be found in section 6.5.6.3.

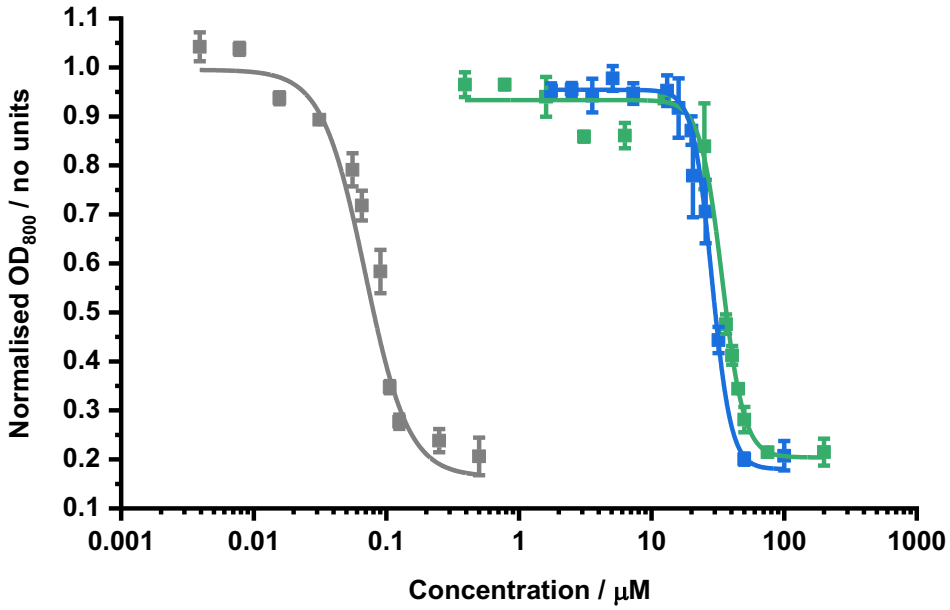

Figure 54 Dosage-response curves of *E. coli* K12 (BW25113) overall growth, 24 h after substrate addition. Data is normalised to 'no addition' controls, for each of moxifloxacin (grey), ***N*-moxi** (green) and ***C*-moxi** (blue), at their varied substrate concentrations under iron-limited (MHII supplemented with 200 μM bpy), micro-aerobic (2% O_2) conditions, at 37 ºC.

This data shows that under these conditions, the minimum inhibitory concentration (MIC) of the active drug, moxifloxacin, is approximately 300 nM, with no antibacterial activity observed at concentrations lower than approximately 10 nM. This is line with literature values for *E. coli*.[160, 161] Both prodrugs possess significantly larger MIC values, both at approximately 100 μM. Consequently, it can be said that the prodrugs are 300 times less active than the parent antibiotic. The similarity of the dosage-response curves for ***N*-moxi** and ***C*-moxi** are surprising, considering ***C*-moxi** possess modification at moxifloxacin's pharmacophore. No antibacterial activity for ***N*-moxi** or ***C*-moxi** is seen at concentrations lower than approximately 10 μM. This means both prodrugs provide a very similar toxicity window, where only

approximately 3% of each prodrug at its upper, non-toxic concentration need activation to completely inhibit bacterial growth under these conditions.

2.4.4 Bacterial Uptake of Moxifloxacin Prodrugs

For prodrug activation inside bacterial cells, it is essential that both reaction components (catalyst and prodrug) are readily taken up by bacteria in sufficient quantities, to allow for enough active drug to be formed for maximum inhibitory effect. Now that the antibacterial prodrugs have been synthesised and their antibacterial activity under relevant conditions determined, their uptake into bacteria need to be measured. Although ***C*-moxi** has been selected as the optimum prodrug for these studies, uptake measurements were also attempted for ***N*-moxi**. Both prodrugs' upper non-toxic concentration is approximately 10 μM, and therefore this amount should be used in bacterial growth assays.

The bacterial uptake of prodrugs was determined using an incubation experiment. Iron-limited MHII was inoculated with an overnight growth culture of *E. coli* K12 (BW25113) and re-grown to its exponential growth phase at 0.1 OD_{600}, under a micro-aerobic atmosphere. After this, the resulting cell suspension was incubated with 10 μM prodrug for 15 min and then spun down to separate the cells from their extracellular media. These cells were then washed with fresh MHII, where this supernatant was also collected. The prodrug amount inside the bacteria was approximated by subtracting the summated amount measured in the extracellular media and wash samples from the amount added at incubation. The amount added at incubation was measured using 'no cell' controls. The amounts of prodrug in the various samples were calculated relative to external standard caffeine, using HPLC analysis. The procedural detail for these experiments is given in section 6.5.5. The bacterial uptake studies results are shown in Table 3. Unfortunately, bacterial uptake studies were unsuccessful for ***N*-moxi** due to precipitation.

It is possible that ***C*-moxi** is in fact stuck on the cell surface. If this is not the case, these data suggests that *E. coli* K12 (BW25113) bacteria grown under iron-limited, micro-aerobic conditions do indeed uptake ***C*-moxi**, at 16% of the prodrug added at 10 μM. This means that for bacteria grown under these conditions, approximately 20% need activation to observe the maximum inhibitory effect of moxifloxacin.

Table 3 Estimated bacterial uptake of ***C*-moxi**. This data shows the percentage ***C*-moxi** present in the extracellular and wash samples, relative to the 'no cell' controls.

Extracellular / %	Wash / %	Remainder / %	Uptake / nmol OD_{600}^{-1}
82.7	0.9	16.4	3.31

2.4.5 Summary

So that the growth effects of catalyst-mediated prodrug activation on bacteria would realistically represent those applied *in vivo*, iron-limited, micro-aerobic conditions were pursued. Two media were successfully identified that displayed iron-limited bacteria growth, under a micro-aerobic atmosphere, (i) minimal, modified MOPS media and (ii) MHII. Due to the literature reported use of the latter media in analogous studies, it was then used in these studies to determine the antibacterial activity of moxifloxacin and its prodrugs.

As desired, both prodrugs (***N*-moxi** and ***C*-moxi**) possess significantly reduced antibacterial activity compared to the parent antibiotic, with MIC values approximately 300 times greater for the prodrugs. These prodrugs also provide a significant toxicity window, where only 3% need activation to observe the maximal inhibitory effect of moxifloxacin, if the prodrug is added at a 10 μM concentration and all is taken up into bacteria. It is surprising to see that both prodrugs have such similar activity profiles; this does not align with the hypothesis made, as it was expected modification of moxifloxacin's *C*-terminus would provide a significantly larger toxicity window, due to modification at the pharmacophore of fluoroquinolones, the β-keto acid motif.

The measurement of prodrug uptake into bacteria was attempted for both prodrugs, however precipitation of ***N*-moxi** during these experiments meant that data was only obtained for ***C*-moxi**. Although uptake was poor, 16% uptake was observed after incubation at 10 μM under conditions which are relevant for future catalyst-prodrug co-addition experiments. As bacterial uptake was only confirmed for ***C*-moxi**, this further supports the lone use of ***C*-moxi** in future studies.

2.5 Summary and Conclusions

Five prodrugs of the fluoroquinolone antibacterials ciprofloxacin and moxifloxacin were successfully synthesised, with a variety of *N*-terminus and *C*-terminus modifications. Considering their solubility profiles, the two moxifloxacin prodrugs ***N*-moxi** and ***C*-moxi** were selected to determine their compatibility for activation with the Kitamura-type catalysts.

HPLC kinetic assays showed that these prodrugs were indeed compatible with the Kitamura-type catalyst **Ru-control** for their activation under biologically-relevant conditions. However, reaction kinetics were significantly faster under a reduced oxygen atmosphere, due to observed oxygen-sensitivity of the active Ru(II) intermediate species. As a result, the potential medicinal application of the overall antibacterial delivery strategy is the treatment of gastrointestinal infections due to the environments low levels of molecular oxygen. It is hoped that under such conditions, catalyst lifetimes will be sufficient.

Two media were identified for the iron-limited, aerobic, and micro-aerobic growth of gut relevant bacteria *E. coli* K12 (BW25113). Initial attempts with a minimal M9 media were unsuccessful due to its high levels of concomitant iron after Chelex treatment which was attributed to its high phosphate content. For the minimal, modified MOPS media, iron-limited growth was obtained by Chelex treatment of the components alone. In contrast, for MHII, this was obtained by a combination of Chelex treatment and supplementation with 200 μM bpy. It is proposed that due to the complex nature of MHII and hence the likelihood of the presence of iron-binding functionalities like phosphates, Chelex treatment is less efficient.

The antibacterial activities of moxifloxacin and its prodrugs ***N*-moxi** and ***C*-moxi** were determined under iron-limited conditions using MHII supplemented with 200 μM bpy, under a micro-aerobic atmosphere to mimic the environment of the gut. Both prodrugs were found to be ~300 times less active compared to the parent antibiotic, with very similar dosage-response curves. However, due the favourable solubility profile of ***C*-moxi** and thus its measurable and estimated bacterial uptake of 16% added at 10 μM, this prodrug was selected for future studies.

Chapter 3 : The Design, Synthesis, and Activity for Prodrug Activation of Catalyst-Siderophore Conjugates

3.1 Introduction

3.1.1 The Synthesis of Kitamura-type Catalysts

There are two main methods for the synthesis of Kitamura-type catalysts: Method A and Method B, Figure 55. The synthesis of the optimised hydroxyquinoline-ligated Kitamura-catalysts reported by Völker and Meggers in 2017 proceeds *via* Method A, whereas Method B is more commonly employed for the synthesis of quinaldic acid-ligated Kitamura-type catalysts.[21, 33] Both methods use the readily available ruthenium precursor tris(acetonitrile)cyclopentadienylruthenium(II) hexafluoro-phosphate. The oxygen and water sensitivity of this precursor means its storage and reaction to form the catalyst is executed under a dry, nitrogen atmosphere. The common solvents employed for these reactions are dichloromethane and acetone, however DMF has also been utilised in some cases.[35] Prior to their use, these solvents must be dried and degassed. Purification of the product is usually achieved by precipitation, where required by the addition of an antisolvent such as dichloromethane, EtOAc or Et_2O.

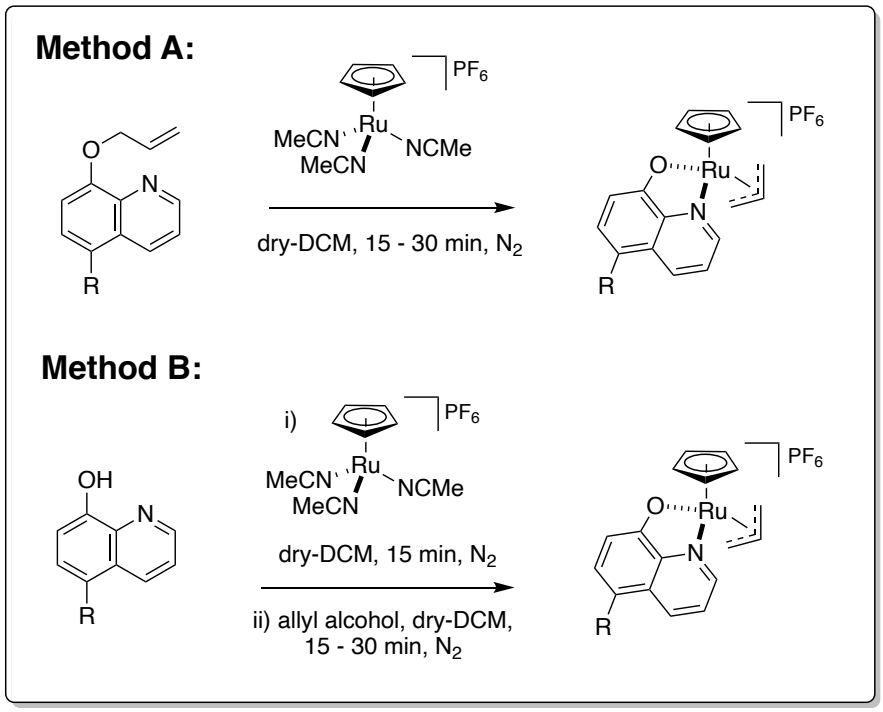

Figure 55 General synthetic routes to the Kitamura-type catalysts.[21, 33] R = various functional groups.

Biomolecule-conjugated Kitamura-type catalysts have been reported in the literature for applications in living systems. The two significant examples of this are catalyst-attachment to biotin for the development of artificial enzymes within streptavidin and triphenyl phosphonium cations for prodrug activation within mitochondria, Figure 56 (section section 1.2.1.2).[31, 35, 36] In both instances, the biomolecules are attached covalently to the quinaldic acid rather than the cyclopentadienyl ligand, so that their syntheses can proceed by Method A or Method B. Most literature applications thus far have utilised the earlier reported quinaldic acid-ligated catalyst, as the optimised hydroxyquinoline-ligated version was not reported until recently. Moreover, as the η^3-allyl ligand is exchangeable in the presence of nucleophiles such as water, attachment through this ligand is not a viable option if sustained attachment is desired.

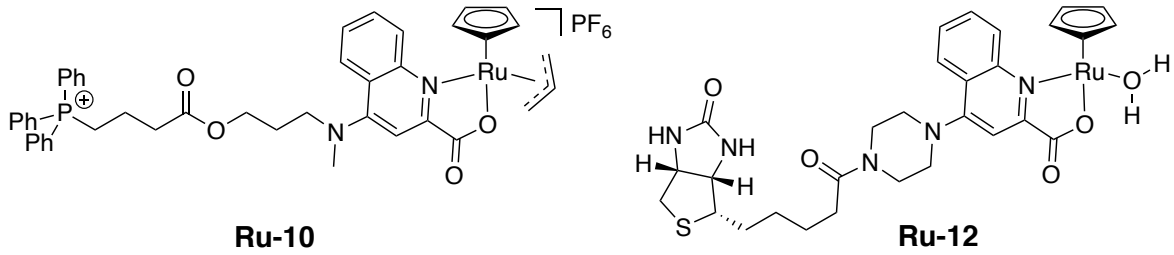

Ru-10 **Ru-12**

Figure 56 Chemical structure of biomolecule-appended Kitamura-type catalysts: **Ru-10** by Tomás-Gamasa *et al.*[31] (Ph = phenyl) and **Ru-12** by Okamoto *et al.*[35] and Heinisch *et al.*[36]

3.1.2 The Synthesis of Trojan Horse Antibacterials

The synthesis of Trojan-Horse antibacterials in the literature in general share a common approach of a convergent synthesis, where the siderophore and antibacterial components are joined together in the penultimate step of the overall synthesis.[146, 162-164] For example, Zheng *et al.* in 2012 reported the synthesis of several enterobactin conjugates with different functional groups, including fluorescent dyes and antibiotics joined together by either polyethylene glycol (PEG) or aliphatic chain linkers, such as Cipro-Ent and Vanco-Ent, Figure 57.[162] Whilst the arguably more important parts of this project investigate the bacterial uptake and antibacterial activity of the conjugates, their synthesis was a significant achievement in itself.

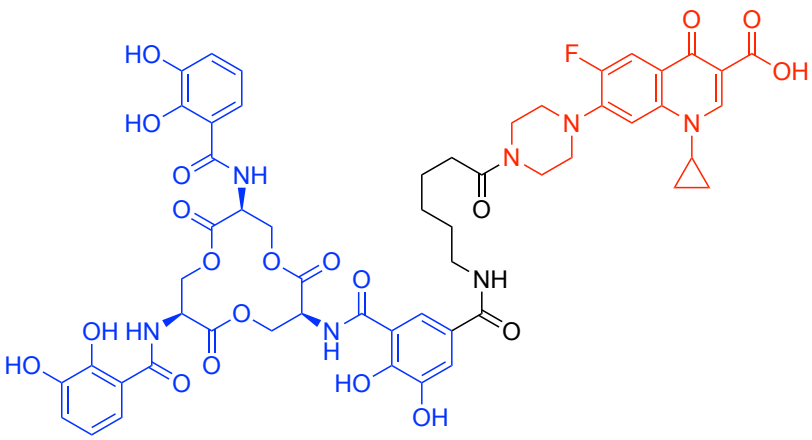

Cipro-Ent

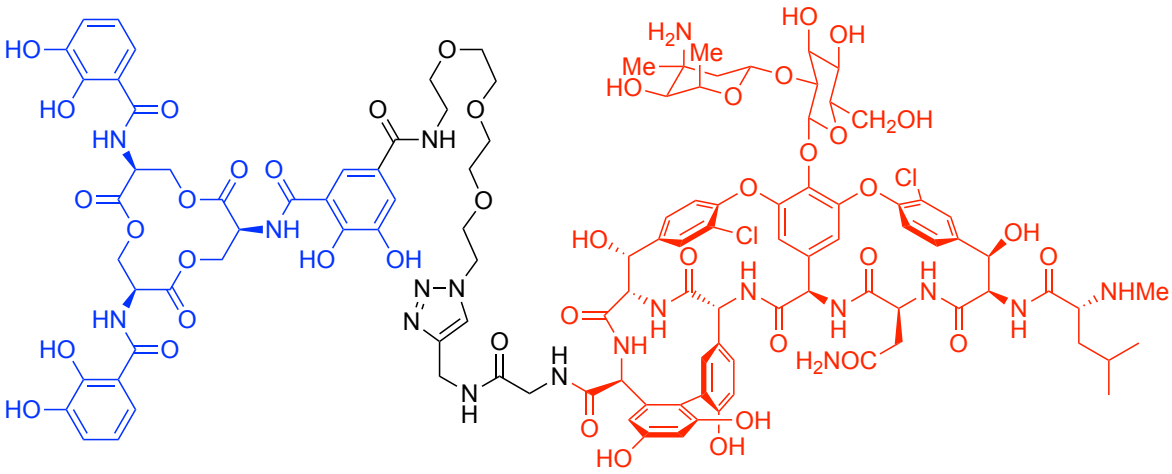

Vanco-Ent

Figure 57 Chemical structures of enterobactin conjugates with ciprofloxacin and vancomycin antibacterials, reported by Zheng *et al.*[162] Antibacterial part = red, siderophore part = blue.

As the siderophore functional groups responsible for iron-binding can interfere with reactions due to their nucleophilic and metal-binding properties under basic conditions, their deprotection is usually in the last step of the overall synthesis. Typical protecting groups for catechol moieties include methoxy, acetal, acetate, benzyl or *para*-methoxybenzoyl (PMB) modification of the phenoxide.

3.1.3 Chapter Aims

The overall aim of this Chapter is to develop synthetic routes for the attachment of siderophores and siderophore mimics to hydroxyquinoline-ligated Kitamura-type

catalysts. It is hoped that these catalysts will hijack siderophore-mediated iron-uptake pathways in bacteria, so that they are internalised preferentially over human cells during the treatment of a bacterial infection. It is difficult to predict the impact of the catalyst moiety on siderophore utilisation and in some cases, the type of siderophores used by the specific bacteria. Therefore, a wide range of different siderophores and siderophore-mimics will be conjugated to the Kitamura-type catalyst. The rationale for the different siderophore mimics chosen for appendage will include relevant literature known Trojan-Horse antibacterials. Following successful syntheses, their activity for prodrug (***C*-moxi**) activation will be tested under biologically-relevant, anaerobic conditions. These studies will evaluate the effect the siderophore attachment has on catalyst activity. The use of biologically-relevant conditions will establish whether the catalysts are viable options for their potential medicinal application.

3.2 The Synthesis of Catalyst-Siderophore Conjugates

3.2.1 Bidentate Catechol-based Siderophores for Catalyst Conjugation

Several bidentate catechol-based siderophore-antibacterial conjugates have been investigated for a Trojan-Horse approach, examples of which are shown in Figure 58.[165-168] The only Trojan-Horse antibacterial to make it to the clinic, cefiderocol (FETROJA®), possesses a bidentate catechol conjugated to a cephalosporin antibiotic, Figure 58.[85-87] The success of cefiderocol is striking as major siderophores for bacteria tend to possess higher denticity forming hexadentate complexes with Fe(III). In work by Neumann *et al.* in 2018, ciprofloxacin conjugates with hydrolysis products of enterobactin showed drastically-reduced antibacterial activities compared to those with enterobactin.[169] All of the exemplar conjugates shown in Figure 58 are β-lactam antibiotics (BRL-41897A, E0702 and cefiderocol) or derivatives (YU253434) and their mode of action is the inhibition of the periplasmic enzyme *DD*-transpeptidase.[165, 166, 168] Hence, bacterial uptake into this region is sufficient for the desired antibacterial effect. This is not the case for

fluoroquinolone antibacterials whose enzyme targets are located in the cytoplasm, meaning uptake through both membranes in Gram-negative bacteria is required.

A recent example of a siderophore-antibacterial conjugate YU253434 was reported by Goldberg *et al.* in 2020.[165] During these studies, a γ-lactam antibiotic was developed, conjugated to a bidentate catechol siderophore-mimic *via* a succinimide functionality, Figure 58. YU253434 targets penicillin-binding proteins and encouraging potencies were observed *versus P. aeruginosa, K. pneumoniae* and *E. coli* compared to its non-conjugated control ceftazidime. Iron-dependent bacterial growth assays suggested bacterial uptake by *P. aeruginosa* (see section 4.1.1).

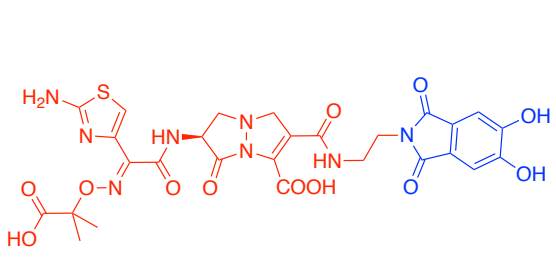

YU253434

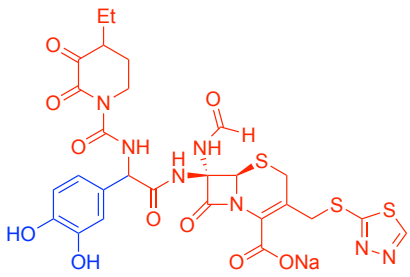

BRL-41897A

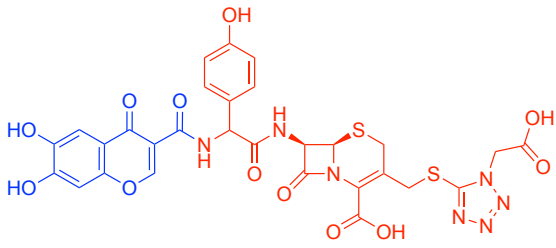

E0702

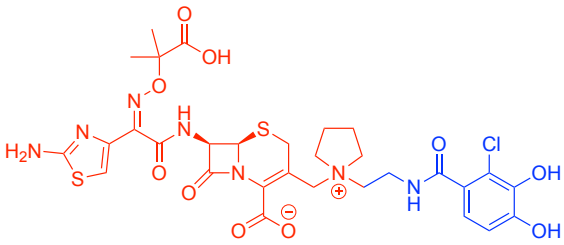

cefiderocol

Figure 58 Chemical structures of compounds investigated for Trojan-Horse antibacterials YU253434, BRL-41897A, E0702, and cefiderocol.[85-87, 165, 166, 168]

3.2.1.1 Synthetic Route 1 – Amide Linkage

Based on typical routes to Kitamura-type catalysts and Trojan-Horse antibacterials, the attachment of the siderophores and siderophore mimics will proceed *via* the hydroxyquinoline ligand prior to ruthenium-complexation to give the final catalyst product. The chemical structure of the first siderophore-catalyst conjugate target **Ru-s1** is shown in Figure 59. The synthetic route toward it is a two-part convergent synthesis, using Method B for ruthenium-complexation, Figure 60 (part 1) and Figure 61 (part 2).

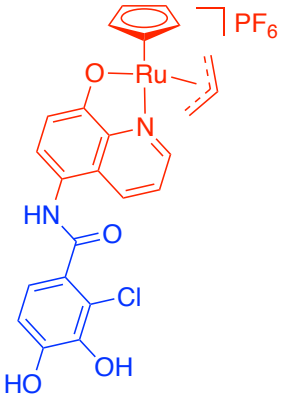

Figure 59 Chemical structure of **Ru-s1**. Catalyst = red, siderophore mimic = blue.

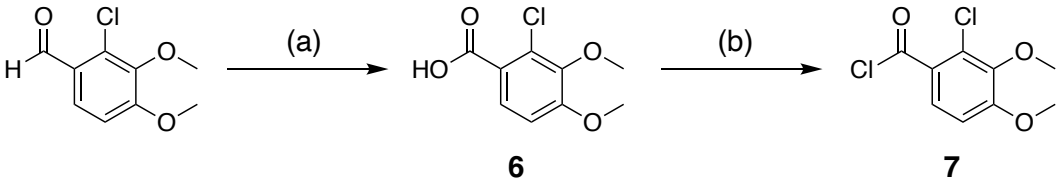

6 **7**

Figure 60 Synthetic route towards **Ru-s1** - part 1. (a) $KMnO_4$, H_2O, 75 °C, 5 h, 78% (b) oxalyl chloride, rt, 2 h, N_2, crude product.

Part one toward the synthesis of **Ru-s1** involves the preparation of an acid chloride of the siderophore-mimic, Figure 60. This siderophore mimic is inspired by the clinically-approved antibacterial cefiderocol.[86, 87] In step (a), 2-chloro-3,4-dimethoxybenzoic acid **6** was obtained from its aldehyde *via* oxidation using potassium permanganate in water at room temperature in a 78% yield, following a literature procedure from Almedia *et al.* for the same compound.[170] Purification involved basification, water washes and formation of the free acid using aqueous hydrochloric acid. Finally, an off-white, crystalline product was obtained by hot recrystallisation in ethanol:water (7:3). The identity and purity of this literature compound were confirmed by ^{1}H and ^{13}C NMR spectroscopy, and HRMS compared to those reported by Almeida *et al.* for the same compound.[170] The crude acid chloride of **7** was obtained based on a reaction procedure reported by Thansandote *et al.* for an analogous compound.[171] This involved stirring **6** in excess oxalyl chloride at room temperature under a dry, nitrogen atmosphere followed by removal of the residual oxalyl chloride and formed water *in vacuo*. This product **7** was used immediately, without characterisation, during part two, step (c) of the synthesis, Figure 61.

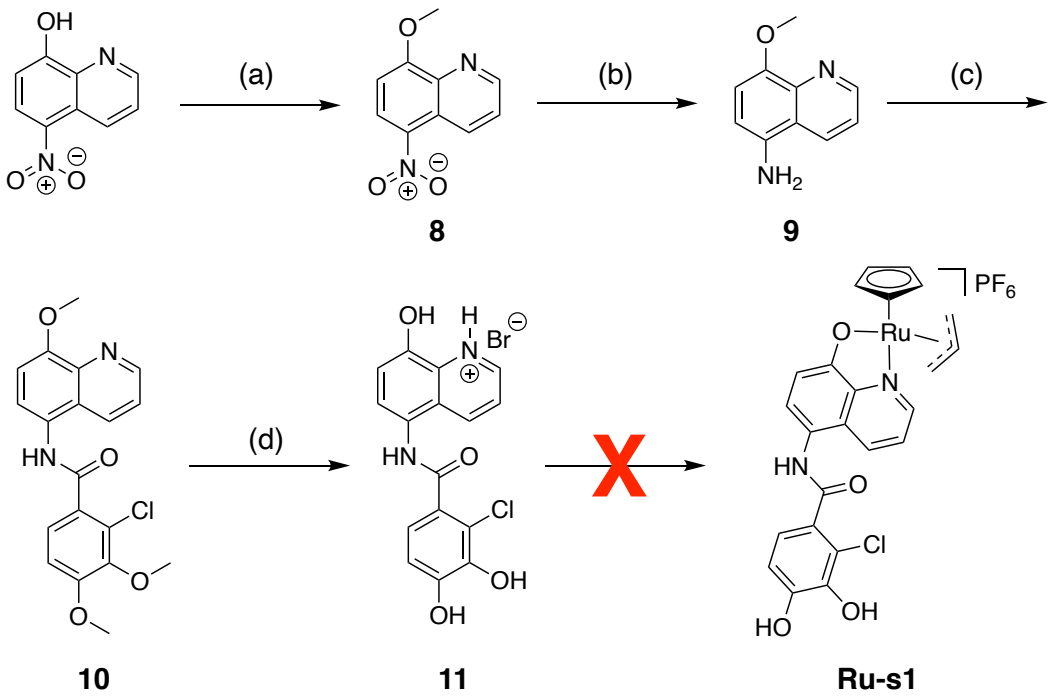

Figure 61 Synthetic route towards **Ru-s1** - part 2. (a) iodomethane, K_2CO_3, dry DMF, 50 °C, 18 h, 84% (b) 5% w/w Pd/C, conc. HCl (aq), H_2 atmosphere, MeOH:THF (2:1), rt, 24 h, 94% (c) **7**, dry dichloromethane, rt, 36 h, N_2, 68% (d) BBr_3 in dichloromethane, dry dichloromethane, -78 °C, 3 d, 63%.

Part two of the synthesis towards **Ru-s1** is shown in Figure 61 which first involves the functionalisation of 8-hydroxy-5-nitroquinoline with an aniline, so that its rection with acid chloride **7** links the parts together *via* an amide bond, step (c). This compound **9** was accessed in two steps. Step (a) involves protection of the phenoxide functionality *via* formation of a methoxy motif, initially attempted *via* formation of the tertbutyldiphenylsilyl ether however this motif was unstable on silica. Formation of the methoxy group was selected so that a global methoxy deprotection can occur following amide coupling, to reveal the final ligand product, **11**. The formation of 8-methoxy-5-nitroquinoline was achieved using iodomethane in dry DMF at 50 °C, however during reaction optimisation it was found the use of excess iodomethane at temperatures above this resulted in the increased formation of a quinolinium by-product. The structure of this by-product is likely either a zwitterion with its phenoxide or an iodide counter-ion, Figure 62. An overlayed ^{1}H NMR spectrum of the desired product **8** and the quinolinium by-product in chloroform-*d* is shown in Figure 63. The most significant change in the quinolinium spectrum

corresponds to the methyl group which in this case is bound to the positively charged tertiary amine and therefore more downfield, 4.3 → 9.0 ppm. The already electron-deficient *ortho*-aromatic position to this positively charged amine is also significantly further downfield, 9.2 → 10.4 ppm. The identity and purity of literature compound **8** was confirmed by ^{1}H and ^{13}C NMR, HRMS and elemental analysis compared to that for the same compound.[172]

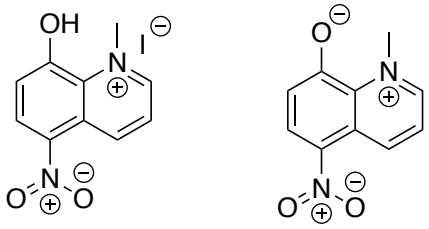

Figure 62 Potential chemical structures of quinolinium by-products: 8-hydroxy-1-methyl-5-nitroquinolin-1-ium iodide (LHS) or 1-methyl-5-nitroquinolin-1-ium-8-olate (RHS).

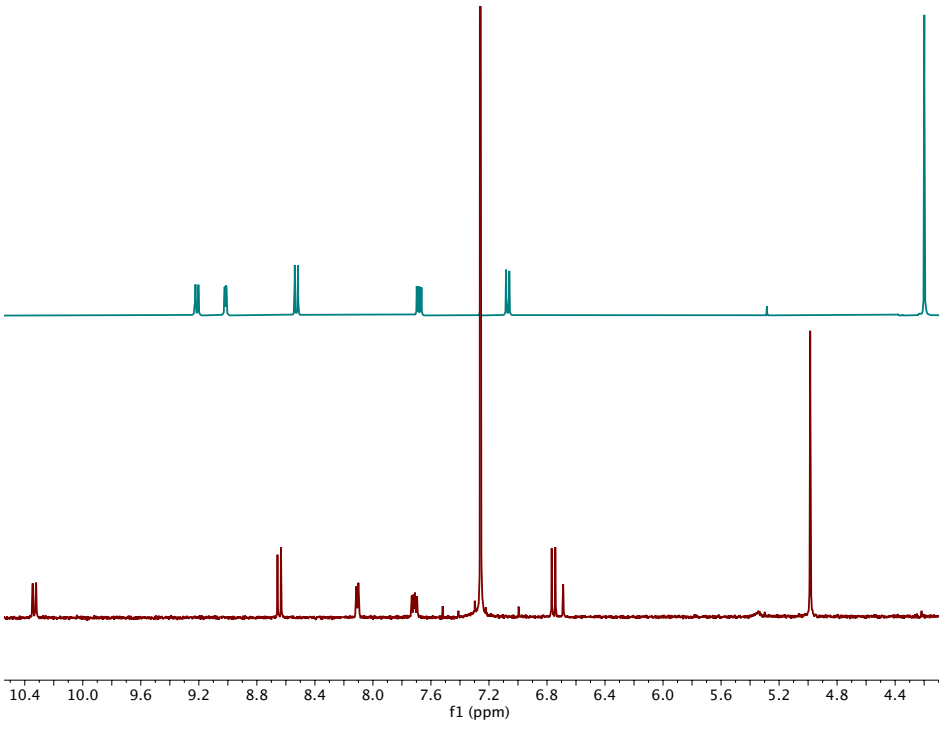

Figure 63 Overlapped ^{1}H NMR spectra of 8-methoxy-5-nitroquinoline, **8** (blue, top) and the quinolinium by-product (red, bottom) in $CDCl_3$.

Step (b) involved the reduction of the nitro functionality in **8** to the form the aniline containing **9** *via* a reduction using 5% w/w Pd/C under a hydrogen atmosphere, in

a 94% yield. The identity and purity of this literature compound were confirmed by comparison of ^{1}H NMR spectroscopy and HRMS to those reported by Cheung *et al.* for the same compound.[173] Step (c) is the converging point in this synthetic route to **10** *via* formation of an amide bond and involves the dropwise addition of **9** in dry dichloromethane to the crude acid chloride **7** in the same solvent under a dry, nitrogen atmosphere. After stirring for 36 h, the reaction was quenched with water to hydrolyse any residual acid chloride and reform the corresponding carboxylic acid **6** which was removed by basic washes, to isolate the desired product **10** as an orange/brown solid. The identity and purity of this novel compound were confirmed by a combination of ^{1}H and ^{13}C NMR, HRMS, IR and elemental analysis. Step (d) was the global methoxy deprotection to give the final ligand product **11**, by stirring with excess tribromoboron in dry dichloromethane at -78 °C for 3 d, to yield the hydrobromide salt in a 63% yield, as a light brown/yellow solid. The identity and purity of this novel compound was confirmed by a combination of ^{1}H and ^{13}C NMR, HRMS, IR and elemental analysis.

The final step to form **Ru-s1**, was attempted using conditions analogous to Method B, Figure 55. This reaction first required the dissolution of ligand **11** in dry dichloromethane with one molar equivalent of DIPEA to generate the free base however, large amounts of dry MeOH were required to aid solubility. Under a dry, nitrogen atmosphere one molar equivalent of tris(acetonitrile) cyclopentadienylruthenium(II) hexafluorophosphate was added dropwise as a solution in dry dichloromethane and left stirring for 15 min. One molar equivalent of allyl alcohol was then added and after an additional 30 min stirring, the reaction solvent was removed *in vacuo*. Unfortunately, analysis by ^{1}H NMR showed a mixture of products, as multiple cyclopentadienyl environments were observed. Analysis by HRMS utilising positive electrospray showed no m/z corresponding to the desired product but did show that of the starting material.

Although the synthesis toward **Ru-s1** was largely successful, apart from the final step involving ruthenium-complexation of the ligand, improvements for the next attempted synthetic route were identified. This included the incorporation of more polar groups in the ligand target, to improve solubility. It was believed that the planar nature of ligand **11** led to its insolubility in the ideal reaction solvent for ruthenium

complexation (dichloromethane) and therefore a longer more flexible linker between the siderophore mimic part and the hydroxyquinoline should be pursued. Moreover, it was decided that Method A for ruthenium-complexation should be utilised, as this is the more common method and the synthesis of **Ru-control** gave better yields using Method A. This in turn meant alternative protection groups for the catechol siderophore-mimic part were required, as the allyl ether is not stable to the strongly Lewis acidic conditions required for methoxy deprotection.

3.2.1.2 Synthetic Route 2 – Click Chemistry Linkage

Based on the results in section 3.2.1.1, it was decided that the ligand for the synthesis of the next siderophore-conjugated catalyst target should have more flexible, polar groups to improve solubility and utilise Method A for ruthenium-complexation. However, since there are few protecting groups for catechol phenoxides that are removable under conditions that do not cleave the essential allyl ether motif, an alternative approach was applied utilising 'click chemistry'.

Click chemistry is a term coined by Sharpless in 2001 and refers to reactions with wide substrate scope and efficient conversion, forming by-products that are easily removed. A well-known example of click chemistry is Huisgen-Meldal-Fokin Cu(I)-catalysed terminal alkene-azide by reported by Meldal *et al.*[174] and Wang *et al.*[175], Figure 64. This reaction has been utilised in a myriad of scenarios such as cell imaging and site-specific cell-surface DNA labelling, due to its compatibility with multiple conditions, Figure 64.[176-178] The first instance of its use in a bio-orthogonal context was by Mahal, Yarema and Bertozzi in 1997, for the engineering of cell surfaces through oligosaccharide biosynthesis.[178]

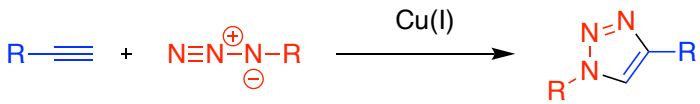

Figure 64 Schematic of the Huisgen-Meldal-Fokin Cu(I)-catalysed terminal alkene-azide reaction. Alkene = blue, azide = red.

It was decided that the catalyst part would bear the terminal alkyne, Figure 65, and the siderophore part the azide. A beneficial aspect of this synthetic approach is that **Ru-13**, can then be used to access several siderophore conjugates if their

corresponding azide conjugates are made. A schematic to show the synthesis toward the alkyne functionalised ruthenium-complex **Ru-13** is shown in Figure 65.

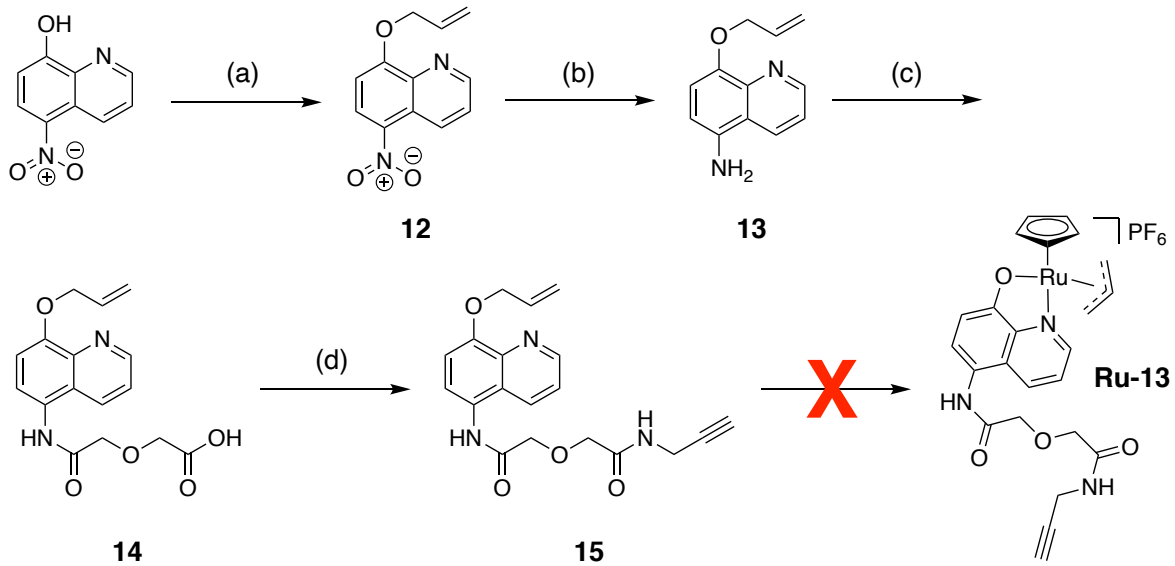

Figure 65 Synthetic route towards **Ru-13**. (a) allyl bromide, K_2CO_3, dry DMF, 60 °C, 24 h, 58% (b) Zn dust, NH_4Cl, MeOH, rt, 24 h, 45% (c) diglycolic anhydride, dry dichloromethane, rt, 1 h, 52% (d) propargyl amine, *N′*-ethylcarbodiimide hydrochloride, 1-hydroxybenzotriazole monohydrate, DIPEA, dry DMF, rt, 18 h, 38%.

Step (a) in the synthesis of the alkyne-functionalised catalyst part **Ru-13** involved generation of the phenoxide ion of 8-hydroxy-5-nitroquinoline using potassium carbonate and subsequent reaction of this group with electrophile allyl bromide at 60 °C in dry DMF to form the allyl ether group **12** in a 58% yield. The identity and purity of this literature compound was confirmed by ^{1}H NMR spectroscopy, HRMS and elemental analysis compared to those reported by Veschi *et al.* for the same compound.[179] Formation of the quinolinium by-product is less significant in this reaction, probably due to the greater steric hinderance that the allyl group possesses with the phenol group on its formation, compared to the methyl group. Step (b) involved the reduction of the nitro group to form the aniline functional group. The reaction conditions to achieve this transformation must be chemo-selective, as to prevent reduction of the alkene functionality. After trialling several reducing agents including iron dust and samarium(II) iodide, zinc dust with ammonium chloride in methanol at room temperature gave **13** in the best yield of 45%, with

minimal by-product formation such as the nitroso intermediate. The identity and purity of this novel compound was characterised by a combination of ^{1}H and ^{13}C NMR, HRMS, IR and elemental analysis. The following reaction step (c) facilitated the conjugation of the aforementioned aniline **13** to diglycolic acid *via* utilising its anhydride, to give **14** in a 52% yield. The identity and purity of this novel compound was confirmed by a combination of ^{1}H and ^{13}C NMR, HRMS, IR and elemental analysis. The penultimate reaction to ruthenium-complexation, step (d), was an amide coupling reaction to attach the terminal alkyne. This was achieved using propargyl amine alongside amide coupling agents *N′*-ethylcarbodiimide hydrochloride (EDC.HCl) and 1-hydroxybenzotriazole monohydrate (HOBt.H_2O) and *N,N*-diisopropylethylamine (DIPEA) in dry DMF at room temperature. Although these reaction conditions did form the desired product **15**, this was in a low yield due to a competing side reaction which formed a cyclic succinimide by-product of **14** which is hypothesised to occur *via* the mechanism shown in Figure 66.

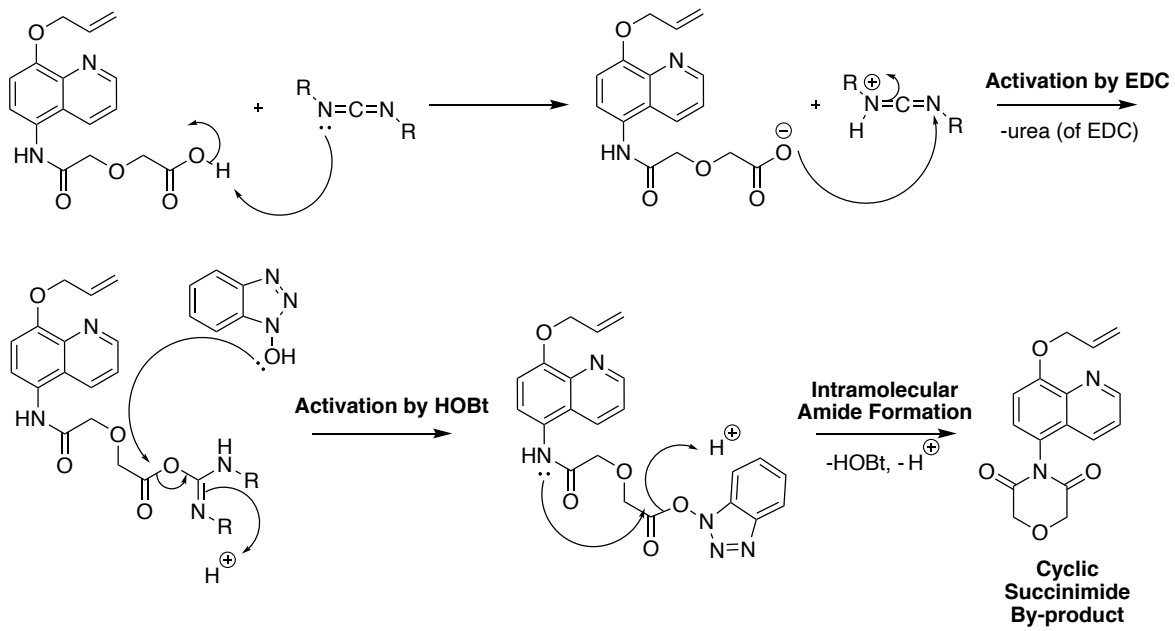

Figure 66 Proposed mechanism for cyclic succinimide by-product formation during amide coupling reactions using **14** in the synthesis of **15**.

The final step to form the alkyne-functionalised ruthenium-complex **Ru-13** was unsuccessful. The conditions for this reaction followed Method A, outlined in Figure 55. Although the solubility of **15** in dichloromethane was better than that of the previous ligand **11**, possibly due to the diglycolic linkage and the ligand's reduced

planarity, it appears competing Ru-mediated reductions of the terminal alkyne take place, as observed by liquid injection field desorption/ionisation (LIFDI) HRMS, Figure 67. This unfortunately meant the use of click chemistry for attachment of the siderophore part to the catalyst was not possible however the benefits of flexibility in the linker for solubility will be considered for future synthetic approaches.

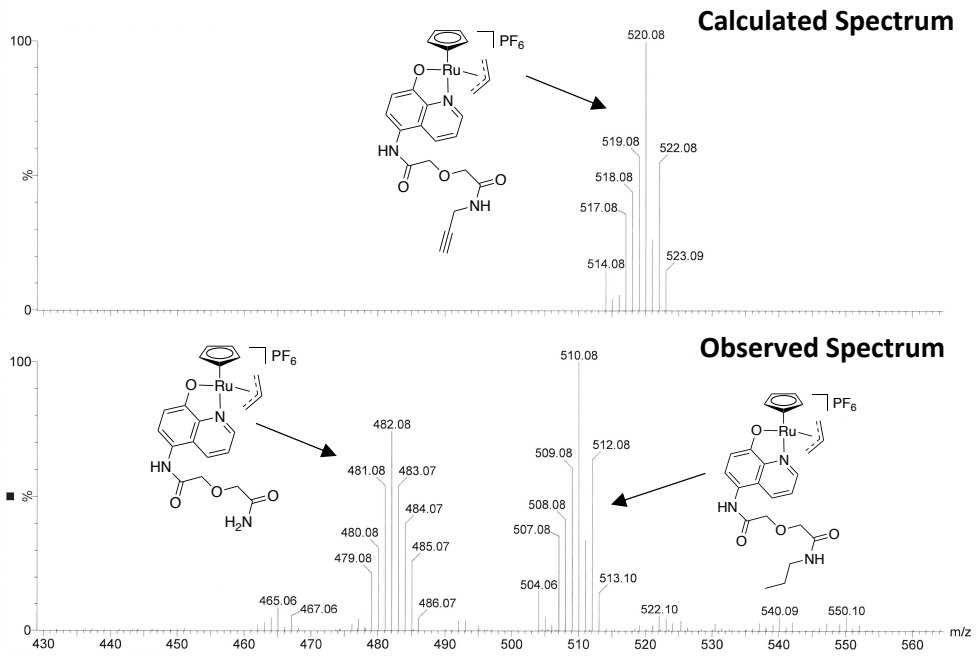

Figure 67 Calculated and observed LIFDI HRMS spectra of reaction mixture toward the synthesis of **Ru-13**, with proposed ruthenium-complex structures shown alongside their corresponding m/z values.

3.2.1.3 Synthetic Route 3 – Glycine Linkage

The chemical structure of the third siderophore-conjugated catalyst target **Ru-s2** is shown in Figure 68. **Ru-s2** possesses an acetate-protected bidentate catechol siderophore part; such groups are present in several conjugates researched for uses as Trojan-Horse antibacterials.[47, 164, 180] It is believed that these groups provide beneficial therapeutic properties *in vivo* by preventing catecholate inactivation by enzymatic methylation.[47, 164, 181] These groups are thought to auto-uncage under biologically-relevant conditions to reveal the catechol.[182] Moreover, it is hoped that these groups will prevent a competing reaction of catechol binding to the ruthenium during the complexation step. Before the synthesis of **Ru-s2** was attempted, a siderophore probe that possesses the acetate-protected catechol motif was

synthesised and its auto-uncaging properties evaluated utilising UV-vis spectroscopy, compared to its uncaged version.

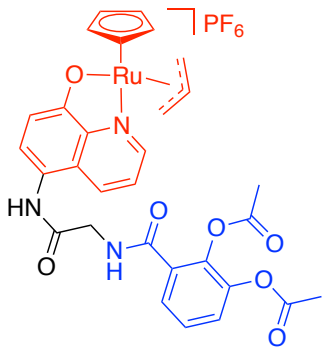

Figure 68 Chemical structure of **Ru-s2**. Catalyst = red, siderophore mimic = blue.

Siderophore Probes for Acetate-protected Catechol Auto-uncaging

The syntheses of the caged **17** and uncaged **18** siderophore probes are shown in Figure 69 and Figure 70, respectively.

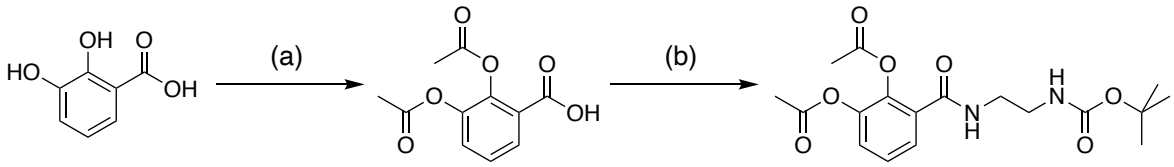

16 **17**

Figure 69 Synthetic route towards **17**. (a) (i) acetic anhydride, conc. H_2SO_4 (aq), rt, 10 min (ii) Et_2O, rt, 24 h, 96% (b) (i) oxalyl chloride, rt, 3 h, crude (ii) *N*-boc-1,2-diaminoethane, DIPEA, dry dichloromethane, 0 °C, 10 min, 13%.

The caged siderophore probe **17** was made in two steps from readily available 2,3-dihydroxybenzoic acid, Figure 69. Step (a) involved the acetate-protection of the phenoxide functionalities that constitute the catechol motif, following a literature procedure for the same compound.[183] This reaction involved the dissolution of 2,3-dihydroxybenzoic acid in acetic anhydride as the reaction solvent, with diluted sulfuric acid. Et_2O was added to this reaction mixture after 10 min, to precipitate the desired product **16** as a white solid in a 96% yield. The identity and purity of this literature compound was confirmed by ^1H and ^{13}C NMR spectroscopy and HRMS compared to those reported by Bergeron *et al.* for the same compound.[183] The final step (b) was amide coupling to the amine decorated *N*-boc-1,2-diaminoethane by

generation of the acid chloride of **16** using oxalyl chloride followed by addition of the amine in dry dichloromethane to give **17** in a 13% yield. The identity and purity of this literature compound was confirmed by ^{1}H and ^{13}C NMR spectroscopy and HRMS compared to those reported by Ferreira *et al.* for the same compound.[182] The poor yield obtained can be attributed to the instability of the acetate groups during purification by column chromatography and nucleophiles, such as the amine used to form the amide bond. In fact, amide coupling reactions using agents such as EDC.HCl gave poorer conversions, due to their slower reaction kinetics and requirement for basic conditions.

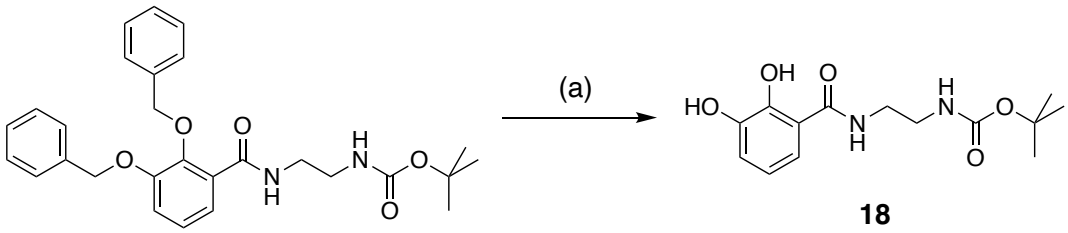

Figure 70 Synthetic route towards **18**. (a) 5% w/w Pd/C, H_2 atmosphere, THF:MeOH (1:1), rt, 16 h, 95%.

The uncaged siderophore probe **18** was accessed *via* the benzyl-protected version provided by Conor Black. This was a hydrogenation reaction using 5% w/w Pd/C under a hydrogen atmosphere in a THF:MeOH (1:1) mixture at room temperature, to give **18** in a 95% yield, after trituration using PET. The identity and purity of this literature compound was confirmed by ^{1}H and ^{13}C NMR spectroscopy and HRMS compared to those reported by Soulere *et al.* for the same compound.[184]

The ability of the caged siderophore probe **17** to auto-uncage under biologically-relevant conditions was evaluated by ERASMUS student Sophie Gutenthaler.[2] To inform auto-uncaging kinetics experiments, the continuous variation method was used to determine how the Fe(III)-binding stoichiometries of the uncaged siderophore probe **18** varied depending on their relative amounts. This method involved the measurement of UV-vis spectra for the uncaged siderophore probe **18** with different known equivalents of Fe(III), at a constant sum of their concentrations. The λ_{max} values for the UV-vis spectra obtained correspond to a ligand-to-metal charge transfer (LCMT) resulting from the catechol-Fe(III) interaction at equilibrium. The variation of this value provides information regarding the Fe(III)-complex

species dominating within the measured sample. An absorbance in the range 560-590 nm is known to correspond to the 2:1 (ligand:iron) species whereas the 3:1 species absorbs in the range 480-495 nm, Figure 71.[185, 186] During measurements of **18**, a shift in the λ_{max} from 494 → 588 nm (purple → red colour change) was observed with increasing Fe(III). Therefore, this λ_{max} shift can be assigned to the formation of the 2:1 species from the 3:1. The maximum absorbance corresponding to the thermodynamically preferred 3:1 species at 494 nm occurs at 80% ligand and therefore auto-uncaging kinetics experiments were conducted at these equivalents.

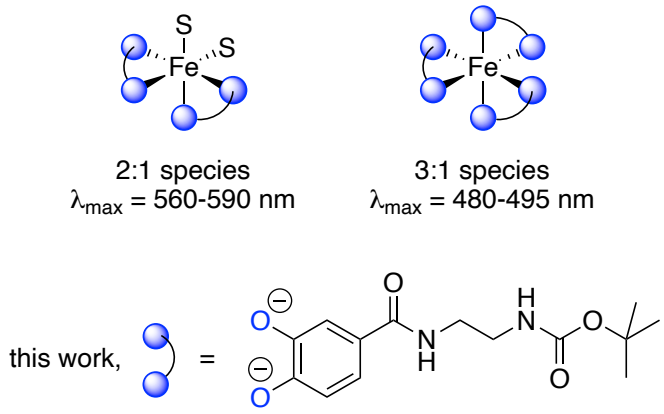

Figure 71 Iron-coordinating geometries of bidentate catechol ligand **18**, and their corresponding UV-vis absorbances. S = solvent.

Kinetics experiments for the auto-uncaging of **17** were approximated based on its relative absorbance at 494 nm compared to the uncaged version **18**. The UV-vis spectra of the reaction mixture over time show a similar λ_{max} shift toward 494 nm corresponding to the increased production of uncaged siderophore probe **18**, Figure 72.[2] The results from the corresponding kinetic trace showed 20% uncaging after 12 h and 50% over 2 d, Figure 73.[2] Measurements after this time were discarded due to the formation of a precipitate (presumed to be iron-phosphate) which interfered with absorbance measurements. Although kinetics for uncaging were slow, these experiments suggest the acetate groups do indeed auto-uncage under biologically-relevant conditions to release the iron-binding catechol motif, as reported by Ferreira *et al.* in 2017.[182] Moreover, this uncaging may be faster in the presence of human and bacterial cells due to the presence of nucleophiles and esterase enzymes.

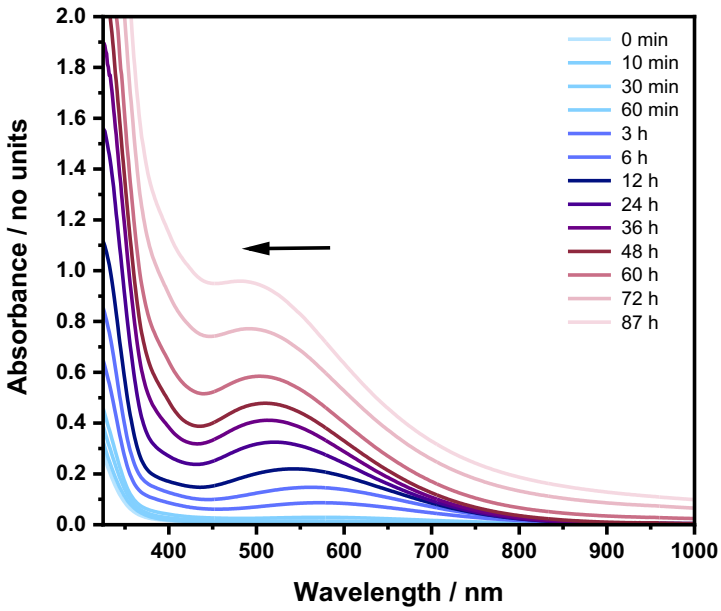

Figure 72 UV-vis spectra of 80% caged siderophore probe **17** to FeNTA at a combined concentration of 800 μM, in 10% DMSO in aqueous M9 buffer (pH 7.4) over 87 h. The arrow indicates the shift in λ_{max}.[2]

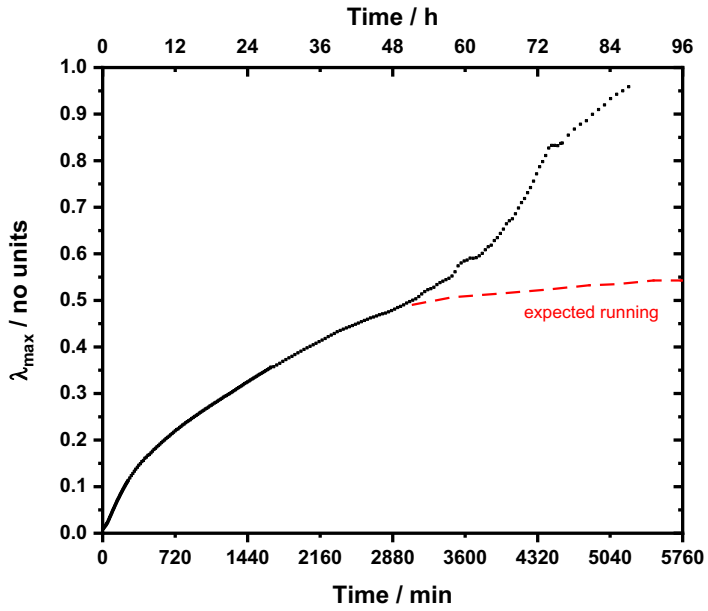

Figure 73 Kinetic trace for auto-uncaging of 80% caged siderophore probe **17** to FeNTA at a combined concentration of 800 μM, in 10% DMSO in aqueous M9 buffer (pH 7.4) with over 87 h.[2]

The Synthesis of a Caged Bidentate Catechol Catalyst Conjugate

Following experiments to confirm the auto-uncaging of the acetate-protected catechols in biologically relevant conditions, the synthesis of **Ru-s2** was initiated. The synthetic route was a three-part convergent synthesis, Figure 74 (part 1), Figure 75 (part 2), and Figure 76 (part 3), which used Method A for ruthenium-complexation.

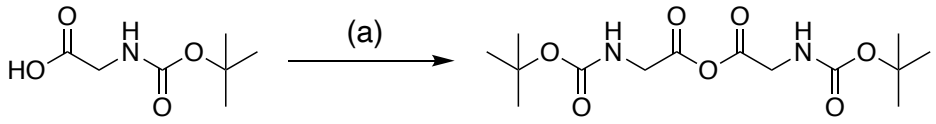

19

Figure 74 Synthetic route towards **Ru-s2** - part 1. (a) dicyclohexylcarbodiimide, dry dichloromethane, rt, 1 h, crude.

Part one involved formation of the literature known anhydride of *N*-boc glycine following a literature procedure by Barden *et al.* for the same compound, Figure 74.[187] This reaction used dicyclohexylcarbodiimide (DCC) in dry dichloromethane, at room temperature to form the desired product **19**. This reaction forms the urea of DCC as a by-product, which was separated by filtration. The desired product was isolated from the filtrate and immediately used crude during part three of the overall synthesis, step (b), without characterisation.

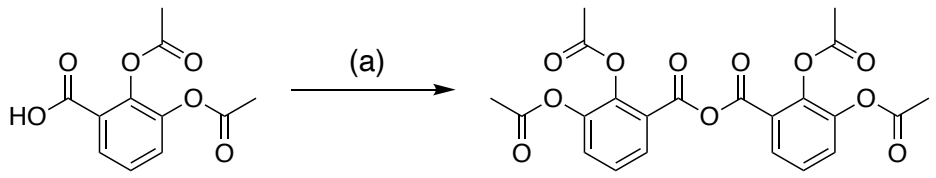

16 **20**

Figure 75 Synthetic route towards **Ru-s2** - part 2. (a) dicyclohexylcarbodiimide, dry dichloromethane, rt, 1 h, crude.

Part two involved formation of the anhydride of previously synthesised 2,3-diacoxybenzoic acid, Figure 75. This reaction used the same conditions as those reported earlier for the synthesis of **20**. This product was immediately used crude during part three of the synthesis, step (e), without characterisation.

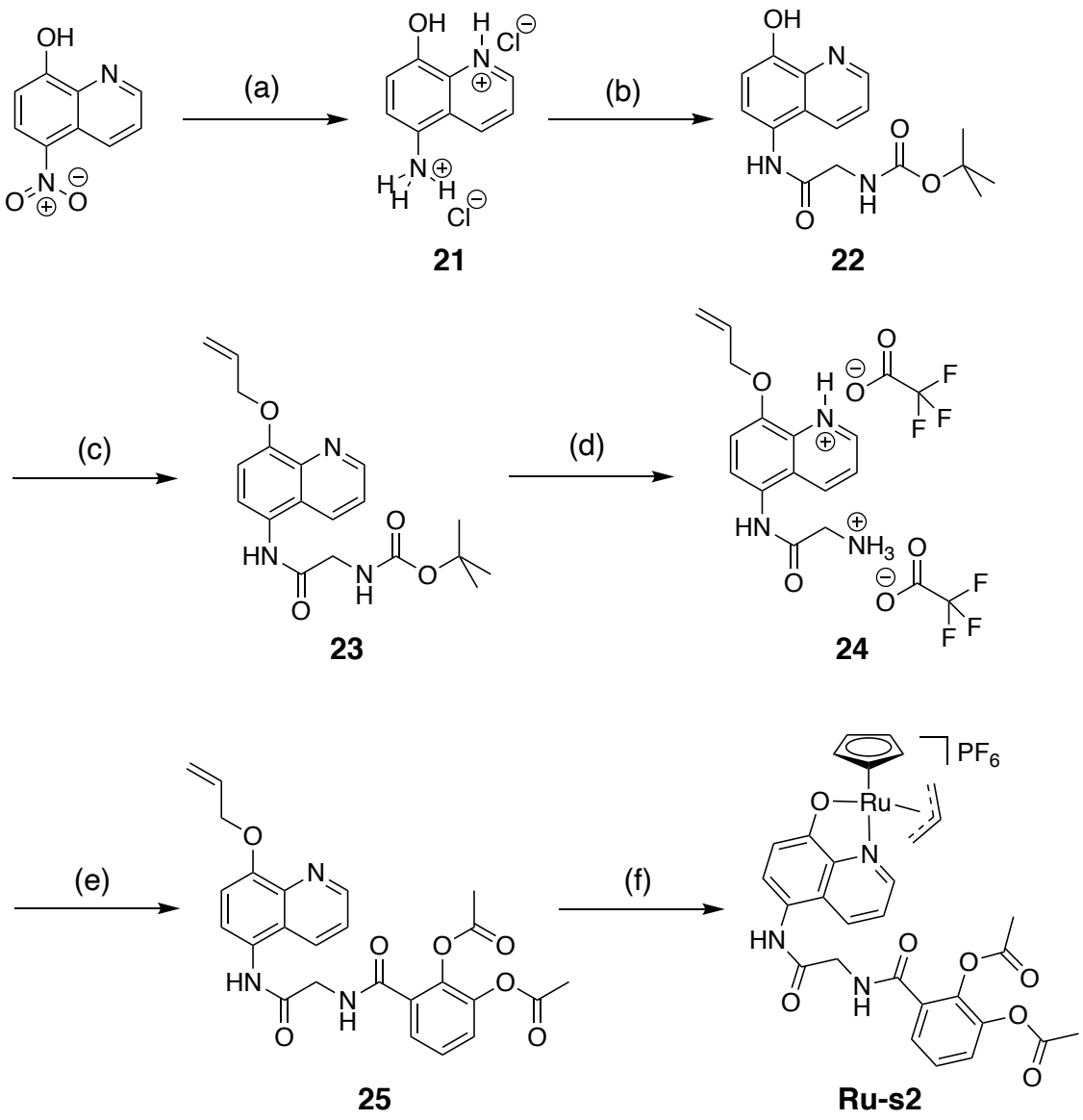

Figure 76 Synthetic route towards **Ru-s2** - part 3. (a) 5% wt. Pd/C, conc. HCl (aq), H_2 atmosphere, H_2O, rt, 24 h, 98% (b) **19**, DIPEA, dry DMF, 0 °C → rt, 2 d, N_2 atmosphere (c) allyl bromide, K_2CO_3, dry DMF, 50 °C, 18 h, 14% (d) trifluoroacetic acid, dichloromethane, 0 °C, 5 h, 99% (e) **20** in dry dichloromethane, dry DMF, rt, 3 h, 45% (f) $[CpRu(MeCN)_3]PF_6$, dry, degassed dichloromethane, rt, 1 h, N_2 atmosphere, 69%.

Part three consists of six steps, Figure 76. Step (a) was a hydrogenation reaction to reduce the nitro functionality in 8-hydroxy-5-nitroquinoline to form the aniline, **21**. This reaction was achieved using conditions reported by Sleath *et al.* for the synthesis of the same compound.[188] The desired product was isolated in a 98% yield by filtration of the reaction mixture through microfibre filter paper, to remove the Pd/C catalyst. The identity and purity of this literature compound was confirmed

by ^{1}H and ^{13}C NMR spectroscopy and HRMS compared to those reported by Sleath *et al.* for the same compound.[188] Step (b) involved amide formation at the aforementioned aniline functionality, utilising the anhydride of *N*-boc glycine made in part 1, Figure 74. To **21** stirred in dry DMF was added **19** dropwise over 30 min at 0 °C under a dry, nitrogen atmosphere. The slow addition of **19** at low temperature was to help prevent potential competing reaction with the phenoxide functionality to form by-products that possess the *N*-boc glycine ester, Figure 77. After further stirring for 2 d at room temperature, any residual glycine anhydride **19** was quenched with water, and the *N*-boc glycine formed removed by washing with aqueous saturated aqueous sodium hydrogencarbonate. The desired product **22** was obtained as a crude product, in a yield of 93%. The identity and acceptable purity of this novel compound was confirmed by a combination of ^{1}H and ^{13}C NMR spectroscopy, HRMS and IR spectroscopy.

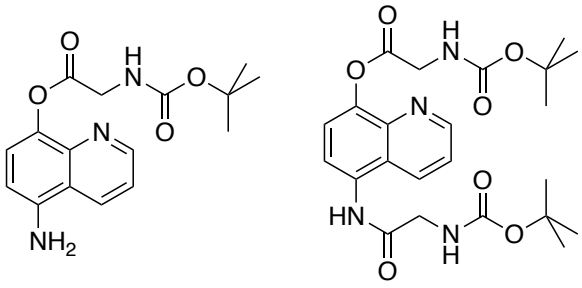

Figure 77 Chemical structure of by-products formed during toward the synthesis of **Ru-s2**, during part 3, step (b).

Step (c) was the formation of the allyl ether at the phenoxide functionality of **22** to give **23** in a 14% yield. The reaction conditions to form this intermediate were the same as those used for the synthesis of **12**, toward the alkyne-functionalised catalyst for click chemistry siderophore-attachment section in section 3.2.1.2, Figure 65, step (a). The identity and purity of this novel compound was confirmed by a combination of ^{1}H and ^{13}C NMR spectroscopy, HRMS, IR spectroscopy and elemental analysis. Step (d) was deprotection of the *N*-boc glycine linker in **23**. The conditions used were TFA in dichloromethane at 0 °C, to give the desired product **24** as a TFA salt in a 99% yield, following co-evaporations with MeOH and trituration in diethyl ether to remove residual TFA. The identity and purity of this novel compound was confirmed by a combination of ^{1}H, ^{19}F and ^{13}C NMR spectroscopy,

HRMS, IR spectroscopy and elemental analysis. The final step in the formation of ligand **25**, involved amide coupling to attach the siderophore mimic part, using the anhydride of 2,3-diacoxybenzoic acid **20** formed in part 2, Figure 75. This reaction involved addition of this anhydride dropwise over 30 min to a solution of **24** and DIPEA in dry DMF at room temperature. DIPEA was added to generate the free base of **24**. The desired product **25** was purified by washes with water and column chromatography and triturated to give a 45% yield, as a beige solid. The identity and purity of this novel compound was confirmed by a combination of ^{1}H and ^{13}C NMR spectroscopy, HRMS, IR spectroscopy and elemental analysis.

The ruthenium-complexation reaction to form **Ru-s2**, step (f), utilised Method A and gave the desired siderophore-conjugated catalyst as a dark brown solid in a yield of 69%, after washes with dichloromethane. The identity and purity of this novel final compound was confirmed by a combination of ^{1}H, ^{19}F, ^{31}P and ^{13}C NMR spectroscopy, HRMS, IR spectroscopy, elemental analysis, and UV-vis spectroscopy.

The Synthesis of an Uncaged Bidentate Catechol Catalyst Conjugate

An uncaged version of bidentate catechol-conjugated catalyst **Ru-s2** was prepared in two steps *via* an intermediate in its synthesis **25**, to give catalyst **Ru-s3**. The structure of and synthetic route to **Ru-s3** are shown in Figure 78 and Figure 79.

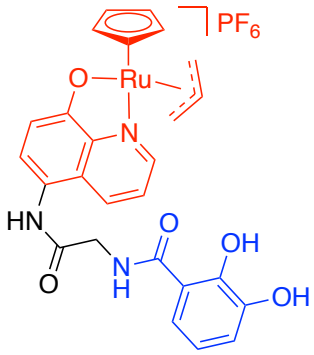

Figure 78 Chemical structure of **Ru-s3**. Catalyst = red, siderophore mimic = blue.

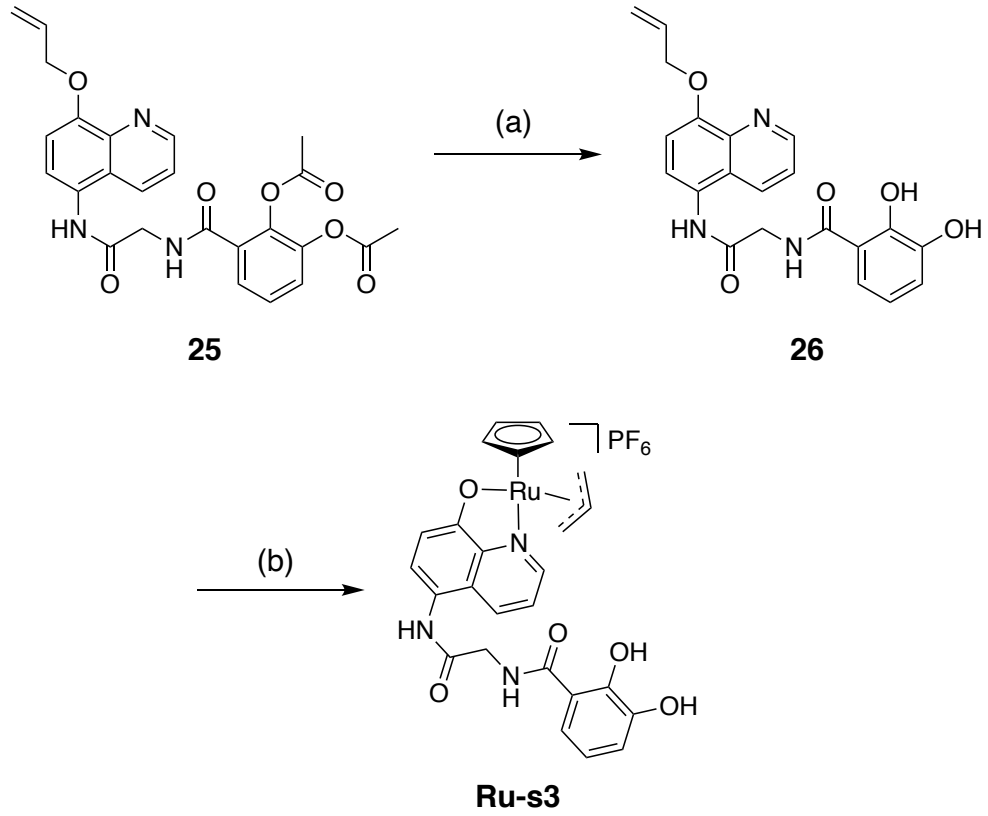

25 **26**

Ru-s3

Figure 79 Synthetic route towards **Ru-s3**. (a) piperidine, dry dichloromethane, 0 °C, 45 min, 95% (b) $[CpRu(MeCN)_3]PF_6$, dry, degassed DMF, rt, 30 min, N_2 atmosphere, 84%.

Step (a) was a deacetylation reaction to reveal the uncaged catechol ligand **26** from **25** in a 95% yield. This reaction takes advantage of the acetates' sensitivity to nucleophiles, as piperidine reacts at the electron deficient carbonyl motif to cleave the existing ester bond and form a more thermodynamically stable amide bond. The identity and purity of this novel compound was confirmed by a combination of ^{1}H and ^{13}C NMR spectroscopy, HRMS, IR spectroscopy and elemental analysis.

The ruthenium-complexation reaction to form **Ru-s2**, step (b) utilised Method A in dry DMF as a reaction solvent. Although there is a competing reaction which is presumed to be due to catechol-ruthenium binding, this by-product was separated by slow precipitation using diethyl ether, to give the desired product as a red/orange solid in a yield of 84%. The identity and purity of this novel final compound was confirmed by a combination of ^{1}H, ^{19}F, ^{31}P and ^{13}C NMR spectroscopy, HRMS, IR spectroscopy, elemental analysis, and UV-vis spectroscopy.

3.2.2 Tetradentate Catechol-based Siderophores for Catalyst Conjugation

In the pursuit of Trojan-Horse antibacterials, there have been numerous examples in the literature bound to tetradentate catechol-based siderophores. This includes compounds attached to penicillin antibiotics *via* a glycine linker, where acetate-protection of the catechol motif is employed, reported in work by Möllmann *et al.* in 2009.[47] In 2018 Neumann *et al.* reported the synthesis and antibacterial activity of ciprofloxacin conjugates with hydrolysis products of enterobactin, including the H_4-linear dimer.[169]

Azotochelin is a tetradentate, catechol-based siderophore produced by *Azotobacter vinelandii*, Figure 80.[189, 190] There is evidence for its use as a siderophore by medicinally relevant *P. aeruginosa* and *E. coli*.[191, 192] Thus, antibiotic conjugates with azotochelin have been reported in the literature.[192-194] Two independent examples of carbacephalosporin conjugates are reported by McKee *et al.* in 1991 and Diarra *et al.* in 1996 with good antibacterial activities *versus E. coli*.[192, 194]

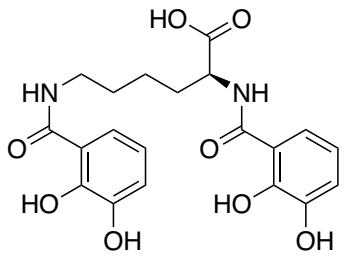

Figure 80 Chemical structure of azotochelin.

More recently in 2020, Sanderson *et al.* synthesised a ciprofloxacin conjugate with a siderophore structurally-related to azotochelin called salmochelin, that possesses glycosylated catechol units, Figure 81.[155] This work involved the use of iron-limited media for the determination of antibacterial activities *versus* two *E. coli* strains K12 and Nissle 1917, and utilised radioactive gallium studies to imply bacterial uptake.

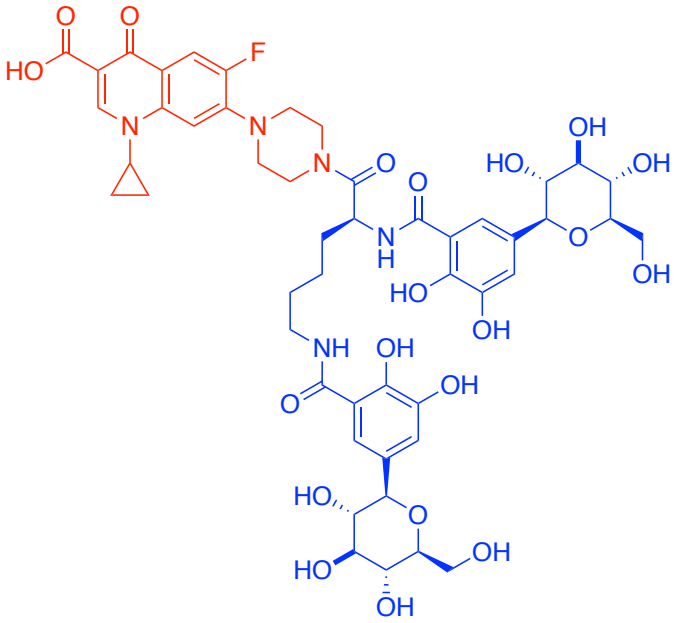

Figure 81 Chemical structure of the ciprofloxacin-salmochelin conjugate reported by Sanderson *et al.*[155] Antibiotic = red, siderophore mimic = blue.

The use of tetradentate siderophores in biological contexts has not been limited to antibacterials and has even found uses in artificial metalloenzymes. In work by Raines *et al.* in 2018, this siderophore was conjugated to an iridium hydrogenation catalyst where its subsequent incorporation into the siderophore transporter protein CeuE (a periplasmic binding protein in *C. jejuini*) facilitated enantioselective imine reductive reactions.[195] The azotochelin-Fe(III) complex that anchored the catalyst to the protein could be reversibly bound as reduction of the Fe(III) complex to Fe(II) resulted in its release from the protein.

The Synthesis of an Azotochelin Catalyst Conjugate

Azotochelin was selected for conjugation to the Kitamura-type catalyst due to the good, reported activity of its antibiotic conjugates *versus E. coli* and the siderophores synthetic tractability. The catalyst-siderophore conjugate will be synthesised using the so called 'glycine linkage' method shown in section 3.2.1.3, taking advantage of azotochelin's carboxylic acid for attachment to the quinoline ligand by amide bond formation. Ruthenium-complexation will use Method A. The structure of and synthetic route to azotochelin-catalyst conjugate **Ru-s4**, are shown in Figure 82 and Figure 83, respectively.

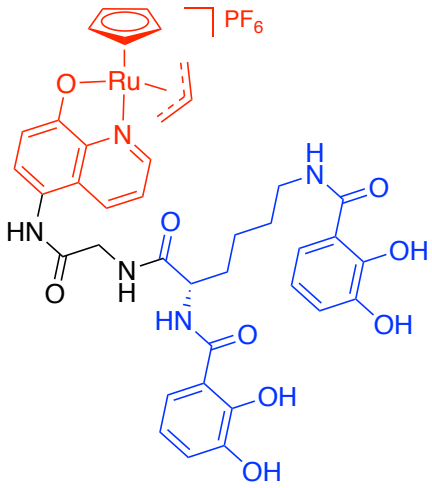

Figure 82 Chemical structure of **Ru-s4**. Catalyst = red, siderophore mimic = blue.

Due to the instability of the allyl ether motif to strong Lewis acids and hydrogenation conditions, acetate protection of the catechol groups was initially investigated as their deprotection uses basic conditions. However, the azotochelin backbone was not stable to the reaction required for their formation. Instead, PMB protecting groups were used as there is literature precedent for their deprotection in acidic conditions such as TFA in dichloromethane and HCl in dioxane.[193]

The successful synthesis of **Ru-s4** consists of six steps, the first three of which are the preparation of PMB-protected azotochelin following a literature procedure reported by Hodgkinson *et al.* in 2018 for the same compound.[193] Conjugation of the siderophore part to the hydroxyquinoline ligand proceeds *via* previously reported intermediate **24**, formed in step (d) toward **Ru-s2**, Figure 76.

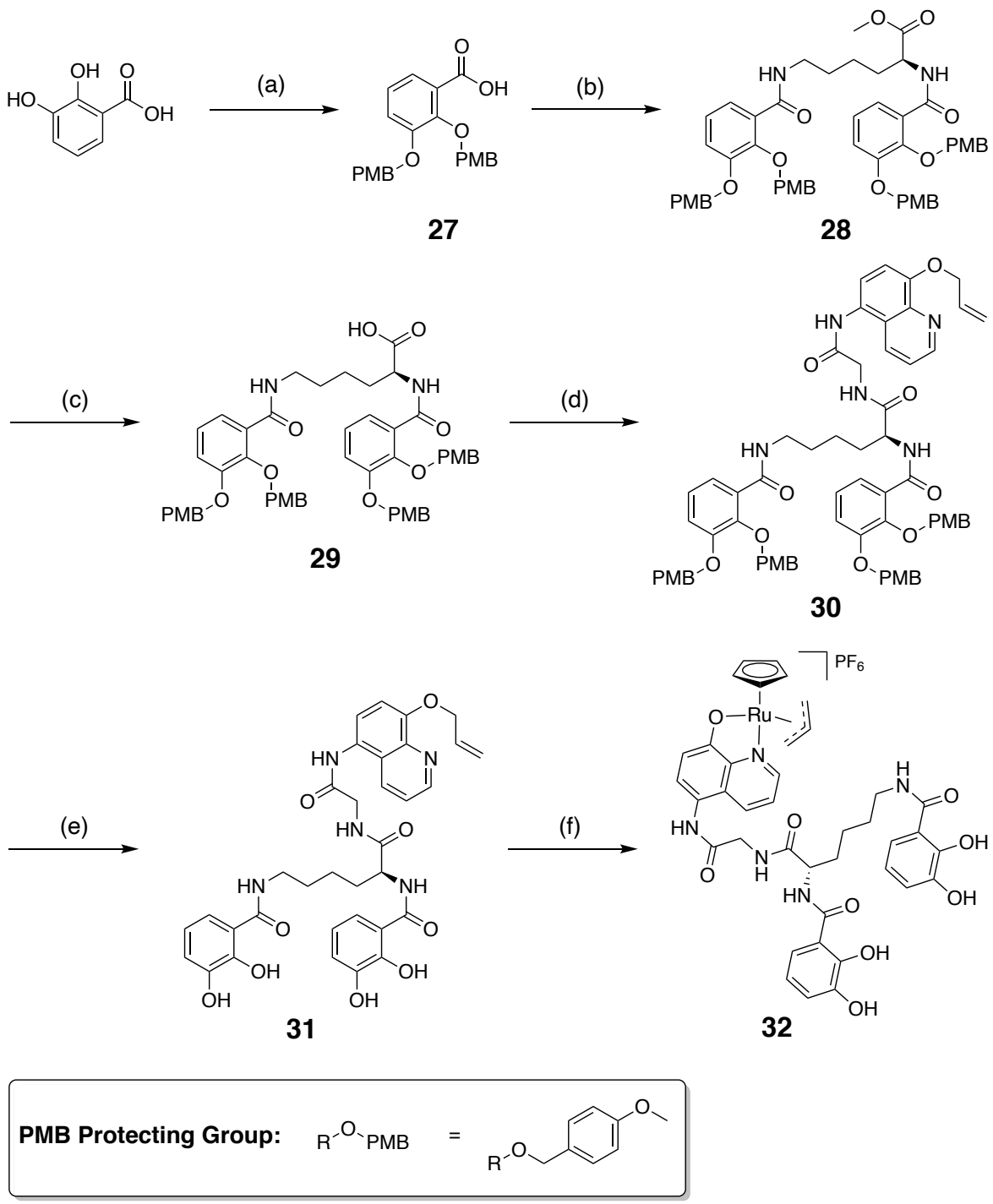

Figure 83 Synthetic route towards **Ru-s4**. (a) (i) *para*-methoxybenzyl chloride, KI, K_2CO_3, acetone, reflux, 18 h (ii) 0.67 M NaOH (aq), dioxane, rt, 24 h, 99% (b) *L*-lysine methyl ester dihydrochloride, *N*′-ethylcarbodiimide hydrochloride, 1-hydroxybenzotriazole monohydrate, DIPEA, dry DMF, rt, 24 h, 72% (c) 40 mM NaOH (aq), THF, rt, 18 h, 88% (d) **24**, *N*′-ethylcarbodiimide hydrochloride, 1-hydroxybenzotriazole monohydrate, DIPEA, dry DMF, rt, 18 h, 55% (e) 0.6 N HCl in dioxane, rt, 5 h, 34% (f) $[CpRu(MeCN)_3]PF_6$, dry, degassed DMF, rt, 30 min, N_2 atmosphere, 43%.

Step (a) is two-part, which first involves protection of 2,3-dihydroxybenzoic acid using *para*-methoxybenzyl chloride in acetone under basic conditions at reflux temperature. The second part is hydrolysis of the ester of the carboxylic acid that forms using aqueous NaOH, to give **27** in a 99% yield. The identity and purity of this literature compound were confirmed by ^{1}H and ^{13}C NMR spectroscopy and HRMS compared to those reported by Hodgkinson *et al.* for the same compound.[193] Step (b) used amide coupling agents EDC.HCl and HOBt.H_2O with DIPEA to form **28**, using two equivalents of **27** and the dihydrochloride salt of *L*-lysine methyl ester. The desired product was isolated by a combination of acidic and basic aqueous washes and column chromatography, to give **28** in a 72% yield. The identity and purity of this literature compound was confirmed by ^{1}H and ^{13}C NMR spectroscopy and HRMS compared to those reported by Hodgkinson *et al.* for the same compound.[193] Step (c) was hydrolysis of the methyl ester of **28** using aqueous NaOH in a mixture of dioxane:water (1:1). The free acid of the product was isolated by acidification of the reaction mixture to pH 2 and extraction with ethyl acetate to give the desired product **29** in an 88% yield. The identity and purity of this literature compound were confirmed by ^{1}H and ^{13}C NMR spectroscopy and HRMS compared to those reported by Hodgkinson *et al.* for the same compound.[193]

Step (d) was an amide coupling reaction to attach the previously synthesised intermediate **24** which contains the hydroxyquinoline ligand part with the siderophore-part *via* the carboxylic acid of PMB-protected azotochelin **29**. These reaction conditions used amide coupling agents EDC.HCl and HOBt.H_2O with DIPEA to form the desired product **30**, which was purified by a combination of acidic and basic aqueous washes and column chromatography, to give a 55% yield. The identity and purity of this novel compound was confirmed by a combination of ^{1}H and ^{13}C NMR spectroscopy, HRMS, IR spectroscopy, and elemental analysis. Step (e) was the final reaction prior to ruthenium complexation and used hydrogen chloride in dioxane at room temperature to cleave the PMB ether functionalities to reveal the free catechol motifs and thus, the desired product **31** in a 34% yield as a beige solid, after isolation by column chromatography. Previous attempts to cleave these groups used trifluoroacetic acid; however, this degraded the product formed. The identity and purity of this novel compound was confirmed by a combination of ^{1}H and ^{13}C NMR spectroscopy, HRMS, IR spectroscopy, and elemental analysis.

The ruthenium-complexation reaction to form **Ru-s4**, step (f) utilised Method A in dry DMF as a reaction solvent. No competing reaction for the binding of azotochelin to ruthenium was observed. The desired product was isolated by precipitation with diethyl ether, in a yield of 43%. The identity and purity of this novel final compound were confirmed by a combination of ^{1}H, ^{19}F, ^{31}P and ^{13}C NMR spectroscopy, HRMS, IR spectroscopy, elemental analysis, and UV-vis spectroscopy.

3.2.3 Hexadentate Hydroxamate-based Siderophores for Catalyst Conjugation

Although the major siderophore of *E. coli* enterobactin is catechol-based, these bacteria are known to utilise alternative iron-binding motifs such as hydroxamates and α-hydroxycarboxylates. A well-known example of a hydroxamate siderophore is DFO which is produced and utilised by *Streptomyces sp.*, Figure 84.[196] Since its discovery, DFO has found medical uses for the treatment of iron-overload with the pharmaceutical name Desferal and thus, has been extensively investigated for utilisation in Trojan-Horse antibacterials.

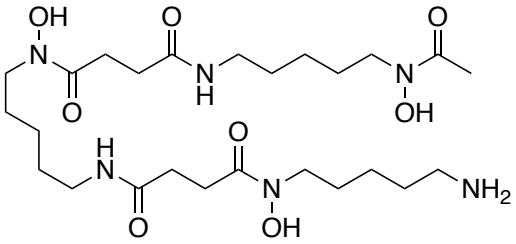

desferrioxamine B

Figure 84 Chemical structure of desferrioxamine B (DFO).

The pursuit of Trojan-Horse antibacterials that use DFO is encouraging as its derivative danoxamine is used in a family of sideromycins called salmycins, isolated from *Streptomyces violaceus* in 1995, Figure 85.[197] Their mode of action is unknown, however it is believed their antibiotic moiety is released inside bacteria *via* an intramolecular nucleophilic displacement, after the release of Fe(III).[198] Salmcyins are predominantly active against Gram-positive bacteria, however after the transformation of *E. coli* K12 with a gene called foxA, which encodes for the cell-surface receptor that facilitates uptake of its iron-bound form ferrioxamine (FO) from *Yersinia enterocolitica*, *E. coli* do become sensitive.[199] These results suggest its

inner-membrane transport protein FhuBCD is less specific and can accommodate sideromycin.

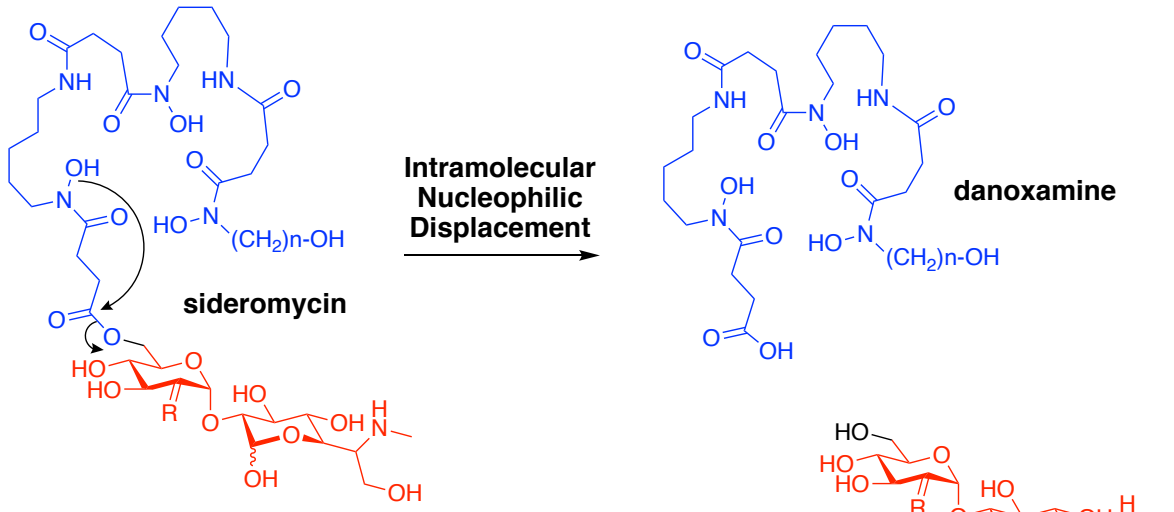

Salmycin A, R = NOH, n = 5
Salmycin B, R = O or OH_2, n = 4
Salmycin C, R = O or OH_2, n = 5
Salmycin D, R = NOH, n = 4

Figure 85 Chemical structure of salmycins (A, B, C and D) and their proposed intramolecular release of the antibiotic warhead inside bacteria after Fe(III) release. Antibiotic part in red, siderophore part in blue.[198]

E. coli are known to possess several different siderophore transport proteins that recognise siderophores that they do not themselves produce (xenosiderophores). Research by Hantke *et al.* in the late 1980s concluded that DFO is used by *E. coli,* however at low levels compared to coprogen or desferrichrome.[82, 200] Furthermore, they reported that its cell-surface receptor was FhuE.[201, 202] More recently in 1992, an additional receptor called FoxB was reported by Nelson *et al.*, whose utilisation is stimulated in the presence of the siderophore.[203-205] Despite its characterised uptake pathways in *E. coli*, the limited use of DFO is supported by studies by Winkelmann *et al.* in 1991.[78]

In 2013, Wencewicz *et al.* reported several synthetic tetradentate and hexadentate hydroxamate conjugates of danoxamine with antibacterials ciprofloxacin and lorabid (a β-lactam antibiotic) where their activity was in-line with aforementioned *E. coli* uptake studies, as they mainly targeted the Gram-positive bacteria *S. aureus*.[145] The

same research team also synthesised DFO conjugates with ciprofloxacin that utilised a bio-labile linker.[206]

The Synthesis of a Ferrioxamine Catalyst Conjugate

As DFO is used in the clinic, possesses an amine functional group for conjugation, and is a readily available starting material, it was selected for attachment to the Kitamura-type catalyst. The synthetic route to such a conjugate was *via* the glycine linkage route first shown in section 3.2.1.3. As the only modifiable functional group of DFO is its primary amine, conjugation to the glycine intermediate **24** utilised diethyl squarate, which has been used by Rudd *et al.* in 2016 to link DFO to another amine-functionalised compound for the development of ^{89}Zr positron emission tomography imaging techniques.[207] As there are examples of ruthenium complexes bound to DFO in work by Laurent *et al.* in 2018, it was decided that the DFO would be protected as its iron-bound form FO.[208] The structure of this target, **Ru-s5** and the synthetic route to it are shown in Figure 86 and Figure 87, respectively.

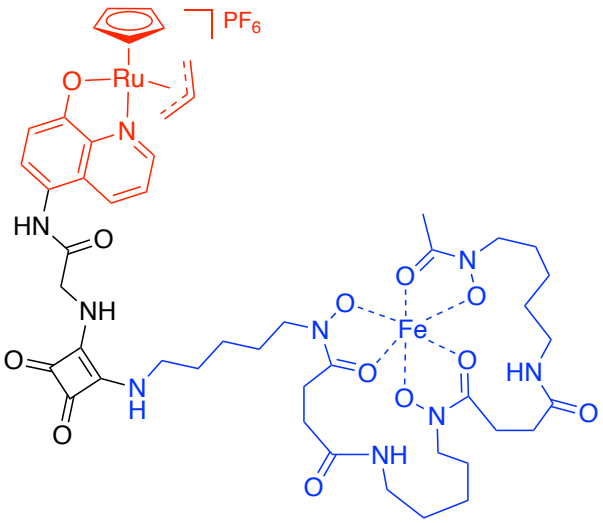

Figure 86 Chemical structure of **Ru-s5**. Catalyst = red, siderophore mimic = blue.

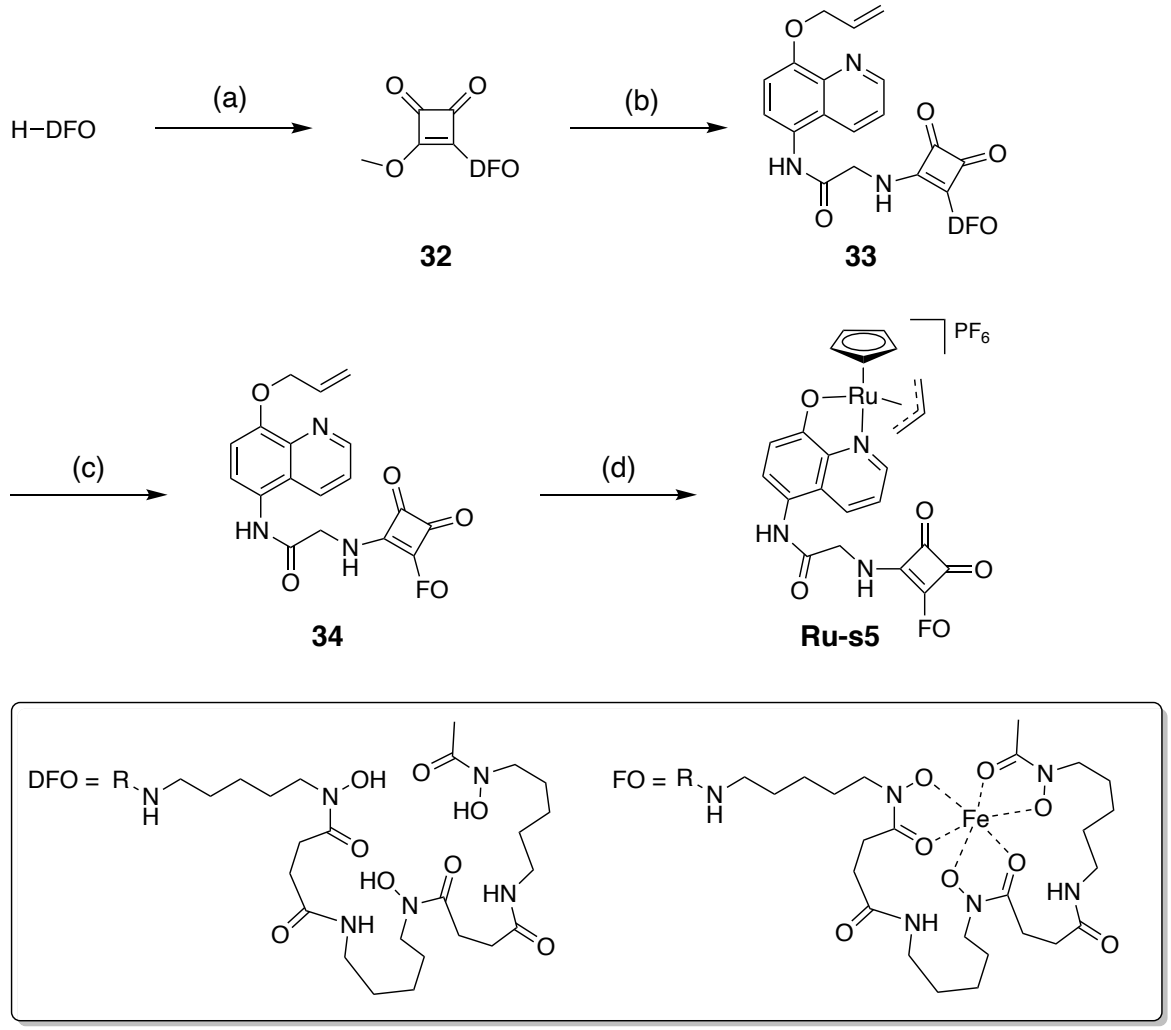

Figure 87 Synthetic route towards **Ru-s5**. (a) (i) DIPEA, dry EtOH, 50 °C, 1 h (ii) diethyl squarate, 50 °C, 18 h, 95% (b) **24**, DIPEA, EtOH: H_2O (8:1), rt, 24 h, 77% (c) iron(III) acetylacetonate, dry DMF, 18 h, 97% (d) $[CpRu(MeCN)_3]PF_6$, dry degassed DMF, rt, 18 h, N_2 atmosphere, 71%.

Step (a) was attachment of DFO to diethyl squarate *via* a nucleophilic substitution reaction using conditions based on those reported by Rudd *et al.*[207] The free base of the primary amine in DFO was generated by the addition of DIPEA from readily available DFO.MsOH, which then displaces ethanol selectively at one side of diethyl squarate to form a more thermodynamically-stable N-C bond. The desired product **32** was purified by washing with room temperature EtOH to give a white solid in 95% yield. The identity and purity of this literature compound was confirmed by ^{1}H NMR spectroscopy and HRMS compared to those reported by Rudd *et al.* for the same compound, despite their NMR assignments for a some signals being incorrect.[207] Step (b) is attachment of the previously synthesised intermediate **24**, to the

remaining available side of the squarate-containing molecule **32** *via* another nucleophilic substitution reaction. The conditions for this reaction vary slightly from the that of the former, as the addition of water is required to help solubilise **32**. The desired product **33** was isolated by washes with acetonitrile, as a light brown solid in a 77% yield. The identity and purity of this novel compound were confirmed by a combination of ^{1}H and ^{13}C NMR spectroscopy, HRMS, IR spectroscopy, elemental analysis, UV-vis spectroscopy and HPLC. Step (c) was the protection of DFO *via* the formation of its iron-bound by the addition of exactly one equivalent of Fe(III) acetylacetonate to **34** in dry DMF at room temperature. The formation of each complex produces three molecules of acetylacetone, where this by-product and residual DMF were washed out using diethyl ether, to give **34** as a red/orange solid in a yield of 97%. The identity and purity of this novel compound was confirmed by a combination of HRMS, IR spectroscopy, UV-vis spectroscopy and HPLC. As Fe(III) is paramagnetic, characterisation by NMR was not possible.

The analysis of **33**, **34** and **Ru-s5** by UV-vis spectroscopy was performed at 25 μM in 10% DMSO in water and the overlayed spectra are shown in Figure 88. The spectra of the iron-free and iron-bound ligands **33** and **34** are very similar where both absorb at λ_{max} = 294 nm, corresponding to a $\pi \rightarrow \pi^*$ transition centred on the quinoline ligand. These spectra also show that complexation of **33** to Fe(III) to form **34**, results in the emergence of a band at λ_{max} = 416 nm which probably corresponds to a ligand-to-metal (LMCT) or metal-to-ligand charge transfer (MLCT). This observation is similar to spectra observed by Tufano and Raymond in 1981 for FO.[209] Whilst **Ru-s5** also absorbs at 294 nm, it possess an additional band at λ_{max} = 266 nm and a shift of the lower frequency band from λ_{max} = 416 → 403 nm. The former probably corresponds to a $\pi \rightarrow \pi^*$ transition centred on the cyclopentadienyl ligand whereas the latter is due to a contributing LMCT or MLCT which occurs *via* the ruthenium metal centre and the cyclopentadienyl and/or quinoline ligand.

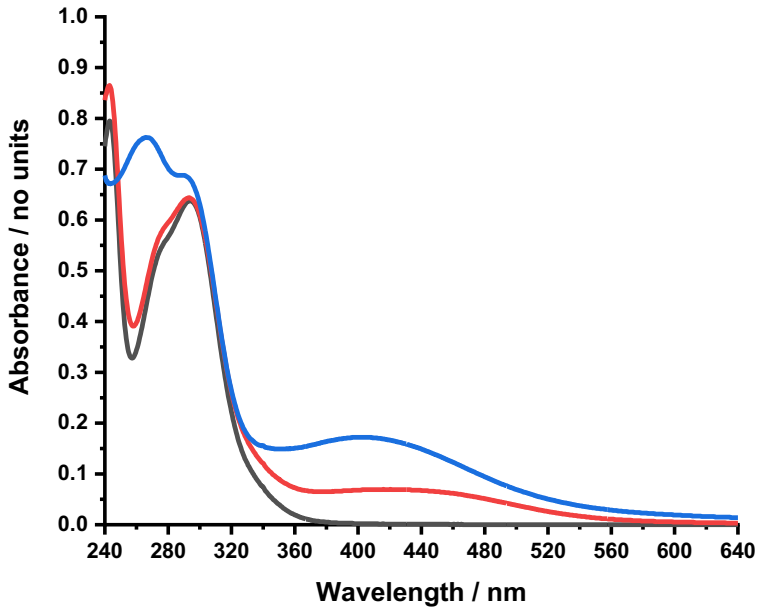

Figure 88 UV-vis spectra of **33** (black), **34** (red) and **Ru-s5** (blue) at 25 μM in 10% DMSO in H_2O (240-640 nm).

The ruthenium-complexation reaction to form **Ru-s5**, step (d) utilised Method A however with longer reaction times due to the poor solubility of **34** in dichloromethane. The desired product was isolated by washes with dichloromethane, in a yield of 71%. The identity and purity of this novel final compound was confirmed by a combination of HRMS, IR spectroscopy, elemental analysis, and UV-vis spectroscopy. As Fe(III) is paramagnetic, characterisation by NMR was not possible.

The Synthesis of a Desferrioxamine Catalyst Conjugate

As the required ligand had already been synthesised, the complexation of **33** to form an iron-free version of **Ru-s5**, **Ru-s6** was attempted. The structure and synthetic route to this catalyst are outlined in Figure 89 and Figure 90, respectively.

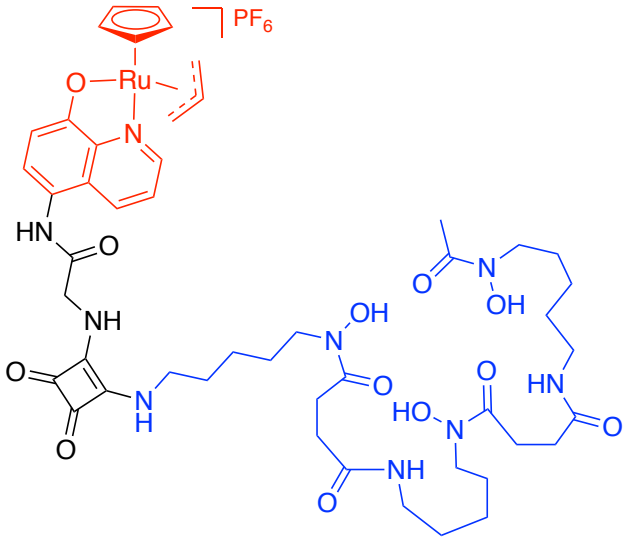

Figure 89 Chemical structure of **Ru-s6**. Catalyst = red, siderophore mimic = blue.

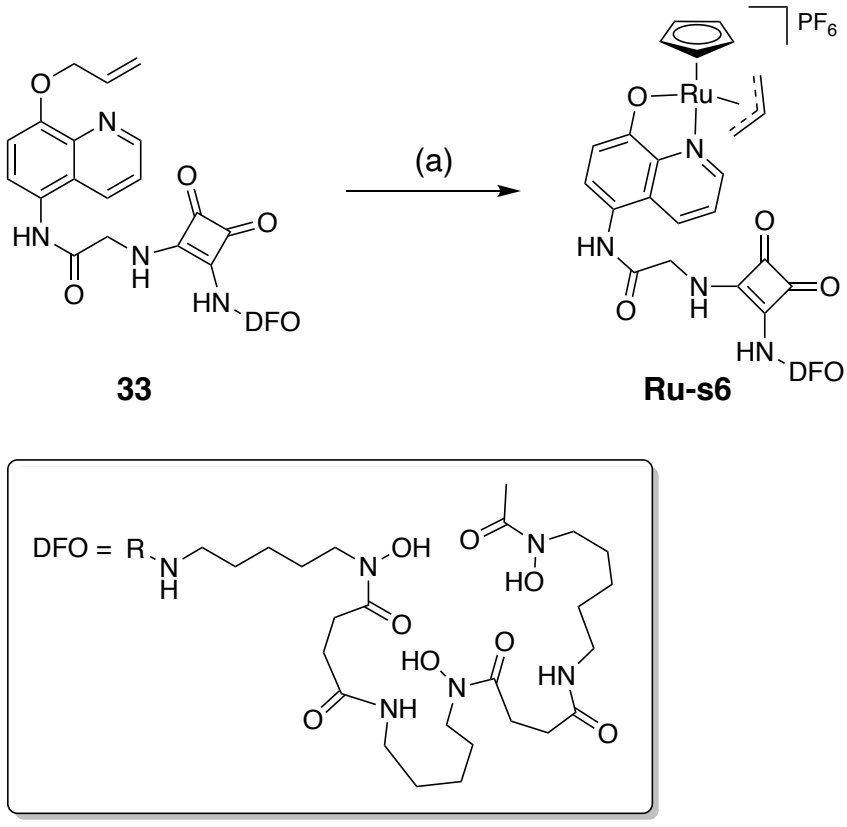

Figure 90 Synthetic route towards **Ru-s6**. (a) $[CpRu(MeCN)_3]PF_6$, dry, degassed DMF, rt, 2 h, N_2 atmosphere, 47%.

The reaction to form **Ru-s6** utilised Method A. Deviation from this method included the use of dry, degassed DMF as the reaction solvent and longer reaction times due to the poor solubility of **33**, even in DMF. Surprisingly, the synthesis of **Ru-s6** was

successful, with no competing ruthenium-binding with the DFO hydroxamates. The catalyst was purified by slow precipitation using diethyl ether and washes with diethyl ether and dichloromethane, as a dark brown solid in a 47% yield. The identity and purity of this novel final compound was confirmed by a combination of ^{1}H, ^{13}C, ^{19}F and ^{31}P NMR spectroscopy, HRMS, IR spectroscopy, elemental analysis, and UV-vis spectroscopy.

3.2.4 Bidentate Hydroxypyridinone- and Hydroxypyranone-based Siderophores for Catalyst Conjugation

There are numerous examples in the literature of hydroxypyridinones and hydroxypyranones used as siderophore-mimics in the search for Trojan-Horse antibacterials.[210-214] The structure of specific examples of these heteroaromatics and their corresponding iron-binding affinities are shown in Figure 91.[215, 216] Two siderophore-conjugated β-lactam antibacterials that made it to clinical trials but not further, called BAL30072 and MC-1 possess hydroxypyridinone and dihydroxypyridinone motifs, respectively, Figure 92. BAL30072 showed potent activity against MDR *P. aeruginosa* and *Acinetobacter sp.* isolates, including carbapenem-resistant strains.[210, 211] MC-1 was first reported by McPherson *et al.* in 2012 and showed TonB-dependent uptake into and potent activity *versus P. aeruginosa*.[214] Moreover, during MC-1's development alternative conjugates were investigated that contained a hydroxypyranone siderophore mimics, although they were found to be less active.[217]

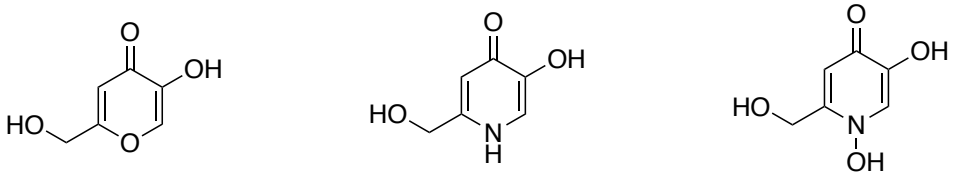

23.1	22.0	20.6
hydroxypyranone	**hydroxypyridinone**	**dihydroxypyridinone**

Figure 91 Chemical structures of hydroxypyranone, hydroxypyridinone and dihydroxypyridinone, with corresponding pFe(III) values.[215, 216]

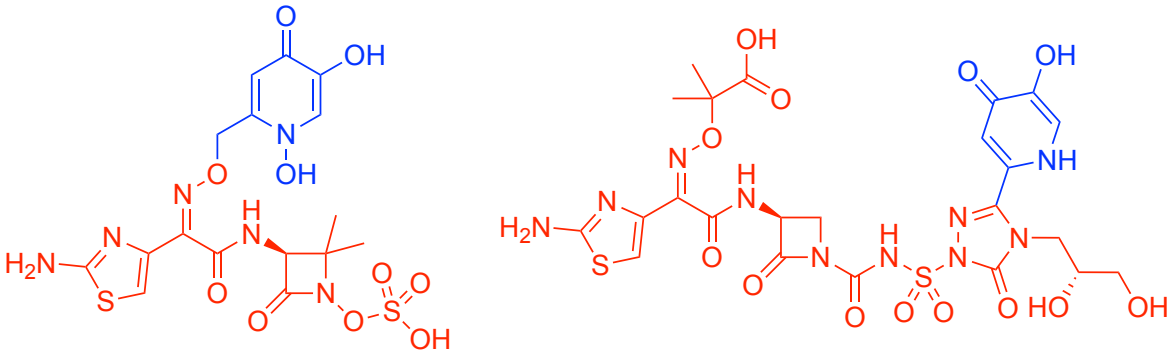

BAL30072 **MC-1**

Figure 92 Chemical structures of BAL30072 and MC-1. Antibiotic = red, siderophore mimic = blue.

The Synthesis of a Dihydroxypyridinone Catalyst Conjugate

Based on the success of BAL30072, the siderophore-mimic dihydroxypyridinone was selected for conjugation to the Kitamura-type catalyst *via* the glycine linkage route first shown in section 3.2.1.3. It was envisioned that its attachment to the glycine amine terminal would be by the formation of a carbamate bond, using conditions reported by Brown *et al.* in 2013 in the conjugation of the siderophore mimics to the antibiotic warhead.[217] The structure of this target **Ru-s7** is shown in Figure 93, and the synthesis towards this catalyst is outlined in Figure 94.

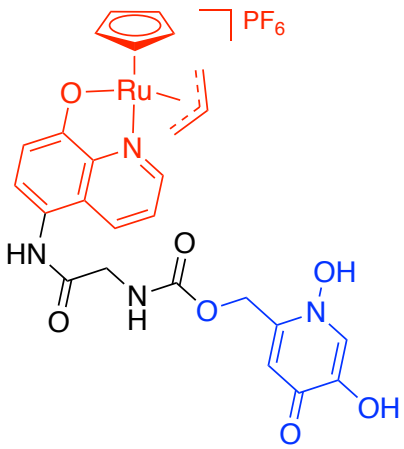

Figure 93 Chemical structure of **Ru-s7**. Catalyst = red, siderophore mimic = blue.

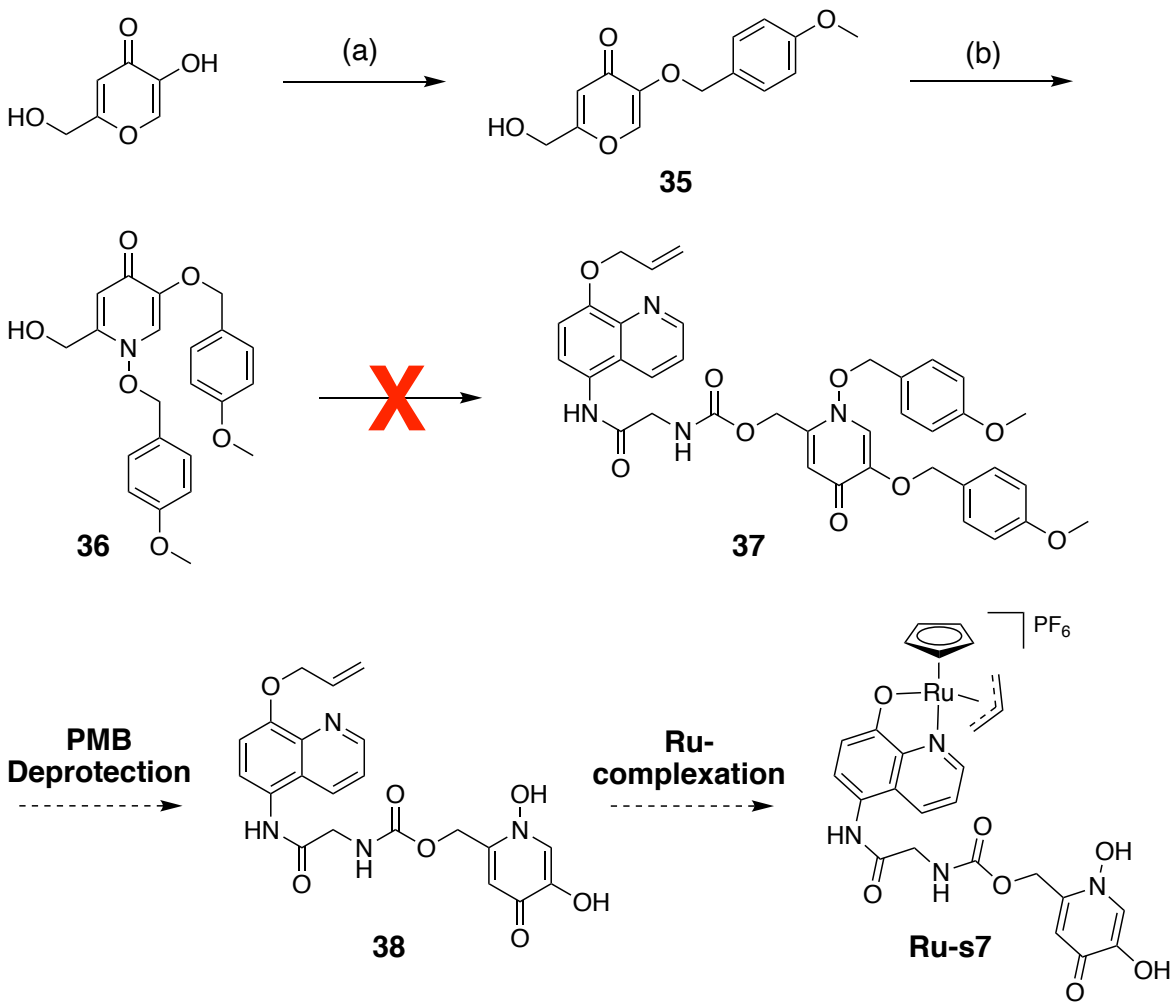

Figure 94 Synthetic route towards **Ru-s7**. (a) *para*-methoxybenzyl chloride, K_2CO_3, dry DMF, 80 °C, 18 h, 74% (b) (i) hydroxylamine hydrochloride, K_2CO_3, 80 °C, dry DMF, 18 h, (ii) *para*-methoxybenzyl chloride, dry DMF, rt, 24 h 49%.

Step (a) followed a literature procedure for the synthesis of PMB-protected hydroxypyranone reported by Ernst *et al.* from readily-available starting material kojic acid.[218] The chemo-selective PMB-protection of the α-hydroxyketone motif used *para*-methoxybenzyl chloride under basic conditions at 80 °C in dry DMF. The desired product **35** was isolated as a beige solid from residual kojic acid and hydrolysed by-product *para*-methoxybenzyl alcohol by trituration in water in a 74% yield. The identity and purity of this literature compound was confirmed by ^{1}H and ^{13}C NMR spectroscopy, HRMS and elemental analysis compared to those reported by Ernst *et al.* for the same compound.[218] Step (b) is a two part reaction using conditions reported by Brown *et al*, where initial conditions facilitate insertion of hydroxylamine into the heteroaromatic ring of **35** followed by its PMB-protection.[217]

The desired product **36** was isolated in a 49% yield by water washes in dichloromethane followed by column chromatography. The identity and purity of this literature compound were confirmed by ^{1}H and ^{13}C NMR spectroscopy and HRMS compared to those reported by Brown *et al.* for the same compound.[217] The next step was conjugation of previously synthesised, amine-functionalised quinoline **24** to the hydroxy-functionalised siderophore part made in step (b). This reaction was attempted using a variety of conditions, the first of which was to form a carbamate linkage utilising conditions reported by Brown *et al.* in the synthesis of Trojan-Horse antibacterials.[217] Unfortunately, this reaction as well as alternative routes attempted which included the transformation of the hydroxyl part of **36** into leaving groups (such as tosylate and chloride) and subsequent nucleophilic substitution by the amine of **24**, were unsuccessful.

The Synthesis of an Hydroxypyranone Catalyst Conjugate

Instead, a related, alternative siderophore-conjugated catalyst was targeted that utilised the intermediate compound **24**, used toward the synthesis of **Ru-s7**. The structure and synthesis of this catalyst target **Ru-s8** are shown in Figure 95 and Figure 96 respectively.

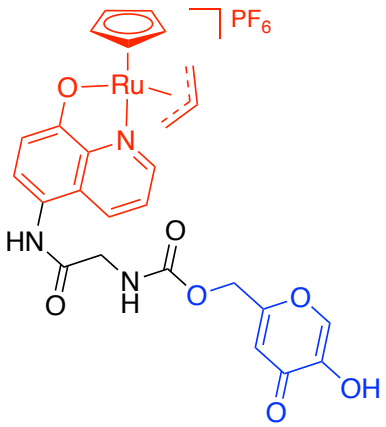

Figure 95 Chemical structure of **Ru-s8**. Catalyst = red, siderophore mimic = blue.

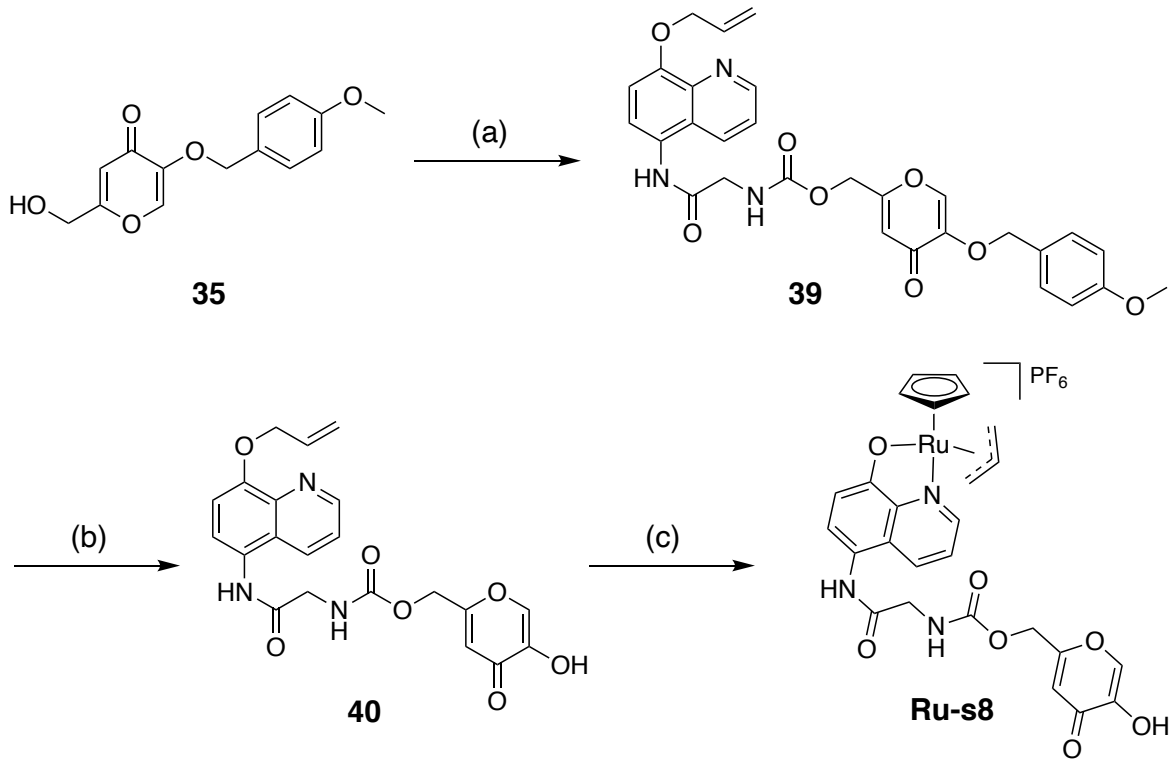

Figure 96 Synthetic route towards **Ru-s8**. (a) (i) carbonyldiimidazole, dry DMF, rt, 22 h (ii) DIPEA, **24**, dry DMF, rt, 18 h, 45% (b) trifluoroacetic acid, dichloromethane, rt, 30 min, 81% (c) $[CpRu(MeCN)_3]PF_6$, dry, degassed DMF, rt, 30 min, N_2 atmosphere, 77%.

Step (a) was the conjugation of **35** to the previously synthesised amine-functionalised intermediate **24** using carbonyldiimidazole (CDI) in a two-part reaction. The first part was the reaction of the nucleophilic hydroxyl group of **35** into one half of the CDI molecule to displace one imidazole motif as a by-product where the second part was the reaction **24** to displace the remaining imidazole leaving group from the CDI intermediate formed. The desired product **39** was isolated using a combination of acidic and basic aqueous washes in dichloromethane followed by column chromatography, in a yield of 45%. The identity and purity of this novel compound was confirmed by a combination of ^{1}H and ^{13}C NMR spectroscopy, HRMS, IR spectroscopy and elemental analysis. As planned, step (b) was the PMB-deprotection of the α-hydroxyketone motif using TFA to form **40** in a yield of 81% following purification using strong cation exchange chromatography and trituration in diethyl ether, to give a beige solid. The identity and purity of this novel compound

was confirmed by a combination of ^{1}H and ^{13}C NMR spectroscopy, HRMS, IR spectroscopy and elemental analysis.

The reaction to form **Ru-s8** utilised Method A. The only deviation from this method was the use of dry degassed DMF as the reaction solvent. The catalyst was purified by precipitation using diethyl ether, followed by washing with diethyl ether and dichloromethane, as a dark orange/brown solid in a 77% yield. The identity and purity of this novel final compound were confirmed by a combination of ^{1}H, ^{19}F, ^{31}P and ^{13}C NMR spectroscopy, HRMS, IR spectroscopy, elemental analysis, and UV-vis spectroscopy.

3.3 Prodrug Activation Kinetics for Siderophore-conjugated Catalysts

A total of six siderophore-catalyst conjugates were synthesised, purified, and characterised, the structures of which are shown below in Figure 97 alongside control catalyst **Ru-control**. These conjugates possess a range of siderophore mimics which contain various denticities, with either catechol, hydroxamate or pyranone iron-binding motifs. The activity of each of these conjugates for prodrug activation under biologically-relevant conditions must be determined. To assess the impact of siderophore attachment on catalytic prodrug activation kinetics, reaction rates and conversions will be compared to those achieved by the control catalyst, **Ru-control**. To achieve this, the HPLC kinetics assay outlined in section 2.3.1 was employed under an anaerobic atmosphere. The procedural detail for these assays is reported in section 6.3. Kinetics data for moxifloxacin formation are shown for each catalyst in Figure 98. Each catalyst's ***C*-moxi** consumption and moxifloxacin formation kinetics are shown in section 6.3.5.

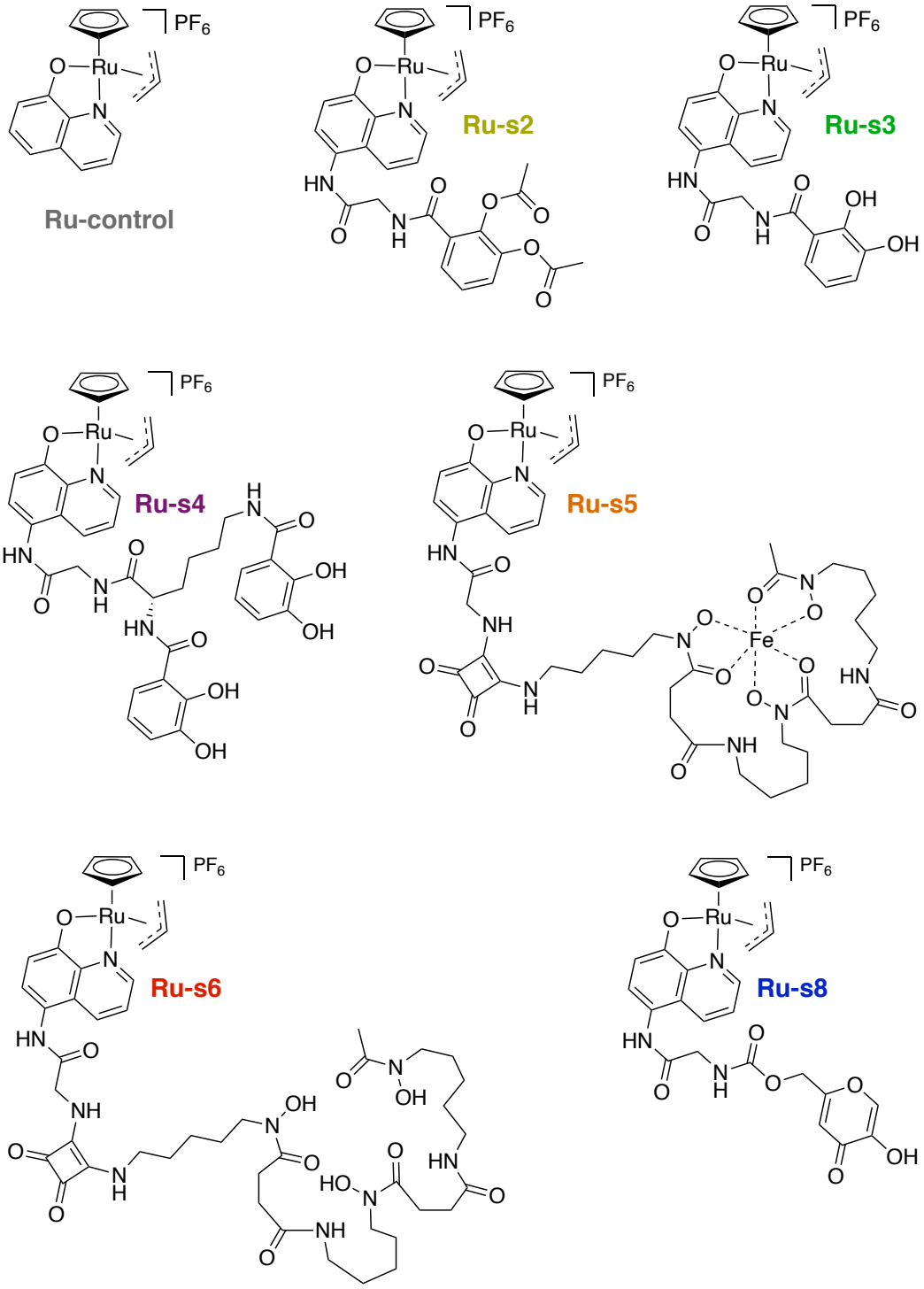

Figure 97 Chemical structures of synthesised catalyst-siderophore conjugates.

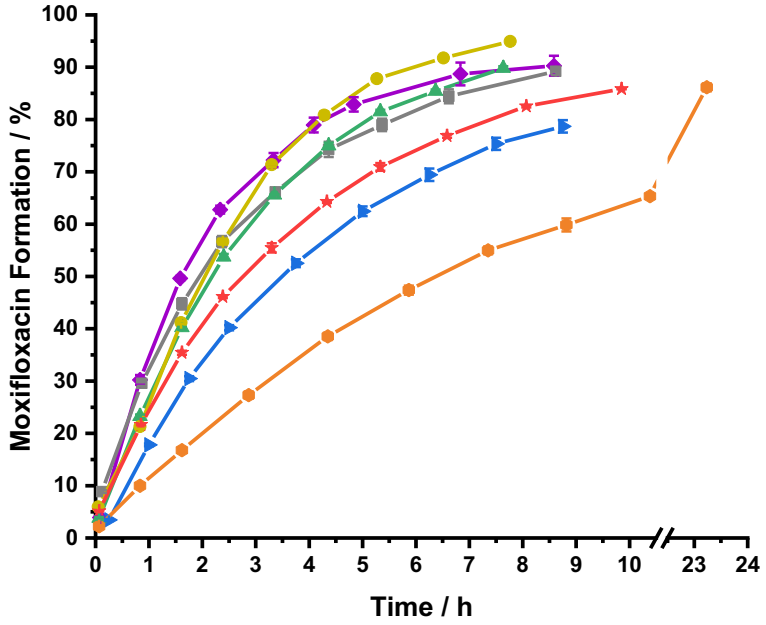

Figure 98 Catalyst-mediated prodrug activation kinetics in 10% DMSO in aqueous MOPS buffer at pH 7.4 at room temperature under an anaerobic atmosphere, showing ***C*-moxi** (100 μM) activation to form moxifloxacin for various synthesised catalysts at 10 mol % loading, in triplicate: (i) **Ru-control** (grey, square), (ii) **Ru-s2** (yellow, circle), (iii) **Ru-s3** (green, triangle), (iv) **Ru-s4** (purple, diamond), (v) **Ru-s5** (orange, hexagon), (vi) **Ru-6** (red, star) and (vii) **Ru-s8** (blue, sideways triangle).

These data show that every catalyst-siderophore conjugate activates the prodrug ***C*-moxi** to form moxifloxacin under biologically-relevant conditions. Most catalysts perform as well as or better than the control catalyst **Ru-control**, with yields of approximately 90% moxifloxacin formation and 10% ***C*-moxi** remaining after 8 h. The exceptions to this include the FO- and DFO-conjugated catalysts **Ru-s5** and **Ru-s6**, respectively. This might be explained by the relative size of their siderophores compared to the those of the other catalysts. The larger siderophores probably sterically hinder the active ruthenium metal centre more, thereby kinetically perturbing its reaction with nucleophiles for catalyst priming and prodrug during substrate activation. The reaction rate for **Ru-s5** is significantly slower, where only 60% conversion is observed after 8 h. An additional measurement for this catalyst at approximately 23 h shows 90% conversion which confirms that the catalyst remains significantly active after 8 h under anaerobic conditions, compared to under aerobic conditions. The poor reactions kinetics observed for the pyranone conjugated catalyst **Ru-s8** cannot be rationally explained. The consumption of ***C*-**

moxi to form moxifloxacin is almost exactly accounted for for most of the catalysts, which suggests minimal by-product formation. One exception is the azotochelin-conjugated catalyst **Ru-4** which shows the fastest initial reaction kinetics.

3.4 Summary and Conclusions

Taking account of literature approaches to the synthesis of Trojan-Horse antibacterials and Kitamura-type catalysts, several synthetic routes to catalyst-siderophore conjugates were explored. Unsuccessful attempts included conjugation by so called 'amide linkage' and 'click chemistry linkage' methods outlined in sections 3.2.1.1 and 3.2.1.2, respectively. A successful synthesis to the first siderophore-conjugated catalyst **Ru-s2** utilised the so called 'glycine linkage' method where ruthenium-complexation used Method A. This method was used to obtain an additional five siderophore-conjugated catalysts (**Ru-s3**, **Ru-s4**, **Ru-s5**, **Ru-s6** and **Ru-s8**), which possessed a range of siderophore mimics such as bidentate catechols, tetradentate catechols, hexadentate hydroxamates and bidentate pyranones. Although all catalysts were accessed by compound **24**, the reaction used for conjugation of the siderophore mimic to the quinoline ligand prior to Ru-complexation used a variety of coupling reactions including the use of diethyl squarate and formation of amide and carbamate bonds. For each catalyst, the final step in their synthesis was ruthenium complexation using Method A. In some cases, this general method was modified to mitigate poor ligand solubilities which included the use of DMF and longer reaction times. Despite the ruthenium-binding abilities of the unprotected siderophores, little formation of such by-products was observed.

The activity of these synthesised catalysts for ***C*-moxi** activation under biologically relevant conditions was tested. All catalysts showed similar catalytic activity to the **Ru-control** catalyst at biologically-relevant concentrations, with minimal *N*-allyl bond formation with the prodrug or drug and good stability due to the exclusion of molecular oxygen. Most catalysts gave conversions in the region of 80-90% after 8 h, apart from FO-conjugated catalyst **Ru-s5** where 60% conversion was observed. However, this catalyst gave 90% conversion after approximately 23 h, confirming improved catalyst stability under an anaerobic atmosphere compared to an aerobic atmosphere.

Chapter 4 : The Biological Activity of the Synthesised Catalyst-Siderophore Conjugates

4.1 Introduction

As Trojan-Horse antibacterials by their definition, are taken up into bacteria *via* siderophore-mediated iron-uptake pathways, an important part in their development involves the quantification and identification of the mechanisms that facilitate this uptake. The various experimental methods utilised to evaluate the bacterial uptake of Trojan-Horse antibacterials were reviewed by Southwell, Black and Duhme-Klair in 2021;[65] three of these methods are highlighted in the sub-sections below. So that any data obtained from bacterial growth studies provide accurate information regarding their medicinal applications, the conditions for bacterial growth are limited to a few select media including MHII. For Trojan-Horse antibacterials, media are often iron-limited to mimic the environment of the human host, in which iron levels are tightly controlled.

4.1.1 Iron-Dependent Antibacterial Activity

The antibacterial activity of compounds is typically quantified by their MIC against medicinally-relevant bacterial strains. As explained in section 1.4.3, iron-uptake pathways in bacteria, including those using siderophores, are controlled by proteins whose expression are repressed on binding to intracellular iron.[51] As bacteria grow and divide, these iron-stores are depleted and siderophore-mediated iron uptake is upregulated. Therefore, if a compound's antibacterial activity decreases with increasing iron-availability, this suggests a successful Trojan-Horse approach.

Iron-dependent antibacterial activity studies are the most common method for certifying Trojan-Horse antibacterials, with several examples reported in the literature.[47, 145, 146, 164-166, 208, 217, 219, 220] In 2016, Ito *et al.* used this method during the development of cefiderocol.[219] Indeed, these studies showed that cefiderocol's MIC *versus P. aeruginosa* PAO1 increased (corresponding to a decrease in activity) for bacteria grown with increasing iron-availability. Whereas the 'no siderophore' control (ceftazidime) possessed no/little iron-dependent activity, Table 4.

Table 4 Iron dependency MIC data for cefiderocol and ceftazidime *versus P. aeruginosa* PAO1.[219]

Iron Concentration (mg/L^{-1})	MIC (μgmL^{-1})	
	Cefiderocol	Ceftazidime
0.02	0.031	0.5
0.12	0.125	1
0.52	0.5	1
1.02	0.5	1
10.02	1	1

Iron-dependent antibacterial activity experiments can be informative and straight-forward to do; however, it is important to employ suitable controls to evaluate the relative contributions of iron-sequestration and/or growth-promotion to toxicity.

4.1.2 Genetic Deletion Studies

A common technique for the identification of mechanisms that facilitate the internalisation of antibacterials involves comparing their activity against bacteria that possess specific, known genetic deletions.[73, 166, 214, 221, 222] If a significant decrease in antibacterial activity is observed for a compound, it can be assumed that the known role of this deleted genetic sequence is crucial for compound activity. In cases where the sequence codes for the biosynthesis of proteins involved in siderophore-mediated iron-uptake, this implies their involvement in the uptake of the tested compound.

In 2012, McPherson *et al.* utilised genetic deletion studies to identify the cell-surface receptors responsible for the internalisation of the β-lactam Trojan-Horse antibacterials BAL30072 and MC-1 into *P. aeruginosa*.[214] Under iron-supplemented conditions, the MIC of both tested Trojan-Horse antibacterials increased significantly for a ΔpiuA deletion mutant, indicating the receptors role in their uptake, Table 5. Although little/no increases were observed on deletion of the known enterobactin cell-surface receptor PirA, the double mutant gave significant MIC

increases suggesting this receptor is a minor, secondary uptake route for these compounds.

Table 5 MIC values for BAL30072 and MC-1 against *P. aeruginosa* PAO1 bacteria and its genetic deletion mutants, related to siderophore cell-surface receptors.

Relevant Genotype(s)	MIC (μg mL^{-1})			
	BAL30072		MC-1	
	+Fe	-Fe	+Fe	-Fe
PAO1	0.25	0.25	4	2
ΔpiuA	8	0.25	16	2
ΔpirA	0.5	0.25	4	2
ΔpiuAΔpirA	32	32	64	64

4.1.2.1 Growth Recovery Assays

If the use of siderophores by bacteria is impeded to the point of iron-deficiency, their overall growth is diminished. If this growth response is due to the deletion of a gene related to siderophore biosynthesis, their growth can be recovered by the artificial introduction of compatible siderophore or siderophore mimics to the growth medium. If an antibacterial conjugate recovers growth at a non-toxic concentration, this suggests a successful Trojan-Horse approach. Furthermore, if this growth recovery is removed for mutants that also possess genetic deletions associated with siderophore uptake and/or iron-release mechanisms, this implies the corresponding deleted protein's involvement in the internalisation of the tested compound. By using a combination of different deletion mutants, not only can uptake be confirmed, but the proteins responsible for this uptake can be identified.

In 2012, Zheng *et al.* utilised growth recovery experiments to identify the mechanisms responsible for the bacterial uptake (if any) of two enterobactin conjugates with ciprofloxacin Cipro-Ent and vancomycin Vanco-Ent, Figure 99. Unfortunately, no growth recovery was observed for these compounds *versus* an *E. coli* strain defective in enterobactin biosynthesis (ΔentA). In fact, conjugate Vanco-

Ent was toxic due to iron sequestration. However, growth recovery was observed for the Cipro-Ent *versus* a double mutant of *P. aeruginosa* defective in the biosynthesis of pyoverdine and pyochelin siderophores (ΔpvdΔpch).

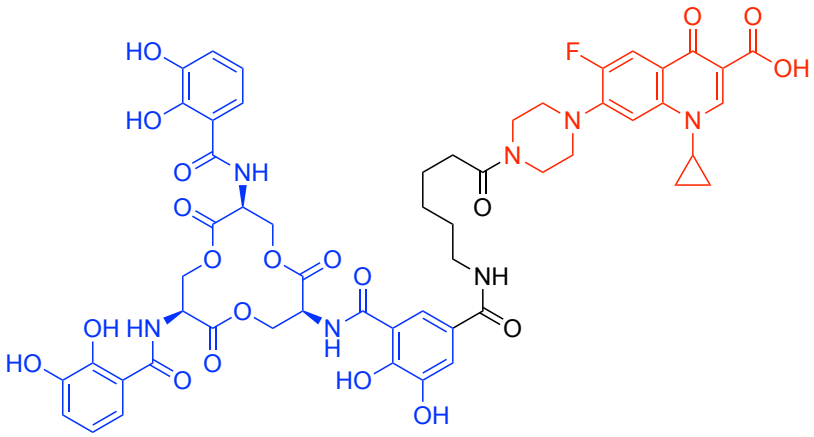

Cipro-Ent

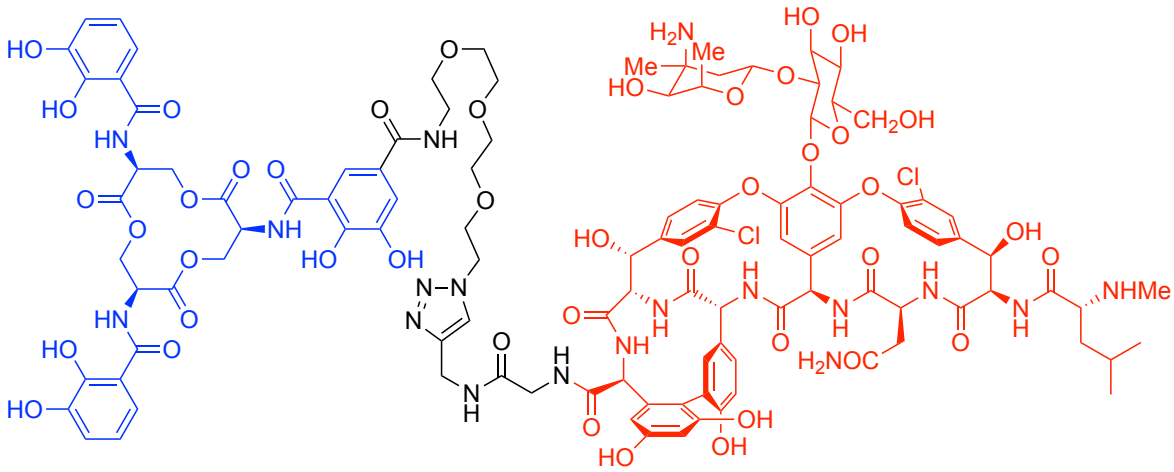

Vanco-Ent

Figure 99 Chemical structures of ciprofloxacin and vancomycin conjugates with enterobactin, reported by Zheng *et al.*[162] Antibiotic = red, siderophore mimic = blue.

For studies centred on *E. coli*, this technique is especially accessible due to the large library of deletion mutants that already exist for the bacterium, and the well-understood function of these genes. Another example of growth recovery studies in *E. coli* was reported by Ferreira *et al.* in 2017 toward the development of siderophores for the imaging of bacterial infections.[182]

4.1.3 Chapter Aims

Now that several different catalyst-siderophore conjugates have been synthesised, their antibacterial activity will be tested to determine their upper, non-toxic concentrations. It is preferred that for a prodrug approach, these catalysts remain non-toxic at high concentrations so that their co-addition provides better bacterial uptake and activation efficiency. The DFO conjugate **Ru-s6** will be used to imply the biological compatibility of both of the FO and DFO conjugates.

Subsequent experiments will involve co-addition of each catalyst alongside prodrug, at their individual upper, non-toxic concentrations. Any observed antibacterial activity relative to 'no addition' and 'no prodrug' controls, can then be attributed to prodrug activation as their activity has already been confirmed in section 3.3. These bacterial growth experiments will provide information regarding the catalyst's stabilities to bacteria and thus, its suitability for potential medicinal applications.

The ultimate goal of the catalysts' attachment to siderophores is to enable their selective accumulation within bacteria so that prodrug activation occurs within cells. Select experimental methods that have been used in the literature to evaluate the uptake of Trojan-Horse antibacterials will be used to inform on the uptake of the catalyst-siderophore conjugates. This includes the use of genetic deletion mutants of *E. coli* and incubation experiments.

4.2 The Antibacterial Activity of Catalyst-Siderophore Conjugates

The antibacterial activity of each catalyst-siderophore conjugate was tested between 0.1 - 10 μM against *E. coli* K12 (BW25113) in iron-limited MHII, under micro-aerobic conditions. This concentration range was chosen as studies by Völker and Meggers in 2017 showed their catalysts were toxic within this range.[33] The growth conditions used are the same as those reported for the determination of the prodrug MICs reported in section 2.4.3, apart from the preparation of the plates inside an anaerobic chamber to mimic the low oxygen atmosphere of the intestine. The data from these experiments are represented as linear dosage-response curves

for each catalyst-siderophore conjugate, Figure 100. This graph shows how the changing concentration of each conjugate affects overall bacterial growth 24 h after addition. The procedural details for these experiments and their data processing can be found in section 6.5.6.4.

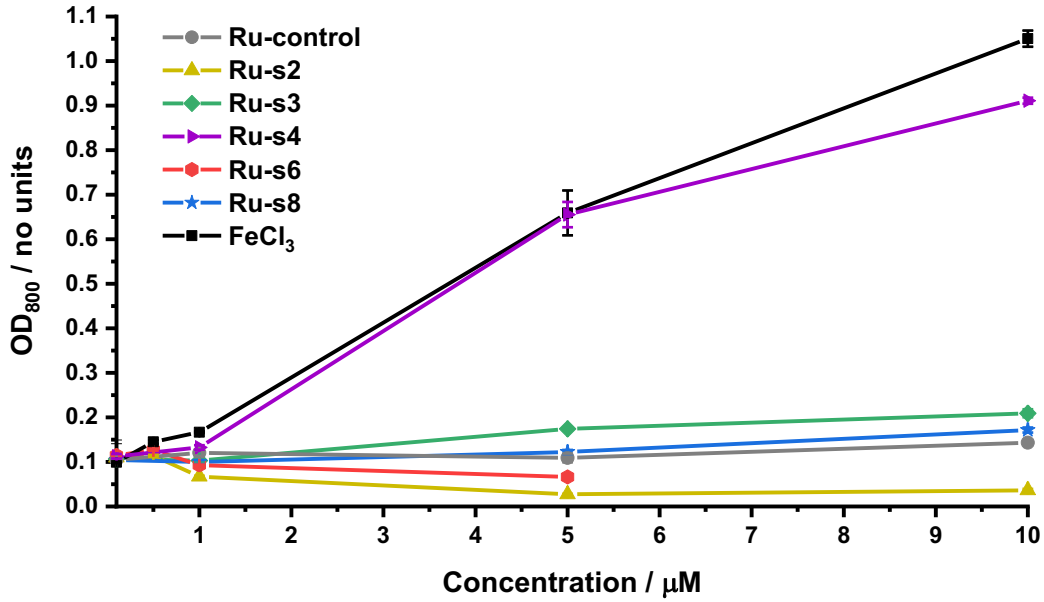

Figure 100 Dosage-response curves of *E. coli* K12 (BW25113) overall growth. Overall growth at 24 h, for each of: **Ru-control**, **Ru-s2**, **Ru-s3**, **Ru-s4**, **Ru-s6**, **Ru-s8** and the iron control ($FeCl_3$) at their varied substrate concentrations under iron-limited (MHII supplemented with 200 μM bpy), micro-aerobic (2% O_2) conditions, in at least technical triplicate.

These data show that 'no addition' controls grow to an OD_{800} of ~ 0.1 and that the Kitamura-type catalyst control (**Ru-control**) has no observable effect on overall bacterial growth, as it produces this same value over its tested concentration range. In contrast, a positive correlation is observed for $FeCl_3$ as overall growth increases 10-fold at 10 μM compared to 'no addition'. Interestingly, the azotochelin conjugate (**Ru-s4**) improves bacterial growth at upper concentrations at a similar rate to the iron control. These results suggest that this conjugate improves the availability of iron to the bacteria. This might indeed be a result of its binding to residual iron in the growth medium and subsequent transportation into bacteria *via* siderophore-mediated iron-uptake pathways, as designed. If this is the case, this means prodrug activation inside bacterial cells is promising for this conjugate. Alternatively, if the catalyst-siderophore conjugate is iron-contaminated, these results might be

explained by increasing overall iron-concentrations. Like the control catalyst (**Ru-control**), no observable effect on bacterial growth was observed for the pyranone conjugate (**Ru-s8**) however overall growth is doubled by the addition of the catechol conjugate (**Ru-s3**) at 10 μM. In contrast, the acetate-protected catechol (**Ru-s2**) and DFO (**Ru-s6**) conjugates gave overall growth reductions at concentrations above 1 μM and 500 nM, respectively. Whilst it is more difficult to reason why **Ru-s2** is more toxic than the other conjugates, the toxicity of **Ru-s6** can be attributed to the iron-sequestering ability of DFO. These results suggest that **Ru-s2** is probably too toxic to be used in prodrug activation studies and that **Ru-s6** is not internalised in high levels.

In order to strengthen claims that **Ru-s4** might facilitate iron-uptake into bacteria, the iron concentration of the media after the addition of each catalyst at 10 μM was determined by ICP-MS, Table 2. The procedural detail for these measurements is shown in 6.5.2. The 'no addition' control showed [^{56}Fe] = 53 μM, which suggests significant concomitant iron levels even after Chelex treatment of the media. Despite this, growth studies in section 2.4.2.2 confirmed that the bacteria are still iron-limited due to the presence of 200 μM bpy. Moreover, the sample that had 100 μM $FeCl_3$ added to it, corresponds roughly to a 100 μM increase in iron levels, [^{56}Fe] = 155 μM. The values for each of the catalyst-siderophore conjugates shows no [^{56}Fe] values greater than that of the 'no-addition' control (apart from FO-conjugate **Ru-s6**), which suggests no significant iron contamination occurs on the addition of these catalysts. However, the fact they mostly give lower [^{56}Fe] values suggest inaccuracies in the technique. It is well known that the measurement of iron using ICP-MS can be perturbed by the generation of argides in the instrument and their incomplete mass separation with iron due to their similar masses.[223, 224]

The concentration of ruthenium was also measured by ICP-MS, Table 2. These results show that the 'no addition' control and iron control have no ruthenium, whereas samples with conjugate possess ruthenium at levels that approximately or exactly correspond to their theoretical values, to the nearest μM. This suggests that the purity of these conjugates is good.

Table 6 Iron content of selected growth media, determined by ICP-MS.

Additive	Additive Concentration / μM	[^{56}Fe] / μM	[^{101}Ru] / μM
No Addition	n/a	53	<LLOQ*
$FeCl_3$	100	155	<LLOQ*
Ru-control	10	19	9
Ru-s2	10	33	9
Ru-s3	10	22	10
Ru-s4	10	43	8
Ru-s6	10	56	9
Ru-s8	10	33	8

* Lowest limit of quantification = 36.2 ppb; detection limit = 12.05 ppb.

4.2.1 Summary

Overall, the antibacterial activity assays show good tolerance for most of the catalyst-siderophore conjugates, apart from **Ru-s2** and **Ru-s6** which become toxic in the low micromolar range. The remaining conjugates are all non-toxic at 10 μM, where azotochelin-conjugate **Ru-s4** enhances growth similar to iron controls. ICP-MS measurements suggest this might be due to the conjugate's action as a siderophore mimic, as the conjugate does not significantly increase iron levels relative to the 'no addition' control. Moreover, ICP-MS studies suggest good purity of the synthesised conjugates, as the measured [^{101}Ru] corresponds approximately to their theoretical values.

4.3 The Antibacterial Activity of the Catalyst-Siderophore Conjugates with Prodrug Co-addition

Now that the upper, non-toxic concentrations have been determined for each of the prodrugs and synthesised catalyst-siderophore conjugates, Table 7, their combined antibacterial activities at these concentrations will be evaluated. Each catalyst was added at their upper, non-toxic concentration with ***C*-moxi** at its upper, non-toxic concentration (10 μM). The data from these experiments are represented in the form of a bar chart, where each bar represents the overall growth of bacteria 24 h after the addition of the respective combination of components, Figure 101. Each co-addition is listed adjacent to its 'just catalyst-siderophore conjugate' control. Additional controls include tests with **Ru-control**, 'just prodrug' (***C*-moxi**) and drug (moxifloxacin), and siderophore controls including DFO, DHB, azotochelin, and citrate. The procedural details for these experiments and their data processing are given in section 6.5.6.4.

Table 7 Upper, non-toxic concentration for each of the prodrugs (***C*-moxi** and ***N*-moxi**) and the catalyst-siderophore conjugates against *E. coli* K12 (BW25113) in iron-limited MHII broth, under a micro-aerobic atmosphere (2% O_2).

Component	Upper, Non-toxic Concentration / μM
***C*-moxi**	10
***N*-moxi**	10
Ru-control	10
Ru-s2	1
Ru-s3	10
Ru-s4	10
Ru-s6	0.5
Ru-s8	10

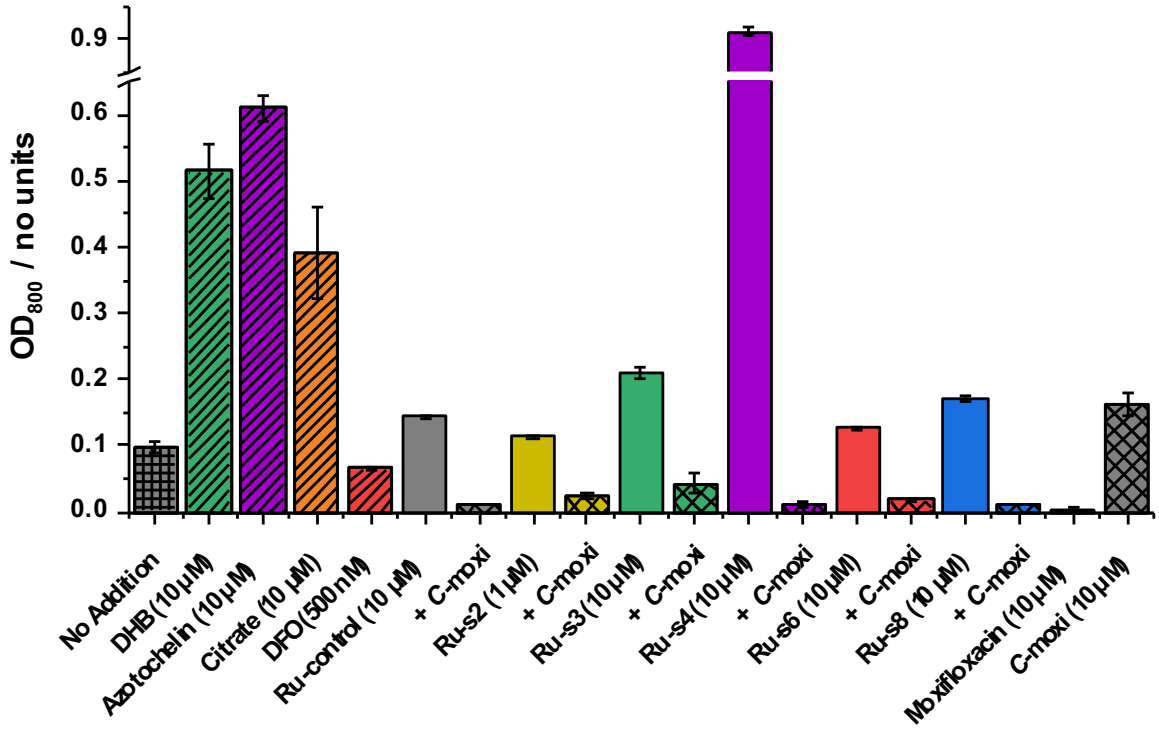

Figure 101 Overall growth of *E. coli* K12 (BW25113) grown under iron-limited (MHII supplemented with 200 μM bpy), micro-aerobic (2% O_2) conditions after 24 h with each catalyst-siderophore conjugate at its upper, non-toxic concentration with and without ***C*-moxi** (10 μM) and siderophore controls, in at least technical triplicate.

Firstly, it is important to analyse the growth effect of the siderophore controls. The siderophores DHB, azotochelin and citrate improve growth relative to the 'no addition' control. The growth enhancement observed for azotochelin is similar to that provided by **Ru-s4** at the same concentration. In contrast, DHB provides significant growth enhancements but neither of the catechol conjugated catalysts **Ru-s2** and **Ru-s3** provide this to the same extent, although **Ru-s3** does double overall growth. The siderophore DFO does not improve growth, confirming it is a poor siderophore for *E. coli*. This explains similar lack of growth improvement for the DFO conjugate **Ru-s6**.

The co-addition experiments for each catalyst result in antibacterial activity comparable to the addition of moxifloxacin at 10 μM, as the overall amount of bacteria diminishes significantly compared to the 'no addition' control and their corresponding 'just catalyst' controls. In fact, the growth enhancement observed for the azotochelin conjugate **Ru-s4** is completely reversed on the addition of prodrug.

These results suggest that the catalysts do indeed work to activate the prodrug ***C*-moxi** to form moxifloxacin under these conditions and that their stability in the presence of bacteria is sufficient to produce a toxic concentration of moxifloxacin. These experiments do not however establish the location of catalyst-mediated prodrug activation, as both are added to the bacterial growth media at the same time. Therefore, additional experiments should be utilised to determine whether this activation can occur or is occurring within the bacterial cells.

4.3.1 Summary

Co-addition of the prodrug ***C*-moxi** with each of the synthesised catalyst-siderophore conjugates results in inhibited bacterial growth similar to the active antibacterial moxifloxacin, when both components are added at their individual upper, non-toxic concentrations. These results suggest that the catalysts are indeed activating the prodrug under these conditions. As they show enhanced bacterial growth in the absence of prodrug and the most significant growth reductions on prodrug co-addition, **Ru-s3** and **Ru-s4** are the most promising conjugates for prodrug activation within bacterial cells. Although these results are positive, one can only infer uptake from these experiments and therefore intracellular prodrug activation cannot be confirmed.

4.4 Evaluating the Bacterial Uptake of Catalyst-Siderophore Conjugates

4.4.1 Growth Recovery

One of the more rigorous methods for determining the bacterial usage of compounds as siderophores for iron-transport involves studies with genetic deletion mutants. As introduced in section 4.1.2.1, the rescued growth of iron-limited bacterial mutants deficient in siderophore biosynthesis by the addition of a compound implies their role as a siderophore.

Growth recovery assays were executed using a mutant of *E. coli* K12 (BW25113) deficient in the biosynthesis of its major siderophore enterobactin, due to the deletion of the entA gene. This gene catalyses the reversible NAD-dependent

formation of 2,3-dihydroxybenzoate from 2,3-dihydro-2,3-dihydroxytbenzoate, Figure 102.[225] The overall growth of *E. coli* K12 (BW25113) (ΔentA) was measured 24 h after the addition of each synthesised catalyst-siderophore conjugate at varied concentrations up to its upper, non-toxic concentration, Figure 103. Additional conditions include 'no addition' and siderophore controls including DHB, azotochelin, citrate and DFO. Whereas the use of citrate and DFO as siderophores by *E. coli* is known but insignificant, that of azotochelin is under dispute whereas DHB is thought to facilitate iron-uptake only into the periplasm by diffusion.[51, 77, 192] Procedural details for this assay can be found in section 6.5.6.5.

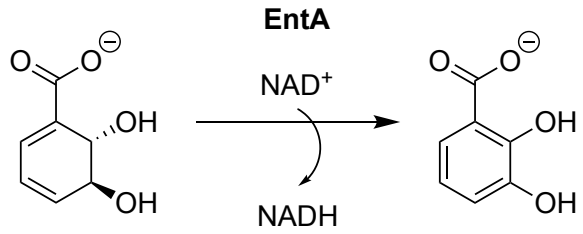

Figure 102 Transformation performed by the EntA enzyme which is coded for by the entA gene, constituting part of the biosynthesis of the major siderophore of *E. coli*, enterobactin.

The only siderophore controls to provide significant growth recovery for the *E. coli* (ΔentA) were DHB and azotochelin which strongly suggests these compounds facilitate iron-uptake. However, whether this is indeed by siderophore transport pathways remains unclear. No growth recovery is provided by citrate despite growth enhancements observed for the non-mutant. In contrast, DFO looks to provide some growth recovery; this result is in line with the literature as cell-surface receptors for the siderophore in *E. coli* are reported however less commonly employed by the bacteria.

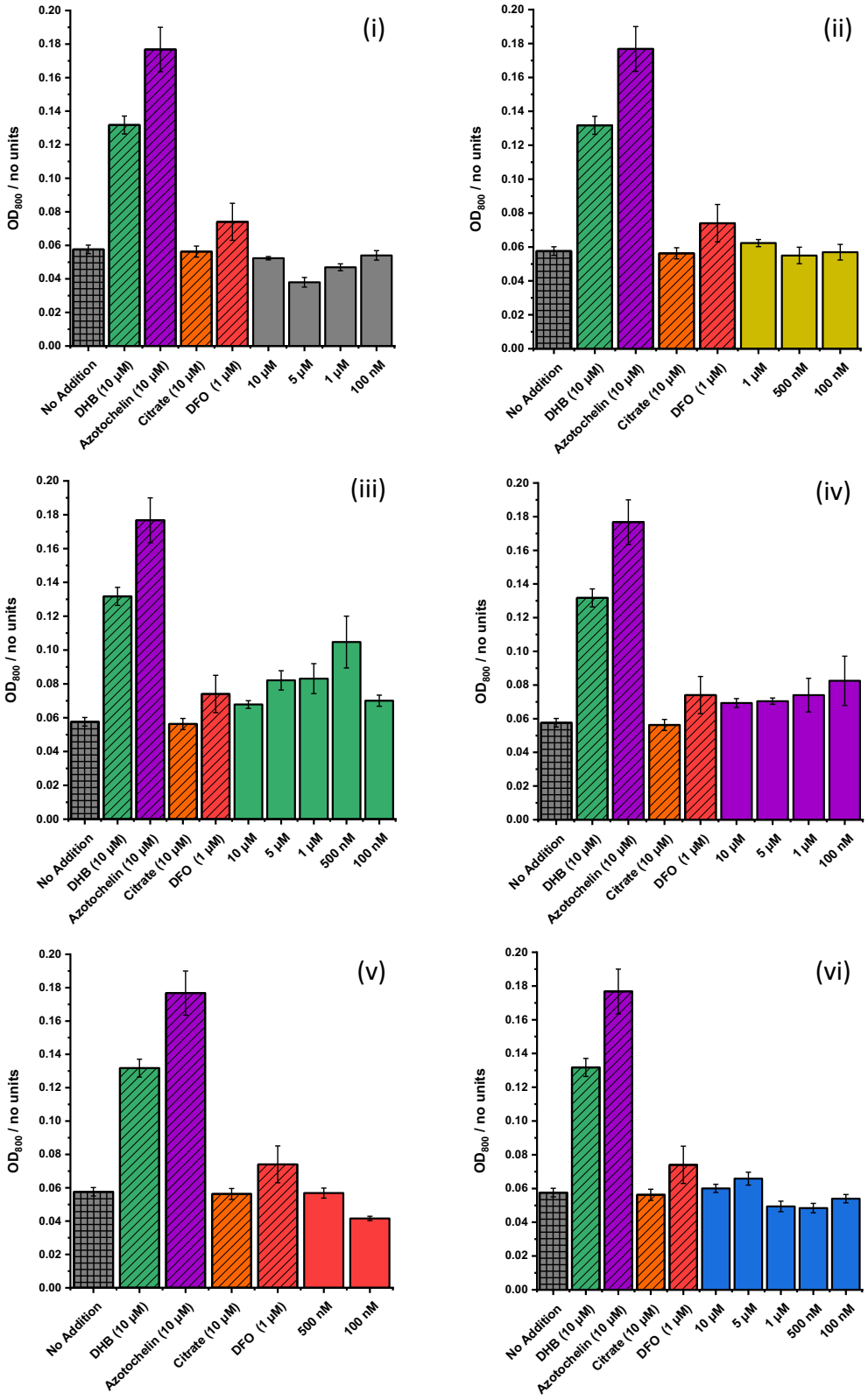

Figure 103 Overall growth of *E. coli* K12 (BW25113) (ΔentA) under iron-limited (MHII supplemented with 200 μM bpy), micro-aerobic (2% O_2) conditions after 24 h with varied concentration of (i) **Ru-control**, (ii) **Ru-s2**, (iii) **Ru-s3**, (iv) **Ru-s4**, (v) **Ru-s6**, (vi) **Ru-s8** compared to 'no addition' and siderophore controls, in at least technical triplicate.

The catalysts **Ru-control**, **Ru-s2**, **Ru-s6**, and **Ru-s8** do not provide any growth recovery at the tested concentrations, as each gives overall growth similar to the levels observed for the 'no addition' control. Although this was expected for **Ru-control** as it possess no siderophore attachment, these results suggest these conjugates are not recognised as siderophores and therefore not internalised into *E. coli* cells, at least not by siderophore-mediated iron-uptake pathways. However, catalyst-siderophore conjugates **Ru-s3** and **Ru-s4** do show some growth recovery although not as significant as their corresponding siderophore controls. The growth recovery provided by the catechol conjugate **Ru-s3** is most significant at a concentration of 500 nM where bacterial growth is increased by ~70%. Growth recovery observed for the azotochelin conjugate **Ru-s4** is less impressive, as overall growth is similar to that provided by DFO. Based on these observations, the catechol and azotochelin conjugates **Ru-s3** and **Ru-s4** respectively, are most promising for bacterial uptake and thus, prodrug activation within bacteria.

4.4.2 Prodrug Incubation

The uptake of prodrug ***C*-moxi** into *E. coli* K12 (BW25113) was inferred by prodrug uptake studies disclosed in section 2.4.4. If bacteria are pre-loaded with the prodrug so that it is only present within cells, any antibacterial activity observed by the addition of synthesised catalyst-siderophore conjugates relative to their corresponding 'no ***C*-moxi**' controls, implies prodrug activation and thus, their uptake. Consequently, prodrug incubation experiments were used to evaluate the bacterial uptake of the catalyst-siderophore conjugates.

4.4.2.1 Antibacterial Activity of Moxifloxacin and *C*-moxi against Bacteria During their Exponential Growth Phase

To encourage uptake, *E. coli* K12 (BW25113) were incubated with ***C*-moxi** during its exponential growth phase, as was the case in previous prodrug uptake studies reported in section 2.4.4. As previous MIC experiments for ***C*-moxi** and moxifloxacin involved their addition during the lag phase, their uptake and therefore toxicity might differ. Therefore, additional MIC data were obtained for ***C*-moxi** and moxifloxacin after addition during the exponential growth phase, represented as dosage

response curves, Figure 104. The procedural detail and data processing for these experiments can be found in section 6.5.6.6.

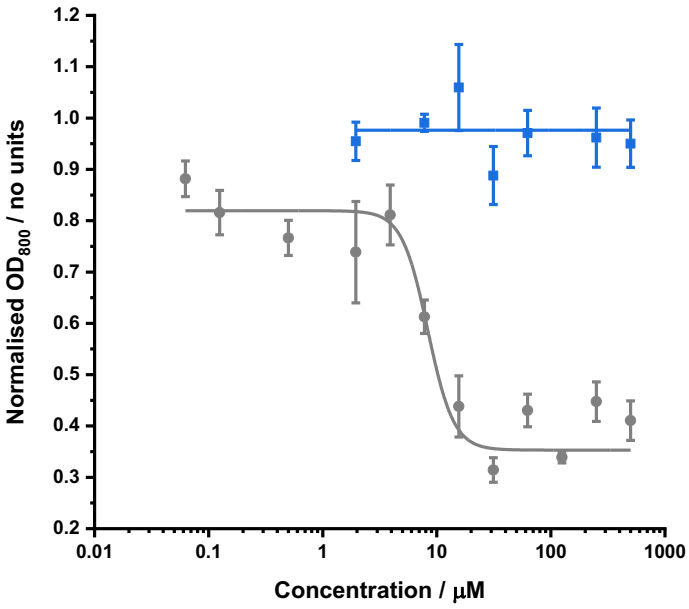

Figure 104 Dosage-response curves of *E. coli* K12 (BW25113) overall growth, 18 h after substrate addition during the exponential growth phase. Data are normalised to 'no addition' controls, for each of moxifloxacin (grey) and ***C*-moxi** (blue), at their varied substrate concentrations under iron-limited (MHII supplemented with 200 μM bpy), micro-aerobic (2% O_2) conditions.

These data show that both the prodrug (***C*-moxi**) and drug (moxifloxacin) are significantly less toxic when added during the exponential phase of bacterial growth compared to the lag phase. The MIC of moxifloxacin is approximately 25 μM whereas for ***C*-moxi**, no antibacterial activity is observed up to its solubility limit at 500 μM. Therefore, moxifloxacin is 80-fold and ***C*-moxi**, at least 50-fold less toxic during these exponential growth phase experiments. This can partly be explained by the relative amounts of substrate to bacteria. During lag phase MIC experiments the substrates were added to bacteria at an OD_{600} = 0.01, whereas during the exponential phase they are added at the same concentration to OD_{600} = 0.1. Therefore, there are approximately 10-fold more bacteria in exponential phase MIC experiments, requiring higher substrate concentrations to enforce the same levels of antibacterial activity. These results mean that ***C*-moxi** concentrations of 500 μM can be used during *E. coli* incubation, and thus only 5% need activation to see the complete inhibition of bacterial growth.

4.4.2.2 Antibacterial Activity of Prodrug Activation within Bacterial Cells

Now that the upper, non-toxic concentration for ***C*-moxi** against *E. coli* K12 (BW25113) bacteria has been determined for addition during the exponential growth phase, prodrug incubation experiments can take place. After overnight growth, the bacteria were incubated with ***C*-moxi** at 500 μM for 15 min at 37 °C. This culture was then spun down, the pellet isolated and resuspended in fresh MHII. This process was repeated twice to ensure no ***C*-moxi** remained in the media, and that any prodrug still present was inside the cells. Each catalyst was added at its upper, non-toxic concentration; in some cases, these concentrations vary from those reported for the lag phase antibacterial assays in section 4.2. The overall growth of these bacteria after 18 h was recorded, represented as a bar chart, Figure 105. For each catalyst, there is also a 'no ***C*-moxi** incubation' control, where the cells were instead incubated with plain DMSO. Since the catalysts perform prodrug activation at a similar rate, the greater reduction in growth from DMSO to ***C*-moxi** incubation, implies better bacterial uptake. Controls include 'no addition' and moxifloxacin addition, with their corresponding DMSO and ***C*-moxi** incubations. Procedural details for this assay can be found in section 6.5.6.7.

These data show no significant difference between incubations with subsequent no addition. This is expected as ***C*-moxi** was shown to be non-toxic at this concentration during the antibacterial activity assays in section 6.5.6.6. There is also no significant difference between incubations with subsequent moxifloxacin addition, as moxifloxacin and ***C*-moxi** do not work in an additive manner. The overall growth is lower for moxifloxacin as the added concentration is above its MIC value.

There is no difference between incubations with subsequent **Ru-control** addition indicating it is not internalised in sufficient amounts to observe an additive antibacterial effect due to ***C*-moxi** activation. Although there is a small difference between incubations for **Ru-s2**, this is not statistically significant. However, there are substantial differences between incubations for the remaining catalyst-siderophore conjugates **Ru-s3**, **Ru-s4**, **Ru-s6** and **Ru-s8**; this is especially the case for **Ru-s3** where overall growth is diminished by ~40%. These data suggest that these conjugates are the most promising for prodrug activation within bacterial cells,

however their growth inhibitions after ***C*-moxi** co-addition are not as significant as the moxifloxacin control. This suggests either insufficient uptake of either ***C*-moxi** or the catalyst-siderophore conjugates, or poor catalyst turnovers. Once more, it is important to also take into consideration the growth improvements provided by the conjugates and thus data are interpreted by evaluating the growth difference between incubations.

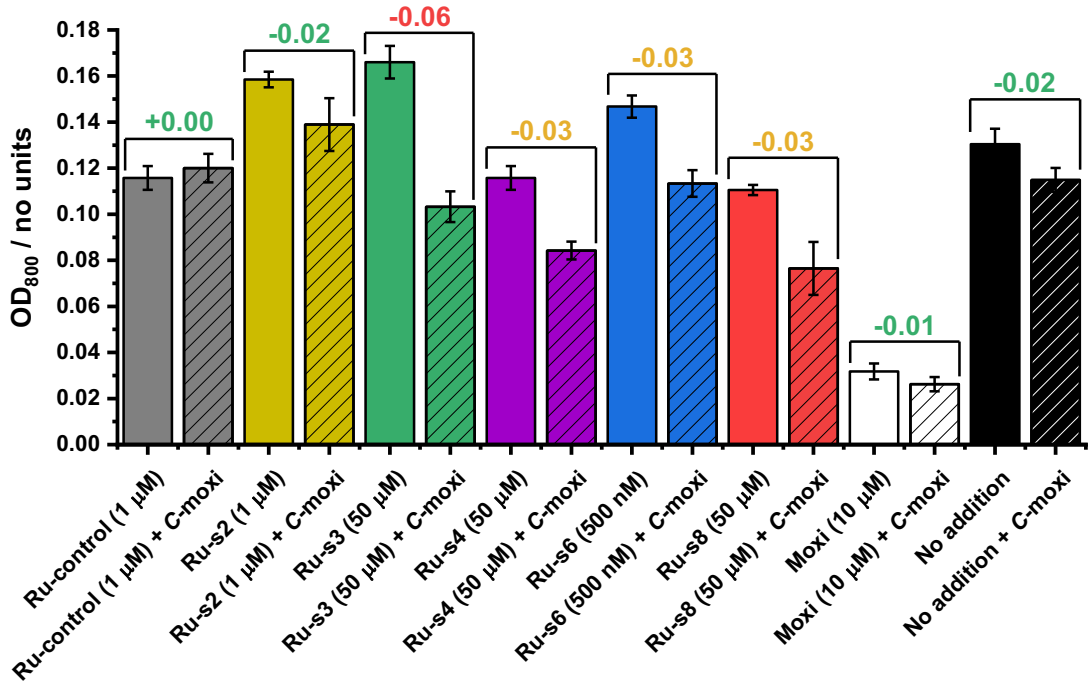

Figure 105 Overall growth of *E. coli* K12 (BW25113) grown under iron-limited (MHII supplemented with 200 µM bpy), micro-aerobic (2% O_2) conditions, 18 h after ***C*-moxi** (hatched bars) or DMSO (solid bars) incubation and subsequent addition of substrate. Substrates include **Ru-control**, **Ru-s2**, **Ru-s3**, **Ru-s4**, **Ru-s6** and **Ru-s8** at their upper, non-toxic concentrations and controls: moxifloxacin (white) and 'no addition' (black). The difference in overall growth between each incubation with and without ***C*-moxi** incubation, is highlighted in a bracket over the corresponding bar charts. Each incubation was carried out in technical triplicate, and each subsequent substrate addition in at least technical triplicate.

4.4.3 Summary

While on the positive side, catalyst-siderophore conjugates **Ru-s3** and **Ru-s4** provided rescued bacterial growth, neither were at levels comparable to their corresponding siderophore controls, DHB and azotochelin, respectively. The

azotochelin conjugate **Ru-s4** merely provides recovery similar to that by DFO, a siderophore that is mainly used by Gram-positive bacteria. The catechol conjugate **Ru-s3** does improve growth by approximately ~40% however this is only ~50% of the growth recovery provided by the DHB control. Nevertheless, these results are encouraging.

Prodrug incubation results somewhat mirror those obtained from the growth recovery experiments, as they suggest two of the synthesised conjugates are promising for bacterial uptake, in the catechol and azotochelin conjugates **Ru-s3** and **Ru-s4**, respectively. Considering the major siderophores for *E. coli* are catechol-based (e.g. enterobactin and its hydrolysis products), it does make sense that these conjugates are most likely to be successful in a Trojan-Horse approach.

4.5 Summary and Conclusions

The growth effects the synthesised catalyst-siderophore conjugates had on the *E. coli* K12 (BW25113) bacteria were measured and largely indicated good tolerance. Although **Ru-s2** and **Ru-s6** were toxic in the low micromolar range, the other conjugates did not inhibit bacterial growth up to 10 μM. In fact, the catechol conjugate **Ru-s3** doubled bacterial growth at 10 μM and impressively, the azotochelin conjugate **Ru-s4** enhanced bacterial growth at levels similar to the $FeCl_3$ control. ICP-MS measurements indicated these observed growth effects were not due to iron contamination of the conjugates.

During co-addition experiments with the prodrug ***C*-moxi**, all the synthesised catalyst-siderophore conjugates at their upper, non-toxic concentrations provided antibacterial activity which can be attributed to their activation of ***C*-moxi** to release moxifloxacin. The activity for these co-addition experiments was similar to levels seen for moxifloxacin addition. Despite the success of these experiments, they do not identify whether this prodrug activation occurs within the cells or in the surrounding media.

Two different methods were employed to imply the bacterial uptake of the synthesised catalyst-siderophore conjugates: growth recovery and prodrug incubation assays. Both experiments allowed the conclusion that the superior

conjugate for bacterial uptake is **Ru-s3** making it the most promising for prodrug activation within bacterial cells. This is as **Ru-s3** provided the most significant growth recovery of the siderophore biosynthesis deficient bacteria, although not to levels provided by its siderophore control, DHB. From these results, it can be assumed DHBs attachment to the catalyst structure impedes its use in iron uptake, as only ~50% growth recovery is observed for the corresponding conjugate, **Ru-s3**. Moreover, the combined antibacterial activity of **Ru-s3** after the bacteria were pre-loaded with ***C*-moxi** was most significant, although not as inhibitory as the moxifloxacin control. Neither of these experiments provide quantifiable data for the bacterial uptake and therefore future work might include more robust experiments to determine the exact location of the catalysts within bacteria, such as confocal microscopy. Despite this, the uptake of **Ru-s3** looks most likely and this result is in line with the fact the most successful Trojan-Horse antibacterial to date cefiderocol also utilises a monocatechol siderophore unit.[219]

Chapter 5 : Summary, Conclusions and Future Work

5.1 Probing Kitamura-type Catalysts for Antibacterial Activation

The Kitamura-type catalysts were selected for prodrug activation. Therefore, antibacterials that possess amine and/or carboxylic acid functional groups that could be modified to form their respective allyl carbamate and allyl esters were pursued. The fluoroquinolone antibacterials ciprofloxacin and moxifloxacin satisfied these requirements and due to its favourable solubility profile, the allyl ester-protected version of moxifloxacin (***C*-moxi**) was chosen as the prodrug for subsequent studies.

The Kitamura-type catalyst **Ru-control** was utilised to probe ***C*-moxi** for moxifloxacin formation under biologically-relevant conditions, to indicate the strategies suitability for medicinal applications. Unfortunately, poor conversions of ~40% were obtained, predominantly due to significant catalyst decomposition within the first few hours. The improved catalytic activity under anaerobic conditions (~90% conversion) indicated the sensitivity of the catalyst to molecular oxygen. ^{1}H NMR studies suggested this decomposition was due to oxidation of the active Ru(II) intermediate species, as initially proposed by Kiesewetter *et al.*[26] Therefore this work targeted enteric pathogens, as oxygen levels in the intestinal parts of the GI tract are low. Alternatively, catalyst modifications could be studied to enhance oxygen tolerance. This might include the conjugation of a reversibly binding donor atom that is covalently bound to the cyclopentadienyl or hydroxyquinoline ligands *via* a flexible linker, in order to protect the +2 oxidation state.[226] Importantly, the Ru-X bond formed must be semi-labile to allow for substrate binding, Figure 106.

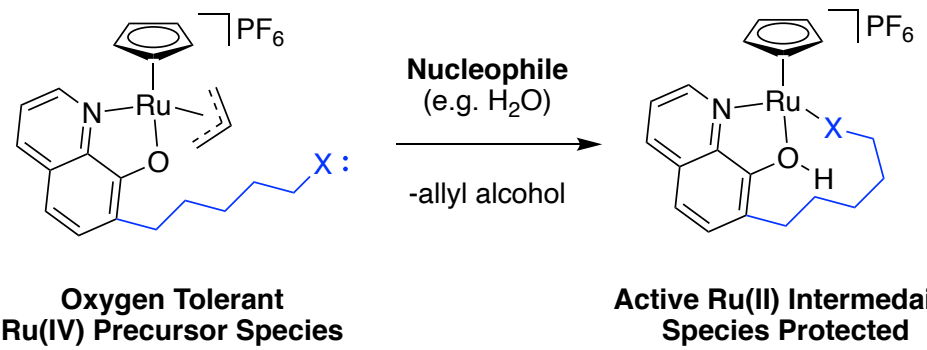

Figure 106 Proposed optimisation of the Kitamura-type catalyst for increased oxygen stability of the active Ru(II) intermediate species. X = donor atom.

The antibacterial activities of the prodrugs ***C*-moxi** and allyl carbamate-protected moxifloxacin (***N*-moxi**) were measured compared to moxifloxacin against gut-relevant bacteria *E. coli* K12 (BW25113) grown under a micro-aerobic atmosphere (2% O_2). This atmosphere and the iron-limited medium used for bacterial growth were chosen to mimic the environment of the intestines. Iron-limitation was achieved by a combination of Chelex treatment and bpy supplementation (200 μM). The antibacterial activities of the prodrugs (***C*-moxi** and ***N*-moxi**) were very similar and approximately 300-fold less than their activated form, moxifloxacin. Future investigations might utilise alternative antibacterials that possess an improved solubility profile and provide a larger toxicity window with their corresponding prodrug.

Bacterial uptake studies for ***C*-moxi** suggested low levels of internalisation into *E. coli* with 16% uptake after incubation at 10 μM for 15 min. These experiments do not indicate whether cytoplasmic accumulation is achieved and therefore the use of antibacterials with periplasmic targets might be prudent, such as the β-lactam antibiotic methicillin, Figure 107. In this case, modification by the formation of a prodrug might counter the drug-degradation action of β-lactamase enzymes released into the extracellular environment by resistant bacteria.[227, 228]

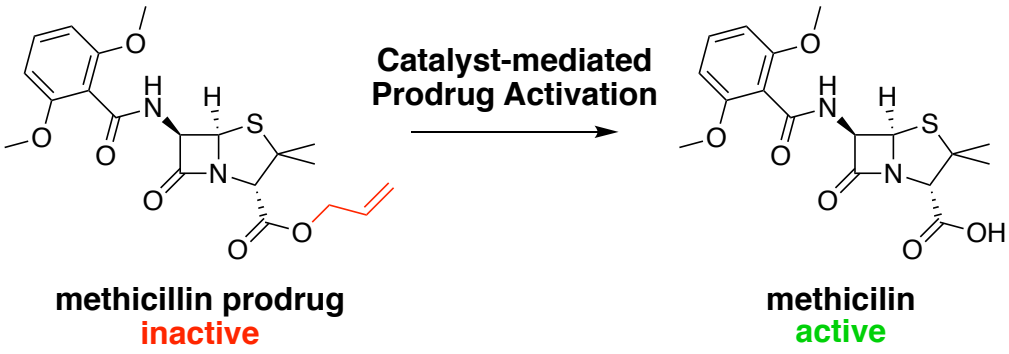

Figure 107 The Kitamura-type catalyst-mediated prodrug activation of methicillin.

5.2 The Design and Synthesis of Catalyst-Siderophore Conjugates

The conjugation of various siderophores to 8-allyloxyquinoline was achieved through covalent attachment *via* the amino acid glycine. The final step to produce

each corresponding siderophore-conjugated Kitamura-type catalyst was Ru-complexation using method A, Figure 55. In some cases, alternative reaction solvents such as DMF, and reaction durations were utilised to compensate for poor ligand solubilities. Consequently, alternative amino acid linkers might be pursued during the synthesis of additional siderophore conjugates to improve organic solubility, which in turn should aid their purification by precipitation.

Kitamura-type catalysts conjugated to an acetate-protected monocatechol siderophore mimic (**Ru-s2**), monocatechol siderophore mimic (**Ru-s3**), azotochelin (**Ru-s4**), ferrioxamine (**Ru-s5**), desferrioxamine (**Ru-s6**) and pyranone siderophore mimic (**Ru-s8**) were synthesised. Logical considerations into the design of siderophore-conjugates can be made to improve the chances of their involvement in bacterial iron-acquisition, such as the incorporation of siderophores known to be used by the targeted bacteria. In this case, pathogenic *E. coli* strains were targeted and therefore any future work for the targeting of this bacterial strain should focus on the synthesis of numerous, additional conjugates that possess alternative linkers and denticities of catechol-based siderophores. More specifically, this might include the attachment of siderophores that mimic enterobactin or its hydrolysis products like those in antibacterial conjugates developed by Neumann *et al.* in 2018.[169]

5.3 The Activities of Catalyst-Siderophore Conjugates for Prodrug Activation

The catalytic activity of the synthesised catalyst-siderophore conjugates for the activation of ***C*-moxi** to form moxifloxacin under biologically-relevant conditions suggested siderophore attachment did not significantly diminish catalyst activity, as all conjugates performed similarly to the 'no siderophore conjugated catalyst' control, **Ru-control**. Exceptions include DFO conjugates **Ru-s5** and **Ru-s6**, where the slower observed reaction kinetics were attributed to the steric bulk of the siderophore. To improve the activity of conjugates, future work might explore the attachment of siderophores *via* the reverse amide, to better mimic the optimised catalyst **Ru-8** reported by Völker and Meggers in 2017.[33]

5.4 Effects of Catalyst-Siderophore Conjugates on Bacterial Growth

The antibacterial activities of the synthesised catalyst-siderophore conjugates were tested against selected strains of *E. coli* under micro-aerobic, iron-limited conditions. Interestingly, conjugates **Ru-s3** and **Ru-s4** increased bacterial growth 2- and 9-fold, respectively. In the case of **Ru-s4**, this growth promotion was at similar levels provided by the iron control, $FeCl_3$. In contrast, no observable growth effects were observed for **Ru-control** and **Ru-s8**. The DFO conjugate **Ru-s6** was toxic above 500 nM, and this may be attributed to the iron-sequestering ability of the siderophore, thus implying poor uptake into bacteria. The toxicity above 1 μM of the acetate-protected mono-catechol conjugate **Ru-s2** is more difficult to rationalise. As **Ru-s3**, **Ru-s4** and **Ru-s8** were non-toxic at their highest tested concentrations, future work might investigate these conjugates at increased concentrations.

The iron concentration of the growth media after the addition of each catalyst at their upper non-toxic concentration was measured using ICP-MS. As iron levels were not too dissimilar from that of the 'no catalyst' control, it is suggested the improved growth provided by **Ru-s3** and **Ru-s4** was due to their facilitation of iron-uptake, and not due to iron-contamination.

5.5 The Antibacterial Activity of Prodrug Activation by Catalyst-Siderophore Conjugates

The antibacterial activity of each catalyst-siderophore conjugate with ***C*-moxi** at their individual upper, non-toxic concentrations was measured against *E. coli*. Every conjugate tested gave antibacterial action during co-addition which was attributed to the catalyst-mediated release of moxifloxacin from ***C*-moxi**. The observed inhibited bacterial growths were similar to that provided by the moxifloxacin control at 10 μM. To investigate the relative performance of each of the catalyst-siderophore conjugates, future work might investigate how growth inhibition varies with changing catalyst and prodrug concentrations.

5.6 Bacterial Uptake of Catalyst-Siderophore Conjugates

Initial experiments employed to imply the bacterial uptake of conjugates were growth recovery assays, where each conjugate was added to an iron-starved, enterobactin biosynthesis deficient mutant of *E. coli* K12 (BW25113) (ΔentA) at varied concentrations. The only conjugates to improve growth were the catechol (**Ru-s3**) and azotochelin (**Ru-s4**) conjugates. The former provided the most significant growth recovery with a 70% growth increase however this was only 50% of its corresponding siderophore control DHB. This suggests conjugation to the Kitamura-type catalyst impedes this siderophore mimic's capacity for iron-uptake. Additional experiments to this end might include studies with double genetic deletion mutants (e.g. ΔentAtonB). The gene tonB codes for the biosynthesis of the protein TonB that takes part in the translocation of siderophore-iron complexes across the outer-membrane to the periplasm in Gram-negative bacteria.[51] Therefore, if the growth recovery provided by **Ru-s3** is removed for this double mutant, this further supports its utilisation as a siderophore. Moreover, double mutants with various deleted genes for specific cell-surface receptors might aid in the identification of the specific transport system providing uptake.

As the bacterial uptake of ***C*-moxi** was inferred through previous studies, bacteria were pre-loaded *via* incubation. Following repeated centrifugation and re-suspension with fresh media, any antibacterial activity observed following the addition of a catalyst-siderophore conjugate indicates their uptake or less desirably, their attachment to the cell surface. Conclusions were based on the growth difference between prodrug *versus* no prodrug incubation, so that the improved bacterial growth provided by some of the conjugates was taken into account. As expected, results from these experiments gave no/little difference in overall bacterial growth for the 'no addition' and 'just moxifloxacin' controls. Unfortunately, no statistically significant difference was observed for incubations with **Ru-s2** indicating its poor uptake. However, decreased growth was observed for ***C*-moxi** incubations with the subsequent addition of **Ru-s3**, **Ru-s4**, **Ru-s6**, and **Ru-s8**, relative to 'no ***C*-moxi**' (DMSO incubations). In these instances, growth inhibitions were not as

significant as that observed for the moxifloxacin control. Conjugate **Ru-s3** gave the most significant antibacterial activity following ***C*-moxi** incubation, as overall growth was decreased by ~40%. Each catalyst possesses similar prodrug activation kinetics and thus, prodrug incubation results suggest **Ru-s3** is internalised at the highest rate, if we assume decomposition rates are the same/similar for each conjugate. Additional experiments in this area might contain incubations with each of the conjugates first, followed by prodrug addition. Alternatively, incubation experiments with fluorescent probes might inform this area, as they are common for determining the uptake of the Kitamura-type catalysts by human cells.[21, 30, 31] The penetration of Gram-negative bacteria is more challenging and therefore a suitable pro-fluorophore must first be identified. Success might be had in this area if smaller probes are used such as the luciferase system reported by Hsu *et al.* in 2016.[30] This work also describes the use of ICP-MS analysis for the uptake of abiotic metals such as ruthenium.

Chapter 6 : Experimental

6.1 General Remarks

6.1.1 Materials

All materials were obtained from commercial suppliers (Acros, Alfa-Aesar, Fisher Chemicals, Fisher Scientific, Fluka, Sigma-Aldrich, Tokyo Chemical Industry) and used as supplied unless otherwise stated.

6.1.2 Instrumentation

^{1}H, $^{13}C\{^{1}H\}$, DEPT 135, HSQC, COSY, HMBC and NOESY NMR spectra were recorded on Jeol EX and ES 400 MHz instruments (^{1}H NMR 400 MHz, ^{13}C NMR 101 MHz), unless stated otherwise. Alternative instruments included a Bruker AV500b (^{1}H NMR 500 MHz, ^{13}C NMR 126 MHz) and a AVIIIHD600 (^{1}H NMR 600 MHz, ^{13}C NMR 151 MHz). Multiplicity abbreviations are as follows; s for singlet, d for doublet, t for triplet, q for quartet qn for quintet, sx for sextet, sp for septet, dd for double doublet, td triple doublet, ddd for doublet of doublet of doublets, m for multiplet, br for broad and app for apparent. NMR assignments were aided by various combinations of DEPT 135, HSQC, COSY, HMBC and NOESY experiments, where required.

Electrospray ionisation mass spectrometry (ESI-MS) was recorded on a Bruker compact® TOF mass spectrometer and Liquid Injection Field Desorption Ionization (LIFDI), on a Waters GCT Premier TOF mass spectrometer by Mr. K. Heaton, Dr. R. Cercola and Mr. A. Lopez. Error is reported in two forms: ‘error (ppm)’ which describes closeness of the measured m/z value to that of the theoretical, and ‘mSigma’ which describes the similarity of the measured isotope patten to that of the theoretical.

Elemental analysis was carried out by Dr. G. McAllister on an Exeter CE-440 elemental analyser and results are within ± 0.5 %, unless stated otherwise.

Analytical HPLC was performed using a Shimadzu Prominence LC 20AD setup, with C18 column and SPD M20A diode array detector under the direction of Ms. A. Dixon and Dr. S. Hicks.

TLC was performed on Merck silica gel 60 F_{254} aluminium backed plates and visualised under a Chromato-vue Model CC-10 UV lamp, unless otherwise stated. Electronic absorption spectra were recorded on a Shimadzu UV-1800 spectrophotometer at ambient temperature.

Infrared (ATIR) spectra were recorded on a Bruker ALPHA II – Platinum FT-IR Spectrometer with Platinum Diamond-ATR QuickSnap Sampling Module, at ambient temperature.

Melting points were determined using a Stuart Scientific SMP3 melting point apparatus.

6.2 Synthesis

1-Cyclopropyl-6-fluoro-4-oxo-7-{4-[(prop-2-en-1-yloxy)carbonyl]piperazin-1-yl}-1,4-dihydroquinoline-3-carboxylic acid, *N*-cipro

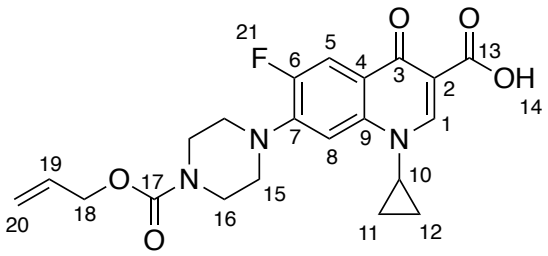

$C_{21}H_{22}FN_3O_5$, 415.421 g mol^{-1}

1-Cyclopropyl-6-fluoro-4-oxo-7-{4-[(prop-2-en-1-yloxy)carbonyl]piperazin-1-yl}-1,4-dihydroquinoline-3-carboxylic acid was prepared based on a procedure from the literature.[128]

To a stirred suspension of ciprofloxacin (2.03 g, 6.12 mmol) and 1,8-bis(dimethylamino)naphthalene (1.31 g, 6.12 mmol) in dry dichloromethane (80 mL) at 0 °C, was added allyl chloroformate (651 μL, 6.12 mmol) dropwise and left to stir for 20 h. After this time, the reaction mixture was washed with a 1:1 mixture of 1M HCl (aq) and brine (30 mL, x3) and the solvent from the produced organic layer was removed *in vacuo*, to yield the title compound as a white solid.

Yield: 2.26 g, 5.54 mmol, 91%

Rf: 0.62 in dichloromethane : MeOH (9:1)

HRMS (ESI+):

Calc. for $[C_{21}H_{22}FN_3O_5]+H^+$ = 416.1616 Found = 416.1625 (-2.1 ppm error, 2.9 mSigma)

Calc. for $[C_{21}H_{22}FN_3O_5]+Na^+$ = 438.1436 Found = 438.1447 (-2.6 ppm error, 5.3 mSigma)

Calc. for $[C_{21}H_{22}FN_3O_5]+K^+$ = 454.1175 Found = 454.1180 (-1.2 ppm error, 14.9 mSigma)

^{1}H NMR: (400 MHz, $CDCl_3$) δ: 14.93 (s, 1H-**14**), 8.77 (s, 1H-**1**), 8.04 (d, *J* = 13.0 Hz, 1H-**5**), 7.37 (d, *J* = 7.0 Hz, 1H-**8**), 6.11 – 5.62 (m, 1H-**19**), 5.33 (dq, *J* = 17.0, 1.5 Hz, 1H-**20(trans)**), 5.25 (dq, *J* = 10.5, 1.5 Hz, 1H-**20(cis)**), 4.64 (dt, *J* = 6.0, 1.0 Hz, 2H-**18**), 3.83 – 3.73 (m, 4H-**16**), 3.54 (tt, *J* = 7.0, 4.0 Hz, 1H-**10**), 3.36 – 3.22 (m, 4H-**15**), 1.40 (q, *J* = 7.0 Hz, 2H-**11+12(trans)**), 1.28 – 1.15 (m, 2H-**11+12(cis)**).

^{13}C NMR: (126 MHz, $CDCl_3$) δ: 177.2 (d, *J* = 2.5 Hz, -**3**, 167.04-**13**, 155.1-**17**, 153.8 (d, *J* = 251.5 Hz, -**6**), 147.7-**1**, 145.8 (d, *J* = 10.5 Hz, -**7**), 139.1-**9**, 132.9-**19**, 120.4 (d, *J* = 7.5 Hz, -**4**), 118.0-**20**, 112.7 (d, *J* = 23.5 Hz, -**5**), 108.3-**2**, 105.2 (d, *J* = 3.0 Hz, -**8**), 66.5-**18**, 49.9-**15**, 43.8-**16**, 35.4-**10**, 8.4-**11+12**.

IR ATIR (cm^{-1}): 3091 w (Aromatic/Alkene C-H stretch), 2868 w (Aliphatic C-H stretch), 1721 s (C=O stretch), 1694 s (C=O stretch), 1628 s (Alkene C=C stretch), 1506 m (Aromatic C=C stretch).

Elemental Analysis:

Calculated for $[C_{21}H_{22}FN_3O_5 \cdot 0.35\ CH_2Cl_2]$: %C 57.61, %H 5.14, %N 9.44
Measured for $[C_{21}H_{22}FN_3O_5 \cdot 0.35\ CH_2Cl_2]$: %C 57.94, %H 5.10 %N 9.14

Melting Point: 296-298 °C

1-Cyclopropyl-6-fluoro-8-methoxy-4-oxo-7-{1-[(prop-2-en-1-yloxy) carbonyl]-octahydro-1*H*-pyrrolo[3,4-b]pyridin-6-yl}-1,4-dihydro-quinoline-3-carboxylic acid, *N*-moxi

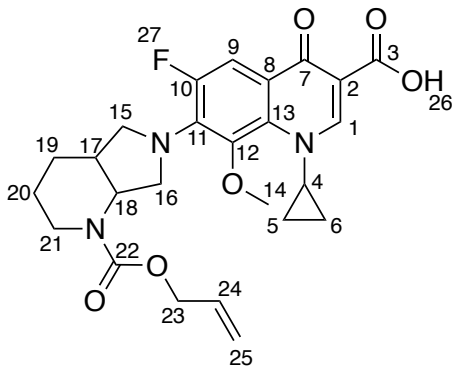

$C_{25}H_{28}FN_3O_6$, 485.512 g mol^{-1}

1-Cyclopropyl-6-fluoro-8-methoxy-4-oxo-7-{1-[(prop-2-en-1-yloxy) carbonyl]-octahydro-1*H*-pyrrolo[3,4-b]pyridin-6-yl}-1,4-dihydro-quinoline-3-carboxylic acid was prepared based on a procedure from the literature.[128]

To a green/yellow suspension of moxifloxacin hydrochloride (50 mg, 0.114 mmol) in dry dichloromethane (3 mL) at room temperature, was added 1,8-bis(dimethyl)naphthalene (24 mg, 0.114 mmol). After cooling the reaction mixture to 0 °C, DIPEA (20 μL, 0.114 mmol) and allyl chloroformate (13 μL, 0.114 mmol) were added to give a yellow, clear solution and left stirring for 18 h at room temperature. After this time, dichloromethane (25 mL) was added and the organic layer was washed with a mixture of 1 M HCl (aq) (10 mL) and brine (10 mL), x3. Solvent was removed *in vacuo*, to give a pale yellow solid. The resulting solid was then triturated in PET and filtered to yield the title compound as an off-white white solid. The resulting pale yellow solid was purified *via* column chromatography, eluting with dichloromethane : MeOH (19:1) and then triturated with Et_2O, to yield the title compound as an off-white solid.

Yield: 54 mg, 111 μmol, 97%

Rf: 0.70 in dichloromethane : MeOH (9:1)

HRMS (ESI+):

Calc. for $[C_{25}H_{28}FN_3O_6]+H^+$ = 486.2035 Found = 486.2043 (-1.6 ppm error, 0.7 mSigma)

Calc. for $[C_{25}H_{28}FN_3O_6]+Na^+$ = 508.1854 Found = 508.1864 (-1.8 ppm error, 1.9 mSigma)

^{1}H NMR: (400 MHz, $CDCl_3$) δ: 14.98 (s, 1H-**26**), 8.75 (s, 1H-**9**), 7.76 (d, *J* = 14.0 Hz, 1H-**1**), 6.00 – 5.89 (m, 1H-**24**), 5.30 (dd, *J* = 17.0, 2.0 Hz, 1H-**25 (trans)**), 5.22 (dd, *J* = 10.0, 1.5 Hz, 1H-**25 (cis)**), 4.82 (brs, 1H-**18**), 4.66 – 4.57 (m, 2H-**23**), 4.18 – 4.06 (m, 2H-**15/16+21**), 4.02 – 3.94 (m, 1H-**4**), 3.93 – 3.85 (m, 1H-**15/16**), 3.57 (s, 3H-**14**), 3.42 (s, 1H-**15/16**), 3.28 (d, *J* = 10.0 Hz, 1H-**15/16**),f 3.02 – 2.89 (m, 1H-**21**), 2.35 – 2.23 (m, 1H-**17**), 1.90 – 1.71 (m, 2H-**19**), 1.61 – 1.42 (m, 2H-**20**), 1.34 – 1.21 (m, 1H-**5**), 1.18 – 1.01 (m, 2H-**5/6**), 0.88 – 0.76 (m, 1H-**6**).

^{13}C NMR: (101 MHz, $CDCl_3$) δ: 176.9-**7**, 167.2-**3**, 155.8-**10,** 152.6 (d, *J* = 19.0 Hz, -**11**) 149.9-**1**, 137.3 (d, *J* = 10.5 Hz-**12**), 134.5-**13**, 133.0-**24**, 118.9 (d, *J* = 9.0 Hz, -**8**), 117.9-**25**, 108.2 (d, *J* = 24.0 Hz, **-9**), 107.8-**2**, 66.5-**23**, 61.3-**14**, 56.6 (d, *J* = 8.5 Hz, -**15**), 52.7-**18**, 49.0 (d, *J* = 6.0 Hz, **-16**), 40.5-**4**, 39.7-**21**, 35.7-**17**, 25.3-**19**, 24.2-**20**, 10.7-**5**, 8.6-**6**.

^{19}F NMR: (376 MHz, $CDCl_3$) δ: -121.1 (s, 1F-**27**)

IR ATIR (cm^{-1}): 3083 w (Aromatic/Alkene C-H stretch), 2922 m (Alkane C-H stretch), 2852 m (Alkane C-H stretch), 1727 s (C=O stretch), 1694 s (C=O stretch), 1617 s (Alkene C=C stretch), 1508 m (Aromatic C=C stretch).

Elemental Analysis:

Calculated for $[C_{25}H_{28}FN_3O_6 \cdot 0.15\ C_4H_{10}O]$: %C 61.94, %H 6.04, %N 8.40
Measured for $[C_{25}H_{28}FN_3O_6 \cdot 0.15\ C_4H_{10}O]$: %C 61.84, %H 5.89, %N 8.27

Melting Point: 90 – 92 °C

UV-vis Spectroscopy:

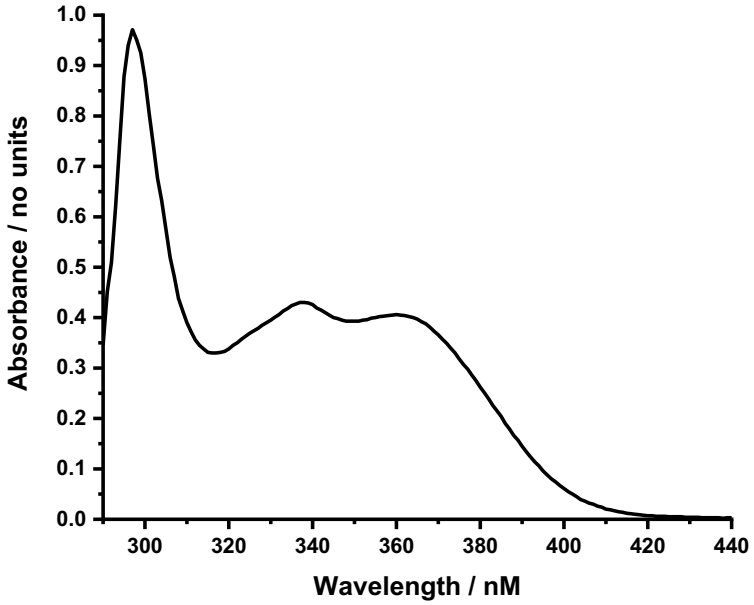

Figure 108 UV-vis spectrum, 100 μM in 10% DMSO in aqueous MOPS buffer (pH 7.4).

7-{4-[(*Tert*-butoxy)carbonyl]piperazin-1-yl}-1-cyclopropyl-6-fluoro-4-oxo-1,4-dihydroquinoline-3-carboxylic acid, 1

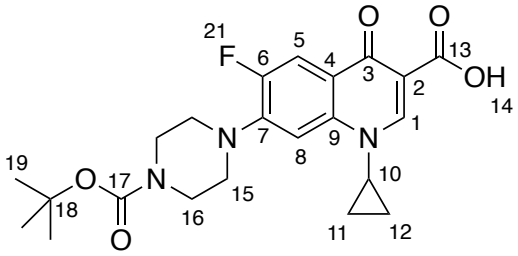

$C_{22}H_{26}FN_3O_5$, 431.464 g mol^{-1}

To a stirred suspension of ciprofloxacin (2.37 g, 7.15 mmol) in dioxane : water (1:1, 40 mL), was added sodium hydroxide (10 mL, 1 M) and then di-*tert*-butyl dicarbonate (2.03 g, 9.29 mmol) at room temperature, and left to stir for 2 h. After this time, the resulting suspension was filtered and washed with acetone (10 mL, x3) to yield the title compound as a white solid.

Yield: 2.42 g, 5.60 mmol, 78%

Rf: 0.59 in dichloromethane : MeOH : DIPEA (90:10:1)

HRMS (ESI+):

Calc. for $[C_{22}H_{26}FN_3O_5]+H^+$ = 432.1929 Found = 432.1928 (0.3 ppm error, 3.4 mSigma)

Calc. for $[C_{22}H_{26}FN_3O_5]+Na^+$ = 454.1749 Found = 454.1751 (-0.4 ppm error, 9.1 mSigma)

^{1}H NMR: (400 MHz, $CDCl_3$) δ: 14.94 (s, 1H-**14**), 8.72 (s, 1H-**1**), 7.97 (d, *J* = 13.0 Hz, 1H-**5**), 7.35 (d, *J* = 7.0 Hz, 1H-**8**), 3.76 – 3.61 (m, 4H-**16**), 3.59 – 3.48 (tt, *J* = 8.0, 4.0 Hz 1H-**10**), 3.32 – 3.21 (m, 4H-**15**), 1.49 (s, 9H-**19**), 1.40 (m, 2H-**11+12(trans)**), 1.20 (m, 2H-**11+12(cis)**).

^{19}F NMR: (376 MHz, $CDCl_3$) δ: -120.8 (dd, *J* = 12.5, 7.0 Hz, 1F-**21**).

NMR spectra are in agreement with literature reports.[127]

IR ATIR (cm^{-1}): 3097 w (Aromatic C-H stretch), 2976 w (Aliphatic C-H stretch), 2856 w (Aliphatic C-H stretch), 1721 s (C=O stretch), 1692 s (C=O stretch), 1614 s (Alkene C=C stretch).

Prop-2-en-1-yl 7-{4-[(*tert*-butoxy)carbonyl]piperazin-1-yl}-1-cyclopropyl-6-fluoro-4-oxo-1,4-dihydroquinoline-3-carboxylate, 2

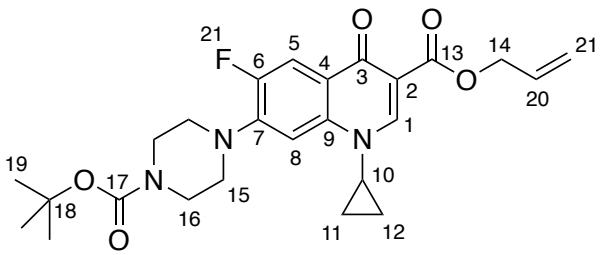

$C_{25}H_{30}FN_3O_5$, 471.529 g mol^{-1}

To a solution of 7-{4-[(*tert*-butoxy)carbonyl]piperazin-1-yl}-1-cyclopropyl-6-fluoro-4-oxo-1,4-dihydroquinoline-3-carboxylic acid (2.42g, 5.60 mmol) in a dry DMF (40 mL) at room temperature, was added K_2CO_3 (1.55 g, 11.2 mmol) and allyl bromide (961 μL, 11.2 mmol). The resulting solution was heated to 80 °C and left stirring at this temperature for 18 h. After this time, solvent was removed *in vacuo* and the residue

formed, dissolved in dichloromethane (50 mL) with minimum MeOH (1 mL). The organic layer was washed with water (50 mL, x3) and the solvent removed *in vacuo* to yield the title compound as a beige solid.

Yield: 2.38 g, 5.05 mmol, 90%

Rf: 0.50 in EtOAc

HRMS (ESI+):

Calc. for $[C_{25}H_{30}FN_3O_5]+H^+$ = 472.2242 Found = 472.2247 (-0.9 ppm error, 2.3 mSigma)

Calc. for $[C_{25}H_{30}FN_3O_5]+Na^+$ = 494.2062 Found = 494.2069 (-1.4 ppm error, 1.8 mSigma)

^{1}H NMR (400 MHz, $CDCl_3$) δ 8.50 (s, 1H-**1**), 7.98 (d, *J* = 13.0 Hz, 1H-**5**), 7.24 (d, *J* = 7.5 Hz, 1H-**8**), 6.04 (ddt, *J* = 16.0, 11.0, 5.5 Hz, 1H-**20**), 5.47 (dd, *J* = 17.0, 1.5 Hz, 1H-**21(trans)**), 5.27 (dd, *J* = 10.5, 2.0 Hz, 1H-**21(cis)**), 3.70 – 3.51 (m, 2H-**14**), 3.42 (tt, *J* = 7.0, 4.0 Hz, 1H-**15**), 3.29 – 3.07 (m, 4H-**16**), 1.48 (s, 9H-**19**), 1.31 (q, *J* = 6.5 Hz, 2H-**11+12(trans)**), 1.16 – 1.09 (m, 2H-**11+12(cis)**).

^{19}F NMR: (376 MHz, $CDCl_3$) δ: -123.7 (dd, *J* = 13.0, 7.0 Hz, 1F-**21**).

^{13}C NMR: (101 MHz, $CDCl_3$) δ: 173.1(d, *J* = 2.5 Hz, -**3**), 165.5-**13**, 154.7-**17**, 153.5 (d, *J* = 248.5 Hz, -**6**), 148.4-**1**, 144.5 (d, *J* = 10.5 Hz, -**7**), 138.0-**9**, 132.5-**20**, 123.4 (d, *J* = 7.0 Hz, -**4**), 118.3-**21**, 113.5 (d, *J* = 23.0 Hz, -**5**), 110.2-**2**, 105.2 (d, *J* = 3.0 Hz, -**8**), 80.3-**18**, 65.6-**14**, 53.6-**16**, 44.0-**15**, 34.7-**10**, 28.5-**19**, 8.3-**11+12**.

IR ATIR (cm^{-1}): 3091 w (Aromatic/Alkene C-H stretch), 2976 w (Aliphatic C-H stretch), 2938 w (Aromatic C-H stretch), 2856 w (Aliphatic C-H stretch), 1721 s (C=O stretch), 1692 s (C=O stretch), 1614 s (Alkene C=C stretch), 1548 m (Aromatic C=C stretch).

Elemental Analysis:

Calculated for $[C_{25}H_{30}FN_3O_5 \cdot 0.05\ CH_2Cl_2 \cdot 0.05\ CH_4O]$: %C 63.15, %H 6.40, %N 8.80

Measured for [$C_{25}H_{30}FN_3O_5$ • 0.05 CH_2Cl_2 • 0.05 CH_4O]: %C 63.49, %H 6.09 %N 8.41

Prop-2-en-1-yl 1-cyclopropyl-6-fluoro-4-oxo-7-(piperazin-1-yl)-1,4-dihydroquinoline-3-carboxylate, *C*-cipro

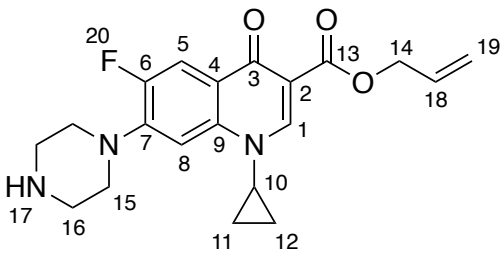

$C_{20}H_{22}FN_3O_3$, 371.412 g mol^{-1}

To a solution of prop-2-en-1-yl 7-{4-[(*tert*-butoxy)carbonyl]piperazin-1-yl}-1-cyclopropyl-6-fluoro-4-oxo-1,4-dihydroquinoline-3-carboxylate (2.36 g, 5.01 mmol) in a dichloromethane (80 mL) at room temperature, was added trifluoroacetic acid (5 mL) and left stirring at this temperature for 2 h. After this time, solvent was removed *in vacuo* and the residue formed dissolved in $CHCl_3$ (30 mL). The organic layer was washed with saturated $NaHCO_3$ (aq) (20 mL, x3), brine (20 mL, x3), water (20 mL), and the solvent removed *in vacuo* with co-evaporation with toluene (10 mL, x3) to yield the title compound as a beige solid.

Yield: 983 mg, 2.65 mmol, 53%

Rf: 0.19 in dichloromethane : MeOH (8:2)

HRMS (ESI+):

Calc. for [$C_{20}H_{22}FN_3O_3$]+H^+ = 372.1718 Found = 372.1720 (-0.7 ppm error, 3.0 mSigma)

Calc. for [$C_{20}H_{22}FN_3O_3$]+Na^+ = 394.1537 Found = 394.1542 (-1.1 ppm error, 1.9 mSigma)

^{1}H NMR: (400 MHz, $CDCl_3$) δ: 8.49 (s, 1H-**1**), 7.96 (d, *J* = 13.5 Hz, 1H-**5**), 7.24 (d, *J* = 7.0 Hz, 1H-**8**), 6.04 (ddt, *J* = 16.0, 10.5, 5.5 Hz, 1H-**18**), 5.46 (dd, *J* = 17.0, 1.5

Hz, 1H-**19(trans)**), 5.37 – 5.22 (m, 1H-**19(cis)**), 4.80 (d, *J* = 5.5 Hz, 2H-**14**), 3.42 (tt, *J* = 7.0, 4.0 Hz, 1H-**10**), 3.22 (dd, *J* = 6.0, 3.5 Hz, 4H-**16**), 3.08 (dd, *J* = 6.5, 3.5 Hz, 4H-**15**), 1.30 (q, *J* = 7.0 Hz, 2H-**11+12(trans)**), 1.17 – 0.98 (m, 2H-**11+12(cis)**).

^{19}F NMR: (376 MHz, $CDCl_3$) δ: -123.4 (dd, *J* = 13.5, 7.0 Hz, 1F-**20**).

^{13}C NMR: (101 MHz, $CDCl_3$) δ: 173.2 (d, *J* = 2.0 Hz, -**3**), 165.5-**13**, 153.5 (d, *J* = 248.5 Hz, -**6**), 148.3-**1**, 145.1 (d, *J* = 10.5 Hz, -**7**), 138.1-**9**, 132.5-**18**, 123.0 (d, *J* = 7.0 Hz, -**4**), 118.3-**19**, 113.3 (d, *J* = 23.5 Hz, -**5**), 110.0-**2**, 104.9 (d, *J* = 3.0 Hz, -**8**), 65.5-**14**, 51.2 (d, *J* = 4.5 Hz, -**15**), 46.1-**16**, 34.6-**10**, 8.2-**11+12**.

IR ATIR (cm^{-1}): 3253 m (N-H stretch), 2941 w (Aromatic/Alkene C-H stretch), 2817 w (Carboxylic Acid O-H stretch), 2798 w (Aliphatic C-H stretch), 2747 w (Aliphatic C-H stretch), 1719 s (C=O stretch), 1622 s (Alkene C=C stretch), 1585 m (Aromatic C=C stretch).

Melting Point: 212-214 °C

7-{1-[(*Tert*-butoxy)carbonyl]-octahydro-1*H*-pyrrolo[3,4-b]pyridin-6-yl}-1-cyclopropyl-6-fluoro-8-methoxy-4-oxo-1,4-dihydroquinoline-3-carboxylic acid, 3

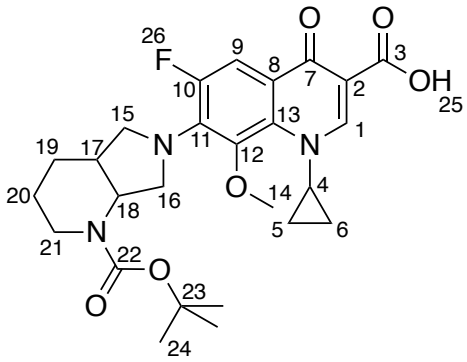

$C_{26}H_{32}FN_3O_6$, 501.555 g mol^{-1}

To a green/yellow suspension of moxifloxacin hydrochloride (423 mg, 0.966 mmol) in a dioxane : water mixture (1:1, 10 mL) at room temperature, was added 1M NaOH (aq) (2 mL) to yield a pale green solution, and then di-*tert*-butyl dicarbonate (1.26 mmol, 274 mg). The resulting solution was left stirring at room temperature for 3 d. After this time, dioxane was removed *in vacuo* and to the remaining aqueous

solution was added dichloromethane (50 mL). The organic layer was washed with 0.1 M formic acid (aq) (30 mL, x3) and solvent removed *in vacuo*, to yield the title compound, as a beige solid.

Yield: 464 mg, 0.925 mmol, 96%

Rf: 0.83 in dichloromethane : MeOH : DIPEA (90:10:1)

HRMS (ESI+):

Calc. for $[C_{26}H_{32}FN_3O_6]+H^+$ = 502.2348 Found = 502.2338 (1.9 ppm error, 3.9 mSigma)

Calc. for $[C_{26}H_{32}FN_3O_6]+Na^+$ = 524.2167 Found = 524.2160 (1.5 ppm error, 9.1 mSigma)

^{1}H NMR: (400 MHz, $CDCl_3$) δ: 15.00 (br s, 1H-**25**), 8.76 (s, 1H-**1**), 7.78 (d, *J* = 13.5 Hz, 1H-**9**), 4.78 (br s, 1H-**18**), 4.12 – 4.03 (m, 2H-**15**+**21**), 4.03 – 3.95 (m, 1H-**4**), 3.86 (td, *J* = 10.5, 3.0 Hz, 1H-**16**), 3.56 (s, 3H-**14**), 3.38 (br s, 1H-**16**), 3.30 – 3.20 (m, 1H-**15**), 2.87 (t, J = 11.5 Hz, 1H-**21**), 2.33 – 2.19 (m, 1H-**17**), 1.86 – 1.72 (m, 2H-**19**+**20**), 1.47 (m, 11H-**19**+**20**+**24**), 1.35 – 1.23 (m, 1H-**5**), 1.18 – 1.00 (m, 2H-**5**+**6**), 0.87 – 0.77 (m, 1H-**6**).

^{19}F NMR: (376 MHz, $CDCl_3$) δ: -120.9 (d, *J* = 10.0 Hz, 1F-**26**).

NMR spectra are in agreement with literature reports.[127]

Prop-2-en-1-yl 7-{1-[(*tert*-butoxy)carbonyl]-octahydro-1*H*-pyrrolo [3,4-b]pyridin-6-yl}-1-cyclopropyl-6-fluoro-8-methoxy-4-oxo-1,4-dihydroquinoline-3-carboxylate, 4

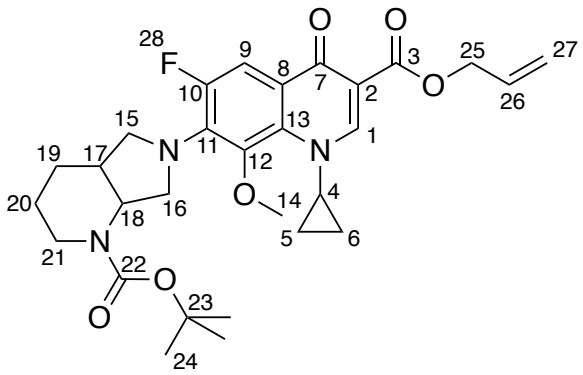

$C_{29}H_{36}FN_3O_6$, 541.620 g mol^{-1}

To a solution of 7-{1-[(*tert*-butoxy)carbonyl]-octahydro-1H-pyrrolo[3,4-b]pyridin-6-yl}-1-cyclopropyl-6-fluoro-8-methoxy-4-oxo-1,4-dihydroquinoline-3-carboxylic acid (445 mg, 0.890 mmol) in a dry DMF (15 mL) at room temperature, was added K_2CO_3 (245 mg, 1.77 mmol) and allyl bromide (152 μL, 1.77 mmol). The resulting solution was heated to 80 °C and left stirring at this temperature for 18 h. After this time, solvent was removed *in vacuo* and the residue formed dissolved in dichloromethane (40 mL). The organic layer was washed with water (30 mL, x3) the solvent removed *in vacuo* to yield the title compound as an orange/yellow foam.

Yield: 454 mg, 0.838 mmol, 94%

Rf: 0.63 in EtOAc

HRMS (ESI+):

Calc. for $[C_{29}H_{36}FN_3O_6]+H^+$ = 542.2667 Found = 542.2667 (-1.0 ppm error, 1.7 mSigma)

Calc. for $[C_{29}H_{36}FN_3O_6]+Na^+$ = 564.2480 Found = 564.2487 (-1.2 ppm error, 2.1 mSigma)

Calc. for $[C_{29}H_{36}FN_3O_6]+K^+$ = 580.2220 Found = 580.2233 (-2.3 ppm error, 33.3 mSigma)

^{1}H NMR: (400 MHz, $CDCl_3$) δ: 8.54 (s, 1H-**1**), 7.82 (d, *J* = 14.0 Hz, 1H-**9**), 6.12 – 5.97 (m, 1H-**26**), 5.46 (dd, J = 17.0, 1.5 Hz, 1H-**27(trans)**), 5.26 (dd, *J* = 9.5, 1.5 Hz, 1H-**27(cis)**), 4.83-4.81 (m, 2H-**25**), 4.76 (br s, 1H-**18**), 4.10 – 3.97 (m, 2H-**15**+**21**), 3.93 – 3.76 (m, 2H-**4**+**16**), 3.55 (s, 3H-**14**), 3.34 (br s, 1H-**16**), 3.25 – 3.13 (m, 1H-**15**), 2.93 – 2.81 (m, 1H-**21**), 2.23 (h, *J* = 5.5 Hz, 1H-**17**), 1.85 – 1.71 (m, 2H-**19**+**20**), 1.30 – 1.15 (m, 1H-**5**), 1.12 – 0.93 (m, 2H-**5**+**6**), 0.86 – 0.71 (m, 1H-**6**).

^{19}F NMR: (376 MHz, $CDCl_3$) δ: 123.2 (s, 1F-**28**).

NMR spectra are in agreement with literature reports.[128]

Prop-2-en-1-yl 1-cyclopropyl-6-fluoro-8-methoxy-7-{octahydro-1*H*-pyrrolo[3,4-b]pyridin-6-yl}-4-oxo-1,4-dihydroquinoline-3-carboxylate, *C*-moxi

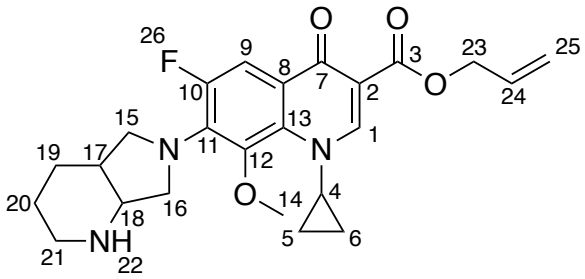

$C_{24}H_{28}FN_3O_4$, 441.503 g mol^{-1}

To a solution of *N*-boc-*C*-moxi (437 mg, 0.81 mmol) in a dichloromethane (15 mL) at room temperature, was added trifluoroacetic acid (1 mL) and left stirring at this temperature for 18 h. After this time, solvent was removed *in vacuo* and the residue formed dissolved in $CHCl_3$ (30 mL). The organic layer was washed with saturated $NaHCO_3$ (aq) (20 mL, x3), and the solvent removed *in vacuo* to yield the title compound as a light brown solid.

Yield: 350 mg, 793 μmol, 98%

HRMS (ESI+):

Calc. for $[C_{24}H_{28}FN_3O_4]+H^+$ = 442.2137 Found = 442.2126 (2.4 ppm error, 1.9 mSigma)

Calc. for $[C_{24}H_{28}FN_3O_4]+Na^+$ = 464.1956 Found = 464.1947 (2.4 ppm error, 6.8 mSigma)

^{1}H NMR: (400 MHz, $CDCl_3$) δ: 8.53 (s, 1H-**1**), 7.77 (d, *J* = 14.5 Hz, 1H-**9**), 6.04 (ddt, *J* = 16.0, 10.5, 5.5 Hz, 1H-**24**), 5.46 (ddd, *J* = 17.0, 2.0 Hz, 1H-**25(trans)**), 5.25 (d, *J* = 10.5 Hz, 1H-**25(cis)**), 4.86 – 4.76 (m, 2H-**23**), 3.99 – 3.82 (m, 3H-**4**+**15**+**16**), 3.54 (s, 3H-**14**), 3.44 – 3.34 (m, 2H-**15**+**16**), 3.31 (m, 1H-**18**), 3.04 (dt, *J* = 11.5, 3.5 Hz, 1H-**21**), 2.73 – 2.69 (td, *J* = 11.5, 3.0 Hz,1H-**21**), 2.29 (tt, *J* = 8.5, 4.0 Hz, 1H-**17**), 1.90 – 1.62 (m, 3H-**19**+**20**), 1.58 – 1.45 (m, 1H-**20**), 1.29 – 1.11 (m, 1H-**5**), 1.11 – 0.94 (m, 2H-**5**+**6**), 0.87 – 0.73 (m, 1H-**6**).

^{13}C NMR: (101 MHz, $CDCl_3$) δ: 172.9 (d, *J* = 2.5 Hz, -**7**), 165.7-**3**, 153.5 (d, *J* = 248.0 Hz-**10**), 150.6-**1**, 140.8 (d, *J* = 7.0 Hz, -**12**), 136.2 (d, *J* = 11.0 Hz, -**11**), 133.5 (d, *J* = 1.0 Hz, -**13**), 132.6-**24**, 121.5 (d, *J* = 8.0 Hz, **8**), 118.2-**25**, 109.6-**2**, 108.7 (d, *J* = 24.0 Hz, -**9**), 65.4-**23**, 60.9-**14**, 58.3 (d, *J* = 6.0 Hz, -**16**), 56.7 (d, *J* = 2.0 Hz, -**18**), 52.4 (d, *J* = 6.5 Hz, -**15**), 45.0-**21**, 39.6-**4**, 36.9 (d, *J* = 1.0 Hz, -**17**), 23.5-**19**, 22.1-**20**, 10.1-**6**, 8.7-**5**.

^{19}F NMR: (376 MHz, $CDCl_3$) δ: 122.9 (d, *J* = 14.0 Hz, 1F-**26**).

NMR spectra are in agreement with literature reports.[128]

IR ATIR (cm^{-1}): 3091 m (Aromatic/Alkene C-H stretch), 3009 w (Aromatic C-H stretch), 2922 m (Alkane C-H stretch), 2871 m (Alkane C-H stretch), 2852 m (Alkane C-H stretch), 1688 s (C=O stretch), 1607 m (Alkene C=C stretch), 1480 m (Aromatic C=C stretch).

Elemental Analysis:

Calculated for $[C_{24}H_{28}FN_3O_4 \cdot 0.05\ CHCl_3 \cdot 0.05\ H_2O]$: %C 64.43, %H 6.33, %N 9.37
Measured for $[C_{24}H_{28}FN_3O_4 \cdot 0.05\ CHCl_3 \cdot 0.05\ H_2O]$: %C 64.64, %H 6.15, %N 9.07

Melting Point: 139 – 141 °C

UV-vis Spectroscopy:

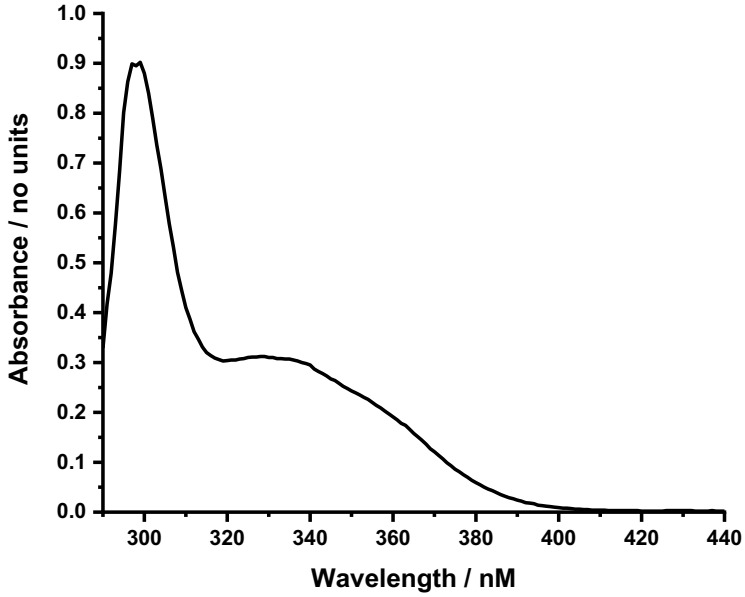

Figure 109 UV-vis spectrum, 50 μM in 10% DMSO in aqueous MOPS buffer (pH 7.4).

Prop-2-en-1-yl 1-cyclopropyl-6-fluoro-4-oxo-7-{4-[(prop-2-en-1-yloxy)carbonyl]piperazin-1-yl}-1,4-dihydroquinoline-3-carboxylate, *N,C*-cipro

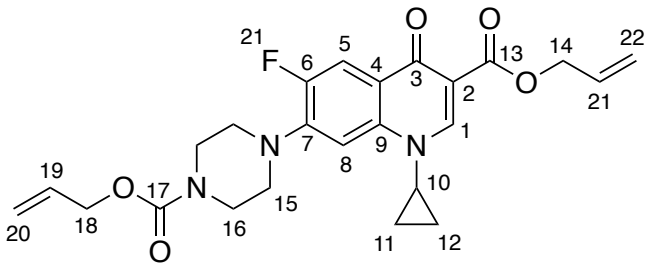

$C_{24}H_{26}FN_3O_5$, 455.486 g mol^{-1}

To a solution of 1-cyclopropyl-6-fluoro-4-oxo-7-{4-[(prop-2-en-1-yloxy)carbonyl]piperazin-1-yl}-1,4-dihydroquinoline-3-carboxylic acid (200 mg, 481 μmol) in dry DMF (20 mL) at room temperature, was added K_2CO_3 (133 mg, 963 μmol) and allyl bromide (84 μL, 963 μmol). The resulting solution was heated to 60 °C and left stirring at this temperature for 24 h. After this time, solvent was removed *in vacuo* and the residue formed dissolved in dichloromethane (50 mL). The organic layer

was washed with water (30 mL, x3) the solvent removed *in vacuo* to yield the title compound as a white solid.

Yield: 197 mg, 433 μmol, 90%

Rf: 0.62 in dichloromethane : MeOH (19:1)

HRMS (ESI+):

Calc. for $[C_{24}H_{26}FN_3O_5]+H^+$ = 456.1929 Found = 456.1932 (-0.6 ppm error, 4.3 mSigma)

Calc. for $[C_{24}H_{26}FN_3O_5]+Na^+$ = 478.1749 Found = 478.1755 (-1.4 ppm error, 3.2 mSigma)

Calc. for $[C_{24}H_{26}FN_3O_5]+K^+$ = 494.1488 Found = 494.1493 (-0.9 ppm error, 4.1 mSigma)

^{1}H NMR: (400 MHz, $CDCl_3$) δ: 8.53 (s, 1H-**1**), 8.01 (d, *J* = 13.0 Hz, 1H-**5**), 7.28 (s, 1H-**8**), 6.14 – 5.87 (m, 1H-**19+21**), 5.49 (dq, *J* = 17.0, 1.5 Hz, 1H-**20(trans)/22(trans)**), 5.34 (dq, *J* = 17.5, 1.5 Hz, 1H-**20(trans)/22(trans)**), 5.33 – 5.21 (m, 2H-**20(cis)+22(cis)**), 4.83 (dt, *J* = 6.0, 1.0 Hz, 2H-**14/18**), 4.65 (dt, *J* = 5.5, 1.5 Hz, 2H-**14/18**), 3.80 – 3.69 (m, 4H-**16**), 3.44 (tt, *J* = 7.1, 4.1 Hz, 1H-**10**), 3.32 – 3.19 (m, 4H-**15**), 1.33 (q, *J* = 6.8 Hz, 1H-**11+12(trans)**), 1.15 (q, *J* = 6.3 Hz, 1H-**11+12(trans)**).

^{13}C NMR: (101 MHz, $CDCl_3$) δ: 173.1 (d, *J* = 2.0 Hz, -**3**), 165.5-**13**, 155.1-**17**, 153.5 (d, *J* = 248.5 Hz, -**6**), 148.5-**1**, 144.4 (d, *J* = 10.5 Hz, -**7**), 138.0-**9**, 132.9-**19/21**, 132.5-**19/21**, 123.5 (d, *J* = 7.0 Hz, -**4**), 118.4-**20/22**, 117.9-**20/22**, 113.5 (d, *J* = 23.0 Hz, -**5**), 110.2-**2**, 105.2 (d, *J* = 2.5 Hz, -**8**), 66.4-**14/18**, 65.6-**14/18**, 50.0-**15**, 43.8-**16**, 34.7-**10**, 8.3-**11+12**.

IR ATIR (cm^{-1}): 3093 w (Aromatic/Alkene C-H stretch), 3007 w (Aromatic/Alkene C-H stretch), 2918 w (Aliphatic C-H stretch), 2850 w (Aliphatic C-H stretch), 1717 s (C=O stretch), 1702 s (C=O stretch), 1616 s (Alkene C=C stretch), 1488 m (Aromatic C=C stretch).

Elemental Analysis:

Calculated for [$C_{24}H_{26}FN_3O_5$ • 0.55 H_2O]: %C 61.94, %H 5.87, %N 9.03
Measured for [$C_{24}H_{26}FN_3O_5$ • 0.55 H_2O]: %C 62.00, %H 5.71 %N 8.86

Melting Point: 196-198 °C

8-(Prop-2-en-1-yloxy)quinoline, 5

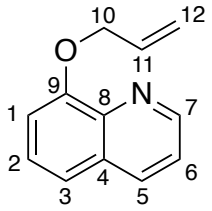

$C_{12}H_{11}NO$, 185.226 g mol^{-1}

8-(Prop-2-en-1-yloxy)quinoline was prepared following a procedure from the literature.[33]

Yield: 284 mg, 1.53 mmol, 74%

Rf: 0.3 in EtOAc : PET (1:3)

HRMS (ESI+):

Calc. for [$C_{12}H_{11}NO$]+H^+ = 186.0913 Found = 186.0910 (1.8 ppm error, 1.5 mSigma)

^{1}H NMR: (400 MHz, $CDCl_3$)) δ: 8.94 (dd, *J* = 4.0, 1.5 Hz, 1H-**7**), 8.11 (dd, *J* = 8.5, 1.5 Hz, 1H-**5**), 7.46 – 7.36 (m, 3H-**6+3+2**), 7.06 (dd, *J* = 7.5, 1.0 Hz, 1H-**1**), 6.26 – 6.16 (m, 1H-**11**), 5.46 (dd, *J* = 17.5, 1.5 Hz, 1H-**12(trans)**), 5.33 (dd, *J* = 10.5, 1.5 Hz, 1H-**12(cis)**), 4.87 (dt, *J* = 5.5, 1.5 Hz, 2H-**10**).

^{13}C NMR: (126 MHz, $CDCl_3$) δ: 154.4-**9**, 149.5-**7**, 140.5-**8**, 136.0-**5**, 133.3-**11**, 129.6-**4**, 126.7-**6/3/2**, 121.7-**6/3/2**, 119.8-**6/3/2**, 118.5-**12**, 109.3-**1**, 69.9-**10**.

NMR spectra are in agreement with literature reports.[33]

Ru-control (Ru-6)

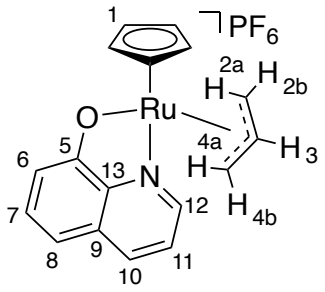

$C_{17}H_{16}F_6NOPRu$, 496.355 g mol^{-1}

Ru-control was prepared following a procedure from the literature.[33]

Yield: 16 mg, 32.2 μmol, 56%

HRMS (ESI+):

Calc. for $[C_{17}H_{16}NORu]^+$ = 352.0270 Found = 352.0272 (0.7 ppm error, 8.6 mSigma)

^{1}H NMR: (400 MHz, acetone-*d*$_6$)) δ: 8.96 (dd, *J* = 5.0, 1.0 Hz, 1H-**12**), 8.49 (dd, *J* = 8.5, 1.0 Hz, 1H-**10**), 7.60 (dd, *J* = 8.5, 5.0 Hz, 1H-**11**), 7.39 (t, *J* = 8.0 Hz, 1H-**7**), 7.04 (d, *J* = 8.0 Hz, 1H-**6/8**), 6.94 (dd, *J* = 8.0, 0.5 Hz, 1H-**6/8**), 6.30 (s, 5H-**1**), 4.77 – 4.56 (m, 2H-**3+2a/4a**), 4.48 – 4.38 (m, 1H-**2a/4a**), 4.38 – 4.31 (m, 1H-**2b/4b**), 4.22 – 4.16 (m, 1H-**2b/4b**).

^{13}C NMR: (101 MHz, acetone-d$_6$) δ: 170.2-**5**, 156.2-**12**, 146.5-**9**, 140.5-**10**, 131.6-**13**, 131.1-**6/7**, 124.5-**11**, 116.6-**6/7**, 112.8-**8**, 99.4-**3**, 97.0-**1**, 69.8-**2/4**, 63.4-**2/4**

^{19}F NMR: (376 MHz, acetone-*d*$_6$) δ: -72.4 (d, *J* = 707.5 Hz, 6F).

^{31}P NMR: (162 MHz, acetone-*d*$_6$) δ: -143.6 (p, *J* = 707.5 Hz, 1P).

NMR spectra are in agreement with literature reports.[33]

IR ATIR (cm^{-1}): 3124 m (Aromatic/Alkene C-H stretch), 3107 w (Aromatic/Alkene C-H stretch), 1585 m (Alkene C=C stretch), 1572 m (Alkene C=C stretch), 1502 m (Aromatic C=C stretch).

Elemental Analysis:

Calculated for [$C_{17}H_{16}F_6NOPRu$ • 0.35 CH_2Cl_2 • 0.5 $C_4H_{10}O$]: %C 40.30, %H 3.48, %N 2.59

Measured for [$C_{17}H_{16}F_6NOPRu$ • 0.35 CH_2Cl_2 • 0.5 $C_4H_{10}O$]: %C 40.54, %H 3.20, %N 2.57

UV-vis Spectroscopy:

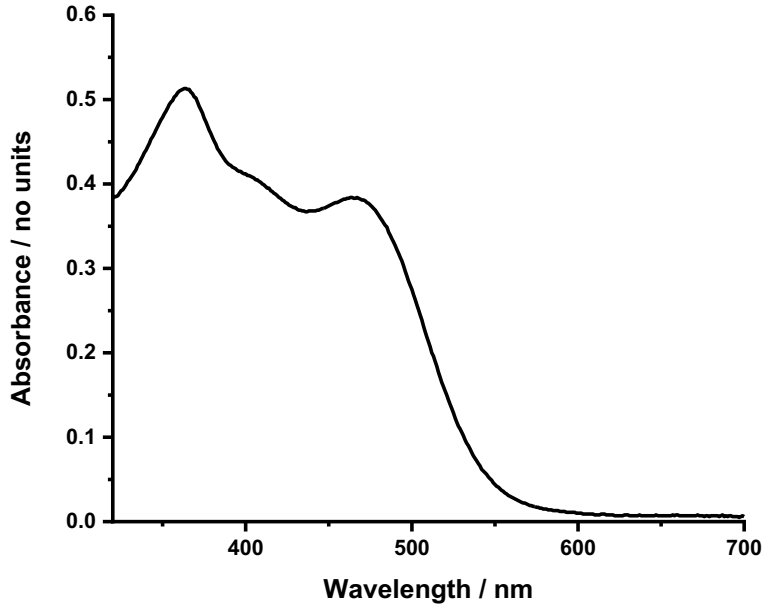

Figure 110 UV-vis spectrum, 200 μM in DMSO.

2-Chloro-3,4-dimethoxybenzoic acid, 6

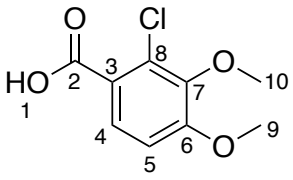

$C_9H_9ClO_4$, 216.620 g mol^{-1}

2-Chloro-3,4-dimethoxybenzoic acid was prepared following a procedure from the literature.[170]

Yield: 3.53 g, 16.3 mmol, 78%

HRMS (ESI-):

Calc. for $[C_9H_9ClO_4]$-H^+ = 215.0117 Found = 215.0114 (1.4 ppm error, 12.8 mSigma)

^{1}H NMR: (400 MHz, DMSO-*d*$_6$) δ: 13.04 (s, 1H-**1**), 7.63 (d, *J* = 9.0 Hz, 1H-**4**), 7.11 (d, *J* = 9.0 Hz, 1H-**5**), 3.88 (s, 3H-**9/10**), 3.74 (s, 3H-**9/10**).

^{13}C NMR: (101 MHz, DMSO-*d*$_6$) δ: 166.1-**2**, 156.0-**6/7**, 145.3-**6/7**, 127.2-**4+8**, 123.3-**3**, 110.8-**5**, 60.1-**9/10**, 56.3-**9/10**.

NMR spectra are in agreement with literature reports.[170]

2-Chloro-3,4-dimethoxybenzoyl chloride, 7

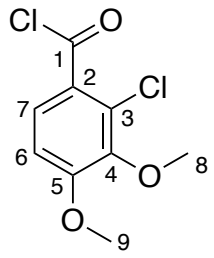

$C_9H_8Cl_2O_3$, 235.060 g mol^{-1}

2-Chloro-3,4-dimethoxybenzoyl chloride was prepared following a procedure from the literature and used crude.[171]

8-Methoxy-5-nitroquinoline, 8

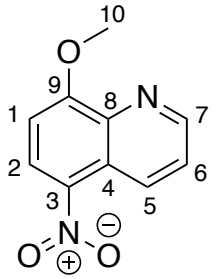

$C_{10}H_8N_2O_3$, 204.185 g mol^{-1}

To a stirred solution of 8-hydroxy-5-nitroquinoline (3.02 g, 15.9 mmol) in dry DMF (180 mL) was added potassium carbonate (2.20 g, 15.9 mmol) and iodomethane (990 μL, 15.9 mmol) at 0 °C. This solution was then heated to 50 °C and left stirring

for 18 h, after which the reaction solvent was removed *in vacuo*, The resulting residue was then re-dissolved in dichloromethane (100 mL), washed with water (100 mL), and the aqueous layer extracted with further dichloromethane (100 mL, x3). The combined organic layers were then dried *in vacuo*, and purified *via* column chromatography, eluting with dichloromethane : MeOH (19:1), to yield the title compound as a dark brown solid.

Yield: 2.72 g, 13.3 mmol, 84%

Rf: 0.64 in dichloromethane : MeOH (19:1)

HRMS (ESI+):

Calc. for $[C_{10}H_8N_2O_3]+H^+$ = 205.0608 Found = 205.0612 (-1.9 ppm error, 0.3 mSigma)

^{1}H NMR: (400 MHz, $CDCl_3$) δ 9.18 (dd, *J* = 9.0, 1.5 Hz, 1H-**5**), 8.99 (dd, *J* = 4.0, 1.5 Hz, 1H-**7**), 8.50 (d, *J* = 9.0 Hz, 1H-**2**), 7.66 (dd, *J* = 9.0, 4.0 Hz, 1H-**6**), 7.05 (d, *J* = 9.0 Hz, 1H-**1**), 4.18 (s, 3H-**10**).

^{13}C NMR: (101 MHz, $CDCl_3$) δ: 160.9-**3**, 150.3-**9**, 139.4-**8**, 137.7-**7**, 132.7-**5**, 127.7-**2**, 124.7-**6**, 123.0-**4**, 105.4-**1**, 57.0-**10**.

^{13}C NMR spectrum is in agreement with literature report.[229]

Elemental Analysis:

Calculated for $[C_{10}H_8N_2O_3 \cdot 0.2\ CH_4O \cdot 0.2\ CH_2Cl_2]$: %C 57.3, %H 4.18, %N 13.04
Measured for $[C_{10}H_8N_2O_3 \cdot 0.2\ CH_4O \cdot 0.2\ CH_2Cl_2]$: %C 57.5, %H 4.02, %N 12.83

8-methoxyquinolin-5-amine, 9

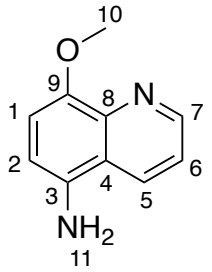

$C_{10}H_{10}N_2O$, 174.203 g mol^{-1}

To a stirred solution of 8-methoxy-5-nitroquinoline (2.35 g, 11.5 mmol) in a MeOH : THF mixture (2:1, 120 mL) was added 5% palladium on carbon (~400 mg) at room temperature. This solution was then placed under a hydrogen atmosphere and left stirring for 24 h. After this time, the reaction mixture was passed through a microfibre filter, and dried *in vacuo* to yield the title compound as a dark brown solid.

Yield: 1.89 g, 10.8 mmol, 94%

Rf: 0.18 in dichloromethane : MeOH (19:1)

HRMS (ESI+):

Calc. for $[C_{10}H_{10}N_2O]+H^+$ = 175.0866 Found = 175.0869 (-2.0 ppm error, 2.2 mSigma)

^{1}H NMR: (400 MHz, $CDCl_3$) δ: 8.93 (dt, *J* = 4.0, 1.5 Hz, 1H-**7**), 8.20 (dt, *J* = 8.5, 2.0 Hz, 1H-**5**), 7.42 (ddd, *J* = 8.5, 4.0, 2.5 Hz, 1H-**6**), 6.90 (dd, *J* = 8.0, 1.5 Hz, 1H-**1/2**), 6.78 (dd, *J* = 8.0, 2.0 Hz, 1H-**1/2**), 4.03 (d, *J* = 1.5 Hz, 3H-**10**).

NMR spectrum is in agreement with literature reports.[173]

2-Chloro-3,4-dimethoxy-*N*-(8-methoxyquinolin-5-yl)benzamide, 10

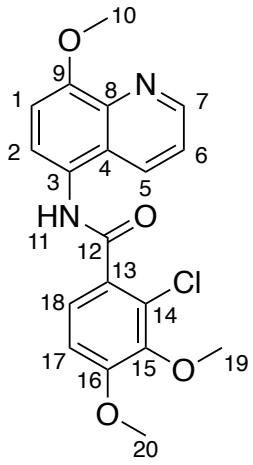

$C_{19}H_{17}ClN_2O_4$, 372.805 g mol^{-1}

To a stirred solution of 2-chloro-3,4-dimethoxybenzoyl chloride (404 mg, 1.72 mmol) in dry dichloromethane (5 mL) was added dropwise a solution of 8-methoxyquinolin-5-amine (100 mg, 574 μmol) in dry dichloromethane (10 mL) at room temperature under a nitrogen atmosphere. After stirring under these conditions for 36 h, the reaction mixture was quenched with ice-cold water (20 mL) and then dried *in vacuo*. The resulting residue was then re-dissolved in $CHCl_3$ (50 mL) and washed with sat. $NaHCO_3$(aq) (x5, 30 mL). The formed organic layer was dried *in vacuo* to give the title compound as an orange/brown solid.

Yield: 145 mg, 389 μmol, 68%

Rf: 0.36 in MeCN

HRMS (ESI+):

Calc. for $[C_{19}H_{17}ClN_2O_4]+H^+$ = 373.0950 Found = 373.0945 (1.1 ppm error, 9,7 mSigma)

^{1}H NMR: (400 MHz, DMSO-d_6) δ: 10.32 (s, 1H-**11**), 8.87 (dd, *J* = 4.0, 1.5 Hz, 1H-**7**), 8.42 (dd, *J* = 8.5, 1.5 Hz, 1H-**5**), 7.64 – 7.59 (m, 2H-**6+1**), 7.48 (d, *J* = 8.5 Hz, 1H-**18**), 7.23 (d, *J* = 8.5 Hz, 1H-**2**), 7.18 (d, *J* = 8.5 Hz, 1H-**17**), 3.98 (s, 3H-**10**), 3.91 (s, 3H-**19**), 3.81 (s, 3H-**20**).

^{13}C NMR: (101 MHz, DMSO-d_6) δ: 166.3-**12**, 154.5-**14**, 154.2-**9**, 149.5-**7**, 145.4-**13**, 140.1-**8**, 132.3-**5**, 130.4-**15**, 126.0-**16**, 125.5-**4**, 125.3-**3**, 124.8-**18**, 124.4-**1**, 122.2-**6**, 111.9-**17**, 108.2-**2**, 60.8-**20**, 56.9-**19**, 56.3-**10**.

IR ATIR (cm^{-1}): 3408 br m (Phenol O-H stretch), 3250 w (Amide N-H stretch), 2922 w (Aliphatic C-H stretch), 2846 w (Aliphatic C-H stretch),1651 s (C=O stretch), 1589 s (Aromatic C=C stretch), 1500 s (Aromatic C=C stretch).

Elemental Analysis:

Calculated for [$C_{19}H_{17}ClN_2O_4$ • 0.35 $C_6H_{18}OSi_2$]: %C 58.99, %H 5.47, %N 6.52
Measured for [$C_{19}H_{17}ClN_2O_4$ • 0.35 $C_6H_{18}OSi_2$]: %C 59.36, %H 5.42, %N 6.13

Melting Point: 185-187 °C

5-(2-Chloro-3,4-dihydroxybenzamido)-8-hydroxyquinolin-1-ium bromide, 11

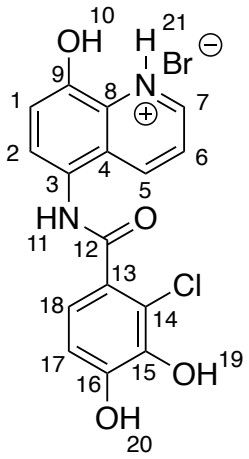

$C_{16}H_{12}BrClN_2O_4$, 411.640 g mol^{-1}

To a stirred solution of 2-chloro-3,4-dimethoxy-*N*-(8-methoxyquinolin-5-yl)benzamide (357 mg, 958 μmol) in dry dichloromethane (10 mL) was added 1M boron tribromide in dichloromethane (28.8 mL, 28.7 mmol) dropwise, at -78 °C under a nitrogen atmosphere. After stirring under these conditions for 3 d, the reaction mixture was quenched with MeOH (30 mL) and then reaction solvent co-evaporated with MeOH (x3, 20 mL), to give the title compound as a light brown/yellow solid.

Yield: 250 mg, 607 μmol, 63%

Rf: 0.36 in $CHCl_3$: MeOH : HCOOH (8:2:1)

HRMS (ESI+):

Calc. for $[C_{16}H_{12}BrClN_2O_4]+H^+$ = 331.0480 Found = 331.0476 (1.2 ppm error, 3.6 mSigma)

^{1}H NMR: (400 MHz, DMSO-*d*$_6$) δ 11.63 (br s, 1H-**10/19/20/21**), 10.45 (s, 1H-**11**), 10.16 (br s, 2H-**10/19/20/21**+**10/19/20/21**), 9.34 (br s, 1H-**10/19/20/21**), 9.10 (d, J = 4.5 Hz, 1H-**7**), 8.99 (d, J = 8.5 Hz, 1H-**5**), 8.04 (dd, J = 8.5, 5.0 Hz, 1H-**6**), 7.78 (d, J = 8.0 Hz, 1H-**2**), 7.45 (d, J = 8.0 Hz, 1H-**1**), 7.07 (d, J = 8.0 Hz, 1H-**18**), 6.88 (d, J = 8.0 Hz, 1H-**17**).

^{13}C NMR: (101 MHz, DMSO-*d*$_6$) δ: 166.6-**12**, 147.9-**16**, 147.5-**9**, 145.3-**7**, 142.3-**15**, 140.6-**5**, 130.8-**8**, 128.0-**14/16**, 126.5-**2**, 125.4-**3/4**, 125.2-**3/4**, 122.1-**5**, 119.3-**18**, 118.0-**14/16**, 114.6-**1**, 113.2-**17**.

IR ATIR (cm^{-1}): 3318 w (Amide N-H stretch), 3237 br m (Phenol O-H stretch), 2924 w (Aliphatic C-H stretch), 2885 w (Aliphatic C-H stretch),1661 s (C=O stretch), 1597 s (Aromatic C=C stretch), 1502 s (Aromatic C=C stretch).

Elemental Analysis:

Calculated for $[C_{16}H_{12}BrClN_2O_4]$: %C 46.69, %H 2.94, %N 6.81
Measured for $[C_{16}H_{12}BrClN_2O_4]$: %C 46.40, %H 3.02, %N 6.47

Melting Point: 260-261 °C

5-Nitro-8-(prop-2-en-1-yloxy)quinoline, 12

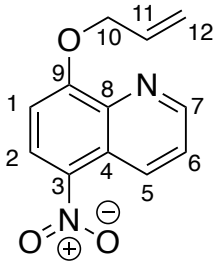

$C_{12}H_{10}N_2O_3$, 230.223 g mol^{-1}

To a solution of 5-nitro-8-hydroxyquinoline (4.00 g, 21.0 mmol) in a dry DMF (100 mL) at room temperature, was added K_2CO_3 (5.81 g, 42.1 mmol) and allyl bromide (3.64 mL, 42.1 mmol). The resulting solution was heated to 60 °C and left stirring at this temperature for 24 h. After this time, solvent was removed *in vacuo* and the residue formed, dissolved in dichloromethane (100 mL). The organic layer was washed with water (100 mL), and the aqueous layer extracted with further dichloromethane (100 mL, x3). The combined organic layer solvent was then removed in vacuo, and purified *via* column chromatography, eluting with PET : EtOAc (1:1 - 0:1), to yield the title compound as a brown solid.

Yield: 2.78 g, 12.1 mmol, 58%

Rf: 0.52 in EtOAc

HRMS (ESI+):

Calc. for $[C_{12}H_{10}N_2O_3]+H^+$ = 231.0764 Found = 231.0764 (0.1 ppm error, 3.9 mSigma)

Calc. for $[C_{12}H_{10}N_2O_3]+Na^+$ = 253.0584 Found = 253.0581 (1.1 ppm error, 9.9 mSigma)

^{1}H NMR: (400 MHz, $CDCl_3$) δ: 9.21 (dd, *J* = 9.0, 1.5 Hz, 1H-**5**), 9.03 (dd, *J* = 4.0, 1.5 Hz, 1H-**7**), 8.49 (d, *J* = 9.0 Hz, 1H-**2**), 7.68 (dd, *J* = 9.0, 4.0 Hz, 1H-**6**), 7.07 (d, *J* = 9.0 Hz, 1H-**1**), 6.18 (ddt, *J* = 17.0, 10.5, 5.5 Hz, 1H-**11**), 5.51 (dd, *J* = 17.5, 1.0 Hz, 1H-**12(trans)**), 5.41 (dd, *J* = 10.5, 1.0 Hz, 1H-**12(cis)**), 4.97 (dt, *J* = 5.5, 1.0 Hz, 2H-**10**).

NMR spectrum is in agreement with literature reports.[179]

Elemental Analysis:

Calculated for [$C_{12}H_{10}N_2O_3$ • 0.05 $C_4H_8O_2$]: %C 62.45, %H 4.47, %N 11.94
Measured for [$C_{12}H_{10}N_2O_3$ • 0.05 $C_4H_8O_2$]: %C 62.58, %H 4.37 %N 11.74

5-Amino-8-(prop-2-en-1-yloxy)quinoline, 13

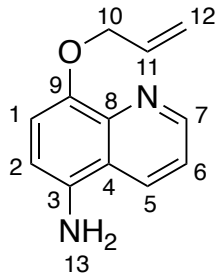

$C_{12}H_{12}N_2O$, 200.241 g mol^{-1}

To a suspension of zinc dust (7.91 g, 121 mmol) and ammonium chloride (3.23 g, 60.5 mmol) in MeOH (60 mL) was added 5-nitro-8-(prop-2-en-1-yloxy)quinoline (2.78 g, 12.1 mmol) at 0 °C. The resulting solution was allowed to slowly warm to room temperature and left stirring for 24 h. After this time, the reaction slurry was filtered, and the resulting filtrate collected and dried *in vacuo*. The resulting residue was then re-dissolved in dichloromethane (100 mL), washed with water (100 mL), and the aqueous layer extracted with further dichloromethane (100 mL, x3). The combined organic layers were then dried *in vacuo*, and purified *via* column chromatography, eluting with EtOAc, to yield the title compound as a brown solid.

Yield: 1.09 g, 5.44 mmol, 45%

Rf: 0.31 in EtOAc

HRMS (ESI+):

Calc. for [$C_{12}H_{12}N_2O$]+H^+ = 201.1022 Found = 200.1025 (-1.3 ppm error, 1.4 mSigma)

Calc. for [$C_{12}H_{12}N_2O$]+Na^+ = 223.0842 Found = 223.0844 (-0.9 ppm error, 1.4 mSigma)

^{1}H NMR: (400 MHz, $CDCl_3$) δ: 8.94 (dd, *J* = 4.0, 1.5 Hz, 1H-**7**), 8.17 (dd, *J* = 8.5, 1.5 Hz, 1H-**5**), 7.39 (dd, *J* = 8.5, 4.0 Hz, 1H-**6**), 6.92 (d, *J* = 8.0 Hz, 1H-**1**), 6.73 (d, *J* = 8.0 Hz, 1H-**2**), 6.19 (ddt, *J* = 17.0, 11.0, 5.5 Hz, 1H-**11**), 5.42 (dq, *J* = 17.5, 1.5 Hz, 1H-**12(trans)**), 5.28 (dq, *J* = 10.5, 1.5 Hz, 1H-**12(cis)**), 4.79 (dt, *J* = 5.5, 1.5 Hz, 2H-**10**), 3.86 (br s, 2H-**13**).

^{13}C NMR: (101 MHz, $CDCl_3$) δ: 149.4-**7**, 147.9-**9**, 140.9-**8**, 135.3-**3**, 133.9-**11**, 130.0-**5**, 120.6-**4**, 120.4-**6**, 118.0-**12**, 110.6-**1**, 110.2-**2**, 70.3-**10**.

IR ATIR (cm^{-1}): 3186 br m (Amine N-H stretch), 3077 w (Aromatic/Alkene C-H stretch), 2914 w (Aliphatic C-H stretch), 2864 w (Aliphatic C-H stretch), 1640 m (Alkene C=C stretch), 1609 s (Amine N-H bend), 1578 m (Aromatic C=C stretch).

Elemental Analysis:

Calculated for [$C_{12}H_{12}N_2O$ • 0.05 H_2O]: %C 71.66, %H 6.06, %N 13.93
Measured for [$C_{12}H_{12}N_2O$ • 0.05 H_2O]: %C 71.58, %H 6.01 %N 13.88

2-({[8-(Prop-2-en-1-yloxy)quinolin-5-yl]carbamoyl}methoxy)acetic acid, 14

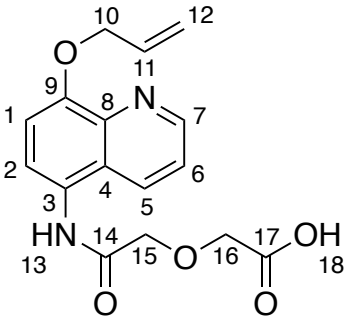

$C_{16}H_{16}N_2O_5$, 316.313 g mol^{-1}

To a stirred solution of 5-amino-8-(prop-2-en-1-yloxy)quinoline (1.09 g, 5.44 mmol) in dry dichloromethane (40 mL) was added diglycolic anhydride (631 mg, 5.44 mmol) at room temperature, and left stirring for 1 h. After this time, the reaction solvent was removed *in vacuo* and the resulting residue then triturated in Et_2O (20 mL), to yield the title compound as a light brown solid.

Yield: 900 mg, 2.85 mmol, 52%

Rf: 0.08 in EtOAc

HRMS (ESI+):

Calc. for $[C_{16}H_{16}N_2O_5]+H^+$ = 317.1132 Found = 317.1139 (-2.3 ppm error, 1.1 mSigma)

Calc. for $[C_{16}H_{16}N_2O_5]+Na^+$ = 339.0951 Found = 339.0961 (-2.9 ppm error, 10.2 mSigma)

^{1}H NMR: (400 MHz, DMSO-*d*$_6$) δ: 9.91 (s, 1H-**13**), 8.89 (d, *J* = 3.0 Hz, 1H-**7**), 8.31 (dd, *J* = 8.5, 1.5 Hz, 1H-**5**), 7.58 (dd, *J* = 8.5, 4.0 Hz, -**6**), 7.53 (d, *J* = 8.5 Hz, 1H-**2**), 7.21 (d, *J* = 8.5 Hz, 1H-**1**), 6.17 (ddt, *J* = 16.0, 10.5, 5.5 Hz, 1H-**11**), 5.59 – 5.45 (dd, *J* = 16.0, 1.5 Hz, 1H-**12(trans)**), 5.32 (d, *J* = 10.5 Hz, 1H-**12(cis)**), 4.78 (d, *J* = 5.0 Hz, 2H-**10**), 4.29 (s, 2H-**15**).4.28 (s, 2H-**16**).

^{13}C NMR: (101 MHz, DMSO-*d*$_6$) δ: 172.4-**17**, 169.5-**14**, 152.7-**9**, 149.5-**7**, 140.3-**8**, 134.2-**11**, 132.1-**5**, 125.9-**3**, 125.4-**4**, 124.0-**2**, 122.1-**6**, 118.4-**12**, 109.8-**1**, 71.0-**15**, 69.6-**10**, 68.7-**16**.

IR ATIR (cm^{-1}): 3274 br m (Carboxylic acid O-H stretch), 3066 w (Aromatic/Alkene C-H stretch), 2978 w (Aromatic/Alkene C-H stretch), 2920 w (Aliphatic C-H stretch), 1720 s (C=O stretch), 1669 s (C=O stretch), 1545 s (Aromatic C=C stretch).

Elemental Analysis:

Calculated for $[C_{16}H_{16}N_2O_5 \cdot 0.01\ H_2O]$: %C 60.41, %H 5.13, %N 8.81
Measured for $[C_{16}H_{16}N_2O_5 \cdot 0.01\ H_2O]$: %C 60.31, %H 4.94, %N 8.81

Melting Point: 198-199 °C

2-({[8-(Prop-2-en-1-yloxy)quinolin-5-yl]carbamoyl}methoxy)-*N*-(prop-2-yn-1-yl)acetamide, 15

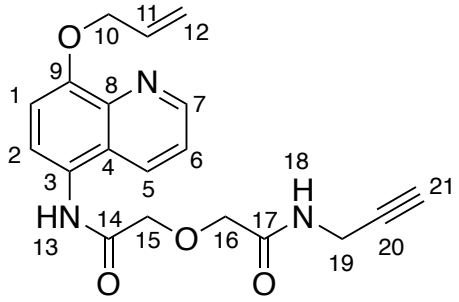

$C_{19}H_{19}N_3O_4$, 353.378 g mol^{-1}

To a stirred solution of 2-({[8-(prop-2-en-1-yloxy)quinolin-5-yl]carbamoyl}methoxy)acetic acid (100 mg, 31.6 μmol) in dry DMF (5 mL) was added *N′*-ethylcarbodiimide hydrochloride (92 mg, 47.4 μmol), 1-hydroxybenzotriazole monohydrate (74 mg, 47.4 μmol), DIPEA (16 μL, 47.4 μmol) and then propargyl amine (21 μL, 33.2 μmol) at room temperature. After stirring at room temperature for 18 h, the reaction solvent was removed *in vacuo* and the resulting residue was re-dissolved in $CHCl_3$ (30 mL), washed with sat. $NaHCO_3$(aq) (20 mL, x3), sat. NH_4Cl(aq) (20 mL, x3), water (20 mL, x3) and then brine (20 mL, x3). The organic layer was dried *in vacuo*, and purified *via* column chromatography, eluting with $CHCl_3$: MeOH : NH_3 (96 : 4: 1), to yield the title compound as a light beige/pink solid.

Yield: 42 mg, 11.9 μmol, 38%

Rf: 0.34 in $CHCl_3$: MeOH (19:1)

HRMS (ESI+):

Calc. for $[C_{19}H_{19}N_3O_4]+H^+$ = 354.1448 Found = 354.1454 (-1.7 ppm error, 2.0 mSigma)

Calc. for $[C_{19}H_{19}N_3O_4]+Na^+$ = 376.1268 Found = 376.1273 (-1.4 ppm error, 21.1 mSigma)

^{1}H NMR: (400 MHz, $CDCl_3$) δ: 8.95 – 8.81 (m, 1H-**7**), 8.69 (s, 1H-**13**), 7.92 (dd, *J* = 8.5, 1.5 Hz, 1H-**5**), 7.72 (t, *J* = 5.0 Hz, 1H-**18**), 7.42 (d, *J* = 8.5 Hz, 1H-**2**), 7.33 (dd, *J* = 8.5, 4.0 Hz, 1H-**6**), 6.90 (d, *J* = 8.5 Hz, 1H-**1**), 6.15 (ddt, *J* = 23.0, 11.0, 5.5 Hz, 1H-**11**), 5.45 (dd, *J* = 17.5, 1.0 Hz, 1H-**12(trans)**), 5.33 (dd, *J* = 10.5, 1.0 Hz, 1H-**12(cis)**), 4.77 (d, *J* = 5.5 Hz, 2H-**10**), 4.20 (s, 2H-**15**), 4.16 (s, 2H-**16**), 4.06 (dd, *J* = 5.5, 2.5 Hz, 2H-**19**), 2.18 (t, *J* = 2.5 Hz, 1H-**21**).

^{13}C NMR: (101 MHz, $CDCl_3$) δ: 168.5-**17**, 168.0-**14**, 152.9-**9**, 149.2-**7**, 140.0-**8**, 132.8-**11**, 130.6-**5**, 124.7-**3**, 123.7-**4**, 123.4-**2**, 121.9-**6**, 118.9-**12**, 108.7-**1**, 79.4-**21**, 71.5-**20**, 71.4-**15**, 71.1-**16**, 70.0-**10**, 28.7-**19**.

IR ATIR (cm^{-1}): 3272 br m (Amide N-H stretch), 3078 w (Aromatic/Alkene C-H stretch), 2920 w (Aliphatic C-H stretch), 2854 w (Aliphatic C-H stretch), 1684 s (C=O stretch), 1663 s (C=O stretch), 1616 m (Alkene C=C stretch), 1504 s (Aromatic C=C stretch).

Elemental Analysis:

Calculated for [$C_{19}H_{19}N_3O_4$ • 0.2 CH_4O • 0.05 $CHCl_3$ • 0.05 H_2O]: %C 63.06, %H 5.48, %N 11.46
Measured for [$C_{19}H_{19}N_3O_4$ • 0.2 CH_4O • 0.05 $CHCl_3$ • 0.05 H_2O]: %C 63.17, %H 5.22, %N 11.19

Melting Point: 154-156 °C

2,3-Bis(acetyloxy)benzoic acid, 16

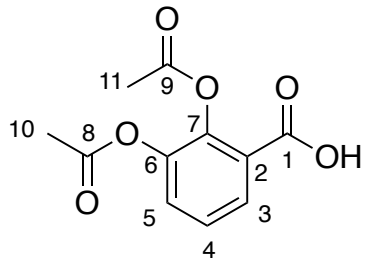

$C_{11}H_{10}O_6$, 238.195 g mol^{-1}

2,3-Bis(acetyloxy)benzoic acid was prepared following a procedure from the literature.[183]

Yield: 7.42 g, 31.2 mmol, 96%

Rf: 0.87 in dichloromethane : MeOH (9:1)

HRMS (ESI+):

Calc. for $[C_{11}H_{10}O_6]+Na^+$ = 261.0370 Found = 261.0365 (1.6 ppm error, 2.4 mSigma)

^{1}H NMR: (400 MHz, $CDCl_3$) δ: 7.99 (dd, *J* = 8.0, 1.5 Hz, 1H-**3**), 7.44 (dd, *J* = 8.0, 1.5 Hz, 1H-**5**), 7.36 (t, *J* = 8 Hz, 1H-**4**), 2.34 (s, 3H-**10**/**11**), 2.23 (s, 3H-**10**/**11**).

^{13}C NMR: (101 MHz, $CDCl_3$) δ: 168.8-**8**/**9**, 168.6-**1**, 168.4-**8**/**9**, 143.8-**2**, 143.3-**7**, 129.8-**3**, 128.9-**5**, 126.4-**4**, 124.0-**6**, 20.8-**10**+**11**.

NMR spectra are in agreement with literature reports.[183]

2-(Acetyloxy)-6-[(2-{[(*tert*-butoxy)carbonyl]amino}ethyl)carbamoyl]phenyl acetate, 17

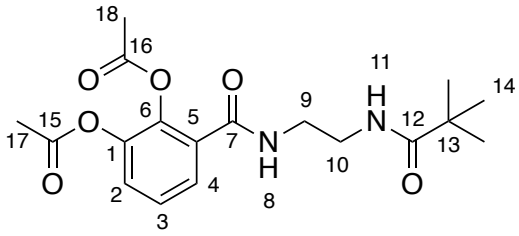

$C_{18}H_{24}N_2O_7$, 380.397 g mol^{-1}

2,3-Bis(acetyloxy)benzoic acid (200 mg, 0.840 mmol) was dissolved in oxalyl chloride (2 mL) under a nitrogen atmosphere and left stirring at room temperature for 3 h. After this time, the oxalyl chloride was removed *in vacuo*. The resulting solid was re-dissolved in dry dichloromethane (2 mL) and to this solution, was added a solution of *N*-boc-1,2-diaminoethane (121 μL, 0.764 mmol) and DIPEA (27 μL, 0.84 mmol) in dry dichloromethane (1 mL) at 0 °C, dropwise over 10 min. The reaction mixture was left to stir at room temperature for 14 h. After this time, dichloromethane (30 mL) was added, and the organic layers were washed with water (30 mL, x3). The resulting organic layer solvent was removed *in vacuo* and purified *via* column

chromatography, eluting with EtOAc : PET (7:3). The resulting solid was then triturated in PET and filtered to yield the title compound as a white solid.

Yield: 41 mg, 108 μmol, 13%

Rf: 0.40 in EtOAc : PET (7:3)

HRMS (ESI+):

Calc. for $[C_{18}H_{24}N_2O_7]+H^+$ = 381.1656 Found = 381.1659 (-0.6 ppm error, 5.9 mSigma)

^{1}H NMR: (400 MHz, $CDCl_3$) δ: 7.52 (dd, *J* = 6.0, 3.5 Hz, 1H-**4**), 7.25 (m, 1H-**2/3**), 7.42 (m, 1H-**2/3**), 6.71 (br s, 1H-**8**), 5.00 (br s, 1H-**11**), 3.45 (q, *J* = 5.5 Hz, 2H-**9**), 3.29 (q, *J* = 5.5 Hz, 2H-**10**), 2.29 (s, 3H-**17/18**), 2.27 (s, 3H-**17/18**), 1.39 (s, 9H-**14**).

^{13}C NMR: (101 MHz, $CDCl_3$) δ: 168.4-**15/16**, 168.3-**15/16**, 165.9-**7**, 156.8-**12**, 143.1-**4**, 140.4-**5**, 130.3-**1**, 126.6-**2/3**, 126.4-**4**, 125.9-**2/3**, 41.0-**9**, 40.3-**10**, 28.5-**13**, 20.8-**14**.

NMR spectra are in agreement with literature reports.[182]

Tert-butyl *N*-{2-[(2,3-dihydroxyphenyl)formamido]ethyl}carbamate, 18

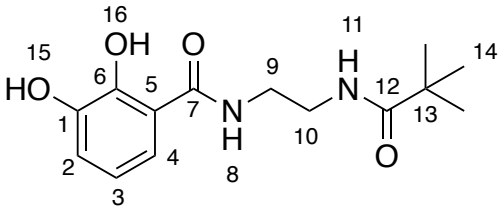

$C_{14}H_{20}N_2O_5$, 296.323 g mol^{-1}

To a solution of *tert*-butyl *N*-(2-{[2,3-bis(benzyloxy)phenyl]formamido}ethyl)carbamate (59 mg, 0.21 mmol) in 1:1 THF : MeOH (40 mL), was added 5% w/w Pd/C (~ 5 mg). The reaction vessel was then placed under a hydrogen atmosphere and left stirring for 16 h, at room temperature. After this time, the reaction mixture was

filtered through microfibre filter paper and the filtrate solvent removed *in vacuo*, to yield the title compound as a white solid.

Yield: 35 mg, 118 μmol, 95%

Rf: 0.56 in dichloromethane : MeOH (9:1)

HRMS (ESI+):

Calc. for $[C_{14}H_{20}N_2O_5]+Na^+$ = 319.1264 Found = 319.1266 (-0.5 ppm error, 2.0 mSigma)

^{1}H NMR: (400 MHz, $CDCl_3$) δ: 12.83 (br s, 1H-**16**), 7.81 (brs,1H-**8**), 7.00 (d, *J* = 8.0 Hz, 2H-**2+4**), 6.74 (t, *J* = 8.0 Hz, 1H-**3**), 5.05 (m, 1H-**11**), 3.52 (q, *J* = 5.0 Hz, 2H-**9**), 3.43 (q, *J* = 5.0 Hz, 2H-**10**), 1.43 (s, 9H-**14**).

^{13}C NMR: (101 MHz, $CDCl_3$) δ: 170.7-**7**, 158.2-**12**, 149.3-**5**, 145.8-**6**, 118.7-**3**, 118.1-**2**/**4**, 116.8-**2**/**4**, 114.0-**1**, 42.6-**9**, 39.6-**10**, 30.4-**13**, 28.4-**14**.

NMR spectra are in agreement with literature reports.[184]

2-{[(*Tert*-butoxy)carbonyl]amino}acetyl 2-{[(*tert*-butoxy)carbonyl]-amino}acetate, 19

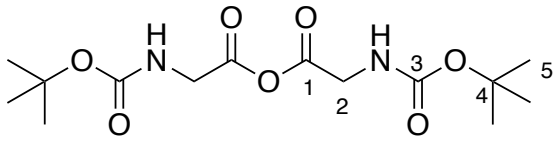

$C_{14}H_{24}N_2O_7$, 332.353 g mol^{-1}

2-{[(*Tert*-butoxy)carbonyl]amino}acetyl 2-{[(*tert*-butoxy)carbonyl]amino}acetate was prepared following a procedure from the literature and used immediately for the synthesis of *tert*-butyl *N*-{[(8-hydroxyquinolin-5-yl)carbamoyl]methyl}carbamate, without characterisation.[187]

2,3-Bis(acetyloxy)benzoyl 2,3-bis(acetyloxy)benzoate, 20

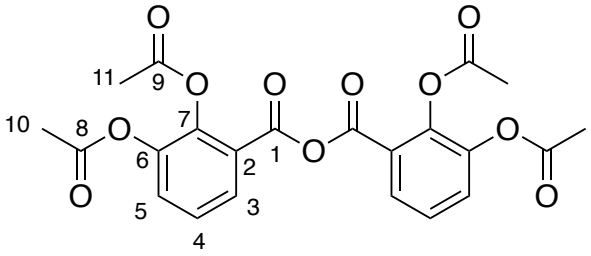

$C_{22}H_{18}O_{11}$, 458.375 g mol^{-1}

2,3-Bis(acetyloxy)benzoyl 2,3-bis(acetyloxy)benzoate was prepared based on a procedure from the literature and used immediately for the synthesis of 2-(acetyloxy)-3-[({[8-(prop-2-en-1-yloxy)quinolin-5-yl]carbamoyl} methyl)carbamoyl]-phenyl acetate, without characterisation.[187]

To a solution of 2,3-bis(acetyloxy)benzoic acid (370 mg, 1.55 mmol) in dry dichloromethane (15 mL), was added dicyclohexylcarbodiimide (160 mg, 0.780 mmol) at room temperature under a nitrogen atmosphere and left stirring for 1 h. After this time, the resulting suspension was filtered, and the filtrate solvent was removed *in vacuo*. The resulting white solid was used immediately for the synthesis of 2-(acetyloxy)-3-[({[8-(prop-2-en-1-yloxy)quinolin-5-yl]carbamoyl} methyl)carbamoyl]phenyl acetate.

5-Azaniumyl-8-hydroxyquinolin-1-ium dichloride, 21

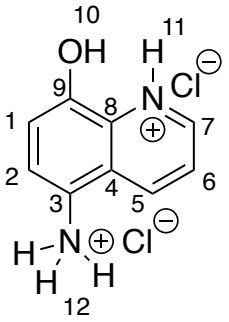

$C_9H_{10}ON_2Cl$, 233.09 g mol^{-1}

5-Azaniumyl-8-hydroxyquinolin-1-ium dichloride was prepared following a procedure from the literature.[188]

Yield: 361 mg, 1.55 mmol, 98%

Rf: 0.67 in dichloromethane : MeOH (9:1)

HRMS (ESI+):

Calc. for $[C_9H_{10}ON_2Cl]+H^+$ = 161.0709 Found = 161.0708 (0.9 ppm error, 5.1 mSigma)

^{1}H NMR: (400 MHz, D_2O) δ: 9.12 – 9.01 (m, 2H-**5+7**), 8.21 – 8.07 (m, 1H-**6**), 7.71 (d, *J* = 8.0 Hz, 1H-**2**), 7.38 (d, *J* = 8.4 Hz, 1H-**1**).

^{13}C NMR: (101 MHz, D_2O) δ: 147.5-**9**, 143.9-**5/7**, 140.7-**5/7**, 129.4-**8**, 125.0-**2**, 123.9-**4**, 123.0-**6**, 119.8-**3**, 115.7-**1**.

Tert-butyl *N*-{[(8-hydroxyquinolin-5-yl)carbamoyl]methyl}carbamate, 22

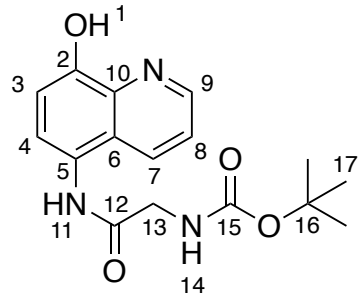

$C_{16}H_{19}N_3O_4$, 317.345 g mol^{-1}

To a solution of 5-amino-8-hydroxyquinoline dihydrochloride (1.00 g, 4.29 mmol) and DIPEA (2.39 mL, 13.7 mmol) in dry DMF, was added 2-{[(*tert*-butoxy)carbonyl]amino}acetyl 2-{[(*tert*-butoxy)carbonyl]amino}acetate (2.16 g, 7.75 mmol) dropwise over 30 min at 0 °C under a nitrogen atmosphere. The reaction mixture was then stirred for 2 d at room temperature. After this time, the mixture was quenched with water (10 mL) and the solvent removed *in vacuo*. The resulting solid was re-dissolved in EtOAc (70 mL) and washed with $NaHCO_3$ (aq) (30 mL, x3) and then water (30 mL, x3). The organic layer solvent was then removed *in vacuo*, to yield the title compound crude, as a green solid.

Yield: 2.29 g, 7.22 mmol, 93% (crude)

Rf: 0.24 in dichloromethane : MeOH : DIPEA (95:15:1)

HRMS (ESI+):

Calc. for $[C_{16}H_{19}N_3O_4]+H^+$ = 318.1448 Found = 318.1443 (1.6 ppm error, 2.0 mSigma)

Calc. for $[C_{16}H_{19}N_3O_4]+Na^+$ = 340.1268 Found = 340.1267 (0.3 ppm error, 1.8 mSigma)

^{1}H NMR: (400 MHz, $CDCl_3$) δ: 8.73 (d, *J* = 4.5 Hz, 1H-**9**), 8.52 (br s, 1H-**11**), 8.16 (d, *J* = 7.0 Hz, 1H-**7**), 7.61 – 7.50 (m, 1H-**4**), 7.37 (dd, *J* = 9.0, 4.0 Hz, 1H-**8**), 7.07 (d, *J* = 8.0 Hz, 1H-**3**), 5.58 – 5.41 (m, 1H-**14**), 4.03 (d, *J* = 6.0 Hz, 1H-**13**), 1.49 (s, 9H-**17**).

^{13}C NMR: (101 MHz, $CDCl_3$) δ: 169.4-**12**, 157.0-**15**, 151.0-**2**, 148.0-**9**, 138.2-**10**, 131.7-**7**, 124.2-**4**, 124.0-**5**, 123.1-**3**, 122.0-**6**, 109.4, 81.0-**13**, 45.6-**16**, 28.5-**17**.

IR ATIR (cm^{-1}): 3322 m (O-H stretch), 3233 m (N-H stretch), 2978 m (Aromatic/Alkene C-H stretch), 2930 m (Alkane C-H stretch), 2801 w (Alkane C-H stretch), 1715 s (C=O stretch), 1691 s (C=O stretch).

Tert-butyl *N*-({[8-(prop-2-en-1-yloxy)quinolin-5-yl]carbamoyl}methyl)carbamate, 23

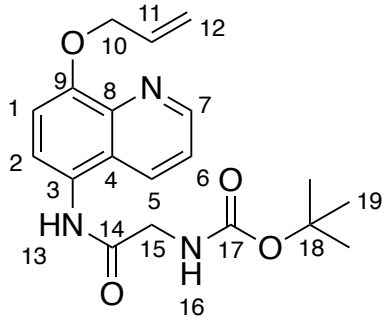

$C_{19}H_{23}O_3N_4$, 357.410 g mol^{-1}

To a stirring solution of crude *tert*-butyl *N*-{[(8-hydroxyquinolin-5-yl)carbamoyl]methyl}-carbamate (28.3 mmol, 8.98 g) in dry DMF (50 mL), was added potassium carbonate (12.4 mmol, 1.71 g) and allyl bromide (12.4 mmol, 1.07

mL) portion-wise, at room temperature. This reaction mixture was then heated to 50 °C and left stirring for 18 h. After this time, reaction solvent was removed *in vacuo* and the residue re-dissolved in dichloromethane (100 mL). This solution was then washed with $NaHCO_3$ (aq) (50 mL, x2) and water (50 mL, x2). The organic layers were combined, and the solvent removed *in vacuo*. The resulting residue was purified *via* column chromatography, eluting with EtOAc : NEt_3 (99:1) and then hot filtration in EtOAc, to yield the title compound as a beige crystalline solid.

Yield: 1.41 g, 3.95 mmol, 14%

Rf: 0.82 in dichloromethane : MeOH (19:1)

HRMS (ESI+):

Calc. for $[C_{19}H_{23}O_3N_4]+H^+$ = 358.1761 Found = 358.1762 (-0.2 ppm error, 0.3 mSigma)

^{1}H NMR: (400 MHz, $CDCl_3$) δ: 8.92 (dd, *J* = 4.0, 2.0 Hz, 1H-**7**), 8.74 (br s, 1H-**13**), 8.21 (d, *J* = 8.5 Hz, 1H-**5**), 7.63 (d, *J* = 8.5 Hz, 1H-**2**), 7.38 (dd, *J* = 8.5, 4.0 Hz, 1H-**6**), 6.98 (dd, *J* = 8.0 Hz, 1H-**1**), 6.15 (ddt, *J* = 16.0, 10.5, 5.5 Hz, 1H-**11**), 5.58 (t, *J* = 6.0 Hz, 1H-**16**), 5.44 (dd, *J* = 17.5, 1.5 Hz, 1H-**12(trans)**), 5.31 (dd, *J* = 10.5, 1.0 Hz, 1H-**12(cis)**), 4.82 (d, *J* = 5.5 Hz, 2H)-**10**, 4.04 (d, *J* = 6.0 Hz, 2H-**15**), 1.47 (s, 9H-**19**).

^{13}C NMR: (101 MHz, $CDCl_3$) δ: 169.4-**14/17**, 157.0-**14/17**, 152.6-**9**, 149.2-**7**, 140.1-**4**, 133.0-**11**, 130.9-**8**, 124.6-**5**, 122.8-**6**, 121.7-**2**, 118.7-**12**, 108.9-**1**, 81.0-**15**, 70.05-**10**, 45.6-**18**, 28.4-**19**.

IR ATIR (cm^{-1}): 3220 m (Amide N-H stretch), 3019 m (Aromatic/Alkene C-H stretch), 2976 m (Aromatic C-H stretch), 1700 s (C=O stretch), 1657 s (C=O stretch), 1618 s (Alkene C=C stretch), 1537 s (Aromatic C=C stretch).

Elemental Analysis:

Calculated for $[C_{19}H_{23}O_3N_4 \cdot 0.05\ H_2O \cdot 0.05\ C_4H_8O_2]$: %C 63.58, %H 6.53, %N 11.58

Measured for [$C_{19}H_{23}O_3N_4$ • 0.05 H_2O • 0.05 $C_4H_8O_2$]: %C 63.53, %H 6.37, %N 11.43

Melting Point: 149 – 151 °C

5-(2-Azaniumylacetamido)-8-(prop-2-en-1-yloxy)quinolin-1-ium ditrifluoroacetate, 24

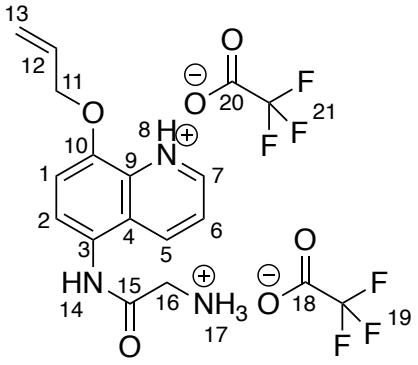

$C_{18}H_{17}F_6N_3O_6$, 485.339 g mol^{-1}

To a solution of *tert*-butyl *N*-({[8-(prop-2-en-1-yloxy)quinolin-5-yl]carbamoyl}-methyl)carbamate (1.129 mmol, 426 mg) in dichloromethane (20 mL), was added TFA (2 mL) at 0 °C. This solution was stirred for 5 h and allowed to warm to room temperature. The reaction solvent was removed *in vacuo* by azeotroping with MeOH (10 mL, x3) and the resulting residue triturated with Et_2O and filtered, to yield the title compound as a beige solid.

Yield: 440 mg, 1.185 mmol, 99%

Rf: 0.45 in dichloromethane : MeOH (8:2) with 1% NH_3 (aq)

HRMS (ESI+):

Calc. for [$C_{14}H_{15}N_3O_2$]+H^+ = 258.1237 Found = 258.1236 (0.3 ppm error, 3.0 mSigma)

Calc. for [$C_{14}H_{15}N_3O_2$]+Na^+ = 280.1056 Found = 280.1055 (0.5 ppm error, 9.4 mSigma)

^{1}H NMR: (400 MHz, DMSO-d_6) δ: 10.42 (s, 1H-**14**), 8.95 (dd, *J* = 4.0, 1.5 Hz, 1H-**7**), 8.52 (d, *J* = 8.5 Hz, 1H-**5**), 8.22 (brs, 3H-**17**), 7.68 (dd, *J* = 8.5, 4.0 Hz, 1H-**6**), 7.60 (d, *J* = 8.5 Hz, 1H-**2**), 7.29 (d, *J* = 8.5 Hz, 1H-**1**), 6.17 (ddt, *J* = 17.0, 10.5, 5.5 Hz, 1H-**12**), 5.52 (dd, *J* = 17.5, 1.5 Hz, 1H-**13(trans)**), 5.33 (dd, *J* = 10.5, 1.5 Hz, 1H-**13(cis)**), 4.81 (d, *J* = 5.5 Hz, 2H-**11**), 3.95 (d, *J* = 5.0 Hz, 2H-**16**).

^{19}F NMR: (376 MHz, MeOD-d_4) δ: -76.8 (s, 6F-**19+21**).

^{13}C NMR: (101 MHz, DMSO-d_6) δ: 166.1-**15**, 158.3 (q, *J* = 34.0 Hz)-**18**/**20**, 151.6-**10**, 148.7-**7**, 138.5-**9**, 133.5-**12**, 132.9-**5**, 125.1-**3**, 124.6-**4**, 123.3-**2**, 121.8-**6**, 118.0-**13**, 109.9-**1**, 69.3-**11**, 40.8-**16**.

IR ATIR (cm^{-1}): 3219 w (N-H stretch), 3050 m (Aromatic/Alkene C-H stretch), 1684 s (C=O stretch), 1671 s (C=O stretch), 1595 w (Aromatic C=C stretch).

Elemental Analysis:

Calculated for [$C_{14}H_{15}N_3O_2$ • 1.9 $C_2HF_3O_2$ • 0.1 $C_4H_{10}O$]: %C 45.79, %H 3.60, %N 8.85
Measured for [$C_{14}H_{15}N_3O_2$ • 1.9 $C_2HF_3O_2$ • 0.1 $C_4H_{10}O$]: %C 45.84, %H 3.61, %N 8.90

Melting Point: 182 – 184 °C

2-(Acetyloxy)-3-[({[8-(prop-2-en-1-yloxy)quinolin-5-yl]carbamoyl} methyl)carbamoyl]phenyl acetate, 25

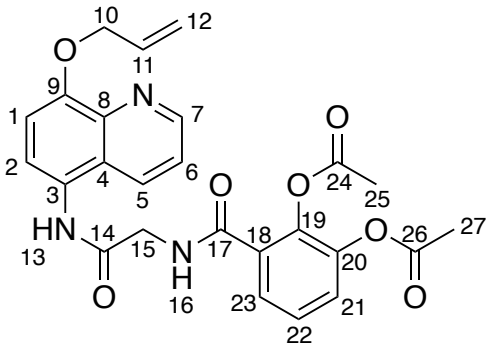

$C_{25}H_{23}N_3O_7$, 477.473 g mol^{-1}

To a stirred solution of 5-(2-azaniumylacetamido)-8-(prop-2-en-1-yloxy)quinolin-1-ium ditrifluoroacetate (100 mg, 0.206 mmol) in dry DMF (20 mL) was added two molar equivalents of crude 2,3-bis(acetyloxy)benzoyl 2,3-bis(acetyloxy)benzoate as a solution in dry dichloromethane (20 mL), dropwise over 30 min, under a nitrogen atmosphere at room temperature. After stirring under these conditions for 3 h, water (10 mL) was added to quench and the solvent removed *in vacuo*. The resulting solid residue was then re-dissolved in EtOAc (30 mL) and washed with water (30 mL, x5). The resulting organic layer solvent was removed *in vacuo* and purified *via* column chromatography, eluting with $CHCl_3$ in MeCN gradient (6:4 - 1:1) and then triturated with Et_2O, to yield the title compound as a beige solid.

Yield: 58 mg, 121 μmol, 45%

Rf: 0.23 in $CHCl_3$: MeCN (6:4)

HRMS (ESI+):

Calc. for $[C_{25}H_{24}O_3N_7]+H^+$ = 478.1609 Found = 478.1616 (-1.6 ppm error, 35.1 mSigma)

^{1}H NMR: (400 MHz, $CDCl_3$) δ: 9.00 (br s, 1H-**13**), 8.89 (dd, *J* = 4.0, 1.5 Hz, 1H-**7**), 8.22 (dd, *J* = 8.5, 1.0 Hz, 1H-**5**), 7.78 (t, *J* = 5.0 Hz, 1H-**16**), 7.62 (dd, J = 7.5, 1.5 Hz, 1H-**21**/**23**), 7.59 (d, J = 8.5 Hz, 1H-**2**), 7.34 – 7.28 (m, 3H-**6**+**21**/**23**), 7.22 (t, *J* = 8.0 Hz, 1H-**22**), 6.98 (d, *J* = 8.5 Hz, 1H-**1**), 6.17 (ddt, *J* = 16.0, 10.5, 5.5 Hz, 1H-**11**), 5.45 (dd, *J* = 17.5, 1.5 Hz, 1H-**12(trans)**), 5.32 (dd, *J* = 10.5, 1.5 Hz, 1H-**12(cis)**), 4.82 (d, *J* = 5.5 Hz, 2H-**10**), 4.44 (d, *J* = 5.0 Hz, 2H-**15**), 2.28 (s, 3H-**25/27**), 2.24 (s, 3H- **25/27**).

^{13}C NMR: (101 MHz, $CDCl_3$) δ: 168.5-**14**, 168.3-**24**+**26**, 165.8-**17**, 152.9-**9**, 149.4-**7**, 143.0-**19**, 140.5-**3**, 140.3-**20**, 133.0-**11**, 131.1-**5**, 128.8-**8**, 127.2-**21/23**, 126.7-**21/23**, 126.7-**22**, 124.8-**4**, 124.6-**18**, 123.1-**2**, 121.9-**6**, 118.7-**12**, 108.7-**1**, 70.1-**15**, 44.6-**10**, 20.8-**25**/**27**, 20.7-**25**/**27**.

IR ATIR (cm^{-1}): 3270 w (Amide N-H stretch), 2924 w (Aromatic/Alkene C-H stretch), 2854 w (Alkane C-H stretch), 1766 s (C=O stretch), 1655 m (Alkene C=C stretch), 1525 (Aromatic C=C stretch).

Elemental Analysis:

Calculated for [$C_{25}H_{23}N_3O_7$ • 0.45 CH_2Cl_2 • 0.55 $C_4H_{10}O$]: %C 59.68, %H 5.33, %N 7.55

Measured for [$C_{25}H_{23}N_3O_7$ • 0.45 CH_2Cl_2 • 0.55 $C_4H_{10}O$]: %C 59.95, %H 4.89, %N 7.13

Ru-s2

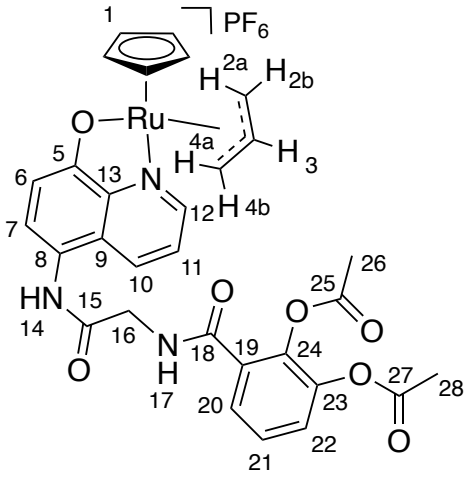

$C_{30}H_{28}F_6N_3O_7PRu$, 788.602 g mol^{-1}

To a solution of tris(acetonitrile)cyclopentadienylruthenium(II) hexafluorophosphate (26 mg, 59.9 μmol) in dry, degassed dichloromethane (20 mL), was added 2(acetyloxy)-3-[({[8-(prop-2-en-1-yloxy)quinolin-5-yl]carbamoyl}methyl)carbamoyl] phenyl acetate (29 mg, 59.9 μmol) in dry, degassed dichloromethane (4 mL) under a dry, nitrogen atmosphere at room temperature to form, at first a dark red solution which turned to a light red solution over 2 min. After stirring under these conditions for 1 h, the reaction suspension was allowed to settle under gravity and the clear, orange supernatant was removed. The remaining solid was washed with dry dichloromethane (1 mL, x3) to yield the title compound as dark brown solid.

Yield: 27 mg, 41.4 μmol, 69%

HRMS (LIFDI):

Calc. for $[C_{30}H_{28}N_3O_7Ru]^+$ = 644.09653 Found = 644.09966 (4.87 ppm error, 18.5 DBE)

^{1}H NMR: (400 MHz, acetone-d_6) δ: 9.17 (s, 1H-**14**), 8.96 (d, *J* = 5.0 Hz, 1H-**12**), 8.50 (d, *J* = 8.5 Hz, 1H-**10**), 8.02 (t, *J* = 4.5 Hz, 1H-**17**), 7.75 (dd, *J* = 5.5, 4.0 Hz, 1H-**20**), 7.60 (dd, *J* = 8.5, 5.0 Hz, 1H-**11**), 7.43 – 7.39 (m, 2H-**21**+**22**), 7.38 (d, *J* = 8.5 Hz, 1H-**6**), 6.90 (d, *J* = 8.5 Hz, 1H-**7**), 6.30 (s, 5H-**1**), 4.75 – 4.62 (m, 2H-**3+2a/4a^{1}**), 4.40 (d, *J* = 10.0 Hz, 1H-**2a/4a^{2}**), 4.36 (dd, *J* = 6.0, 3.0 Hz, 1H-**2b/4b^{2}**), 4.30 (d, *J* = 5.5 Hz, 2H-**16**), 4.18 (dd, *J* = 6.0, 3.0 Hz, 1H-**2b/4b^{1}**), 2.30 (s, 3H-**26/28**), 2.28 (s, 3H-**26/28**).

^{13}C NMR: (126 MHz, acetone-d_6) δ: 169.6-**15**, 169.1-**5**, 168.8-**25/27**, 168.8-**25/27**, 165.8-**18**, 156.3-**12**, 146.3-**9**, 144.4-**19**, 141.7-**23**, 137.3-**10**, 130.8-**24**, 128.4-**6**, 127.6-**20**, 127.5-**13**, 127.1-**21/22**, 127.1-**21/22**, 124.2-**11**, 119.9-**8**, 115.1-**7**, 99.5-**3**, 97.0-**1**, 70.0-**2/4**, 63.6-**2/4**, 44.4-**16**, 20.7-**26/28**, 20.5-**26/28**.

^{19}F NMR: (565 MHz, acetone-d_6) δ: -72.5 (d, *J* = 707.5 Hz, 6F).

^{19}P NMR: (243 MHz, acetone-d_6) δ: -144.3 (sp, *J* = 707.0 Hz, 1P).

IR ATIR (cm^{-1}): 3393 w br (Amide N-H stretch), 3117 w br (Aromatic/Alkene C-H stretch), 2964 m (Aromatic/Alkene C-H stretch), 2912 w (Aromatic/Alkene C-H stretch), 2801 w (Alkane C-H stretch), 1769 s (C=O stretch), 1696 s (C=O stretch), 1660 s (Alkene C=C stretch), w 1573 (Aromatic C=C stretch).

Elemental Analysis:

Calculated for [$C_{30}H_{28}F_6N_3O_7PRu$ • 2 CH_2Cl_2]: %C 40.10, %H 3.37, %N 4.38
Measured for [$C_{30}H_{28}F_6N_3O_7PRu$ • 2 CH_2Cl_2]: %C 39.71, %H 3.37, %N 3.93

UV-vis Spectroscopy:

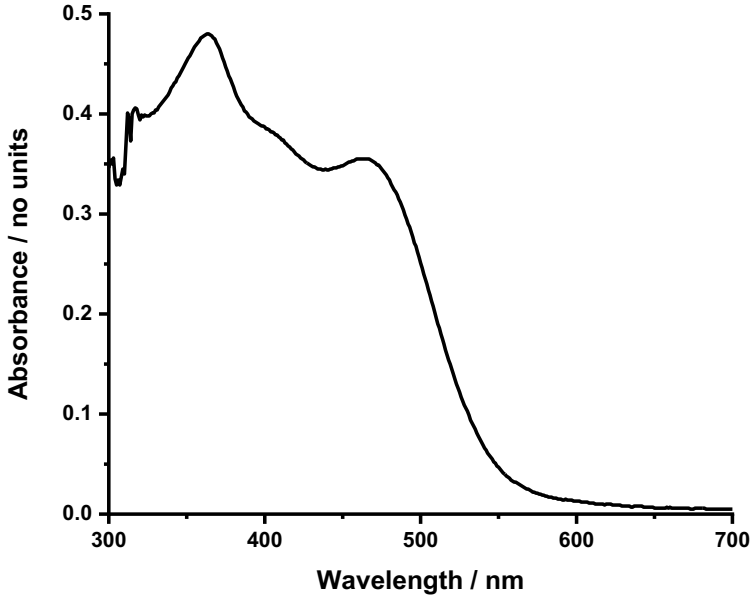

Figure 111 UV-vis spectrum, 200 μM in DMSO.

2-[(2,3-Dihydroxyphenyl)formamido]-*N*-[8-(prop-2-en-1-yloxy) quinolin-5-yl]acetamide, 26

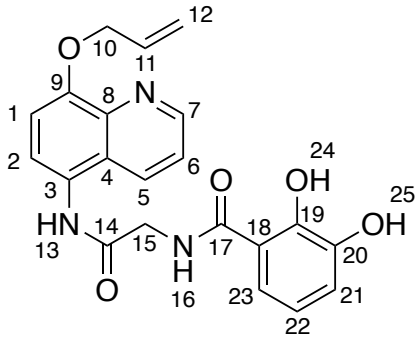

$C_{21}H_{19}N_3O_5$, 393.40 g mol^{-1}

To a stirred solution of 2-(acetyloxy)-3-[({[8-(prop-2-en-1-yloxy)quinolin-5-yl]carbamoyl}methyl)carbamoyl]phenyl acetate (111 mg, 0.232 mmol) in dry dichloromethane (3 mL) at 0 °C was added piperidine (138 μL, 1.40 mmol), and the resulting mixture was left stirring for 45 min. After this time, the solvent was removed *in vacuo* and the resulting residue was triturated in Et_2O (10 mL), and then washed with dichloromethane (x3, 5 mL) to yield the title compound as a white solid.

Yield: 87 mg, 221 μmol, 95%

Rf: 0.56 in dichloromethane : MeOH (4:1)

HRMS (ESI-):

Calc. for $[C_{21}H_{19}N_3O_5]$-H^+ = 392.1252 Found = 392.1257 (-1.4 ppm error, 1.9 mSigma)

^{1}H NMR: (600 MHz, DMSO-*d*$_6$) δ: 16.17 – 15.95 (br s, 1H-**24**), 10.02 (s, 1H-**13**), 9.37 (s, 1H-**25**), 8.88 (dd, *J* = 4.0, 1.5 Hz, 1H-**7**), 8.39 (dd, *J* = 8.5, 1.5 Hz, 1H-**5**), 7.59 (dd, *J* = 8.5, 4.0 Hz, 1H-**6**), 7.51 (d, *J* = 8.5 Hz, 1H-**1**), 7.34 (d, *J* = 8.0 Hz, 1H-**23**), 7.20 (d, *J* = 8.5 Hz, 1H-**2**), 6.90 (d, *J* = 7.5 Hz, 1H-**21**), 6.66 (br s, 1H-**22**), 6.16 (ddd, *J* = 22.5, 10.5, 5.5 Hz, 1H-**11**), 5.51 (dd, *J* = 17.5, 2.0 Hz 1H-**12(trans)**), 5.35 – 5.23 (dd, *J* = 10.5, 1.5 Hz 1H-**12(cis)** 2H), 4.78 (d, *J* = 5.0 Hz, 2H-**10**), 4.22 (d, *J* = 5.5 Hz, 2H-**15**).

^{13}C NMR: (151 MHz, DMSO-*d*$_6$) δ: 170.4-**17**, 168.9-**14**, 152.6-**9**, 149.5-**7**, 146.7-**18**, 140.3-**3**, 134.2-**11**, 132.2-**6**, 126.3-**4**, 125.3-**8**, 123.7-**2**, 121.9-**5**, 119.1-**19**, 118.3-**21/23/12**, 118.2-**21/23/12+21/23/12**, 115.8-**20**, 109.8-**1**, 69.6-**10**, 43.33-**15**.

In some cases, peaks appear to overlap and therefore are hidden by others. This is believed to be the case at:

- 118.2 ppm = two of **21**, **23**, and **12** - which are undistinguishable
- 118.3 ppm = one of **21**, **23**, and **12** - which are undistinguishable

IR ATIR (cm^{-1}): 3301 m (O-H stretch), 3072 w (Aromatic/Alkene C-H stretch), 2936 w (Alkane C-H stretch), 2852 w (Alkane C-H stretch), 2714 w (Alkane C-H stretch), 1684 m (C=O stretch), 1585 s (Aromatic C=C stretch).

Elemental Analysis:

Calculated for $[C_{21}H_{19}N_3O_5 \cdot 0.4\ CH_2Cl_2 \cdot 0.05\ C_4H_{10}O]$: %C 60.18, %H 4.75, %N 9.44
Measured for $[C_{21}H_{19}N_3O_5 \cdot 0.4\ CH_2Cl_2 \cdot 0.05\ C_4H_{10}O]$: %C 60.48, %H 4.50, %N 9.44

Melting Point: 209 – 211 °C

Ru-s3

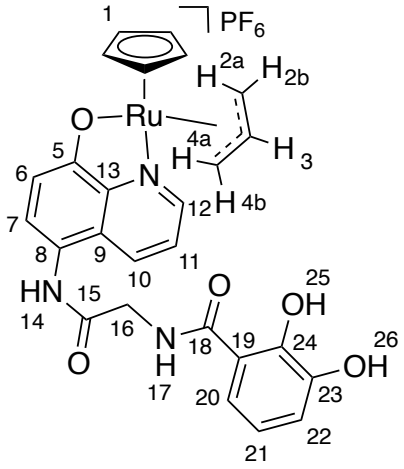

$C_{26}H_{24}F_6N_3O_5PRu$, 704.528 g mol^{-1}

To a stirred solution of tris(acetonitrile)cyclopentadienylruthenium(II) hexafluorophosphate (12.47 mg, 28.7 μmol) in dry, degassed DMF (0.5 mL) was added 2-[(2,3-dihydroxyphenyl)formamido]-*N*-[8-(prop-2-en-1-yloxy) quinolin-5-yl]acetamide (10.49 mg, 28.7 μmol) as a solution in dry, degassed DMF (3 mL) under a dry, nitrogen atmosphere at room temperature to form, at first a dark red solution which turned to a light red solution over 2 min. After stirring for 30 min under these conditions, the ruthenium-complex was precipitated using dry Et_2O (45 mL), where the resulting supernatant was decanted to leave the solid. This solid was washed with dry Et_2O (20 mL, x4) and then dry dichloromethane (20 mL, x2), to yield the title compound as a red/orange solid.

Yield: 17 mg, 24.1 μmol, 84%

HRMS (ESI+):

Calc. for $[C_{23}H_{20}N_3O_5Ru]^+$ = 520.0441 Found = 520.0412 (6.8 ppm error, 46.7 mSigma)

Calc. for $[C_{23}H_{19}N_3O_5Ru]+Na^+$ = 542.0260 Found = 542.0236 (5.7 ppm error, 39.2 mSigma)

Calc. for $[C_{23}H_{18}N_3O_5Ru]+2Na^+$ = 564.0080 Found = 564.0079 (1.2 ppm error, 160.2 mSigma)

Calc. for $[C_{23}H_{19}N_3O_7Ru]+Na^+$ = 574.0159 Found = 574.0121 (7.6 ppm error, 249.0 mSigma)

Calc. for $[C_{23}H_{18}N_3O_7Ru]+2Na^+$ = 595.9966 Found = 595.9978 (3.1 ppm error, 167.2 mSigma)

^{1}H NMR: (600 MHz, acetone-d_6) δ: 12.64 (s, 1H-**25/26**), 9.34 (s, 1H-**14**), 8.98 (d, *J* = 5.0 Hz, 1H-**12**), 8.64 (br s, 1H), 8.50 (dd, *J* = 9.0, 1.0 Hz, 1H-**10**), 7.84 (br s, 1H), 7.62 (dd, *J* = 8.5, 5.0 Hz, 1H-**11**), 7.34 (d, *J* = 8.5, 1H-**6**), 7.32 (dd, *J* = 8.0, 1.0 Hz, 1H-**20**), 7.01 (d, *J* = 8.0 Hz, 1H-**22**), 6.89 (d, *J* = 8.5 Hz, 1H-**7**), 6.77 (t, *J* = 8.0 Hz, 1H-**21**), 6.32 (s, 5H-**1**), 4.79 – 4.57 (m, 2H-**3+2a/4a**), 4.42 (d, *J* = 10.0 Hz, 1H-**2a/4a**), 4.38 (dd, *J* = 5.5, 2.5 Hz, 1H-**2b/4b**), 4.31 (d, *J* = 5.5 Hz, 2H-**16**), 4.19 (dd, *J* = 6.0, 3.0 Hz, 1H-**2b/4b**).

^{19}F NMR: (471 MHz, acetone-d_6) δ: -72.5 (d, *J* = 707.5 Hz, 6F).

^{19}P NMR: (202 MHz, acetone-d_6) δ: -144.2 (sp, *J* = 707.5 Hz, 1P).

^{13}C NMR: (126 MHz, acetone-d_6) δ: 172.0-**18**, 169.3-**15/5**, 169.1-**15/5**, 156.3-**12**, 150.8-**8**, 147.3-**23**, 146.3-**9**, 137.4-**10**, 128.5-**24/6**, 128.4-**24/6**, 127.6-**13**, 124.2-**11**, 120.0-**19**, 119.7-**22**, 119.3-**21**, 118.0-**20**, 115.1-**7**, 99.5-**16**, 97.1-**1,** 70.0-**2/4**, 63.6-**2/4**, 44.1-**16**.

IR ATIR (cm^{-1}): 3388 w br (Amide N-H stretch), 3117 w br (Aromatic/Alkene C-H stretch), 3107 m (Aromatic C-H stretch), 1644 m (C=O stretch), 1572 m (C=O stretch), 1537 s (Aromatic C=C stretch).

Elemental Analysis:

Calculated for $[C_{26}H_{24}F_6N_3O_5PRu \cdot 0.15\ C_4H_{10}O \cdot 0.1\ C_3H_7NO \cdot 0.75\ CH_2Cl_2]$: %C 42.22, %H 3.55, %N 5.52
Measured for $[C_{26}H_{24}F_6N_3O_5PRu \cdot 0.15\ C_4H_{10}O \cdot 0.1\ C_3H_7NO \cdot 0.75\ CH_2Cl_2]$: %C 42.12, %H 3.63, %N 5.53

UV-vis Spectroscopy:

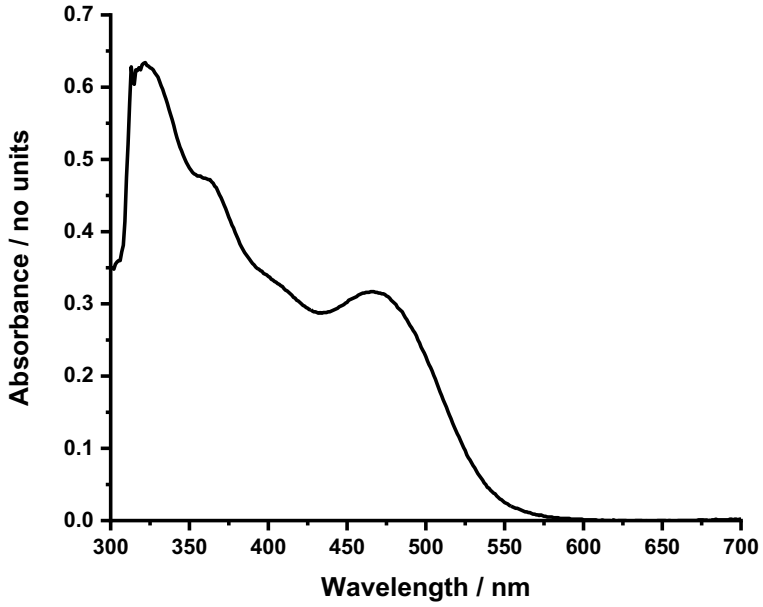

Figure 112 UV-vis spectrum, 200 μM in DMSO.

2,3-Bis[(4-methoxyphenyl)methoxy]benzoic acid, 27

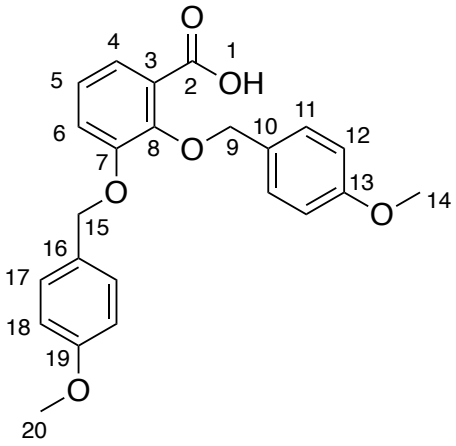

$C_{23}H_{22}O_6$, 394.42 g mol^{-1}

2,3-Bis[(4-methoxyphenyl)methoxy]benzoic acid was prepared following a procedure from the literature.[193]

Yield: 3.60 g, 9.13 mmol, 99%

Rf: 0.20 in EtOAc : PET (1:1)

HRMS (ESI+):

Calc. for $[C_{23}H_{22}O_6]+H^+$ = 393.1344 Found = 393.1237 (4.3 ppm error, 22.9 mSigma)

^{1}H NMR: (400 MHz, $CDCl_3$) δ: 7.72 (dd, *J* = 8.0, 1.5 Hz, 1H-**4**), 7.41 (d, *J* = 8.5 Hz, 1H-**12**), 7.27 – 7.21 (m, 3H-**6+18**), 7.17 (t, *J* = 8.0 Hz, 1H-**5**), 6.96 (d, *J* = 8.5 Hz, 1H-**11**), 6.83 (d, *J* = 8.5 Hz, 1H-**17**), 5.19 (s, 2H-**15**), 5.11 (s, 2H-**9**), 3.84 (s, 3H-**14/20**), 3.79 (s, 3H-**14/20**).

^{13}C NMR: (126 MHz, $CDCl_3$) δ: 165.4-**2**, 160.5-**19**, 160.0-**13**, 151.5-**8**, 147.2-**7**, 131.3-**18**, 129.8-**12**, 128.0-**10**, 126.9-**16**, 125.1-**5**, 124.5-**4**, 123.0-**3**, 119.1-**6**, 114.3-**11+17**, 77.0-**15**, 71.45-**9**, 55.5-**14/20**, 55.4-**14/20**.

Methyl (2*S*)-2,6-bis({2,3-bis[(4-methoxyphenyl)methoxy]phenyl} formamido)hexanoate, 28

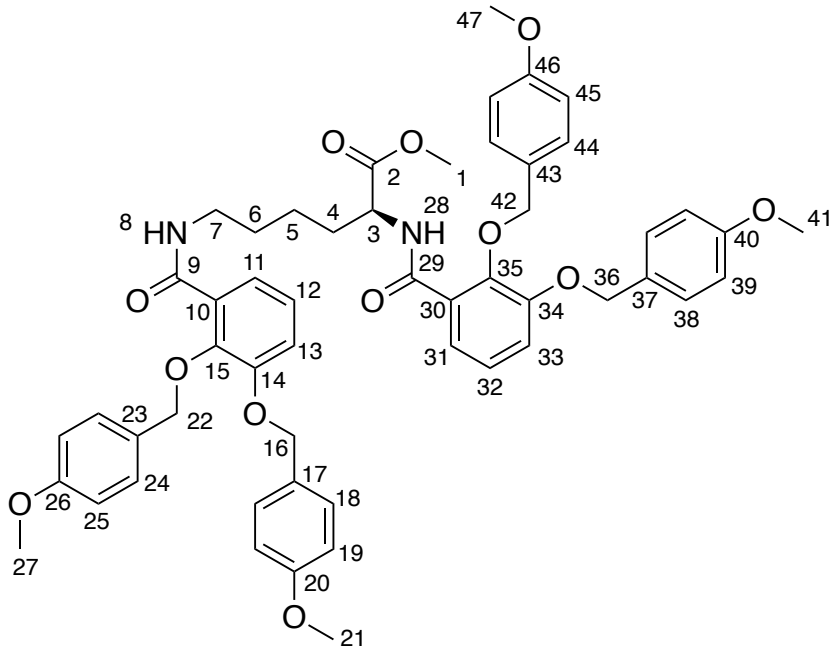

$C_{53}H_{56}N_2O_{12}$, 913.03 g mol^{-1}

Methyl (2*S*)-2,6-bis({2,3-bis[(4-methoxyphenyl)methoxy]phenyl}formamido) hexanoate was prepared following a procedure from the literature.[193]

Yield: 1.611 g, 1.76 mmol, 72%

Rf: 0.22 in EtOAc : PET (1:1)

HRMS (ESI+):

Calc. for $[C_{53}H_{56}N_2O_{12}]+H^+$ = 913.3906 Found = 913.3919 (-1.4 ppm error, 4.6 mSigma)

Calc. for $[C_{53}H_{56}N_2O_{12}]+Na^+$ = 935.3725 Found = 935.3729 (-0.4 ppm error, 3.0 mSigma)

^{1}H NMR: (400 MHz, $CDCl_3$) δ: 8.55 (d, *J* = 7.5 Hz, 1H-**28**), 7.95 (t, *J* = 5.5 Hz, 1H-**8**), 7.73 – 7.68 (m, 2H-**11**+**31**), 7.39 (d, *J* = 7.5 Hz, 4H-**Ar**), 7.28 (d, *J* = 8.5 Hz, 2H-**Ar**), 7.20 (d, *J* = 8.5 Hz, 2H-**Ar**), 7.15 – 7.10 (m, 4H-**12+13+32+33**), 6.93 (d, *J* = 8.5 Hz, 4H-**Ar**), 6.81 (d, *J* = 8.5 Hz, 2H-**Ar**), 6.77 (d, *J* = 8.5 Hz, 2H-**Ar**), 5.11 – 5.00 (m, 6H-**16/22/36/42+16/22/36/42+16/22/36/42**), 4.97 (s, 2H-**16/22/36/42**), 4.62 (td, *J* = 7.5, 6.0 Hz, 1H-**3**), 3.84 (s, 3H-**27/47**), 3.83 (s, 3H-**27/47**), 3.75 (s, 3H-**21/41**), 3.74 (s, 3H-**1**),3.71 (s, 3H-**21/41**), 3.16 (m, 2H-**7**), 1.70 – 1.62 (m, 2H-**4**), 1.51 – 1.41 (m, 1H-**4**), 1.32 – 1.23 (m, 2H-**6**), 1.23 – 1.13 (m, 2H-**5**).

^{13}C NMR: (126 MHz, $CDCl_3$) δ: 172.9-**2**, 165.2-**29/19**, 165.2-**29/19**, 160.0-**20/26/40/46**, 159.9-**20/26/40/46**, 159.8-**20/26/40/46**, 159.8-**20/26/40/46**, 151.9-**17/23/37/43**, 151.9-**17/23/37/43**, 147.2-**17/23/37/43**, 147.0-**17/23/37/43**, 130.78-**19/25/39/45+19/25/39/45**, 130.6-**19/25/39/45+19/25/39/45**, 129.8-**18/24/38/44+18/24/38/44**, 129.6-**18/24/38/44+18/24/38/44**, 128.6-**14/15/34/35+14/15/34/35**, 128.5-**14/15/34/35+14/15/34/35**, 127.4-**10/30**, 126.6-**10/30**, 124.4-**13/33**, 124.3-**13/33**, 123.3-**11/31**, 123.3-**11/31**, 117.3-**12/32**, 117.1-**12/32**, 114.2-**19/25/39/45+19/25/39/45**, 114.1-**19/25/39/45**, 113.9-**19/25/39/45**, 76.1-**22/42**, 76.0-**22/42**, 71.2-**16/36**, 71.2-**16/36**, 55.5-**21/27/41/47+21/27/41/47**, 55.4-**21/27/41/47/1+21/27/41/47/1**, 55.3-**21/27/41/47**, 52.7-**3**, 52.3-**21/27/41/47**, 39.4-**7**, 31.8-**4**, 29.0-**6**, 23.2-**5**.

In some cases, peaks overlap and therefore are hidden by others. This is believed to be the case at:

- 55.4 ppm = two of **21**, **27**, **41** and **47** - which are undistinguishable
- 114.2 ppm = two of **19**, **25**, **39** and **45** - which are undistinguishable

- 129.8 and 129.6 ppm, each = two of **18**, **24**, **38**, **44** - which are undistinguishable
- 130.8 and 130.6 ppm, each = two of **19**, **25**, **39**, **45** - which are undistinguishable

NMR spectra are in agreement with literature reports.[193]

(2*S*)-2,6-Bis({2,3-bis[(4-methoxyphenyl)methoxy]phenyl}formamido)hexanoic acid, 29

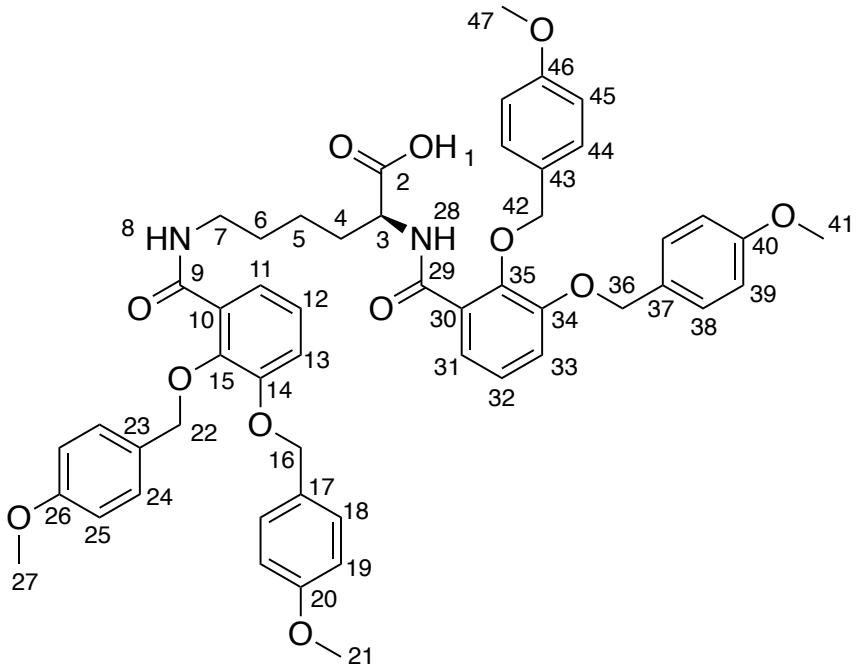

$C_{52}H_{54}N_2O_{12}$, 899.01 g mol^{-1}

(2*S*)-2,6-Bis({2,3-bis[(4-methoxyphenyl)methoxy]phenyl}formamido)hexanoic acid was prepared following a procedure from the literature.[193]

Yield: 742 mg, 0.825 mmol, 88%

Rf: 0.34 in dichloromethane : MeOH (9:1)

HRMS (ESI+):

Calc. for $[C_{52}H_{54}N_2O_{12}]+H^+$ = 899.3750, Found = 899.3765 (-1.7 ppm error, 14.5 mSigma)

Calc. for $[C_{52}H_{54}N_2O_{12}]+Na^+$ = 921.3569 Found = 921.3587 (-1.9 ppm error, 9.9 mSigma)

^{1}H NMR: (400 MHz, $CDCl_3$) δ: 8.64 (d, *J* = 7.0 Hz, 1H-**28**), 8.02 (t, *J* = 5.5 Hz, 1H-**8**), 7.69 (td, *J* = 7.0, 2.5 Hz, 2H-**11**+**31**), 7.38 (d, *J* = 8.5 Hz, 4H-**Ar**), 7.24 (d, *J* = 8.5 Hz, 2H-**Ar**), 7.19 (d, *J* = 8.5 Hz, 2H-**Ar**), 7.14 – 7.09 (m, 4H-**12+13+32+33**), 6.92 (d, *J* = 8.5 Hz, 4H-**Ar**), 6.80 (d, *J* = 8.5 Hz, 2H-**Ar**), 6.75 (d, *J* = 8.5 Hz, 2H-**Ar**), 5.04 (d, *J* = 3.5 Hz, 6H-**16/21/36/42+16/21/36/42+16/21/36/42**), 4.96 (s, 2H-**16/21/36/42**), 4.55 (q, *J* = 7.0 Hz, 2H-**3**), 3.83 (s, 6H-**27/47**), 3.73 (s, 3H-**21/41**), 3.71 (s, 3H-**21/41**), 3.15 (dh, *J* = 13.3, 6.7 Hz, 2H-**7**), 1.74 (dq, *J* = 13.0, 7.0, 6.0 Hz, 1H-**4**), 1.46 (dq, *J* = 14.4, 7.5 Hz, 1H-**4**), 1.33 – 1.13 (m, 4H-**5+6**).

^{13}C NMR: (126 MHz, $CDCl_3$) δ: 174.3-**2**, 166.2-**29/19**, 165.5-**29/19**, 160.0-**20/26/40/46**, 156.0-**20/26/40/46**, 159.8-**20/26/40/46**, 159.8-**20/26/40/46**, 151.9-**17/23/37/43**, 151.8-**17/23/37/43**, 147.3-**17/23/37/43**, 147.0-**17/23/37/43**, 130.9-**19/25/39/45+19/25/39/45**, 130.6-**19/25/39/45+19/25/39/45**, 129.8-**18/24/38/44+18/24/38/44**, 129.6-**18/24/38/44+18/24/38/44**, 128.6-**14/15/34/35**, 128.6-**14/15/34/35**, 128.5-**14/15/34/35**, 128.4-**14/15/34/35**, 127.1-**10/30**, 126.1-**10/30**, 124.4-**13**+**33**, 123.3-**11/31**, 123.2-**11/31**, 117.6-**12/32**, 117.2-**12/32**, 114.2-**19/25/39/45+19/25/39/45**, 114.1-**19/25/39/45**, 114.0-**19/25/39/45**, 76.2-**22/42**, 76.1-**22/42**, 71.2-**16/36**, 71.2-**16/36**, 55.4-**21/27/41/47+21/27/41/47**, 55.4-**21/27/41/47**, 55.3-**21/27/41/47**, 53.0-**3**, 39.5-**7**, 31.1-**4**, 29.0-**6**, 23.0-**5**.

In some cases, peaks overlap and therefore are hidden by others. This is believed to be the case at:

- 55.4 and 55.4 ppm, each = two of **21**, **27**, **41** and **47** - which are undistinguishable
- 114.2 ppm = two of **19**, **25**, **39** and **45** - which are undistinguishable
- 129.8 and 129.6 ppm, each = two of **18**, **24**, **38**, **44** - which are undistinguishable
- 130.9 and 130.6 ppm, each = two of **19**, **25**, **39**, **45** - which are undistinguishable

NMR spectra are in agreement with literature reports.[193]

(2*S*)-2,6-Bis({2,3-bis[(4-methoxyphenyl)methoxy]phenyl}formamido)-*N*-({[8-(prop-2-en-1-yloxy)quinolin-5-yl]carbamoyl}methyl)hexanamide, 30

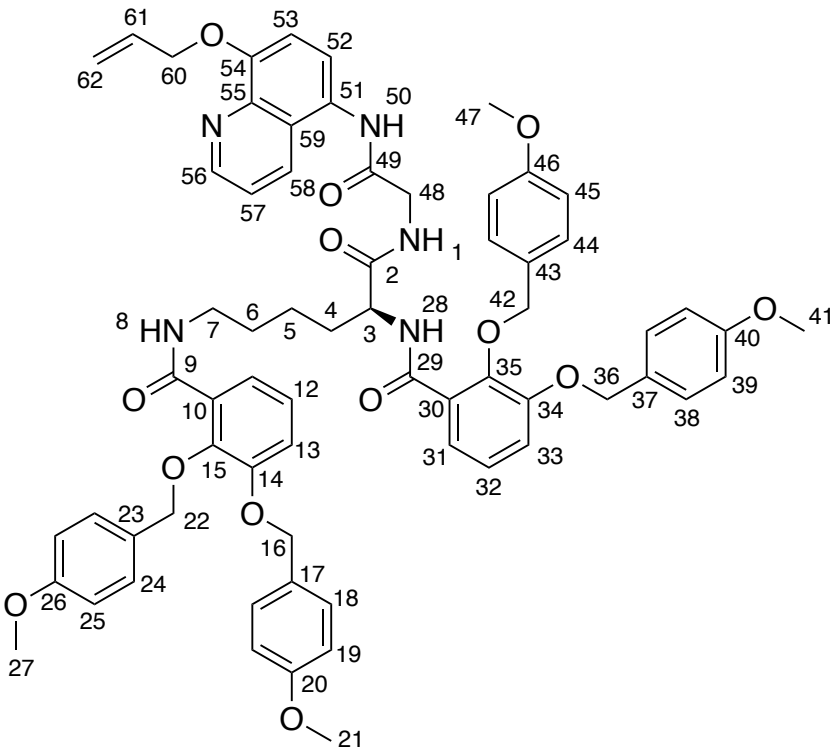

$C_{66}H_{67}N_5O_{13}$, 1138.28 g mol^{-1}

(2*S*)-2,6-bis({2,3-bis[(4-Methoxyphenyl)methoxy] phenyl}formamido)-*N*-({[8-(prop-2-en-1-yloxy)quinolin-5-yl]carbamoyl}methyl)hexanamide was prepared based on a procedure from the literature.[193]

To a solution of (2*S*)-2,6-bis({2,3-bis[(4-methoxyphenyl)methoxy]phenyl}formamido)hexanoic acid (299 mg, 0.355 mmol) in dry DMF (5 mL) was added *N'*-ethylcarbodiimide hydrochloride (102 mg, 0.533 mmol), hydroxybenzotriazole monohydrate (82 mg, 0.522 mmol) and DIPEA (216 μL, 1.24 mmol), and then 5-(2-azaniumylacetamido)-8-(prop-2-en-1-yloxy)quinolin-1-ium ditrifluoroacetate (172 mg, 0.355 mmol). The resulting solution was left stirring for 18 h at room temperature and after this time, the reaction solvent was removed *in vacuo*. The produced dark purple residue was re-dissolved in dichloromethane (30 mL) and washed with saturated NH_4Cl(aq) (30 mL, x3) and then saturated $NaHCO_3$(aq) (30 mL, x3). The organic layer solvent was removed *in vacuo* to leave an orange/brown foam. This

solid was purified *via* column chromatography, eluting with dichloromethane : MeOH : NEt_3 (100:3:1), and then triturated in Et_2O, to yield the title compound as a white solid.

Yield: 222 mg, 0.195 mmol, 55%

Rf: 0.17 in dichloromethane : MeOH : NEt_3 (100:3:1)

HRMS (ESI+):

Calc. for $[C_{66}H_{67}N_5O_{13}]+H^+$ = 1138.4808, Found = 1138.4862 (-4.8 ppm error, 5.3 mSigma)

Calc. for $[C_{66}H_{67}N_5O_{13}]+Na^+$ = 1160.4628 Found = 1160.4691 (-5.4 ppm error, 4.2 mSigma)

^{1}H NMR: (400 MHz, $CDCl_3$) δ 9.18 (s, 1H-**50**), 8.85 (dd, *J* = 4.0, 1.0 Hz, 1H-**56**), 8.61 (d, *J* = 4.5 Hz, 1H-**28**), 8.25 (d, *J* = 8.5 Hz, 1H-**58**), 8.07 (t, *J* = 5.5 Hz, 1H-**8**), 7.60 (dd, *J* = 7.5, 2.0 Hz, 1H-**11/31**), 7.56 (d, *J* = 8.5 Hz, 1H-**11/31**), 7.38 (dd, *J* = 8.5, 2.0 Hz, 4H-**Ar**), 7.31 (d, *J* = 8.5 Hz, 2H-**Ar**), 7.21 (d, *J* = 8.5 Hz, 2H-**Ar**), 7.17-7.05 (m, 6H-**57**+**12/32+13+33+52/53**), 7.03 (d, *J* = 8.5 Hz, 1H-**12/32**), 6.93 (d, *J* = 8.5 Hz, 4H-**Ar**), 6.87 (d, *J* = 8.0 Hz, 1H-**52/53**), 6.84 – 6.78 (m, 4H-**Ar**), 6.25 – 6.12 (m, 1H-**61**), 5.46 (dd, *J* = 17.0, 1.5 Hz, 1H-**62(trans)**), 5.32 (dd, *J* = 10.5, 1.5 Hz, 1H-**62(cis)**), 5.06 (s, 6H-**16/21/36/42+16/21/36/42+16/21/36/42**), 4.98 (s, 2H-**16/21/36/42**), 4.83 (d, *J* = 5.5 Hz, 2H-**60**), 4.22 (dd, *J* = 17.0, 7.0 Hz, 1H-**48**), 4.17-4.07 (m, 1H-**3**), 3.99 (dd, *J* = 17.0, 5.5 Hz, 1H-**48**), 3.82 (d, 6H-**27+47**), 3.75 (s, 3H-**21/41**), 3.71 (s, 3H-**21/41**), 3.21 (q, *J* = 6.5 Hz, 2H-**7**), 1.68 (dq, *J* = 13.5, 7.0, 6.5 Hz, 1H-**4**), 1.39 (dt, *J* = 14.0, 7.5 Hz, 1H-**4**), 1.34 – 1.26 (m, 2H-**6**), 1.20 (q, *J* = 6.5, 5.5 Hz, 2H-**5**).

^{13}C NMR: (126 MHz, $CDCl_3$) δ: 173.2-**2**, 169.1-**49**, 166.8-**29/19**, 165.5-**29/19**, 160.2-**20/26/40/46**, 160.0-**20/26/40/46**, 159.8-**20/26/40/46**, 159.8-**20/26/40/46**, 151.9-**17/23/37/43+54**, 151.7-**17/23/37/43**, 148.5-**56**, 147.2-**17/23/37/43**, 146.9-**17/23/37/43**, 133.1-**58**, 130.9-**19/25/39/45+19/25/39/45**, 130.6-**19/25/39/45+19/25/39/45**, 129.7-**18/24/38/44+18/24/38/44**, 129.7-**18/24/38/44+18/24/38/44**, 128.7-**14/15/34/35**, 128.5-**14/15/34/35**, 128.4-

14/15/34/35, 128.3-**14/15/34/35**, 127.0-**51/55**, 125.7-**51/55**, 125.4-**10/30**, 125.2-**10/30**, 124.5-**59**, 124.3-**13/33**, 124.2-**13/33**, 123.1-**11/31**, 122.8-**11/31**, 121.5-**57**, 118.7-**62**, 117.8-**12/32**, 117.1-**12/32**, 114.2-**19/25/39/45**, 114.2-**19/25/39/45**, 114.2-**19/25/39/45+19/25/39/45**, 76.2-**22/42**, 76.1-**22/42**, 71.2-**16/36**, 71.2-**16/36**, 70.2-**60**, 55.5-**21/27/41/47**, 55.5-**21/27/41/47+21/27/41/47**, 55.4-**21/27/41/47**, 44.0-**62**, 39.0-**7**, 30.2-**4**, 28.9-**6**, 23.1-**5**.

In some cases, peaks overlap and therefore are hidden by others. This is believed to be the case at:

- 55.5 = two of **21**, **27**, **41** and **47** - which are undistinguishable
- 114.2 ppm = two of **19**, **25**, **39** and **45** - which are undistinguishable
- 129.7 and 129.7 ppm, each = two of **18**, **24**, **38**, **44** - which are undistinguishable
- 130.9 and 130.6 ppm, each = two of **19**, **25**, **39**, **45** - which are undistinguishable

NMR spectra are in agreement with literature reports.[193]

IR ATIR (cm^{-1}): 3351 m br (N-H stretch), 3270 m br (N-H stretch), 3066 w (Aromatic/Alkene C-H stretch), 2930 m (Alkane C-H stretch), 2871 m (Alkane C-H stretch), 2838 m (Alkane C-H stretch), 1642 m (C=O stretch), 1611 (Alkene C=C stretch), 1513 (Aromatic C=C stretch).

Elemental Analysis:

Calculated for [$C_{66}H_{67}N_5O_{13}$ • 0.4 CH_2Cl_2 • 0.15 CH_4O]: %C 67.91, %H 5.86, %N 5.95

Measured for [$C_{66}H_{67}N_5O_{13}$ • 0.4 CH_2Cl_2 • 0.15 CH_4O]: %C 68.09, %H 5.85, %N 5.77

Melting Point: 78-80 °C

2,6-Bis[(2,3-dihydroxyphenyl)formamido]-*N*-({[8-(prop-2-en-1-yloxy)quinolin-5-yl]carbamoyl}methyl)hexanamide, 31

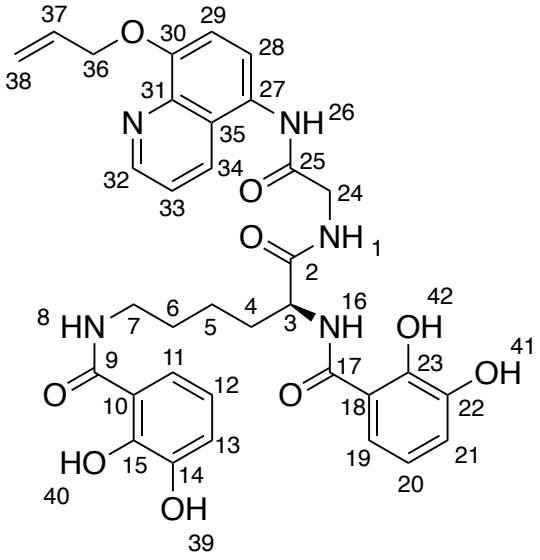

$C_{34}H_{35}N_5O_9$, 657.68 g mol^{-1}

To a stirred solution of (2*S*)-2,6-bis({2,3-bis[(4-methoxyphenyl)methoxy]-phenyl} formamido)-*N*-({[8-(prop-2-en-1-yloxy)quinolin-5-yl]carbamoyl}methyl)hexanamide (222 mg, 195 μmol) in dioxane (9 mL) was added 4 N HCl in dioxane (2.2 mL) dropwise and left stirring for 5 h at room temperature. After this time, the reaction solvent was removed *in vacuo* and the produced residue was purified *via* column chromatography, eluting with 9 : 1 dichloromethane : MeOH, and then triturated in Et_2O, to yield the title compound as a beige solid.

Yield: 30 mg, 65.4 μmol, 34%

Rf: 0.44 in dichloromethane : MeOH (8:2)

HRMS (ESI-):

Calc. for $[C_{34}H_{35}N_5O_9]$-H^+ = 656.2362, Found = 656.2373 (-1.7 ppm error, 6.7 mSigma)

^{1}H NMR: (400 MHz, MeOD-d_4) δ: 8.77 – 8.68 (m, 1H-**32**), 8.33 (d, *J* = 8.5 Hz, 1H-**34**), 7.46 (d, *J* = 8.5 Hz, 1H-**28/29**), 7.41 (dd, *J* = 8.5, 4.5 Hz, 1H-**33**), 7.26 – 7.21 (m, 1H-**11/19**), 7.16 – 7.10 (m, 2H-**11/19+28/29**), 6.92 – 6.86 (m, 2H-**13+21**), 6.64

(td, *J* = 8.0, 4.0 Hz, 2H-**12+20**), 6.19 (ddt, *J* = 16.0, 10.5, 5.5 Hz, 1H-**37**), 5.47 (dd, *J* = 17.5, 1.5 Hz, 1H-**38(trans)**), 5.30 (dd, *J* = 10.5, 1.5 Hz, 1H-**38(cis)**), 4.80 (d, *J* = 5.0 Hz, 2H-**36**), 4.54 (t, *J* = 7.0 Hz, 1H-**3**), 4.25 – 4.05 (m, 2H-**24**), 3.37 (t, *J* = 6.5 Hz, 2H-**7**), 2.08 – 1.84 (m, 2H-**4**), 1.71 – 1.62 (m, 1H-**6**), 1.60 – 1.47 (m, 2H-**5**).

^{13}C NMR: (126 MHz, MeOD-*d*$_4$) δ: 175.6-**2**, 171.6-**9/17/25**, 171.5-**9/17/25**, 171.4-**9/17/25**, 153.9-**30**, 150.2-**15/23**, 149.7-**32**, 149.5-**15/23**, 147.3-**14/22**, 147.1-**14/22**, 140.5-**27**, 134.4-**37**, 134.0-**34**, 130.9-**15/23**, 130.7-**15/23**, 127.2-**35**, 126.2-**31**, 126.0-**28/29**, 123.0-**33**, 119.9-**12/20/13/21**, 119.8-**12/20/13/21**, 119.8-**12/20/13/21**, 119.5-**12/20/13/21**, 118.6-**11/19**, 118.4-**11/19**, 116.9-**10/18**, 116.7-**10/18**, 110.2-**28/29**, 70.9-**36**, 55.8-**3**, 44.2-**24**, 40.1-**7**, 32.1-**4**, 30.0-**6**, 24.3-**5**.

IR ATIR (cm^{-1}): 3332 w br (O-H stretch), 3046 w (Aromatic/Alkene C-H stretch), 2943 w (Alkane C-H stretch), 1638 s (C=O stretch), 1587 s (Alkene C=C stretch), 1535 s (Aromatic C=C stretch), 1504 s (Aromatic C=C stretch).

Elemental Analysis:

Calculated for [$C_{34}H_{35}N_5O_9$ • 0.05 CH_2Cl_2 • 1.1 $C_4H_{10}O$]: %C 62.12, %H 6.25, %N 9.42

Measured for [$C_{34}H_{35}N_5O_9$ • 0.05 CH_2Cl_2 • 1.1 $C_4H_{10}O$]: %C 62.35, %H 5.82, %N 9.01

Melting Point: 157-159 °C

Ru-s4

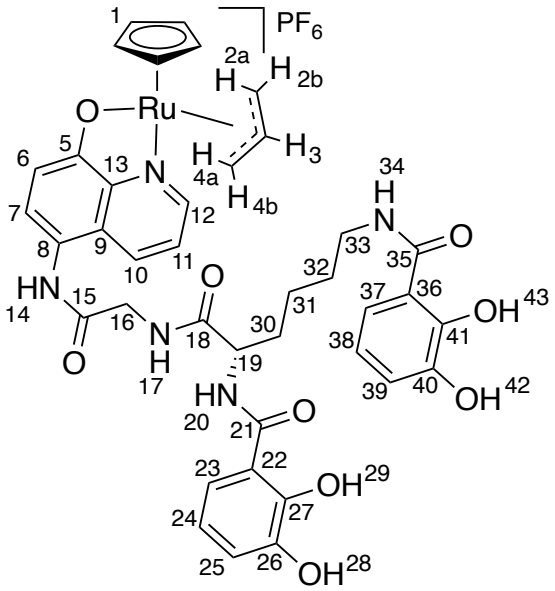

$C_{39}H_{40}F_6N_5O_9PRu$, 968.809 g mol^{-1}

To a stirred solution of tris(acetonitrile)cyclopentadienylruthenium(II) hexafluorophosphate (12.85 mg, 29.6 μmol) in dry, degassed DMF (0.5 mL) was added 2,6-bis[(2,3-dihydroxyphenyl)formamido]-*N*-({[8-(prop-2-en-1-yloxy)quinolin-5-yl]carbamoyl}methyl)hexanamide (24.32 mg, 29.6 μmol) as a solution in dry, degassed DMF (3 mL) under a dry, nitrogen atmosphere at room temperature to form, at first a dark red solution which turned to a light red solution over 2 min. After stirring for 30 min under these conditions, the ruthenium-complex was precipitated using dry Et_2O (45 mL). The precipitate was re-dissolved in dry DMF (5 mL) and precipitated using dry Et_2O (15 mL). The produced solid was washed with more dry Et_2O (20 mL, x3) and then dry dichloromethane (10 mL x3), to yield the title compound as a dark brown solid.

Yield: 12.2 mg, 12.6 μmol, 43%

HRMS (ESI+):

Calc. for $[C_{36}H_{35}N_5O_9Ru]+Na^+$ = 806.1370, Found = 806.1408 (-3.3 ppm error, 65.0 mSigma)

Calc. for $[C_{39}H_{40}N_5O_9Ru]^+$ = 656.2362, Found = 656.2373 (-3.0 ppm error, 22.7 mSigma)

^{1}H NMR: (500 MHz, DMSO-*d*$_6$) δ: 12.81 (s, 1H-**29/43**), 11.85 (d, *J* = 10.5 Hz, 1H-**29/43**), 9.60 (d, *J* = 8.0 Hz, 1H-**14**), 9.27 (br s, 1H-**28/42**), 9.09 (br s, 1H-**28/42**), 8.86 (s, 1H-**12**), 8.82 (d, *J* = 6.5 Hz, 1H-**20**), 8.75 (s, 1H-**34**), 8.57 – 8.50 (m, 1H-**17**), 8.37 – 8.31 (m, 1H-**10**), 7.55 (d, *J* = 8.0 Hz, 1H-**11**), 7.40 (d, *J* = 7.0 Hz, 1H-**23**), 7.26 (d, *J* = 9.0 Hz, 1H-**7**), 7.24 (d, *J* = 8.0 Hz, 1H-**37**), 6.93 (d, *J* = 8.0 Hz, 1H-**25**), 6.89 (d, *J* = 8.0 Hz, 1H-**39**), 6.86 (d, *J* = 8.5 Hz, 1H-**6**), 6.69 (dt, *J* = 8.0, 4.0 Hz, 2H-**24**), 6.64 (t, *J* = 8.0 Hz, 1H-**38**), 6.25 (s, 5H-**1**), 4.58 – 4.41 (m, 3H-**2a/4a+3+19**), 4.25 (d, *J* = 9.0 Hz, 1H-**2a/4a**), 4.09 (s, 1H-**2b/4b**), 4.04 – 3.93 (d, *J* = 17.5 Hz, 3H-**2b/4b+16**), 3.34 (s, 2H-**33**), 3.29 – 3.17 (m, 1H-**33**), 1.92 – 1.74 (m, 2H-**30**), 1.62 – 1.52 (m, 2H-**32**), 1.50 – 1.30 (m, 2H-**31**).

^{13}C NMR: (151 MHz, DMSO-*d*$_6$) δ: 172.2-**18**, 169.7-**35**, 169.1-**21**, 168.8-**15**, 167.3-**5**, 155.6-**12**, 149.7-**41**, 148.7-**27**, 146.2-**22/36**, 146.0-**22/36**, 144.8-**13**, 135.9-**10**, 126.7-**7**, 126.0-**9**, 123.2-**11**, 118.9-**25/39**, 118.7-**25/39**, 118.7-**8**, 118.4-**23**, 118.1-**24**, 117.9-**38**, 117.0-**37**, 115.6-**26**, 114.9-**40**, 113.8-**6**, 98.0-**3**, 95.8-**1**, 68.2-**2/4**, 63.1-**2/4**, 53.4-**19**, 42.6-**16**, 38.8-**7**, 31.1-**30** 28.6-**32**, 23.1-**31**.

^{19}F NMR: (471 MHz, DMSO-*d*$_6$) δ: -70.2 (d, *J* = 711.0 Hz, 6F).

^{31}P NMR: (202 MHz, DMSO-*d*$_6$) δ: -146.0 (d, *J* = 711.0 Hz, 1P).

IR ATIR (cm^{-1}): 3507 w br (O-H stretch), 3325 m br (Amide N-H stretch), 3111 w (Aromatic/Alkene C-H stretch), 2939 w (Alkane C-H stretch), 2868 w (Alkane C-H stretch), 1640 s (C=O stretch), 1588 s (Alkene C=C stretch), 1532 s (Aromatic C=C stretch).

Elemental Analysis:

Calculated for $[C_{39}H_{40}F_6N_5O_9PRu \cdot 1.0\ CH_2Cl_2 \cdot 0.5\ C_4H_{10}O]$: %C 46.25, %H 4.34, %N 6.42

Measured for $[C_{39}H_{40}F_6N_5O_9PRu \cdot 1.0\ CH_2Cl_2 \cdot 0.5\ C_4H_{10}O]$: %C 46.55, %H 4.04, %N 6.15

UV-vis Spectroscopy:

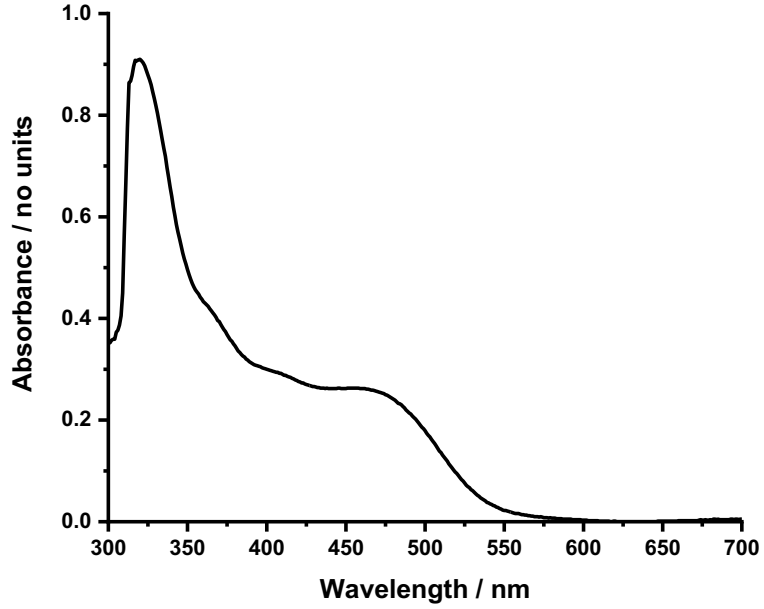

Figure 113 UV-vis spectrum, 200 μM in DMSO.

N-{5-[(2-Ethoxy-3,4-dioxocyclobut-1-en-1-yl)amino]pentyl}-*N*-hydroxy-*N′*-[5-(*N*-hydroxy-3-{[5-(*N*-hydroxyacetamido)pentyl]carbamoyl}propanamido)pentyl]butanediamide, 32

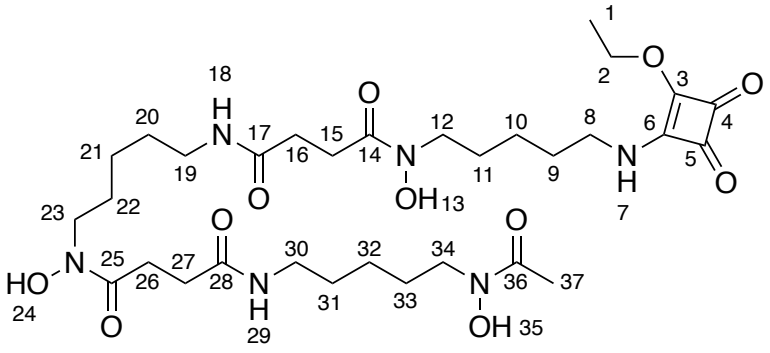

$C_{31}H_{52}N_6O_{11}$, 684.788 g mol^{-1}

N-{5-[(2-Ethoxy-3,4-dioxocyclobut-1-en-1-yl)amino]pentyl}-*N*-hydroxy-*N′*-[5-(*N*-hydroxy-3-{[5-(*N*-hydroxyacetamido)pentyl]carbamoyl}propanamido)pentyl]butanediamide was prepared based on a procedure from the literature.[207]

A white suspension of desferrioxamine mesylate (492 mg, 0.749 mmol) and DIPEA (131 μL) in dry EtOH (20 mL) was heated to 50 ºC for 1 h. After this time, 2,3-diethoxy-3-cyclobutene-1,2-dione (333 μL, 2.25 mmol) was added and the resulting mixture was left to stir at 50 ºC for 18 h. Reaction solvent was then removed *in vacuo* and washed with room temperature EtOH (20 mL, x3), to yield the title compound as a fluffy white solid.

Yield: 488 mg, 0.713 mmol, 95%

Rf: 0.13 in dichloromethane : MeOH (9:1)

HRMS (ESI+):

Calc. for $[C_{31}H_{52}N_6O_{11}]+H^+$ = 685.3767 Found = 685.3769 (-0.3 ppm error, 25.2 mSigma)

Calc. for $[C_{31}H_{52}N_6O_{11}]+Na^+$ = 707.3586 Found = 707.3571 (2.1 ppm error, 5.7 mSigma)

^{1}H NMR: (400 MHz, DMSO-d_6) δ: 9.84-9.44 (m, 3H-**13+24+35**), 8.80 (t, *J* = 5.0 Hz, 1H-**7(rotamer 1)**), 8.60 (t, *J* = 5.5 Hz, 1H-**7(rotamer 2)**), 7.82 – 7.75 (m, 2H-**18**+**29**), 4.71 – 4.58 (m, 2H-**2**), 3.45 (t, *J* = 7.0 Hz, 6H-**12**+**23**+**34+8(rotamer 2)**), 3.26 (q, *J* = 6.5 Hz, 2H-**8(rotamer 1)**), 2.99 (q, *J* = 7.0 Hz, 4H-**19**+**30**), 2.57 (t, *J* = 7.5 Hz, 4H-**15**+**26**), 2.26 (t, *J* = 7.5 Hz, 4H-**16**+**27**), 1.96 (s, 3H-**37**), 1.50 (q, *J* = 7.5 Hz, 8H-**9**+**11**+**22**+**33**), 1.37 (m, 7H-**1**+**20**+**31**), 1.22 (m, 6H-**10**+**21**+**32**).

For this compound, it is believed two rotamers exist. The only two environments that change in magnetic environment between these rotamers are **7** and **8**.

NMR spectra of this compound in literature reports are incorrectly assigned. Despite this, comparison of the spectra obtained in this study to that of Rudd *et al.* 2016, suggests the desired compound was successfully obtained.[207]

N-[5-({3,4-Dioxo-2-[({[8-(prop-2-en-1-yloxy)quinolin-5-yl]carbamoyl}methyl)amino]cyclobut-1-enz-1-yl}amino)pentyl]-*N*-hydroxy-*N*′-[5-(*N*-hydroxy-3-{[5-(*N*-hydroxyacetamido)pentyl]carbamoyl}propanamido)pentyl]butanediamide, 33

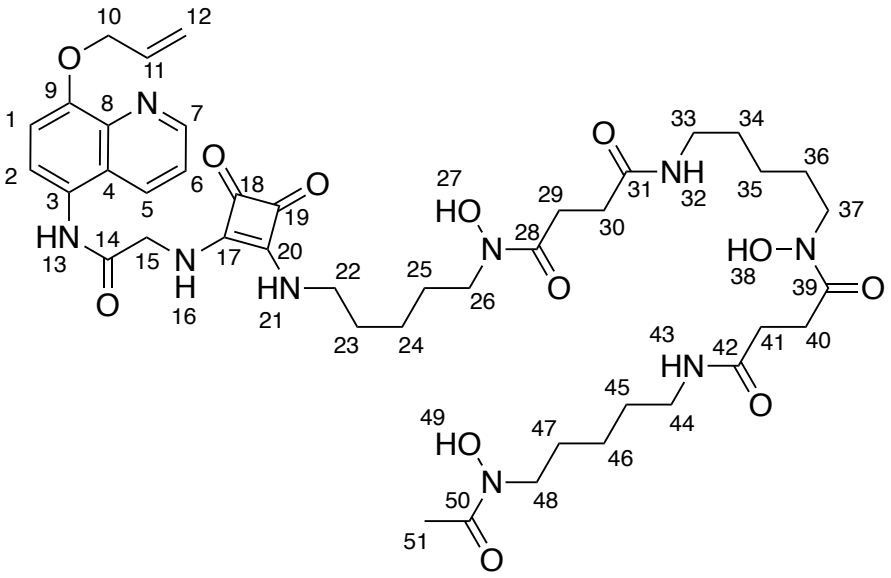

$C_{43}H_{61}N_9O_{12}$, 896.012 g mol^{-1}

To a pale yellow/orange solution of *N*-{5-[(2-ethoxy-3,4-dioxocyclobut-1-en-1-yl)amino]pentyl}-*N*-hydroxy-*N*′-[5-(*N*-hydroxy-3-{[5-(*N*-hydroxyacetamido)pentyl]carbamoyl}propanamido)pentyl]butanediamide (80 mg, 0.123 mmol) and DIPEA (107 μL, 0.614 mmol) in a solvent mixture of EtOH : H_2O (6 mL, 4:1) was added 5-(2-azaniumylacetamido)-8-(prop-2-en-1-yloxy)quinolin-1-ium ditrifluoroacetate, (114 mg, 0.235 mmol) in EtOH (4 mL). After stirring for 24 h at room temperature, reaction solvent was removed *in vacuo*. The resulting residue was re-suspended in MeCN (40 mL), where the produced supernatant was decanted to leave the solid. This solid was washed with further MeCN (20 mL, x4), to yield the title compound as a light brown solid.

Yield: 85 mg, 94.9 μmol, 77%

HRMS (ESI+):

Calc. for $[C_{43}H_{61}N_9O_{12}]+H^+$ = 896.4512 Found = 896.4531 (-2.1 ppm error, 30.2 mSigma)

Calc. for $[C_{43}H_{61}N_9O_{12}]+Na^+$ = 918.4332 Found = 918.4361 (-3.2 ppm error, 39.5 mSigma)

^{1}H NMR: (400 MHz, DMSO-d_6) δ: 10.10 (br s, 1H-**13**), 9.77 – 9.46 (m, 3H-**27**+**38**+**49**), 8.88 (d, *J* = 4.0 Hz, 1H-**7**), 8.39 (d, *J* = 8.5 Hz, 1H-**5**), 7.79 (t, *J* = 5.5 Hz, 2H-**32**+**43**), 7.67 (br s, 1H-**16/21**), 7.58 (dd, *J* = 8.5, 4.0 Hz, 1H-**6**), 7.52 (d, *J* = 8.5 Hz, 1H-**1**), 7.21 (d, *J* = 8.5 Hz, 1H-**2**), 6.16 (ddt, *J* = 16.0, 10.5, 5.5 Hz, 1H-**11**), 5.51 (d, *J* = 17.5 Hz, 1H-**12**(**trans)**), 5.32 (d, *J* = 10.5 Hz, 1H-**12(cis)**), 4.77 (d, *J* = 5.5 Hz, 2H-**10**), 4.56 (br s, 2H-**16/21**), 3.56 – 3.42 (m, 10H-**22+15**+**26**+**37**+**48**), 2.99 (q, *J* = 6.5 Hz, 4H-**33**+**44**), 2.57 (t, *J* = 7.5 Hz, 4H-**29**+**40**), 2.26 (t, *J* = 7.5 Hz, 4H-**30**+**41**), 1.96 (s, 3H-**51**), 1.59 – 1.43 (m, 8H-**23**+**25**+**36**+**46**), 1.43 – 1.32 (m, 4H-**34**+**45**), 1.32 – 1.16 (m, 6H-**24**+**35**+**47**).

^{13}C NMR: (126 MHz, DMSO-d_6) δ: 182.6-**18**+**19**, 172.0-**28**+**39**, 171.4-**14**+**31**+**42**, 170.2-**50**, 152.2-**9**, 149.1-**7**, 139.8-**3**, 133.7-**11**, 131.7-**5**, 125.52-**4**, 124.8-**8**, 123.2-**2**, 121.6-**6**, 117.8-**12**, 109.3-**1**, 69.2-**10**, 47.1-**17+20**, 47.1-**15**, 46.8-**15**+**26**+**37**+**48+17+20**, 46.1-**15**+**26**+**37**+**48+17+22**, 43.3-**22**, 38.4-**33**+**44**, 30.4 **23**+**25**+**36**+**47**, 29.9-**30**+**41**, 28.8-**34**+**45**, 27.6-**29**+**40**, 26.0-**23**+**25**+**36**+**47**, 23.5-**24**+**35**+**46**, 23.0-**24**+**35**+**46**, 20.4-**51**.

In some cases, different peaks that correspond to numerous environments are undistinguishable and therefore the number of environments that correspond to each is unknown. This is the case at:

- 23.0 ppm = one or two of **34**, **35**, and **46** - which are undistinguishable
- 23.5 ppm = one or two of **34**, **35**, and **46** - which are undistinguishable
- 46.1 ppm = one, two, three, four or five of **15**, **26**, **37**, **48**, **17**, and **20** - which are undistinguishable
- 46.8 ppm = one, two, three, four or five of **15**, **26**, **37**, **48**, **17**, and **20** - which are undistinguishable

IR ATIR (cm^{-1}): 3225 m br (O-H stretch), 3091 m (Aromatic/Alkene C-H stretch), 2928 m (Alkane C-H stretch), 2860 m (Alkane C-H stretch), 1803 w (Alkene C-H stretch), 1644 s (C=O stretch), 1574 s (Alkene C=C stretch), 1550 s (Aromatic C=C stretch).

Elemental Analysis:

Calculated for [$C_{43}H_{61}N_9O_{12}$ • 1.15 H_2O]: %C 56.34, %H 6.96, %N 13.75

Measured for [$C_{43}H_{61}N_9O_{12}$ • 1.15 H_2O]: %C 56.48, %H 6.57, %N 13.62

Melting Point: 155 – 157 °C

UV-vis Spectroscopy:

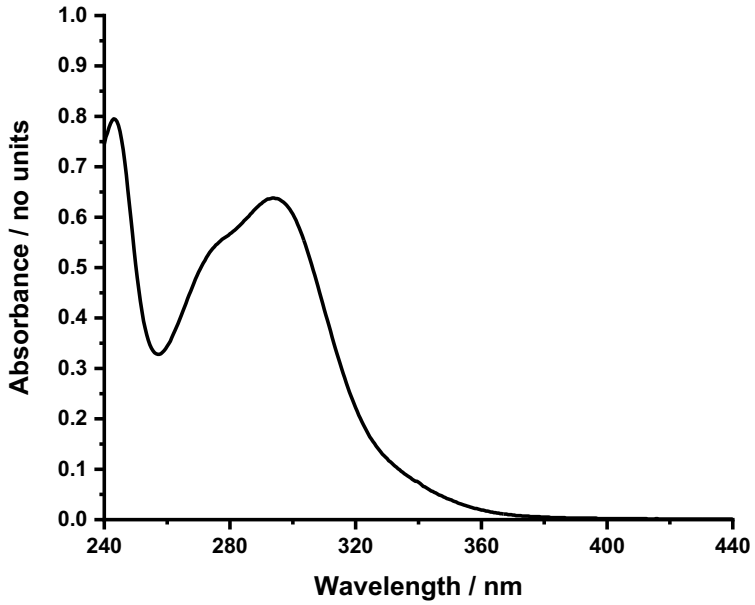

Figure 114 UV-vis spectrum, 25 μM in 10% DMSO in water.

HPLC:

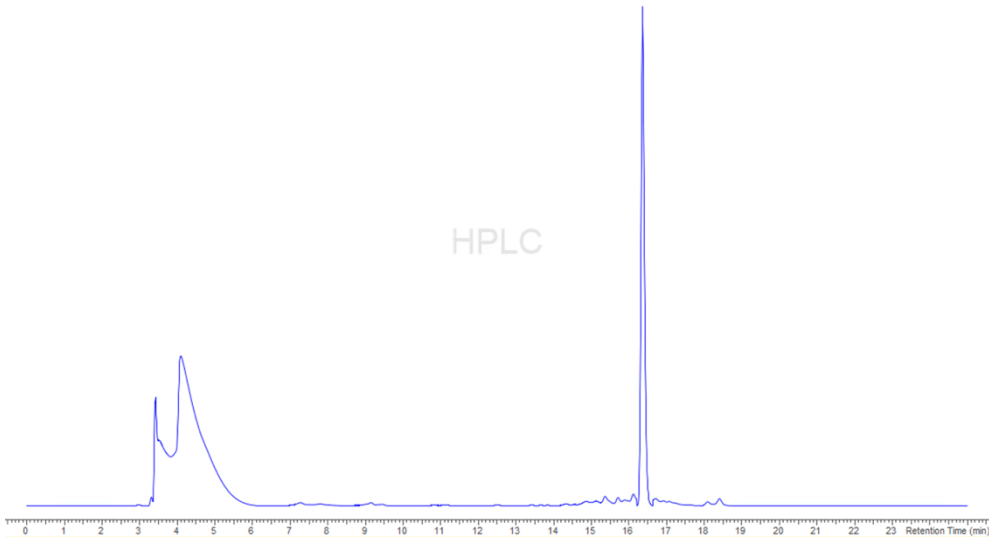

Figure 115 HPLC chromatogram, 10 μL injection, 40 °C oven temperature, eluted with 1-20% MeCN in water over 25 min. Rt = 16.4 min, 94% purity. Ignore absorbances between 3.0-5.5 min due to solvent.

2-({2-[(5-{25-Acetyl-4,7,15,18-tetraoxo-2,26,27-trioxa-3,8,14,19,25-pentaaza-1-ferrabicyclo[12.12.1]heptacosan-3-yl}pentyl)amino]-3,4-dioxocyclobut-1-en-1-yl}amino)-*N*-[8-(prop-2-en-1-yloxy)quinolin-5-yl]acetamide, 34

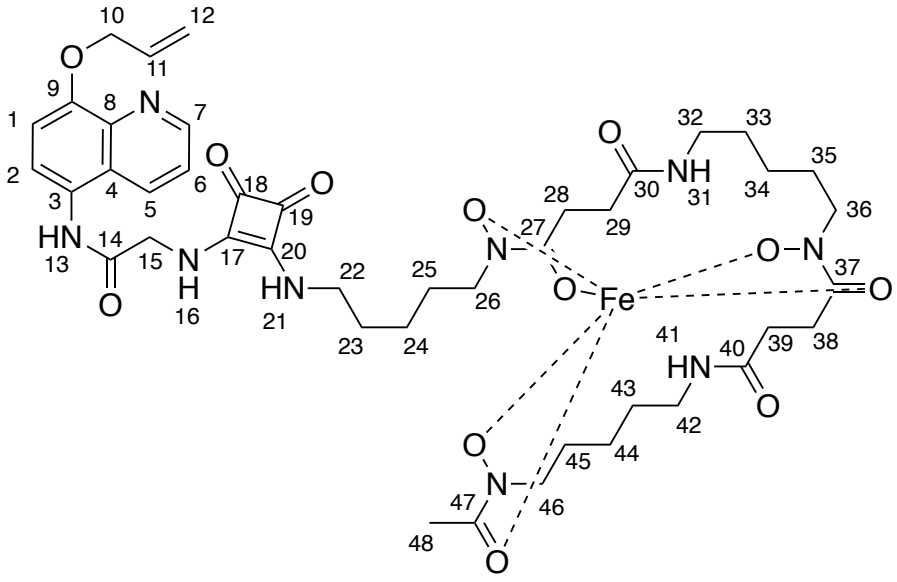

$C_{43}H_{58}FeN_9O_{12}$, 948.833 g mol^{-1}

To a suspension of *N*-[5-({3,4-dioxo-2-[({[8-(prop-2-en-1-yloxy)quinolin-5-yl]carbamo-yl}methyl)amino]cyclobut-1-enz-1-yl}amino)pentyl]-*N*-hydroxy-*N'*-[5-(*N*-hydroxy-3-{[5-(*N*-hydroxyacetamido)pentyl]carbamoyl}prop-anamido)pentyl]butan-ediamide (53.7 mg, 59.9 μmol) in dry DMF (20 mL) was added iron(III) acetylacetonate (21.2 mg, 59.9 μmol), to form an orange suspension. After stirring for 18 h at room temperature, the reaction solvent was removed *in vacuo*. The resulting residue was re-suspended in Et_2O (40 mL), where the produced supernatant was decanted to leave the solid This solid was then washed with further Et_2O (20 mL, x3), to yield the title compound as a red/orange solid.

Yield: 55 mg, 58.0 μmol, 97%

HRMS (ESI+):

Calc. for $[C_{43}H_{58}FeN_9O_{12}]+H^+$ = 949.3627 Found = 949.3592 (3.8 ppm error, 31.6 mSigma)

Calc. for $[C_{43}H_{58}FeN_9O_{12}]+Na^+$ = 971.3447 Found = 971.3409 (3.9 ppm error, 20.4 mSigma)

IR ATIR (cm^{-1}): 3472 m br (O-H stretch), 3258 m br (N-H stretch), 2924 m (Alkane C-H stretch), 2856 m (Alkane C-H stretch), 1799 w (Alkene C-H stretch), 1651 s (C=O stretch), 1574 (Alkene C=C stretch), 1525 (Aromatic C=C stretch).

Melting Point: decomposes before melting

UV-vis Spectroscopy:

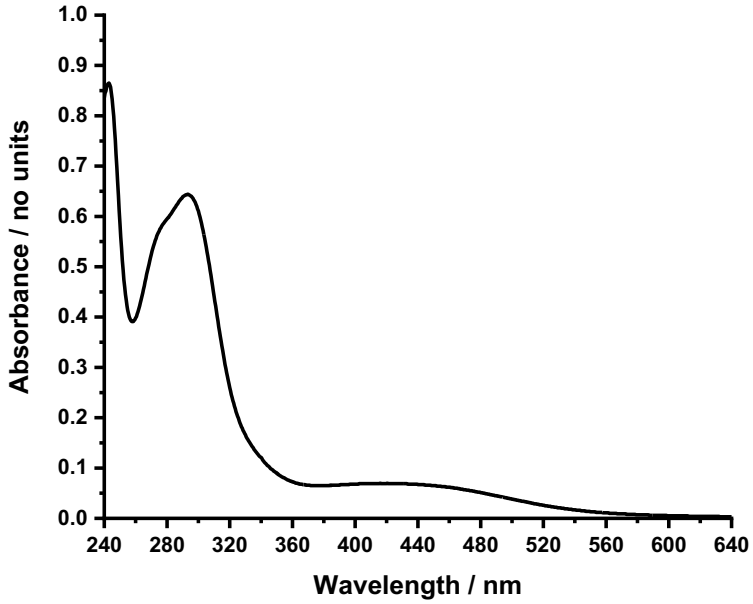

Figure 116 UV-vis spectrum, 25 μM in 10% DMSO in water.

HPLC Analysis:

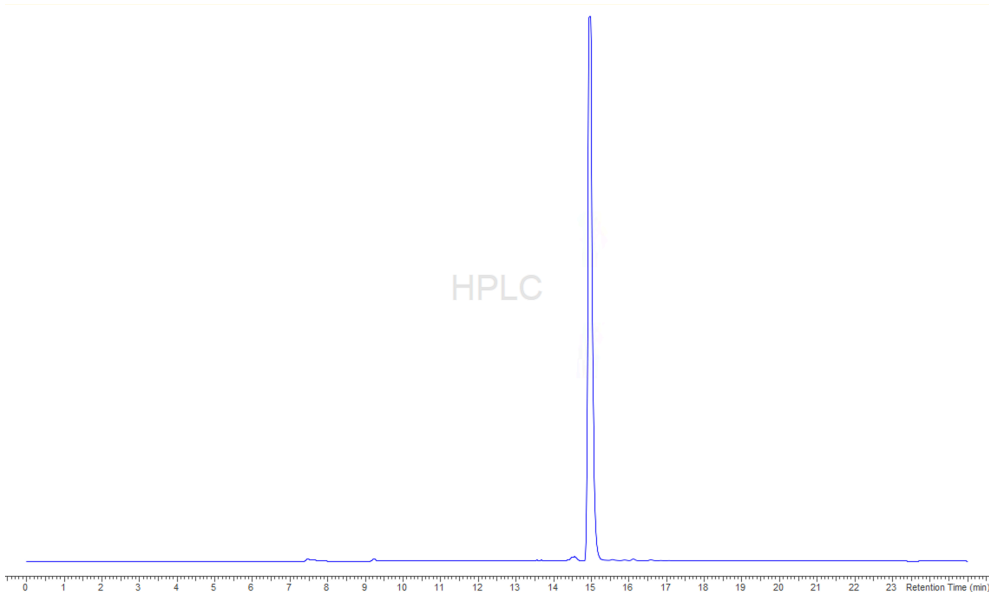

Figure 117 HPLC chromatogram, 10 μL injection, 40 °C oven temperature, eluted with 1-20% MeCN in water over 25 min, sunfire reverse phase column. Rt = 15.0 min, 99% purity.

Ru-s5

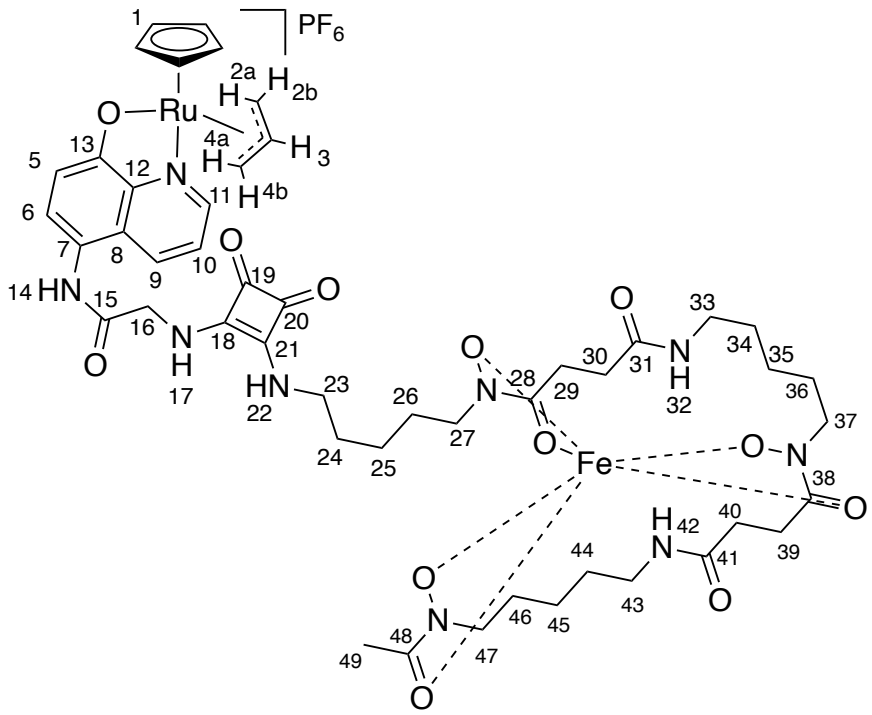

$C_{48}H_{63}F_6FeN_9O_{12}PRu$, 1259.962 g mol^{-1}

To a stirred solution of 2-({2-[(5-{25-acetyl-4,7,15,18-tetraoxo-2,26,27-trioxa-3,8,14,19,25-pentaaza-1-ferrabicyclo [12.12.1]heptacosan-3-yl}pentyl)amino]-3,4-dioxocyclobut-1-en-1-yl}amino)-*N*-[8-(prop-2-en-1-yloxy) quinolin-5-yl]acetamide (25.6 mg, 0.027 mmol) in dry, degassed dichloromethane (3 mL) was added tris-(acetonitrile)cyclopentadienylruthenium(II) hexafluorophosphate (11.7 mg, 26.9 μmol) in dry, degassed dichloromethane (2 mL) to form an red/orange suspension, under a nitrogen atmosphere. After stirring for 18 h at room temperature under these conditions a brown precipitate was observed. The reaction mixture was diluted in dichloromethane (40 mL), and the resulting supernatant was decanted to leave the solid. This solid was then washed with further dichloromethane (20 mL, x3), to yield the title compound as a light brown solid.

Yield: 24.2 mg, 19.2 μmol, 71%

HRMS (ESI+):

Calc. for $[C_{45}H_{59}FeN_9O_{12}Ru]^+$ = 1075.2581 Found = 1075.2676 (2.3 ppm error, 103.5 mSigma)

Calc. for $[C_{45}H_{58}FeN_9O_{12}Ru]+Na^+$ = 1097.2496 Found = 1097.2500 (0.5 ppm error, 91.6 mSigma)

Calc. for $[C_{45}H_{59}FeN_9O_{14}Ru]^+$ = 1107.2574 Found = 1107.2581 (0.2 ppm error, 91.5 mSigma)

Calc. for $[C_{48}H_{63}FeN_9O_{12}Ru]^+$ = 1115.2989 Found = 1115.2946 (4.8 ppm error, 94.2 mSigma)

Calc. for $[C_{45}H_{58}FeN_9O_{14}Ru]+Na^+$ = 1129.2394 Found = 1075.2367 (3.2 ppm error, 40.4 mSigma)

IR ATIR (cm^{-1}): 3266 m br (N-H stretch), 2941 m (Alkane C-H stretch), 2866 m (Alkane C-H stretch), 1801 w (Alkene C-H stretch), 1651 m (C=O stretch), 1574 (Alkene C=C stretch), 1539 (Aromatic C=C stretch).

Elemental Analysis:

Calculated for $[C_{48}H_{63}F_6FeN_9O_{12}PRu \cdot 2.4\ CH_2Cl_2]$: %C 41.35, %H 4.67, %N 8.61
Measured for $[C_{48}H_{63}F_6FeN_9O_{12}PRu \cdot 2.4\ CH_2Cl_2]$: %C 41.07, %H 4.81, %N 8.93

UV-vis Spectroscopy:

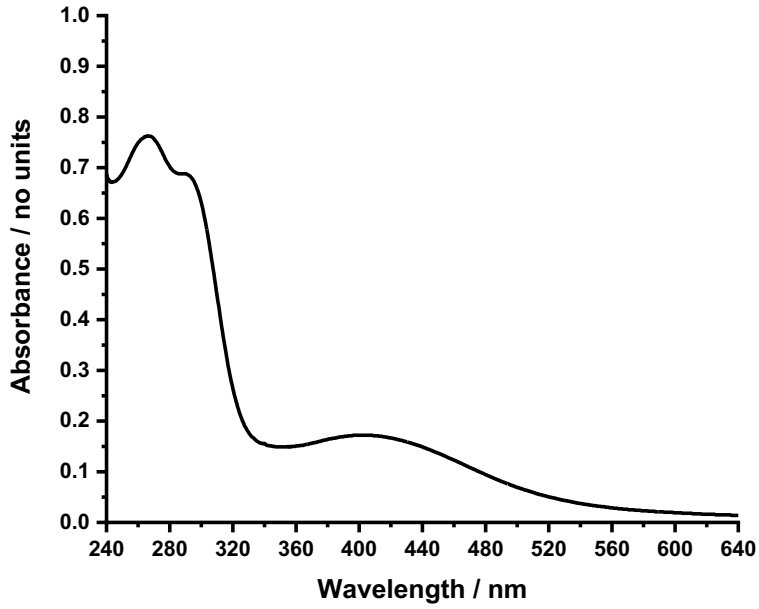

Figure 118 UV-vis spectrum, 25 μM in 10% DMSO in water.

Ru-s6

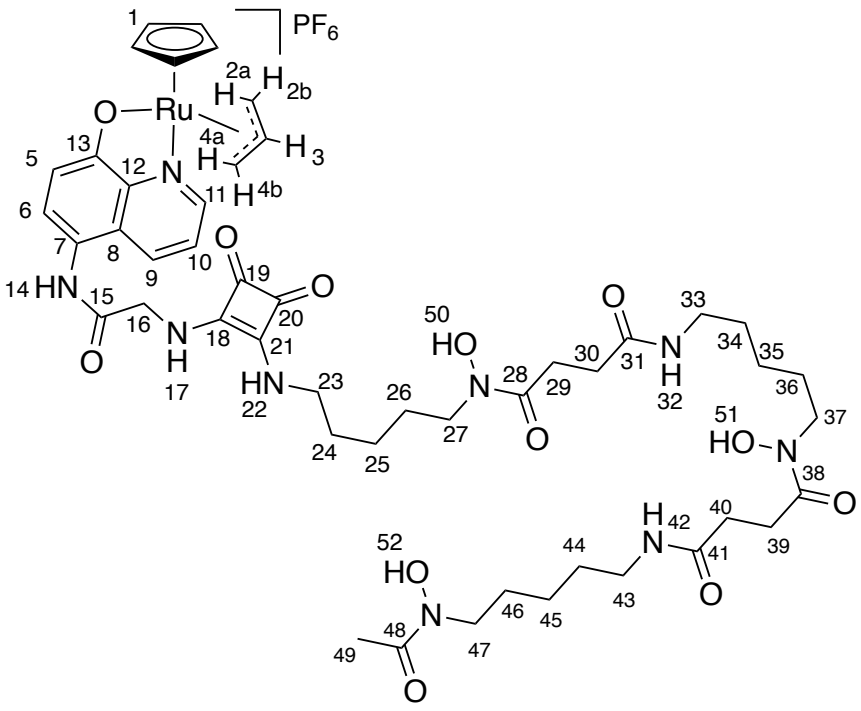

$C_{48}H_{66}F_6N_9O_{12}PRu$, 1207.1412 g mol^{-1}

To a stirred solution of tris(acetonitrile)cyclopentadienylruthenium(II) hexafluorophosphate (15.50 mg, 35.7 μmol) in dry, degassed DMF (0.5 mL) was added *N*-[5-({3,4-dioxo-2-[({[8-(prop-2-en-1-yloxy)quinolin-5-yl]carbamo-yl}methyl) amino]cyclobut-1-enz-1-yl}amino)pentyl]-*N*-hydroxy-*N'*-[5-(*N*-hydroxy-3-{[5-(*N*-hydroxyacetamido)pentyl]carbamoyl}propanamido)pentyl]butanediamide (27.19 mg, 29.7 μmol) as a solution in dry, degassed DMF (19 mL) under a dry, nitrogen atmosphere at room temperature to form, a dark red solution. After stirring for 2 h under these conditions, the ruthenium-complex was precipitated using dry Et_2O (45 mL) and the resulting supernatant decanted to leave a dark orange solid. This solid was then re-suspended in dry DMF (5 mL). The resulting supernatant was collected and the complex precipitated using dry Et_2O (45 mL). This precipitate was then washed with further dry Et_2O (20 mL, x3) and then dry dichloromethane (10 mL x3), to yield the title compound as a dark brown solid.

Yield: 16.7 mg, 13.8 μmol, 47%

HRMS (ESI+):

Calc. for $[C_{47}H_{60}N_9O_{12}PRu]^+$ = 1044.3399 Found = 1044.3434 (-2.0 ppm error, 90.6 mSigma)

Calc. for $[C_{48}H_{66}N_9O_{12}Ru]^+$ = 1062.3839 Found = 1062.3891 (-0.8 ppm error, 49.3 mSigma)

Calc. for $[C_{48}H_{65}N_9O_{12}PRu]+Na^+$ = 1084.3688 Found = 1084.3687 (1.4 ppm error, 173.5 mSigma)

^{1}H NMR: (500 MHz, DMSO-d_6) δ: 9.95 (s, 1H-**14**), 9.69 – 9.45 (m, 3H-**50+51+52**), 8.90 (d, *J* = 4.5 Hz, 1H-**11**), 8.44 (d, *J* = 8.5 Hz, 1H-**9**), 7.76 (t, *J* = 5.0 Hz, 2H-**32+42**), 7.69 – 7.48 (m, *J* = 17.5, 9.0 Hz, 1H-**10**), 7.30 (d, *J* = 8.5 Hz, 1H-**5**), 6.88 (d, *J* = 8.5 Hz, 1H-**6**), 6.25 (s, 5H-**1**), 4.51 – 4.43 (m, 2H-**3+2a/4a**), 4.25 (d, *J* = 9.5 Hz, 1H-**2a/4a**), 4.14 – 4.08 (m, 1H-**2b/4b**), 4.05 – 3.99 (m, 1H-**2b/4b**), 3.52 – 3.41 (m, 10H-**16+23+27+37+47**), 2.99 (dd, *J* = 13.0, 6.5 Hz, 4H-**33+43**), 2.57 (t, *J* = 7.0 Hz, 4H-**29+39**), 2.26 (t, *J* = 7.5 Hz, 4H-**30+40**), 1.96 (s, 3H-**49**), 1.56 – 1.45 (m, 1H-**24+26+36+46**), 1.42 – 1.33 (m, 4H-**34+44**), 1.31 – 1.18 (m, 6H-**25+35+45**).

^{13}C NMR: (151 MHz, DMSO-d_6) δ: 182.6-**19+20**, 172.0-**28+38**, 171.3-**15+31+42**, 170.1-**48**, 167.3-**13**, 155.7-**11**, 144.7-**8**, 136.0-**9**, 126.7-**5**, 125.8-**12**, 123.3-**10**, 118.6-**7**, 113.8-**6**, 98.0-**3**, 95.8-**1**, 68.2-**2/4**, 63.1-**2/4**, 47.1-**18+21**, 46.8-**16+27+37+47+18+21**, 45.9-**16+27+37+47+18+21**, 43.2-**23**, 38.4-**33+43**, 30.4-**24+26+37+47**, 29.9-**30+40**, 28.8-**34+44**, 27.5-**29+39**, 26.0-**24+26+37+47**, 23.5-**25+35+46**, 23.0-**25+35+46**, 20.3-**49**.

The additional peak at 85.6 ppm is due to the cyclopentadienyl environment of the active Ru(II) intermediate species that is presumed to form *in situ* on reaction with residual water in the NMR solvent.

In some cases, different peaks that correspond to numerous environments are undistinguishable and therefore the number of environments that correspond to each is unknown. This is the case at:

- 23.0 ppm = one or two of **25**, **35**, and **46** - which are undistinguishable
- 23.5 ppm = one or two of **25**, **35**, and **46** - which are undistinguishable

- 45.9 ppm = one, two, three, four or five of **16**, **27**, **37**, **47**, **18**, and **21** - which are undistinguishable
- 46.8 ppm = one, two, three, four or five of **16**, **27**, **37**, **47**, **18**, and **21** - which are undistinguishable

^{19}F NMR: (471 MHz, DMSO-d_6) δ: -70.2 (d, J = 711.0 Hz, 6F).

^{31}P NMR: (202 MHz, DMSO-d_6) δ: -142.4 (d, J = 711.0 Hz, 1P).

IR ATIR (cm^{-1}): 3361 m br (Alcohol O-H stretch), 3276 m br (Amide N-H stretch), 2928 m (Alkane C-H stretch), 2860 m (Alkane C-H stretch), 1803 w (Alkene C-H stretch), 1649 s (C=O stretch), 1622 s (C=O stretch), 1587 (Alkene C=C stretch), 1560 (Aromatic C=C stretch).

Elemental Analysis:

Calculated for [$C_{48}H_{66}F_6N_9O_{12}PRu$ • 1.5 CH_2Cl_2]: %C 45.24, %H 5.28, %N 9.66
Measured for [$C_{48}H_{66}F_6N_9O_{12}PRu$ • 1.5 CH_2Cl_2]: %C 45.40, %H 5.10, %N 9.50

UV-vis Spectroscopy:

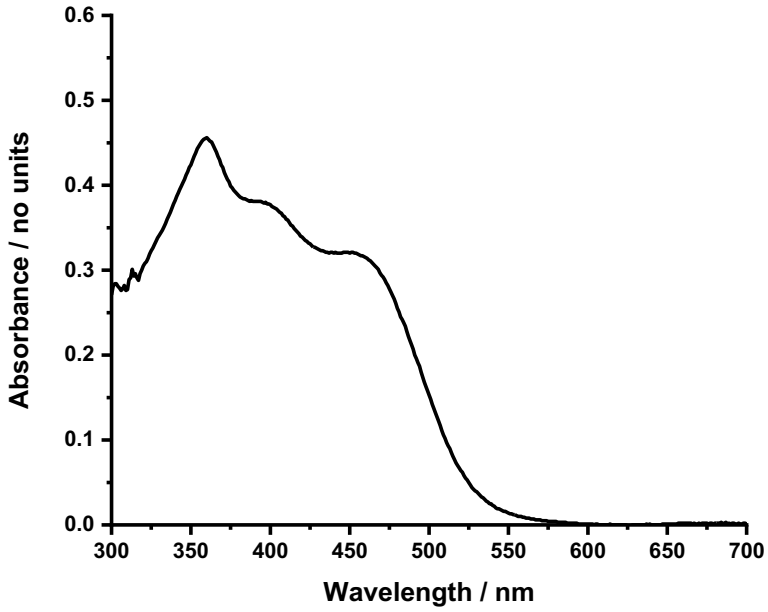

Figure 119 UV-vis spectrum, 200 μM in 10% DMSO in water.

2-(Hydroxymethyl)-5-[(4-methoxyphenyl)methoxy]-4H-pyran-4-one, 35

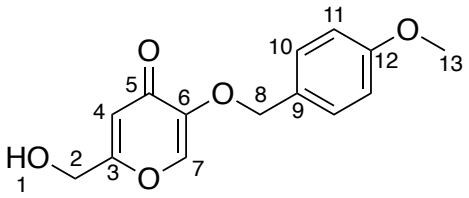

$C_{14}H_{14}O_5$, 262.26 g mol^{-1}

2-(Hydroxymethyl)-5-[(4-methoxyphenyl)methoxy]-4H-pyran-4-one was prepared based on a procedure from the literature.[218]

A suspension of kojic acid (2.29 g, 16.0 mmol), potassium carbonate (2.66 g, 19.3 mmol), 4-methoxybenzyl chloride (2.39 mL, 17.7 mmol) in dry DMF was heated to 80 °C and left stirring for 18 h. After this time, the reaction solvent was removed *in vacuo*, and the resulting beige residue was re-suspended and sonicated in water (100 mL) for 2 h. The solid produced from this sonication was isolated by filtration and washed with more water (100 mL) and finally EtOAc (50 mL) to give the title compound as a beige solid.

Yield: 3.14 g, 12.0 mmol, 74%

Rf: 0.56 in dichloromethane : MeOH (8:2)

HRMS (ESI+):

Calc. for $[C_{14}H_{14}O_5]+Na^+$ = 285.0733 Found = 285.0731 (0.9 ppm error, 3.1 mSigma)

^{1}H NMR: (400 MHz, DMSO-*d*$_6$) δ 8.15 (s, 1H-**7**), 7.34 (d, *J* = 8.5 Hz, 2H-**10**), 6.95 (d, *J* = 8.5 Hz, 2H-**11**), 6.31 (s, 1H-**4**), 5.69 (br s, 1H-**1**), 4.85 (s, 2H-**8**), 4.29 (s, 2H-**2**), 3.76 (s, 3H-**13**).

^{13}C NMR: (126 MHz, DMSO-*d*$_6$) δ: 173.3-**5**, 168.0-**3**, 159.3-**12**, 146.6-**6**, 141.1-**7**, 130.1-**10**, 128.1-**9**, 113.8-**11**, 111.2-**4**, 70.3-**8**, 59.3-**2**, 55.1-**13**.

NMR spectra are in agreement with literature reports.[218]

Elemental Analysis:

Calculated for [$C_{14}H_{14}O_5$ • 0.25 H_2O]: %C 63.03, %H 5.48

Measured for [$C_{14}H_{14}O_5$ • 0.25 H_2O]: %C 63.00, %H 5.24

2-(Hydroxymethyl)-1,5-bis[(4-methoxyphenyl)methoxy]-1,4-dihydropyridin-4-one, 36

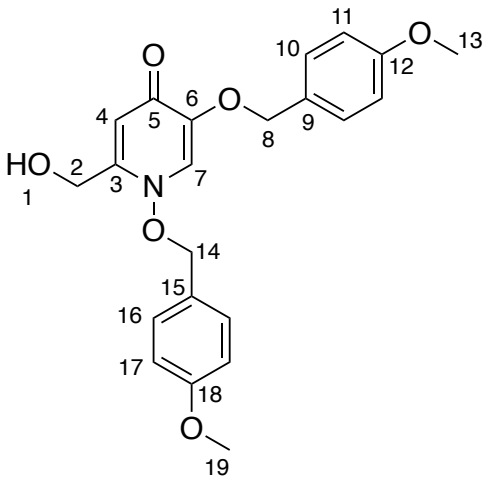

$C_{22}H_{23}NO_6$, 397.43 g mol^{-1}

2-(Hydroxymethyl)-1,5-bis[(4-methoxyphenyl)methoxy]-1,4-di-hydropyridin-4-one was prepared based on a procedure from the literature.[217]

To a stirred solution of 2-(hydroxymethyl)-5-[(4methoxyphenyl)methoxy]-4H-pyran-4-one (666 mg, 2.54 mmol) and potassium carbonate (1.05 g, 7.62 mmol) in dry DMF (10 mL), was added hydroxylamine hydrochloride (529 mg, 7.62 mmol) at room temperature. This solution was then heated to 70 °C and left stirring for 18 h. After this time, 4-methoxybenzyl chloride (516 μL, 3.81 mmol) was added at room temperature, and the resulting solution left stirring for another 24 h. After this time, the reaction solvent was removed *in vacuo*, the resulting residue re-dissolved in dichloromethane (50 mL) and washed with water (50 mL). The aqueous layer was extracted with dichloromethane (50 mL, x2), the organic layers were combined, and the solvent removed *in vacuo*. The resulting orange oil purified *via* column chromatography, eluting with dichloromethane : MeOH (20:1 – 5:1) and then triturated with diethyl ether, to yield the title compound as a light orange solid.

Yield: 193 mg, 1.23 mmol, 49%

Rf: 0.12 in dichloromethane : MeOH (19:1)

HRMS (ESI+):

Calc. for $[C_{14}H_{14}O_5]+H^+$ = 398.1598 Found = 398.1597 (0.4 ppm error, 4.2 mSigma)

Calc. for $[C_{14}H_{14}O_5]+Na^+$ = 420.1418 Found = 420.1413 (1.0 ppm error, 1.0 mSigma)

Calc. for $[C_{14}H_{14}O_5]+K^+$ = 436.1157 Found = 436.1153 (0.8 ppm error, 5.2 mSigma)

^{1}H NMR: (400 MHz, DMSO-*d*$_6$) δ 7.93 (s, 1H-**4**), 7.41 (d, *J* = 8.5 Hz, 2H-**16**), 7.36 (d, *J* = 8.5 Hz, 2H-**10**), 6.98 (t, *J* = 9.0 Hz, 2H-**17**), 6.96 (t, *J* = 9.0 Hz, 2H-**11**), 6.09 (s, 1H-**7**), 5.56 (t, *J* = 6.0 Hz, 1H-**1**), 5.16 (s, 2H-**14**), 4.91 (s, 2H-**8**), 4.35 (d, *J* = 6.0 Hz, 2H-**2**), 3.78 (s, 3H-**19**), 3.76 (s, 3H-**13**).

^{13}C NMR: (126 MHz, DMSO-*d*$_6$) δ: 170.9-**5**, 160.2-**18**, 159.2-**12**, 147.6-**3**, 146.5-**6**, 132.1-**16**, 130.0-**10**, 128.6-**9**, 125.1-**15**, 122.9-**4**, 114.0-**11/17**, 113.8-**11/17**, 110.7-**7**, 79.8-**14**, 70.3-**8**, 56.8-**2**, 55.2-**19**, 55.1-**13**.

NMR spectra are in agreement with literature reports.[217]

{5-[(4-Methoxyphenyl)methoxy]-4-oxo-4*H*-pyran-2-yl}methyl-*N*-({[8-(prop-2-en-1-yloxy)quinolin-5-yl]carbamoyl}methyl)carbamate, 39

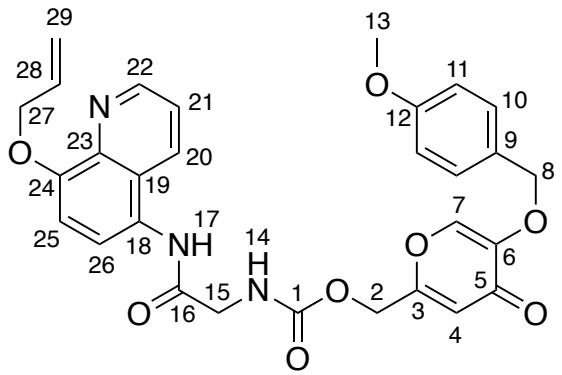

$C_{29}H_{27}N_3O_8$, 545.548 g mol^{-1}

{5-[(4-Methoxyphenyl)methoxy]-4-oxo-4H-pyran-2-yl}methyl-*N*-({[8-(prop-2-en-1-yloxy)quinolin-5-yl]carbamoyl}methyl)carbamate was prepared based on a procedure from the literature.[217]

To a stirred solution of 2-(hydroxymethyl)-5-[(4-methoxyphenyl)methoxy]-4H-pyran-4-one (60 mg, 0.229 mmol) in dry DMF (3 mL) was added carbonyldiimidazole (133 mg, 0.817 mmol) and left stirring for 22 h, at room temperature. After this time, a solution of DIPEA (57 μL, 0.326 mmol) and 5-(2-azaniumylacetamido)-8-(prop-2-en-1-yloxy)quinolin-1-ium ditrifluoroacetate (61 mg, 0.163 mmol) in dry DMF (2 mL) was added dropwise and the mixture was left stirring for an additional 18 h, at room temperature. The reaction solvent was then removed *in vacuo*, and the resulting residue re-dissolved in dichloromethane (40 mL) and washed with sat. NH_4Cl(aq) (20 mL, x3) and then sat. $NaHCO_3$(aq) (20 mL, x3). The organic layer solvent was then removed *in vacuo*, and purified *via* column chromatography, eluting with EtOAc : MeOH (23:2) to yield the title compound as a beige solid.

Yield: 40 mg, 72.8 μmol, 45%

Rf: 0.46 in EtOAc : MeOH (9:1)

HRMS (ESI+):

Calc. for $[C_{29}H_{27}N_3O_8]+H^+$ = 546.1871 Found = 546.1858 (2.3 ppm error, 29.2 mSigma)

Calc. for $[C_{29}H_{27}N_3O_8]+Na^+$ = 568.1690 Found = 568.1680 (1.8 ppm error, 5.8 mSigma)

^{1}H NMR: (400 MHz, DMSO-*d*$_6$) δ: 9.92 (s, 1H-**17**), 8.88 (dd, *J* = 4.5, 1.5 Hz, 1H-**22**), 8.33 (dd, *J* = 8.5, 1.5 Hz, 1H-**20**), 8.22 (s, 1H-**7**), 7.89 (t, *J* = 6.0 Hz, 1H-**14**), 7.58 (dd, *J* = 8.5, 4.0 Hz, 1H-**21**), 7.50 (d, *J* = 8.5 Hz, 1H-**25/26**), 7.34 (d, *J* = 8.5 Hz, 2H-**10**), 7.20 (d, *J* = 8.5 Hz, 1H-**25/26**), 6.95 (d, *J* = 8.5 Hz, 2H-**11**), 6.44 (s, 1H-**4**), 6.17 (ddt, *J* = 17.4, 10.5, 5.5 Hz, 1H-**28**), 5.51 (dd, *J* = 17.0, 2.0 Hz, 1H-**29(trans)**), 5.31 (dd, *J* = 10.5, 1.5 Hz, 1H-**29(cis)**), 4.94 (s, 2H-**2**), 4.85 (s, 2H-**8**), 4.77 (dt, *J* = 5.5, 1.5 Hz, 2H-**27**), 3.96 (d, *J* = 6.0 Hz, 2H-**15**), 3.75 (s, 3H-**13**).

^{13}C NMR: (126 MHz, DMSO-*d*$_6$) δ: 173.0-**5**, 168.8-**1/16**, 162.6-**1/16**, 159.3-**12**, 155.8-**3**, 152.1-**24**, 149.0-**22**, 146.8-**6**, 141.4-**7**, 139.8-**18**, 133.7-**28**, 131.2-**20**, 130.1-**10**, 127.9-**9**, 125.7-**19/23**, 124.8-**19/23**, 123.2-**26**, 121.5-**21**, 117.8-**29**, 113.8-**11**, 113.2-**4**, 109.3-**25**, 70.3-**2**, 69.1-**27**, 61.2-**8**, 55.1-**13**, 43.9-**15**.

IR ATIR (cm^{-1}): 3202 m br (N-H stretch), 3035 w br (Aromatic/Alkene C-H stretch), 2951 w (Aromatic/Alkene C-H stretch), 1731 s (C=O stretch), 1659 s (C=O stretch), 1550 s (Alkene C=C stretch), 1504 m (Aromatic C=C stretch).

Elemental Analysis:

Calculated for [$C_{29}H_{27}N_3O_8$ • 0.5 H_2O]: %C 62.81, %H 5.09, %N 7.58
Measured for [$C_{29}H_{27}N_3O_8$ • 0.5 H_2O]: %C 62.54, %H 4.82 %N 7.63

Melting Point: 180-182 °C

(5-Hydroxy-4-oxo-4H-pyran-2-yl)methyl-*N*-({[8-(prop-2-en-1-yloxy) quinolin-5-yl]carbamoyl}methyl)carbamate, 40

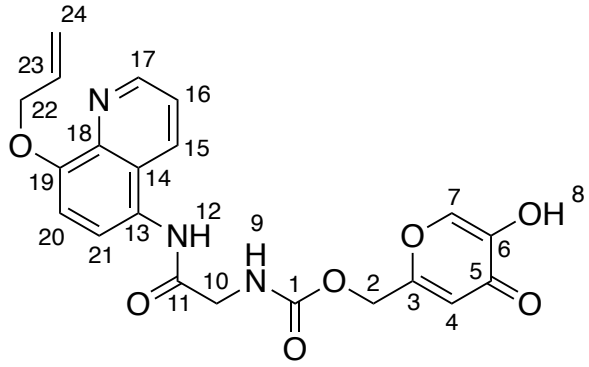

$C_{21}H_{19}N_3O_7$, 425.397 g mol^{-1}

To a stirred solution of {5-[(4-methoxyphenyl)methoxy]-4-oxo-4*H*-pyran-2-yl}methyl-*N*-({[8-(prop-2-en-1-yloxy)quinolin-5-yl]carbamoyl}methyl)carbamate (25.7 mg, 0.0471 mmol) in dichloromethane (2.5 mL) was added trifluoroacetic acid (0.25 mL, 32.7 mmol) dropwise at room temperature, and the resulting solution was left to stir under these conditions for 30 min. After this time, the solvent was removed *in vacuo* with co-evaporation with MeOH (x3, 5 mL), free-based using an SCX cartridge, loading in minimum dichloromethane : MeOH (1:1), washing with MeOH (x3, 5 mL) and eluted with 7N NH_3 in MeOH (5 mL). The resulting solution was then dried *in*

vacuo, re-dissolved in minimum dichloromethane : MeOH (1:1) and precipitated with Et_2O to yield the title compound as a beige solid.

Yield: 16.2 mg, 38.1 μmol, 81%

Rf: 0.17 in EtOAc : MeOH (23:1)

HRMS (ESI+):

Calc. for $[C_{21}H_{19}N_3O_7]+H^+$ = 426.1296 Found = 426.1290 (1.4 ppm error, 5.5 mSigma)

Calc. for $[C_{21}H_{19}N_3O_7]+Na^+$ = 448.1115 Found = 448.1118 (-0.5 ppm error, 17.9 mSigma)

^{1}H NMR: (400 MHz, MeOD-*d_4* : $CDCl_3$ (5:3)) δ: 9.02 (d, *J* = 3.5 Hz, 1H-**17**), 8.51 (d, *J* = 8.5 Hz, 1H-**15**), 8.06 (s, 1H-**7**), 7.71 (dd, *J* = 14.5, 6.0 Hz, 2H-**16+20/21**), 7.29 (d, *J* = 8.5 Hz, 1H-**20/21**), 6.70 (s, 1H-**4**), 6.37 (ddt, *J* = 16.0, 10.5, 5.5 Hz, 1H-**23**), 5.65 (d, *J* = 17.0 Hz, 1H-**24(trans)**), 5.51 (d, *J* = 10.5 Hz, 1H-**24(cis)**), 5.17 (s, 2H-**2**), 5.02 (d, *J* = 5.0 Hz, 2H-**22**), 4.27 (s, 2H-**10**).

^{13}C NMR: (126 MHz, MeOD-*d_4* : $CDCl_3$ (5:3)) δ: 175.6-**5**, 170.9-**11+1**, 164.1-**3**, 157.2, 153.3-**19**, 149.3-**17**, 147.0-**6**, 140.4-**7**, 140.1-**13**, 133.5-**15**, 133.2-**28**, 126.4-**14/18**, 125.5-**14/18**, 125.1-**20/21**, 122.5-**16**, 118.5-**24**, 112.1-**4**, 109.6-**20/21**, 70.5-**22**, 62.6-**2**, 44.9-**10**.

IR ATIR (cm^{-1}): 3248 m br (O-H stretch), 3077 w (Aromatic/Alkene C-H stretch), 1745 s (C=O stretch), 1649 s (C=O stretch), 1609 s (Alkene C=C stretch), 1580 m (Aromatic C=C stretch).

Elemental Analysis:

Calculated for $[C_{21}H_{19}N_3O_7]$: %C 62.81, %H 5.09, %N 7.58
Measured for $[C_{21}H_{19}N_3O_7]$: %C 62.54, %H 4.82 %N 7.63

Melting Point: 174-176 °C

Ru-s8

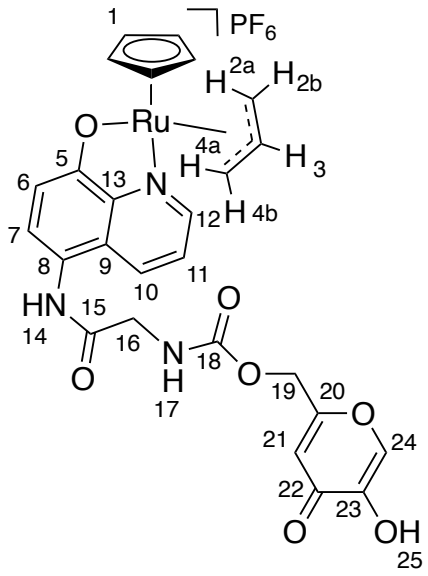

$C_{26}H_{24}F_6N_3O_7PRu$, 736.526 g mol^{-1}

To a stirred solution of tris(acetonitrile)cyclopentadienylruthenium(II) hexafluorophosphate (7.68 mg, 17.7 μmol) in dry, degassed DMF (0.5 mL) was added (5-hydroxy-4-oxo-4H-pyran-2-yl)methyl-*N*-({[8-(prop-2-en-1-yloxy)quinolin-5-yl]carbamoyl}methyl)carbamate (7.52 mg, 17.7 μmol) as a solution in dry, degassed DMF (3 mL) under a dry, nitrogen atmosphere at room temperature to form, at first a dark red solution which turned to a light red solution over 2 min. After stirring for 30 min under these conditions, the reaction mixture was precipitated using dry Et_2O (45 mL), centrifuged (10 min, at 4.4 rps) where the resulting supernatant was decanted to leave the solid. This solid was washed with dry Et_2O (20 mL, x4) and then dry dichloromethane (20 mL, x2), to yield the title compound as a dark orange/brown solid.

Yield: 10.0 mg, 13.6 μmol, 77%

HRMS (ESI+):

Calc. for $[C_{23}H_{19}N_3NaO_7Ru]^+$ = 574.0159 Found = 574.0172 (-1.1 ppm error, 23.7 mSigma)

Calc. for $[C_{26}H_{24}N_3O_7Ru]^+$ = 592.0652 Found = 592.0652 (-0.2 ppm error, 68.3 mSigma)

Calc. for $[C_{23}H_{19}N_3NaO_9Ru]^+$ = 606.0057 Found = 606.0011 (8.7 ppm error, 153.4 mSigma)

^{1}H NMR: (500 MHz, DMSO-*d*$_6$) δ: 9.79 (s, 1H-**14**), 9.21 (s, 1H-**25**), 8.89 (d, *J* = 4.5 Hz, 1H-**12**), 8.35 (d, *J* = 8.5 Hz, 1H-**10**), 8.08 (s, 1H-**24**), 7.84 (t, *J* = 6.0 Hz, 1H-**17**), 7.63 (dd, *J* = 8.5, 5.0 Hz, 1H-**11**), 7.27 (d, *J* = 8.5 Hz, 1H-**7**), 6.87 (d, *J* = 8.5 Hz, 1H-**6**), 6.43 (s, 1H-**21**), 6.25 (s, 5H-**1**), 4.92 (s, 2H-**19**), 4.54 – 4.42 (m, 2H-**3+2a/4a**), 4.25 (d, *J* = 9.5 Hz, 1H-**2a/4a**), 4.14 – 4.09 (m, 1H-**2b/4b**), 4.04 – 3.99 (m, 1H-**2b/4b**), 3.90 (d, *J* = 6.0 Hz, 2H-**16**).

^{13}C NMR: (126 MHz, DMSO-*d*$_6$) δ: 173.6-**22**, 168.9-**15**, 167.2-**5**, 162.5-**20**, 155.8-**18**, 155.7-**12**, 146.0-**23**, 144.7-**13**, 139.7-**24**, 135.9-**10**, 126.7-**7**, 125.9-**9**, 123.3-**11**, 118.9-**8**, 113.8-**6**, 111.9-**27**, 98.0-**3**, 95.8-**1**, 68.2-**2/4**, 63.0-**2/4**, 61.4-**19**, 43.8-**16**.

^{19}F NMR: (471 MHz, DMSO-*d*$_6$) δ: -70.2 (d, *J* = 711.0 Hz, 6F).

^{19}P NMR: (202 MHz, DMSO-*d*$_6$) δ: -144.2 (sp, *J* = 711.0 Hz, 1P).

IR ATIR (cm^{-1}): 3266 w br (O-H stretch), 3110 w (Aromatic/Alkene C-H stretch), 1721 m (C=O stretch), 1649 m (C=O stretch), 1572 m (Alkene C=C stretch), 1500 m (Aromatic C=C stretch).

Elemental Analysis:

Calculated for $[C_{26}H_{24}F_6N_3O_7PRu \cdot 1.0\ CH_2Cl_2 \cdot 0.25\ C_4H_{10}O]$: %C 40.04, %H 3.42, %N 5.00
Measured for $[C_{26}H_{24}F_6N_3O_7PRu \cdot 1.0\ CH_2Cl_2 \cdot 0.25\ C_4H_{10}O]$: %C 40.45, %H 2.98 %N 4.56

UV-vis Spectroscopy:

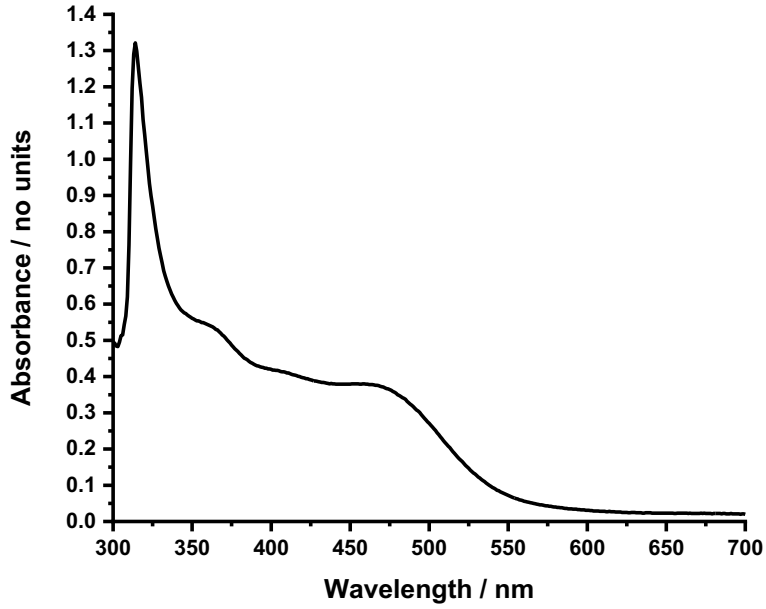

Figure 120 UV-vis spectrum, 200 μM in DMSO.

6.3 Catalyst-mediated Prodrug Activation Kinetics using HPLC

Reaction kinetics for catalyst-mediated prodrug activation were measured using an HPLC assay, the procedure of which is detailed below, separated into sections labelled: sample conditions, column conditions, calibration curves and kinetic runs. This assay was carried out by taking aliquots of a sample, at specific time intervals during a kinetic run under sample conditions and injecting them onto an HPLC column. The solvent gradient for elution was optimised for the separation of reaction components, which were subsequently quantified using calibration curve data that is obtained for each reaction component by measuring UV-vis absorbance relative to an internal standard. This data was plotted to represent data as conversion as a function of time.

6.3.1 Sample Conditions

10% DMSO in aqueous buffer (see below) with 500 μM caffeine (internal standard) +/- glutathione (5 mM), at a specified pH at room temperature under aerobic or anaerobic conditions (see 6.3.4).

Buffers:

- Aqueous M9 buffer (pH 7.0, 70 mM)
- Aqueous MOPS buffer (pH 7.4, 40 mM)

6.3.2 Column Conditions

Elution: (i) 20-27% acetonitrile in water over 5 min, (ii) 27-99% over 5 min, (iii) 99-20% for 5 min (total run time = 15 min). Both acetonitrile and water mobiles phases contained 0.1% w/v formic acid.

Column: Sunfire reverse phase column.

Oven Temperature: 40 °C.

Injection Volume: 20 μL.

6.3.3 Calibration Curves

The area under the curve (AUC) for the UV-vis absorbance of moxifloxacin, ***N*-moxi**, and ***C*-moxi** was measured at 290 nm, relative to the internal standard caffeine (500 μM) at room temperature, over a concentration range that contains those expected during kinetic runs. The obtained relative absorbance data (reagent AUC / caffeine AUC) at 290 nm was then plotted against the known reagent concentration.

6.3.3.1 Calibration Curves for Moxifloxacin, *N*-moxi and *C*-moxi in Aqueous M9 Buffer

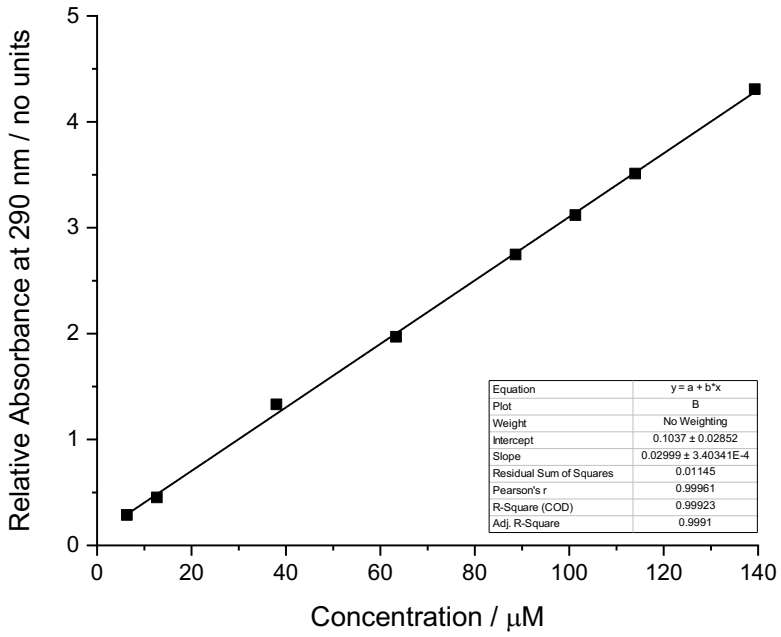

Figure 121 Calibration curve for moxifloxacin (5 – 140 μM) as relative absorbance at 290 nm to caffeine (500 μM) in aq. M9 buffer (70 mM) at pH 7.0 at room temperature.

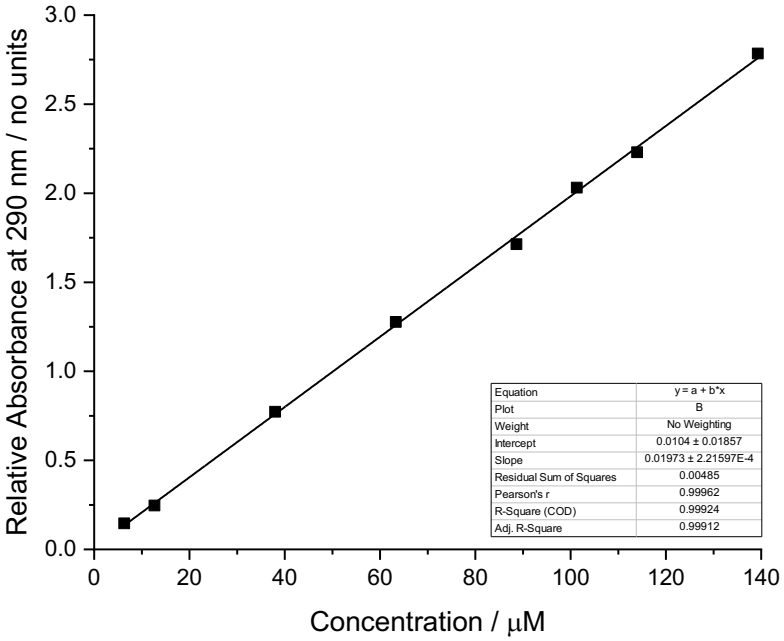

Figure 122 Calibration curve for ***N*-moxi** (5 – 140 μM) as relative absorbance at 290 nm to caffeine (500 μM) in aq. M9 buffer (70 mM) at pH 7.0 at room temperature.

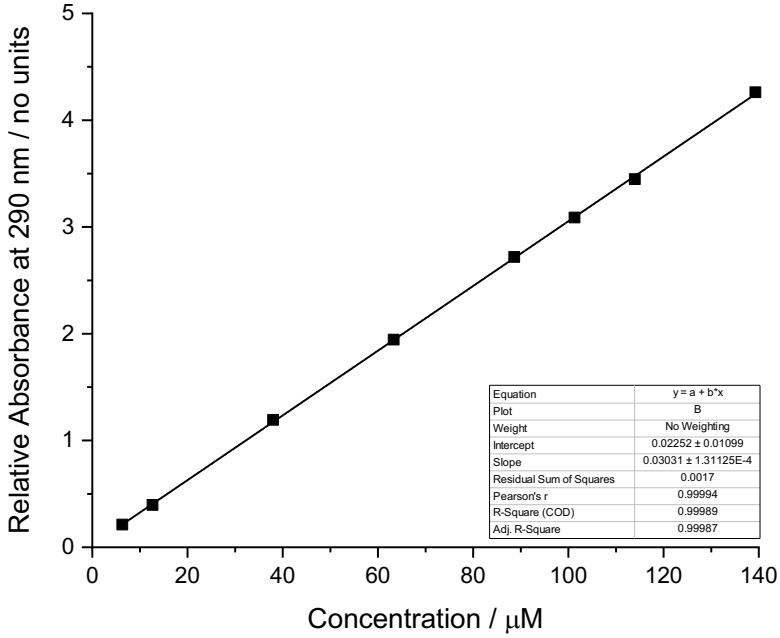

Figure 123 Calibration curve for ***C*-moxi** (5 – 140 μM) as relative absorbance at 290 nm to caffeine (500 μM) in aq. M9 buffer (70 mM) at pH 7.0 at room temperature.

6.3.3.2 Calibration Curves for Moxifloxacin and *C*-moxi in Aqueous MOPS Buffer

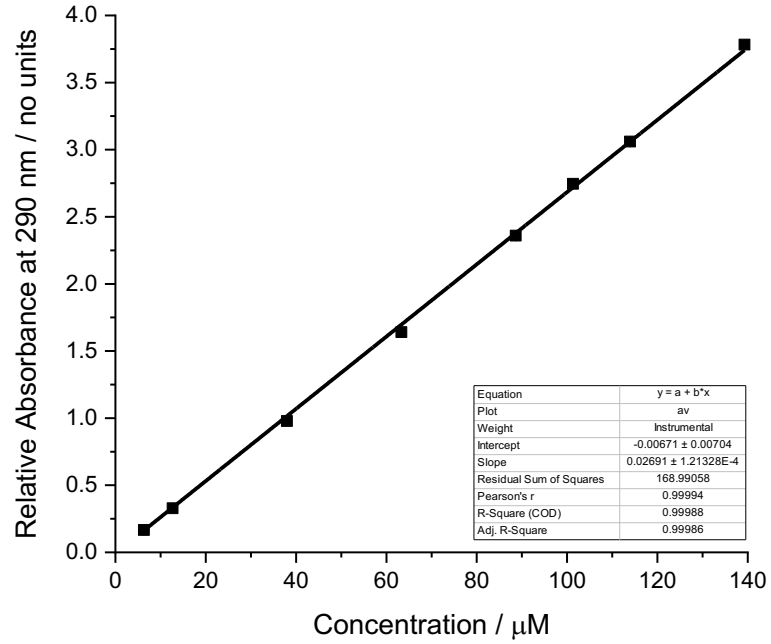

Figure 124 Calibration curve for moxifloxacin (5 – 110 μM) as relative absorbance at 290 nm to caffeine (500 μM) in aq. MOPS buffer (40 mM) at pH 7.0 at room temperature.

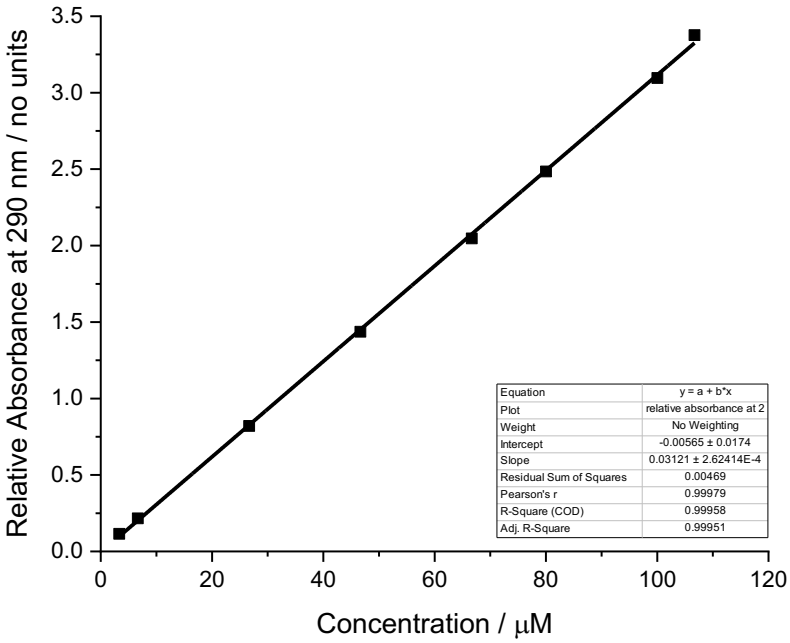

Figure 125 Calibration curve for ***C*-moxi** (5 – 140 μM) as relative absorbance at 290 nm at caffeine (500 μM) in aq. MOPS buffer (40 mM) at pH 7.0 at room temperature.

6.3.4 Kinetic Run Procedure

AUC data for each reaction component and caffeine (internal standard) was extracted and converted to conversion % using the relevant calibration curves obtained in section 6.3.3 as a function of time, in hours. In some cases, prodrug consumption is omitted for clarity. The length of kinetic runs varies depending on the kinetic profile.

6.3.4.1 Aerobic Conditions

Reaction samples were made up into 2 mL HPLC vials at a volume of 1.6 mL. T = 0 at time of catalyst addition. Prodrug starting concentration was 100 μM. Reaction aliquots for measurement were taken at intervals, which vary depending on the experiment. Experimental triplicates (where relevant) were ran at 15-minute staggered start times, so that injection is taken at the same reaction time. Injection time corresponds to reaction time.

6.3.4.2 Anaerobic Conditions

Reaction samples were made up in a Schlenk tube under a nitrogen atmosphere at a volume of 3.2 mL in de-gassed solvent. T = 0 at time of catalyst addition. Prodrug

starting concentration was 100 μM. Reaction aliquots of 0.2-0.3 mL for measurement were taken at intervals which vary depending on the experiment, from the Schlenk tube and filter transferred into high-recovery HPLC vials. Experimental triplicates (where relevant) were ran at 15-minute staggered start times, so that injection is taken at the same reaction time. Injection time corresponds to reaction time.

6.3.5 Additional Data for *C*-moxi Activation by Catalyst-Siderophore Catalyst Conjugates

This section includes ***C*-moxi** consumption and corresponding moxifloxacin formation kinetic data for each of the synthesised catalyst-siderophore conjugates and the control catalyst (**Ru-control**) under biologically relevant conditions under an anaerobic atmosphere.

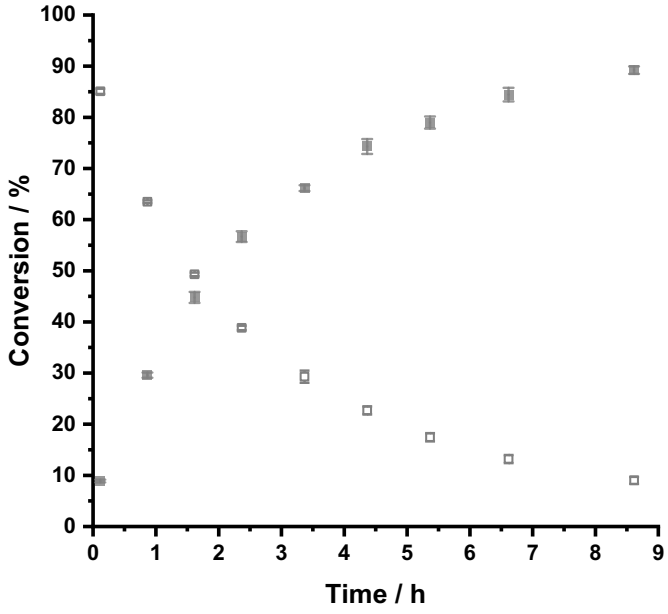

Figure 126 Catalyst-mediated prodrug activation kinetics in 10% DMSO in aqueous MOPS buffer at pH 7.4 at room temperature under an anaerobic atmosphere, showing ***C*-moxi** (100 μM) consumption (empty squares) and moxifloxacin formation (solid squares) for **Ru-control** at 10 mol % loading.

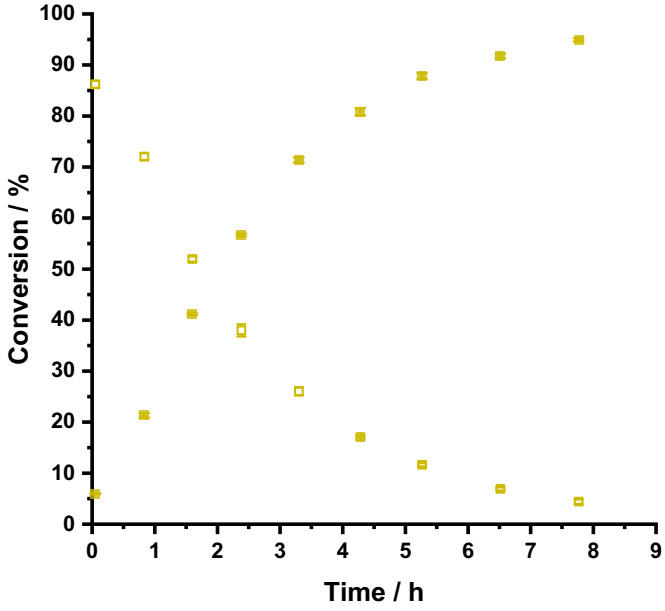

Figure 127 Catalyst-mediated prodrug activation kinetics in 10% DMSO in aqueous MOPS buffer at pH 7.4 at room temperature under an anaerobic atmosphere, showing ***C*-moxi** (100 μM) consumption (empty squares) and moxifloxacin formation (solid squares) for **Ru-s2** at 10 mol % loading.

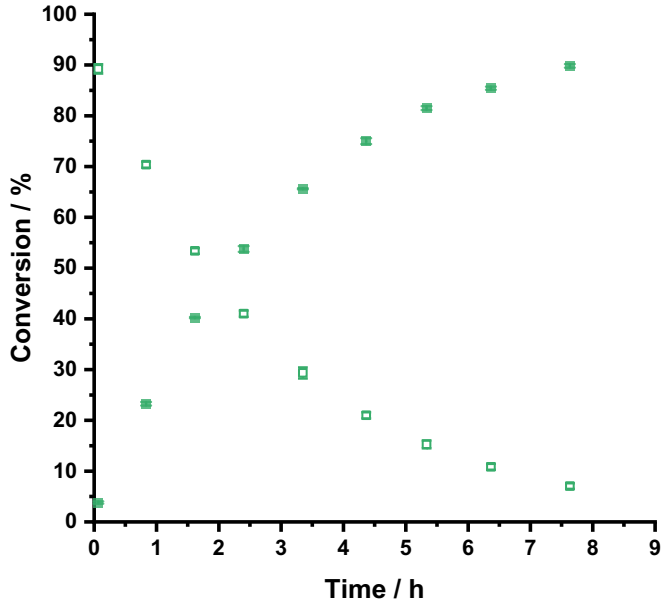

Figure 128 Catalyst-mediated prodrug activation kinetics in 10% DMSO in aqueous MOPS buffer at pH 7.4 at room temperature under an anaerobic atmosphere, showing ***C*-moxi** (100 μM) consumption (empty squares) and moxifloxacin formation (solid squares) for **Ru-s3** at 10 mol % loading.

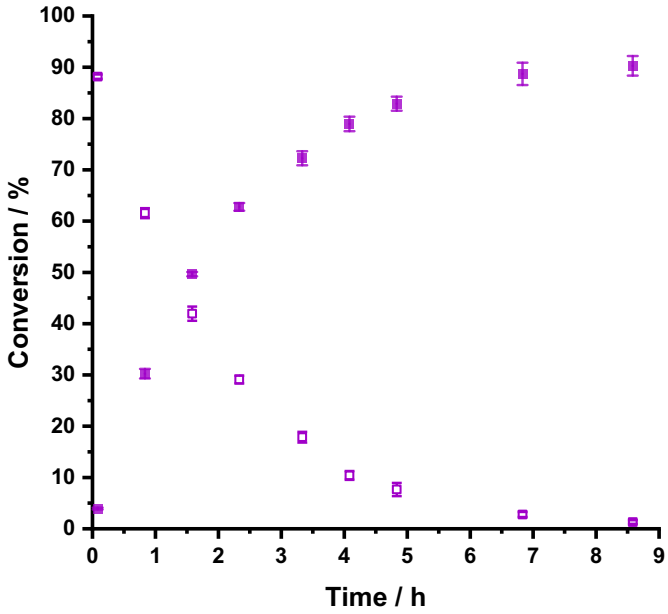

Figure 129 Catalyst-mediated prodrug activation kinetics in 10% DMSO in aqueous MOPS buffer at pH 7.4 at room temperature under an anaerobic atmosphere, showing ***C*-moxi** (100 μM) consumption (empty squares) and moxifloxacin formation (solid squares) for **Ru-s4** at 10 mol % loading.

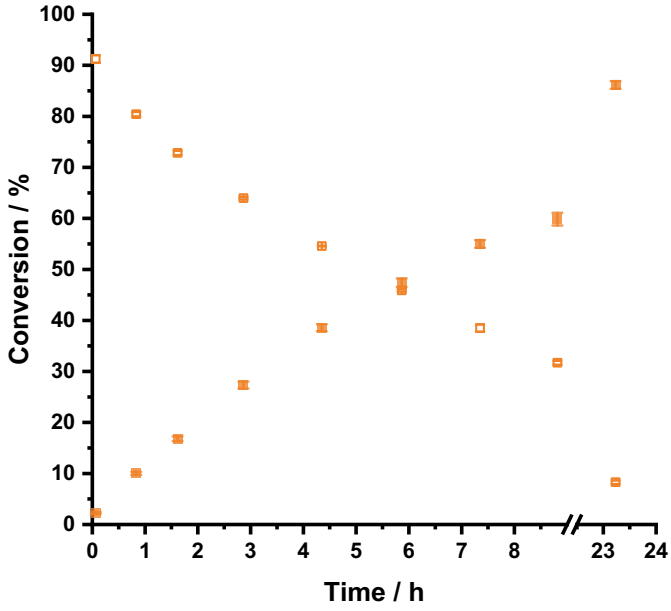

Figure 130 Catalyst-mediated prodrug activation kinetics in 10% DMSO in aqueous MOPS buffer at pH 7.4 at room temperature under an anaerobic atmosphere, showing ***C*-moxi** (100 μM) consumption (empty squares) and moxifloxacin formation (solid squares) for **Ru-s5** at 10 mol % loading.

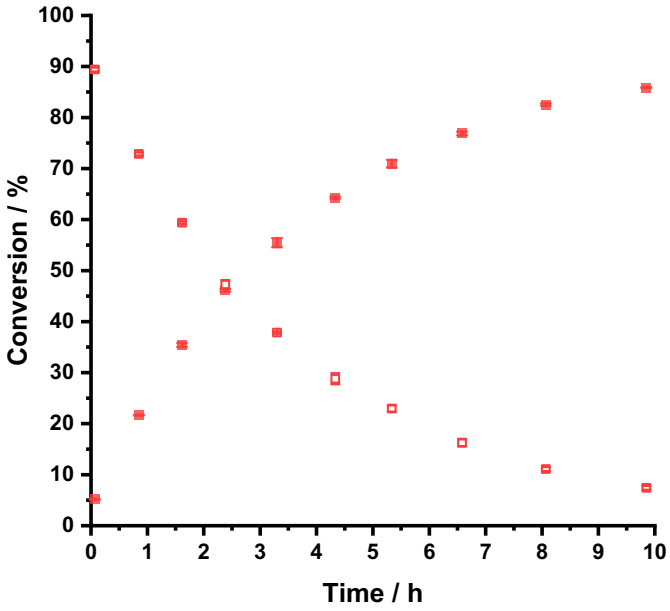

Figure 131 Catalyst-mediated prodrug activation kinetics in 10% DMSO in aqueous MOPS buffer at pH 7.4 at room temperature under an anaerobic atmosphere, showing ***C*-moxi** (100 μM) consumption (empty squares) and moxifloxacin formation (solid squares) for **Ru-s6** at 10 mol % loading.

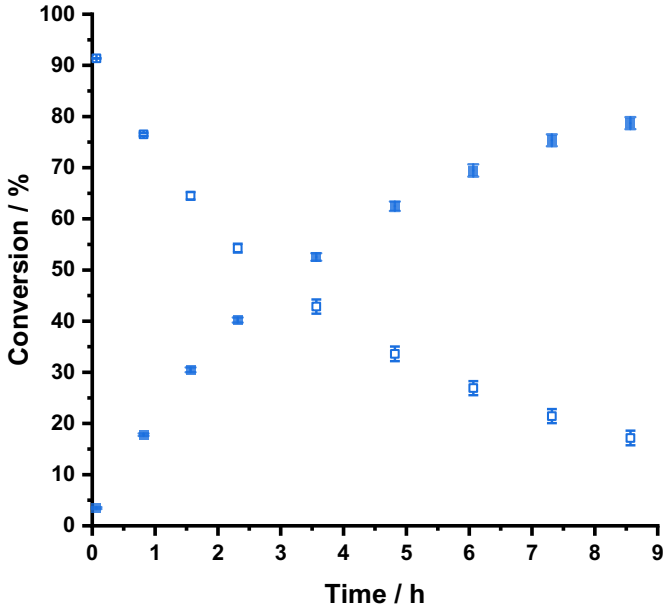

Figure 132 Catalyst-mediated prodrug activation kinetics in 10% DMSO in aqueous MOPS buffer at pH 7.4 at room temperature under an anaerobic atmosphere, showing ***C*-moxi** (100 μM) consumption (empty squares) and moxifloxacin formation (solid squares) for **Ru-s8** at 10 mol % loading.

6.4 Calculated Octanol-water Coefficients

Calculated octanol-water coefficients at pH 7.4, were calculated using the Marvin Sketch 21.12 plug-in, ChemAxon, with electrolyte concentrations: of 0.1 M Na^+ K^+ and 0.1 M Cl^-.

6.5 Bacteria Growth Assays

6.5.1 Media Recipes

Minimal M9 and minimal modified MOPS media stocks were made from individual stock solutions, using milli-Q pure water and stirred, in 10% w/v Chelex® 100 sodium form, 50-100 mesh (dry) resin (Sigma Aldrich, C7901), for 1 h and then filter sterilised before combining to give the desired media. MHII was made using milli-Q pure water and stirred in 20% w/v Chelex for 24 h and then filter sterilised. Minimal, modified MOPS media and MHII were pH adjusted after Chelex treatment (and cation-re-supplementation). Minimal M9 media was not pH adjusted.

All media was prepared and used in either sterile plastics (e.g. falcon tubes) or acid-treated glassware. Acid treatment involved the stirring of 6M hydrochloride in water in glassware for 18 h, followed by decanting, rinsing with acetone, and oven drying.

6.5.1.1 Minimal M9 Media

The following recipe is reported by Sanderson *et al.*[155]

To make a 10 mL stock of M9 media, was added 7.779 mL milli-Q pure water, 2 mL M9, minimal salts, 5X (Sigma Aldrich, M6030), 200 μL 20% w/v glucose, 20 μL 1M $MgSO_4$ and 1 μL 1M $CaCl_2$. The final concentrations of each component in M9 media are as follows: 48 mM Na_2HPO4, 22 mM KH_2PO_4, 19 mM NH_4Cl, 9 mM NaCl, 22 mM glucose, 2 mM $MgSO_4$ and 0.1 mM $CaCl_2$.

6.5.1.2 Modified, Minimal MOPS Media

The following recipe is reported by Sanderson *et al.*[155]

To make a 10 mL stock of minimal, modified-MOPS media, was added 7.047 mL milli-Q pure water, 1 mL 10X MOPS/tricine stocks (400 mM and 40 mM, respectively), 1 mL 500 mM NaCl, 732 μL 1.67 mM NaOAc, 100 μL 132 mM K_2HPO_4, 100 μL 952 mM NH_4Cl, 20 μL 1M $MgSO_4$ and 1 μL 1M $CaCl_2$. The resulting solution was then adjusted to pH 7.4, using chelexed 4M NaOH. The final concentrations of each component in this media are as follows: 40 mM MOPS, 4 mM tricine, 50 mM NaCl, 0.12 mM NaOAc, 1.32 mM K_2HPO_4, 9.52 mM NH_4Cl, 2 mM MgSO4 and 0.1 mM $CaCl_2$.

6.5.1.3 Müller-Hinton II Broth

The following recipe is based on those reported by Ito *et al*.[219]

To make a 200 mL stock of MHII, 200 mL milli-Q pure water was added to 4.4 g Müller Hinton Broth 2 (Sigma Aldrich, 90922). After Chelex treatment, this stock was re-supplemented with 0.4 mM $MgSO_4$ and 0.5 mM $CaCl_2$.

6.5.2 ICP-MS Measurements for the Iron and Ruthenium Content of Media

Some of these results are reported by Sanderson *et al*.[155]

ICP-MS measurements were carried out by John Angus using a microwave dilution assay, at the Biorenewables Development Centre, Chessingham Park, Dunnington, York.

Samples for measurement were made up to 2 mL in 15 mL sterile falcon tubes and contained 1% DMSO in the specified media (minimal M9 media, minimal, modified MOPS media and MHII with 200 μM bpy). Samples made up to determine the iron and ruthenium concentrations of the MHII following the introduction of each synthesised catalyst-siderophore conjugate contained them at 10 μM.

6.5.3 Bacterial Strains

E. coli K12 (BW25113) is a widely used K12 derivative laboratory strain. *E. coli* (BW25113) (ΔentA) is an entA gene deletion mutant.

6.5.4 Iron-starved Bacteria

The following procedure is reported by Sanderson *et al*.[155]

E. coli K12 (BW25113) were grown overnight in chelexed M9 supplemented with 10% w/v casamino acids at 37 °C, 180 rpm. Each sample was centrifuged at 3000 g, 4 °C and the solution decanted. The remaining solid was gently re-suspended in chelexed M9 media (10 mL), and centrifuged again, at 3000 g, 4 °C and the solution decanted (x2). The solid was then made to an OD_{600} of 0.05 in chelexed M9 media (20 mL) and grown for 24 h at 37 °C, 180 rpm. This overnight culture was then diluted by adding 0.4 mL to 0.1 mL chelexed glycerol in water and stored at -80 °C. All growth assays that used *E. coli* K12 (BW25113) used these 'iron starved' bacteria stocks.

6.5.5 Prodrug Uptake Assay

The uptake of the prodrug ***C*-moxi** into *E. coli* K12 (BW25113) was measured utilising an incubation experiment that uses HPLC analysis to quantify the amount of the prodrug that remains in the extracellular environment after its addition to bacteria in their exponential growth, under iron-limited and micro-aerobic conditions. The amount up-taken into bacteria can then be approximated by subtracting this value from the amount added.

The amount of ***C*-moxi** in the extracellular environment was measured using the procedure detailed below, which is separated into sections labelled: incubation preparation, HPLC sample preparation, column conditions, calibration curves and incubation run procedure. This assay works by taking aliquots of a sample, at and injecting them onto a HPLC column which is optimised for the separation of reaction components which are subsequently quantified using calibration curve data that is obtained for ***C*-moxi** component by measuring UV-vis absorbance relative to an external standard. This data is then plotted to represent data as conversion as a function of time.

6.5.5.1 Incubation Preparation

Four *E. coli* K12 (BW25113) cultures were prepared in MHII (pH 7.4, total volume 5 mL) overnight at 37 °C with shaking at 180 rpm, in a 50 mL falcon tube, to OD_{600} values in the range of 1.61 – 1.66.

Each overnight culture was diluted to OD_{600} = 0.01 in degassed MHII (pH 7.4) supplemented with 200 μM Bpy, 0.5% DMSO, into the four central wells of a COSTAR 24-well plate (with the surrounding wells filled with degassed water). The plate was covered with a PCR film. These samples were then grown in an Epoch 2 Microplate Spectrophotometer (Biotek) at 37 °C with shaking at 282 rpm, with OD_{600} measurement every 10 min, until an average OD_{600} = 0.1, compared to a 'no cell' control (exponential growth phase).

After this, 1.99 mL aliquots of each sample well were taken into 2 mL Eppendorfs, and to three of them was added 10 μL of ***C*-moxi** (2 mM), to form triplicate. To the remaining sample was added 10 μL of DMSO, as a 'no prodrug' control. These samples were incubated at 37 °C for 15 min.

After incubation, the samples were centrifuged at 3000 g for 10 min at 4 °C, and the supernatant filtered through a 0.2 μm filter where 475 μL was taken for HPLC sample preparation (extracellular sample). The remaining cells were then re-suspended in fresh MHII and also centrifuged at 3000 g, 10 min at 4 °C, and the supernatant filtered through a 0.2 μm filter where 475 μL was taken for HPLC sample preparation (wash sample).

6.5.5.2 HPLC Sample Preparation

To each of the extracellular and wash samples obtained during incubation, was added 25 μL caffeine in water (10 mM), so that caffeine concentration = 500 μM, including the 'no prodrug' control. Three 'no cell' controls were made up by adding 10 μL ***C*-moxi** (2 mM) to 1990 μL MHII. A 475 μL aliquot of each was taken, and to it was added 25 μL caffeine in water (10 mM), so that caffeine concentration equalled 500 μM. Each sample was then filtered again through a 0.2 μm filter immediately prior to HPLC

6.5.5.3 HPLC Column Conditions

Elution: (i) 0-20% acetonitrile in water over 7 min, (ii) 20-80% acetonitrile in water over 5 min, (iii) 80-10% acetonitrile in water over 6 s (iv) 10% acetonitrile in water for 2.5 min (total run time = 15 min). Both acetonitrile and water mobiles phases contained 0.1% w/v formic acid.

Column: Waters Eterra®MS C18 reverse phase column.

Oven Temperature: 40 °C.

Injection Volume: 50 μL.

6.5.5.4 Calibration Curve

The area under the curve (AUC) for the UV-vis absorbance of ***C*-moxi** was measured at 290 nm, relative to internal standard caffeine (500 μM) at room temperature, over a concentration range that contains those expected during incubation runs. The obtained relative absorbance data (reagent AUC / caffeine AUC) at 290 nm was then plotted against the known ***C*-moxi** concentration.

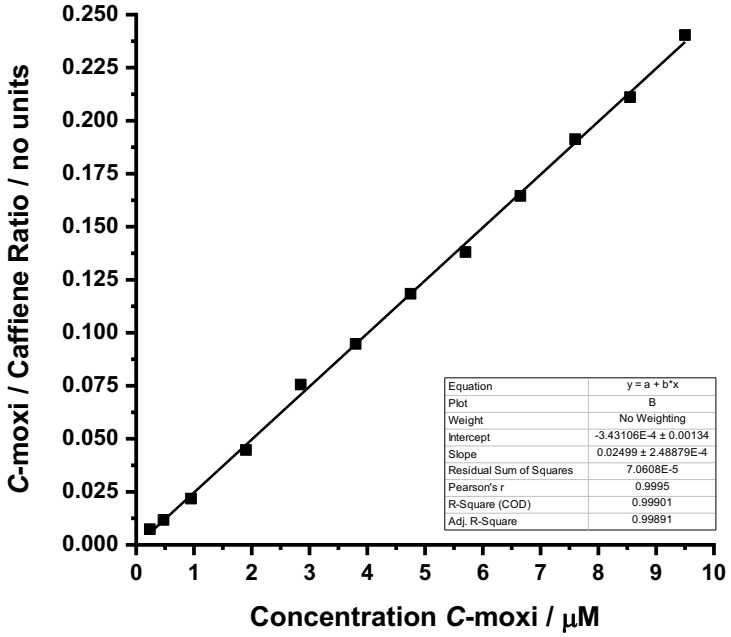

Figure 133 Calibration curve for ***C*-moxi** (0.3 – 10 μM) as relative absorbance at 290 nm *versus* caffeine (500 μM) in MHII (pH 7.4) at room temperature.

6.5.5.5 Data Processing

Each of the extracellular and wash samples, including 'no cell' controls, were made up and measured in triplicate. Those for the 'no prodrug addition' control was made up and measured in singlet. A mean average of the ***C*-moxi** incubated samples and 'no cell' controls' relative AUC to the internal standard caffeine, was calculated. Using the line of best fit acquired in section 6.5.5.4, ***C*-moxi** concentration for each sample was calculated, and considering the volume of these samples, amount in moles was determined. The percentage ***C*-moxi** in the extracellular and wash samples was calculated by dividing the mean amount (in moles) of ***C*-moxi** by that of the 'no cell' control. The percentage up-taken into bacteria was approximated by subtracting the summated percentage of ***C*-moxi** in the extracellular and wash samples from that of the 'no cell' control. The molar uptake per OD_{600} was calculated by dividing the approximated molarity inside the bacteria, by the incubation OD_{600} value (0.1).

6.5.6 Plate Assays

6.5.6.1 Probing Iron-limitation of Minimal, Modified MOPS Media

Bacteria Growth

E. coli K12 (BW25113) was grown in minimal M9 media supplemented with 10% w/v casamino acids (total volume 20 mL), overnight at 37 °C with shaking at 180 rpm, in a 100 mL conical flask, typically to an $OD_{600} \sim 1.7$.

Plate Preparation Procedure

Growth assays were carried out in NUNC 96-well plates (Sigma Aldrich, M9410-1CS), with 350 μL wells. To each well was added a total volume of 200 μL. Well conditions were minimal, modified MOPS media (pH 7.4) with 1% DMSO. For iron-limited conditions: 150 μL of minimal, modified MOPS media with 1.33% DMSO was added. For iron-supplemented conditions: 100 μL of minimal, modified MOPS media with 2% DMSO was added alongside 50 μL 400 μM $FeCl_3$ in minimal, modified MOPS media. Each well was then inoculated to a starting of $OD_{600} = 0.01$, by adding a 4X concentrated stock of the overnight *E. coli* K12 (BW25113) culture, with mixing.

Moats and surrounding wells were filled with de-ionised water (2 mL and 200 μL, respectively).

Plate Incubation Procedure

Aerobically-grown plates were incubated in an Epoch 2 Microplate Spectrophotometer (Biotek) at 37 °C, shaken continuously in a double orbital pattern (282 rpm). Absorbances at OD_{600} for each well were recorded at t = 0 and every 60 min, for 48 h.

Anaerobically-grown plates were incubated in a FLUOstar Omega microplate reader from BMG LABTECH at 37 °C, shaken continuously in a double orbital pattern (180 rpm) with attached Atmosphere Control Unit (ACU) ensuring a 2% O_2 atmosphere using an attached N_2 gas cylinder. Absorbances at OD_{600} for each well were recorded at t = 0 and every 60 min, for 75 h.

Data Processing

Data was processed in Excel software by first subtracting the average of the no cell controls from all read data. At this point, obvious anomalies were discarded. All data was obtained in at least technical triplicate. For each cell condition, a mean average and error as standard deviation was calculated.

Data is plotted using Origin software, as a growth curve. The mean average absorbance and its corresponding error for each well condition was taken at each time point. This data is shown as absorbance as a function of time.

6.5.6.2 Probing Iron-limitation of Müller-Hinton Broth II

Bacteria Growth

E. coli K12 (BW25113) was grown in MHII (total volume 5 mL), overnight at 37 °C with shaking at 180 rpm, in a 50 mL falcon tube, typically to an $OD_{600} \sim 1.7$.

Plate Preparation Procedure

Growth assays were carried out in NUNC 96-well plates (Sigma Aldrich, M9410-1CS), with 350 μL wells. To each well was added a total volume of 200 μL. Well

conditions were MHII (pH 7.4) with 1% DMSO, with and without 100 μM $FeCl_3$ for iron-supplemented and iron-limited conditions, respectively. For no addition conditions: 150 μL of MHII was added. For iron-limited conditions, no iron: 100 μL of MHII was added, alongside 50 μL 800 μM Bpy in 4% DMSO in MHII. For iron-supplemented, with bpy conditions: 50 μL 800 μM Bpy in 4% DMSO in MHII, 50 μL of MHII was added with 4% DMSO alongside 50 μL 400 μM $FeCl_3$ in MHII. For iron-supplemented, no bpy conditions: 100 μL of MHII was added with 4% DMSO alongside 50 μL 400 μM $FeCl_3$ in MHII. Each well was then inoculated to a starting OD_{600} = 0.01, by adding 50 μL of a 4X concentrated stock of the overnight *E. coli* K12 (BW25113) culture diluted in fresh MHII, with mixing. Moats and surrounding wells were filled with de-ionised water (2 mL and 200 μL, respectively).

Plate Incubation Procedure

Aerobically grown plates were incubated in an Epoch 2 Microplate Spectrophotometer (Biotek) at 37 °C, shaken continuously in a double orbital pattern (282 rpm). Absorbances at OD_{800} for each well were recorded at t = 0 and every 30 min, for 24 h.

Anaerobically-grown plates were incubated in a FLUOstar Omega microplate reader from BMG LABTECH at 37 °C, shaken continuously in a double orbital pattern (180 rpm) with attached Atmosphere Control Unit (ACU) ensuring a 2% O_2 atmosphere using an attached N_2 gas cylinder. Absorbances at OD_{800} for each well were recorded at t = 0 and every 30 min, for 24 h.

Data Processing

Data was processed in Excel software by first subtracting the average of the no cell controls from all read data. At this point, obvious anomalies were discarded. All data was obtained in at least technical triplicate. For each cell condition, a mean average and error as standard deviation was calculated.

Data is plotted using Origin software, as a growth curve. The mean average absorbance and its corresponding error for each well condition was taken at each time point. This data is shown as absorbance as a function of time.

6.5.6.3 Antibacterial Activity of Moxifloxacin and Prodrugs

Bacteria Growth

E. coli K12 (BW25113) was grown in MHII (total volume 5 mL), overnight at 37 °C with shaking at 180 rpm, in a 50 mL falcon tube, typically to an OD_{600} ~ 1.7.

Plate Preparation Procedure

Growth assays were carried out in NUNC 96-well plates (Sigma Aldrich, M9410-1CS), with 350 μL wells. To each well was added a total volume of 200 μL. Well conditions were 200 μM Bpy in MHII (pH 7.4) with 1% DMSO for iron-limited conditions with a starting OD_{600} = 0.01 by dilution of the overnight *E. coli* K12 (BW25113) culture. Substrates were added at 50 μL as X4 stocks in 2% DMSO in MHII. For co-addition experiments, substrates were added at 0.5 μL as X400 stocks in DMSO. Each well was mixed and then the moats and surrounding wells were filled with de-ionised water (2 mL and 200 μL, respectively). Prepared plates were then transported in a sealed container to the plate reader, so that they remained under an anaerobic atmosphere. Moats and surrounding wells were filled with de-ionised water (2 mL and 200 μL, respectively).

Plate Incubation Procedure

Plates were incubated in a FLUOstar Omega microplate reader from BMG LABTECH at 37 °C, shaken continuously in a double orbital pattern (180 rpm) with attached Atmosphere Control Unit (ACU) ensuring a 2% O_2 atmosphere using an attached N_2 gas cylinder. Absorbances at OD_{800} for each well were recorded at t = 0 and every 30 min, for 24 h.

Data Processing

Data was processed in Excel software by first subtracting the average of the no cell controls from all read data. At this point, obvious anomalies were discarded. All data was obtained in at least technical triplicate. For each cell condition, a mean average and error as standard deviation was calculated.

Data is plotted using Origin software, as a dosage response curve. The mean average absorbance at OD_{800} for each well condition was taken at 24 h, along with its corresponding error, and converted to normalised OD_{800} by diving by the mean average growth of the no addition control. This data was then plotted as a function of substrate concentration on a logarithmic scale. A line of best was determined by for each substrate using Origin's default sigmoidal fit analysis.

6.5.6.4 Antibacterial Activity of Catalyst-Siderophore Conjugates and their Co-addition with Prodrug *C*-moxi

Bacteria Growth

E. coli K12 (BW25113) was grown in MHII (total volume 5 mL), overnight at 37 °C with shaking at 180 rpm, in a 50 mL falcon tube, typically to an $OD_{600} \sim 1.7$.

Plate Preparation Procedure

Growth assays were carried out in NUNC 96-well plates (Sigma Aldrich, M9410-1CS), with 350 μL wells and prepared in an anaerobic chamber. All stocks were degassed in the chamber at least 3 d prior to their use in assays. To each well was added a total volume of 200 μL. Well conditions were 200 μM Bpy in MHII (pH 7.4) with 1% DMSO for iron-limited conditions with a starting $OD_{600} = 0.01$ by dilution of the overnight *E. coli* K12 (BW25113) culture. For catalyst-siderophore conjugate antibacterial activity experiments, substrates were added at 1 μL as X200 stocks in DMSO. For co-addition experiments, substrates were added at 0.5 μL as X400 stocks in DMSO. Each well was mixed and then the moats and surrounding wells were filled with de-ionised water (2 mL and 200 μL, respectively). Prepared plates were then transported in a sealed container to the plate reader, so that they remained under an anaerobic atmosphere.

Plate Incubation Procedure

Plates were incubated in a FLUOstar Omega microplate reader from BMG LABTECH at 37 °C, shaken continuously in a double orbital pattern (180 rpm) with attached Atmosphere Control Unit (ACU) ensuring a 2% O_2 atmosphere using an

attached N_2 gas cylinder. Absorbances at OD_{800} for each well were recorded at t = 0 and every 30 min, for 24 h.

Data Processing

Data was processed in Excel software by first subtracting the average of the no cell controls from all read data. At this point, obvious anomalies were discarded. All data was obtained in at least technical triplicate*. For each cell condition, a mean average and error as standard deviation was calculated.

For catalyst-siderophore conjugate antibacterial activity experiments, data is plotted using Origin software, as a dosage response curve. The mean average absorbance at OD_{800} for each well condition was taken at 24 h, along with its corresponding error. This data was then plotted as a function of substrate concentration on a linear scale. The data points are joined by straight lines to depict a general trend.

*Apart from during the antibacterial activity determination of **Ru-control** at 100 nM, **Ru-s3** at 10 μM and 1 μM and **Ru-s8** at 1 μM, which were technical duplicates due to the appearance of obvious anomalies.

For co-addition experiments, data is plotted using Origin software, as a bar chart. The mean average absorbance at OD_{800} for each well condition was taken at 24 h, along with its corresponding error. This data was then plotted with the labelled specific conditions underneath each bar.

6.5.6.5 Growth Recovery Experiments

Bacteria Growth

E. coli K12 (BW25113) (ΔentA) was grown in MHII (total volume 5 mL), overnight at 37 °C with shaking at 180 rpm, in a 50 mL falcon tube, typically to an OD_{600} ~ 0.5.

Plate Preparation Procedure

Growth assays were carried out in NUNC 96-well plates (Sigma Aldrich, M9410-1CS), with 350 μL wells and prepared in an anaerobic chamber. All stocks were degassed in the chamber at least 3 d prior to their use in assays. To each well was added a total volume of 200 μL. Well conditions were 200 μM Bpy in MHII (pH 7.4)

with 1% DMSO for iron-limited conditions with a starting OD_{600} = 0.01 by dilution of the overnight *E. coli* K12 (BW25113) (ΔentA) culture. Substrates were added at 1 μL as X200 stocks in DMSO. Each well was mixed and then the moats and surrounding wells were filled with de-ionised water (2 mL and 200 μL, respectively). Prepared plates were then transported in a sealed container to the plate reader, so that they remained under an anaerobic atmosphere.

Plate Incubation Procedure

Plates were incubated in a FLUOstar Omega microplate reader from BMG LABTECH at 37 °C, shaken continuously in a double orbital pattern (180 rpm) with attached Atmosphere Control Unit (ACU) ensuring a 2% O_2 atmosphere using an attached N_2 gas cylinder. Absorbances at OD_{800} for each well were recorded at t = 0 and every 30 min, for 24 h.

Data Processing

Data was processed in Excel software by first subtracting the average of the no cell controls from all read data. At this point, obvious anomalies were discarded. All data was obtained in at least technical triplicate. For each cell condition, a mean average and error as standard deviation was calculated.

Data is plotted using Origin software, as a bar chart. The mean average absorbance at OD_{800} for each well condition was taken at 24 h, along with its corresponding error. This data was then plotted with the labelled specific conditions underneath each bar.

6.5.6.6 Antibacterial Activity of Moxifloxacin and *C*-moxi During the Exponential Growth Phase

Bacteria Growth

E. coli K12 (BW25113) was grown in MHII (total volume 5 mL), overnight at 37 °C with shaking at 180 rpm, in a 50 mL falcon tube, typically to an OD_{600} ~ 1.7.

Plate Preparation 1

Growth assays were carried out in NUNC 96-well plates (Sigma Aldrich, M9410-1CS), with 350 μL wells and prepared in an anaerobic chamber. All stocks were degassed in the chamber at least 3 d prior to their use in assays. To each well was added a total volume of 199 μL. Well conditions were 200 μM Bpy in MHII (pH 7.4) with 1% DMSO for iron-limited conditions with a starting OD_{600} = 0.01 by dilution of the overnight *E. coli* K12 (BW25113) culture. Each well was mixed and then the moats and surrounding wells were filled with de-ionised water (2 mL and 200 μL, respectively). Prepared plates were the covered with a PCR film and their lid, then transported in a sealed container to the plate reader, so that they remained under an anaerobic atmosphere.

Plate Incubation Procedure 1

Plates were incubated in an Epoch 2 Microplate Spectrophotometer (Biotek) at 37 °C, with no shaking, until absorbances OD_{600} reached values 0.1 greater than the average of 'no cell' controls (exponential growth phase). These plates were then transported back to the anaerobic chamber.

Plate Preparation 2

The PCR film was removed and to each well was added substrate at 1 μL as a X200 concentrated stock in DMSO with mixing. Prepared plates were then transported in a sealed container to the plate reader, so that they remained under an anaerobic atmosphere.

Plate Incubation Procedure 2

Plates were incubated in a FLUOstar Omega microplate reader from BMG LABTECH at 37 °C, shaken continuously in a double orbital pattern (180 rpm) with attached Atmosphere Control Unit (ACU) ensuring a 2% O_2 atmosphere using an attached N_2 gas cylinder. Absorbances at OD_{800} for each well were recorded at t = 0 and every 30 min, for 18 h.

Data Processing

Data was processed in Excel software by first subtracting the average of the no cell controls from all read data. At this point, obvious anomalies were discarded. All data was obtained in at least technical triplicate. For each cell condition, a mean average and error as standard deviation was calculated.

Data is plotted using Origin software, as a dosage response curve. The mean average absorbance at OD_{800} for each well condition was taken at 18 h, along with its corresponding error, and converted to normalised OD_{800} by diving by the mean average growth of the no addition control. This data was then plotted as a function of substrate concentration on a logarithmic scale. A line of best was determined by for each substrate using Origin's default sigmoidal fit analysis.

6.5.6.7 Antibacterial Activity of Catalyst-Siderophore Conjugates following Bacteria Incubation with Prodrug During the Exponential Growth Phase

Bacteria Growth

E. coli K12 (BW25113) was grown in MHII (total volume 5 mL), overnight at 37 °C with shaking at 180 rpm, in a 50 mL falcon tube, typically to an $OD_{600} \sim 1.7$.

Plate Preparation 1

Growth assays were carried out in COSTAR 24-well plates (Sigma Aldrich, CLS3527), with 3.4 mL wells and prepared in an anaerobic chamber. All stocks were degassed in the chamber at least 3 d prior to their use in assays. To each well was added a total volume of 2.5 mL. Well conditions were 200 μM Bpy in MHII (pH 7.4) with 1% DMSO for iron-limited conditions with a starting $OD_{600} = 0.01$ by dilution of the overnight *E. coli* K12 (BW25113) culture. Each well was mixed and then the moats and surrounding wells were filled with de-ionised water (2.5 mL). Prepared plates were the covered with a PCR film and their lid, then transported in a sealed container to the plate reader, so that they remained under an anaerobic atmosphere.

Plate Incubation Procedure 1

Plates were incubated in an Epoch 2 Microplate Spectrophotometer (Biotek) at 37 °C, with no shaking, until absorbances OD_{600} reached values 0.1 greater than the average of 'no cell' controls (= exponential growth). These plates were then transported back to the anaerobic chamber.

Spin Down and Washing Procedure

A volume of 1.99 mL was taken from each well into a 2 mL Eppendorf and to it was added was added either 10 μL of a X200 concentrated ***C*-moxi** stock in DMSO (for ***C*-moxi** incubation), or plain DMSO (for non-***C*-moxi** incubation controls), with mixing. These Eppendorfs were placed into a sealed container and transferred to the 37 °C room and shaken for 15 min at 180 rpm. After this time, the Eppendorfs were spun down (3000g, 10 min, 4 °C), the pellet isolated and then re-suspended in 2 mL of 200 μM Bpy in MHII (pH 7.4) with 1% DMSO (x3).

Plate Preparation 2

Subsequent growth assays were carried out in NUNC 96-well plates (Sigma Aldrich, M9410-1CS), with 350 μL wells and prepared in an anaerobic chamber. To each well was added a total volume of 199 μL from the aforementioned stocks prepared during the 'Spin Down and Washing Procedure'. Well conditions were 200 μM Bpy in MHII (pH 7.4) with 1% DMSO for iron-limited conditions with a starting OD_{600} = 0.1. Substrates were added at 1 μL as X200 stocks in DMSO. Each well was mixed and then the moats and surrounding wells were filled with de-ionised water (2 mL and 200 μL, respectively). Prepared plates were transported in a sealed container to the plate reader, so that they remained under an anaerobic atmosphere.

Plate Incubation Procedure 2

Plates were incubated in a FLUOstar Omega microplate reader from BMG LABTECH at 37 °C, shaken continuously in a double orbital pattern (180 rpm) with attached Atmosphere Control Unit (ACU) ensuring a 2% O_2 atmosphere using an attached N_2 gas cylinder. Absorbances at OD_{800} for each well were recorded at t = 0 and every 30 min, for 18 h.

Data Processing

Data was processed in Excel software by first subtracting the average of the no cell controls from all read data. At this point, obvious anomalies were discarded. Incubations were employed in technical triplicate, and subsequent data for each in at least technical duplicate. For each cell condition, a mean average and error as standard deviation was calculated.

Data is plotted using Origin software, as a bar chart. The mean average absorbance at OD_{800} for each well condition was taken at 18 h, along with its corresponding error. This data was then plotted with the labelled specific conditions underneath each bar. The difference between incubations (OD_{800} for substrate following ***C*-moxi** incubation – OD_{800} for substrate following DMSO incubation), is shown above the corresponding bars in the bar chart.

Abbreviations

°	degrees
°C	degrees celsius
5-FU	5-fluorouracil
Å	angstrom
ABC	ATP-binding cassette
Acetone-d_6	deuterated acetone
ADEPT	antibody-directed enzyme prodrug therapy
aq	aqueous
ATIR	attenuated total reflectance infrared
ATP	adenosine triphosphate
AUC	area under the curve
Boc	*tert*-butyloxycarbonyl
bpy	bypyridin
c (prefix)	centi
C. jejuni	*Campylobacter jejuni*
$CDCl_3$	deuterated chloroform
CDI	1,1'-carbonyldiimidazole
CHN	carbon hydrogen nitrogen
Conc.	concentrated
COSY	correlation spectroscopy
Cp	cyclopentadienyl
D_2O	deuterated water
DCC	dicyclohexylcarbodiimide

DEPT	directed enzyme prodrug therapy
DEPT	distortionless enhancement of polarisation transfer
DFO	desferrioxamine B
DHB	2,3-dihydroxybenzoic acid
DHBA	2,3-dihydroxy-*N,N'*-dimethylbenzamide,
DHBS	2,3-dihydroxybenzylserine
DIPEA	*N,N'*-diisopropylethylamine
DMF	dimethylformamide
DMSO	dimethylsulfoxide
DMSO-d_6	deuterated dimethylsulfoxide
DNA	deoxyribonucleic acid
DNP	2,4-dinitrophenol
DrxR	diphtheria toxin repressor
E. coli	*Escherichia coli*
EDC	1-ethyl-3-(3-dimethylaminopropyl)carbodiimide
EDTA	ethylenediaminetetraacetic acid
ESI	electrospray ionisation
EtOAc	ethyl acetate
EtOH	ethanol
FNR	fumarate and nitrate reductase
FO	ferrioxamine
Fur	ferric uptake regulator
g	grams
GFP	green fluorescent protein
GI	gastrointestinal tract

GSH	glutathione
HMBC	heteronuclear multiple-bond correlation
HMQC	heteronuclear multiple quantum correlation
HOBt	hydroxybenzotriazole
HPLC	high performance liquid chromatography
HRMS	high resolution mass spectrometry
HSAB	hard-soft acid base
Hz	hertz
ICP	inductively-coupled plasma
IR	infrared
K (prefix)	kilo
K_f	formation constant
K. pneumoniae	*Klebsiella pneumoniae*
L	litre
LB	lysogeny broth
LIFDI	liquid injection field desorption/ionisation
λ_{max}	wavelength of maximum absorbance
LMCT	ligand-to-metal charge transfer
m	metre
M	molar
m (prefix)	milli
m/z	mass/charge
MCR-1	mobilised colistin resistance 1
MDR	multi-drug resistant
MeCN	acetonitrile

MeOD-d_4	deuterated methanol
MeOH	methanol
MHII	müller-hinton broth II
MIC	minimum inhibitory concentration
min	minute/s
MLCT	metal-to-ligand charge transfer
mol	mole
MOPS	3-morpholinopropane-1-sulfonic acid
MRSA	methicillin-resistant *Staphylococcus Aureus*
MS	mass spectrometry
n (prefix)	nano
NAD	nicotinamide adenine dinucleotide
NADH	reduced nicotinamide adenine dinucleotide
ncAA	non-conical amino acid
NMR	nuclear magnetic resonance
NTA	nitriloacetic acid
OD_{600}	optical density at 600 nm
OD_{800}	optical density at 800 nm
OTS	orthogonal translation system
P. aeruginosa	*Pseudomonas aeruginosa*
PBP	periplasmic binding protein
PEG	polyethylene glycol
PET	40-60 ºC petroleum ethers
PMB	*para*-methoxybenzyl
ppb	parts per billion

ppm	parts per million
R_f	retention factor
Rho	rhodamine 110
RNA	ribonucleic acid
ROS	reactive oxygen species
rpm	revolutions per minute
s	seconds
S. aureus	*Staphylococcus aureus*
SAR	structure activity relationship
Ser	serine
TFA	trifluoracetic acid
THF	tetrahydrofuran
TLC	thin layer chromatography
TON	turnover number
tRNA	transcription ribonucleic acid
TSB	tryptic soy broth
TTP	triphenylphoshonium
UV-visible	ultraviolet-visible
v/v	volume by volume
w/v	weight by volume
WHO	world health organization
μ (prefix)	micro

References

1. Böswald, I. Erasmus Report: Inorganic Chemistry. University of York, 2019.

2. Gutenthaler, S. M. ERASMUS Report: Synthesis and Characterisation of Catecholamide Siderophores. University of York, 2018.

3. Kerns, E. H.; Di, L., *Drug-like Properties: Concepts, Structure Design and Methods*. Academic Press: California, 2008; p 229-240.

4. Ettmayer, P.; Amidon, G. L.; Clement, B.; Testa, B., *J. Med. Chem.* **2004,** *47*, 2393-2404.

5. Lindberg, P.; Nordberg, P.; Alminger, T.; Braendstroem, A.; Wallmark, B., *J. Med. Chem.* **1986,** *29*, 1327-1329.

6. Senn-Bilfinger, J.; Krueger, U.; Sturm, E.; Figala, V.; Klemm, K.; Kohl, B.; Rainer, G.; Schaefer, H.; Blake, T. J., *J. Org. Chem.* **1987,** *52*, 4582-4592.

7. Hanahan, D.; Weinberg, Robert A., *Cell* **2011,** *144*, 646-674.

8. Marshall, J. L.; Hwang, J. J., *Expert Opin. Pharmaco.* **2002,** *3*, 733-743.

9. Niculescu-Duvaz, I.; Springer, C. J., *Adv. Drug Deliv. Rev.* **1997,** *26*, 151-172.

10. Sharma, S. K.; Bagshawe, K. D., *Adv. Drug Deliv. Rev.* **2017,** *118*, 2-7.

11. Springer, C. J.; Antoniw, P.; Bagshawe; Searle, F.; Bisset, G. M. F.; Jarman, M., *J. Med. Chem.* **1990,** *33*, 677-681.

12. Hang, H. C.; Yu, C.; Kato, D. L.; Bertozzi, C. R., *Proc. Natl. Acad. Sci. USA* **2003,** *100*, 14846-14851.

13. Rebelein, J. G.; Ward, T. R., *Curr. Opin. Biotech.* **2018,** *53*, 106-114.

14. Ngo Anh, H.; Bose, S.; Do Loi, H., *Chem. Eur. J.* **2018,** *24,* 10584-10594.

15. Martínez-Calvo, M.; Mascareñas, J. L., *Coord. Chem. Rev.* **2018,** *359*, 57-79.

16. Du, B.; Li, D.; Wang, J.; Wang, E., *Adv. Drug Deliv. Rev.* **2017,** *118*, 78-93.

17. van de L'Isle, M. O. N.; Ortega-Liebana, M. C.; Unciti-Broceta, A., *Curr. Opin. Chem. Biol.* **2021,** *61*, 32-42.

18. Destito, P.; Vidal, C.; López, F.; Mascareñas, J. L., *Chem. Eur. J.* **2021,** *27*, 4789-4816.

19. Soldevila-Barreda, J. J.; Bruijnincx, P. C. A.; Habtemariam, A.; Clarkson, G. J.; Deeth, R. J.; Sadler, P. J., *Organometallics* **2012,** *31*, 5958-5967.

20. Soldevila-Barreda, J. J.; Romero-Canelón, I.; Habtemariam, A.; Sadler, P. J., *Nat. Commun.* **2015,** *6*, 6582.

21. Völker, T.; Dempwolff, F.; Graumann, P. L.; Meggers, E., *Angew. Chem. Int. Ed.* **2014,** *53*, 10536-10540.

22. Yusop, R. M.; Unciti-Broceta, A.; Johansson, E. M. V.; Sánchez-Martín, R. M.; Bradley, M., *Nat. Chem.* **2011,** *3*, 239-243.

23. Tsubokura, K.; Vong Kenward, K. H.; Pradipta Ambara, R.; Ogura, A.; Urano, S.; Tahara, T.; Nozaki, S.; Onoe, H.; Nakao, Y.; Sibgatullina, R.; Kurbangalieva, A.; Watanabe, Y.; Tanaka, K., *Angew. Chem. Int. Ed.* **2017,** *56*, 3579-3584.

24. Tanaka, S.; Saburi, H.; Ishibashi, Y.; Kitamura, M., *Org. Lett.* **2004,** *6*, 1873-1875.

25. Kitamura, M.; Tanaka, S.; Yoshimura, M., *J. Org. Chem.* **2002,** *67*, 4975-4977.

26. Kiesewetter, M. K.; Waymouth, R. M., *Organometallics* **2010,** *29*, 6051-6056.

27. Streu, C.; Meggers, E., *Angew. Chem.* **2006,** *118*, 5773-5776.

28. Kaplowitz, N.; Aw, T. Y.; Ookhtens, M., *Annu. Rev. Pharmcol. Toxicol.* **1985,** *25*, 715-744.

29. Tanaka, S.; Saburi, H.; Hirakawa, T.; Seki, T.; Kitamura, M., *Chem. Lett.* **2009,** *38*, 188-189.

30. Hsu, H.-T.; Trantow, B. M.; Waymouth, R. M.; Wender, P. A., *Bioconj. Chem.* **2016,** *27*, 376-382.

31. Tomás-Gamasa, M.; Martínez-Calvo, M.; Couceiro, J. R.; Mascareñas, J. L., *Nat. Commun.* **2016,** *7*, 12538.

32. Das, R.; Landis, R. F.; Tonga, G. Y.; Cao-Milán, R.; Luther, D. C.; Rotello, V. M., *ACS Nano* **2019,** *13*, 229-235.

33. Völker, T.; Meggers, E., *ChemBioChem* **2017,** *18*, 1083-1086.

34. Rubini, R.; Ivanov, I.; Mayer, C., *Chem. Eur. J.* **2019,** *25*, 16017-16021.

35. Okamoto, Y.; Kojima, R.; Schwizer, F.; Bartolami, E.; Heinisch, T.; Matile, S.; Fussenegger, M.; Ward, T. R., *Nat. Commun.* **2018,** *9*, 1943.

36. Heinisch, T.; Schwizer, F.; Garabedian, B.; Csibra, E.; Jeschek, M.; Vallapurackal, J.; Pinheiro, V. B.; Marlière, P.; Panke, S.; Ward, T. R., *Chem. Sci.* **2018,** *9*, 5383-5388.

37. Brötz-Oesterhelt, H.; Sass, P., *Future Microbiol.* **2010,** *5*, 1553-1579.

38. Durand, G. A.; Raoult, D.; Dubourg, G., *Int. J. Antimicrob. Agents* **2019,** *53*, 371-382.

39. Levy, S. B.; Marshall, B., *Nat. Med.* **2004,** *10*, 122-129.

40. Blair, J. M. A.; Webber, M. A.; Baylay, A. J.; Ogbolu, D. O.; Piddock, L. J. V., *Nat. Rev. Microbiol.* **2014,** *13*, 42-51.

41. Douafer, H.; Andrieu, V.; Phanstiel, O.; Brunel, J. M., *J. Med. Chem.* **2019,** *62*, 8665-8681.

42. Lakemeyer, M.; Zhao, W.; Mandl Franziska, A.; Hammann, P.; Sieber Stephan, A., *Angew. Chem. Int. Ed.* **2018,** *57,* 14440-14475.

43. Freire-Moran, L.; Aronsson, B.; Manz, C.; Gyssens, I. C.; So, A. D.; Monnet, D. L.; Cars, O., *Drug Resist. Updat.* **2011,** *14*, 118-124.

44. Gallagher, J. Infections resist 'last antibiotic' in US. (accessed July 2021).

45. WHO, Antibacterial Agents in Clinical Development. (WHO, Geneva, 2017).

46. Górska, A.; Sloderbach, A.; Marszałł, M. P., *Trends Pharmacol. Sci.* **2014,** *35*, 442-449.

47. Möllmann, U.; Heinisch, L.; Bauernfeind, A.; Köhler, T.; Ankel-Fuchs, D., *BioMetals* **2009,** *22*, 615-624.

48. Klahn, P.; Bronstrup, M., *Nat. Prod. Rep.* **2017,** *34*, 832-885.

49. Miethke, M.; Marahiel, M. A., *Microbiol. Mol. Biol. Rev.* **2007,** *71*, 413-451.

50. Liu, Z. D.; Hider, R. C., *Coord. Chem. Rev.* **2002,** *232*, 151-171.

51. Hider, R. C.; Kong, X., *Nat. Prod. Rep.* **2010,** *27*, 637-657.

52. Drechsel, H.; Jung, G., *J. Pept. Sci.* **1998,** *4*, 147-181.

53. Pearson, R. G., *J. Am. Chem. Soc.* **1963,** *85*, 3533-3539.

54. Francis, J.; Madinaveitia, J.; Macturk, H. M.; Snow, G. A., *Nature* **1949,** *163*, 365-366.

55. Loomis, L. D.; Raymond, K. N., *Inorg. Chem.* **1991,** *30*, 906-911.

56. Bickel, H.; Keberle, H.; Vischer, E., *Helv. Chim. Acta* **1963,** *46*, 1385-1389.

57. Weitl, F. L.; Raymond, K. N., *J. Am. Chem. Soc.* **1979,** *101*, 2728-2731.

58. Spiro, T. G.; Bates, G.; Saltman, P., *J. Am. Chem. Soc.* **1967,** *89*, 5559-5562.

59. Harris, W. H.; Raymond, K. N., *J. Am. Chem. Soc.* **1979,** *101*, 6534-6541.

60. Hantke, K., *MGG* **1981,** *182*, 288-292.

61. Zimmermann, L.; Hantke, K.; Braun, V., *J. Bacteriol.* **1984,** *159*, 271-277.

62. Stojiljkovic, I.; Bäumler, A. J.; Hantke, K., *J. Mol. Biol.* **1994,** *236*, 531-545.

63. Braun, V., *FEMS Microbiol. Rev.* **1995,** *16*, 295-307.

64. Köster, W., *Res. Microbiol.* **2001,** *152*, 291-301.

65. Southwell, J. W.; Black, C. M.; Duhme-Klair, A.-K., *ChemMedChem* **2021,** *16*, 1063-1076.

66. Pollack, J. R.; Neilands, J. B., *Biochem. Biophys. Res. Commun.* **1970,** *38*, 989-992.

67. O'Brien, I. G.; Gibson, F., *Biochim. Biophys. Acta* **1970,** *215*, 393-402.

68. Boukhalfa, H.; Crumbliss, A. L., *Biometals* **2002,** *15*, 325-339.

69. Köster, W.; Braun, V., *Mol. Gen. Genet.* **1989,** *217*, 233-239.

70. Braun, V.; Braun, M., *FEBS Lett.* **2002,** *529*, 78-85.

71. Lin, H.; Fischbach, M. A.; Liu, D. R.; Walsh, C. T., *J. Am. Chem. Soc.* **2005,** *127*, 11075-11084.

72. Scarrow, R. C.; Ecker, D. J.; Ng, C.; Liu, S.; Raymond, K. N., *Inorg. Chem.* **1991,** *30*, 900-906.

73. Hantke, K., *FEMS Microbiol. Lett.* **1990,** *67*, 5-8.

74. O'Brien, I. G.; Cox, G. B.; Gibson, F., *Biochim. Biophys. Acta.* **1971,** *237*, 537-549.

75. Zamora, C. Y.; Madec, A. G. E.; Neumann, W.; Nolan, E. M.; Imperiali, B., *Bioorg. Med. Chem.* **2018,** *26*, 5314-5321.

76. Palyada, K.; Threadgill, D.; Stintzi, A., *J. Bacteriol.* **2004,** *186*, 4714-4729.

77. Hancock, R. E. W.; Hantke, K.; Braun, V., *Arch. Microbiol.* **1977,** *114*, 231-239.

78. Rabsch, W.; Winkelmann, G., *Biol. Metals* **1991,** *4*, 244-250.

79. Braun, V.; Hantke, K., *Transition Metals in Microbiol Metabolism*. 1 ed.; Harwood: London, 2000.

80. Hussein, S.; Hantke, K.; Braun, V., *Eur. J. Biochem.* **1981,** *117*, 431-437.

81. Passmore Ian, J.; Dow Jennifer, M.; Coll, F.; Cuccui, J.; Palmer, T.; Wren Brendan, W.; Galperin Michael, Y., *J. Bacteriol.* **2020,** *202*, e00541-19.

82. Rohrbach, M. R.; Braun, V.; Köster, W., *J. Bacteriol.* **1995,** *177*, 7186-7193.

83. Köster, W., *Biol. Metals* **1991,** *4*, 23-32.

84. Reynolds, D. M.; Schatz, A.; Waksman, S. A., *Proc. Soc. Exp. Biol. Med.* **1947,** *64*, 50-54.

85. *Antibacterial Agents in Clinical Development*, World Health Organization, Geneva, 2017.

86. Butler, M. S.; Blaskovich, M. A.; Cooper, M. A., *J. Antibiot.* **2013,** *66*, 571-591.

87. Page, M. G. P., *Clin. Infect. Dis.* **2019,** *69*, S529-S537.

88. Sestok, A. E.; Linkous, R. O.; Smith, A. T., *Metallomics* **2018,** *10*, 887-898.

89. Kiley, P. J.; Beinert, H., *FEMS Microbiol. Rev.* **1998,** *22*, 341-352.

90. Carpenter, C.; Payne, S. M., *J. Inorg. Biochem.* **2014,** *133*, 110-117.

91. Kammler, M.; Schön, C.; Hantke, K., *J. Bacteriol.* **1993,** *175*, 6212.

92. Beauchene, N. A.; Mettert, E. L.; Moore, L. J.; Keleş, S.; Willey, E. R.; Kiley, P. J., *PNAS* **2017,** *114*, 12261-12266.

93. Beauchene, N. A.; Myers, K. S.; Chung, D.; Park, D. M.; Weisnicht, A. M.; Keleş, S.; Kiley, P. J., *mBio* **2015,** *6*, e01947-15.

94. Kortman, G. A. M.; Raffatellu, M.; Swinkels, D. W.; Tjalsma, H., *FEMS Microbiol. Rev.* **2014,** *38*, 1202-1234.

95. Pi, H.; Jones, S. A.; Mercer, L. E.; Meador, J. P.; Caughron, J. E.; Jordan, L.; Newton, S. M.; Conway, T.; Klebba, P. E., Role of catecholate siderophores in gram-negative bacterial colonization of the mouse gut. *PloS one* **2012,** *7*, e50020-e50020.

96. Neilands, J. B., *Arch. Biochem. Biophys.* **1993,** *302*, 1-3.

97. Konopka, K.; Bindereif, A.; Neilands, J. B., *Biochemistry* **1982,** *21*, 6503-6508.

98. Litwin, C. M.; Calderwood, S. B., *Clin. Microbiol. Rev.* **1993,** *6*, 137-149.

99. Emmerson, A. M.; Jones, A. M., *J. Antimicrob. Chemther.* **2003,** *51*, 13-20.

100. Chu, D. T.; Fernandes, P. B., *Antimicrob. Agents Chemother.* **1989,** *33*, 131-135.

101. Hooper, D. C., *Drugs* **1999,** *58*, 6-10.

102. Wohlkonig, A.; Chan, P. F.; Fosberry, A. P.; Homes, P.; Huang, J.; Kranz, M.; Leydon, V. R.; Miles, T. J.; Pearson, N. D.; Perera, R. L.; Shillings, A. J.; Gwynn, M. N.; Bax, B. D., *Nat. Struct. Mol. Biol.* **2010,** *17*, 1152-1153.

103. Mustaev, A.; Malik, M.; Zhao, X.; Kurepina, N.; Luan, G.; Oppegard, L. M.; Hiasa, H.; Marks, K. R.; Kerns, R. J.; Berger, J. M.; Drlica, K., *J. Biol. Chem.* **2014**. *289*, 12300-12312.

104. Norrby, S. R., *Eur. J. Clin. Microbiol. Infect. Dis.* **1991,** *10*, 378-383.

105. Meena, M.; Prajapat, A.; Deori, N.; Gurjar, T.; Patel, P.; Saini, S., *J. Entomol. Zool. Stud.* **2019,** *7*, 929-934.

106. Campoli-Richards, D. M.; Monk, J. P.; Price, A.; Benfield, P.; Todd, P. A.; Ward, A., *Drugs* **1988,** *35*, 373-447.

107. Pham, T. D. M.; Ziora, Z. M.; Blaskovich, M. A. T., *Med. Chem. Commun.* **2019,** *10*, 1719-1739.

108. FDA updates warnings for fluoroquinolone antibiotics. https://www.fda.gov/news-events/press-announcements/fda-updates-warnings-fluoroquinolone-antibiotics (accessed April 2020).

109. Aldred, K. J.; Kerns, R. J.; Osheroff, N., *Biochemistry* **2014,** *53*, 1565-1574.

110. Fàbrega, A.; Madurga, S.; Giralt, E.; Vila, J., *Microb. Biotech.* **2009,** *2*, 40-61.

111. Delcour, A. H., *Biochim. Biophys. Acta, Proteins and Proteomics* **2009,** *1794*, 808-816.

112. Huang, R.; Li, C.-H.; Cao-Milán, R.; He, L. D.; Makabenta, J. M.; Zhang, X.; Yu, E.; Rotello, V. M., *J. Am. Chem. Soc.* **2020,** *142*, 10723-10729.

113. Cao-Milán, R.; Gopalakrishnan, S.; He, L. D.; Huang, R.; Wang, L.-S.; Castellanos, L.; Luther, D. C.; Landis, R. F.; Makabenta, J. M. V.; Li, C.-H.; Zhang, X.; Scaletti, F.; Vachet, R. W.; Rotello, V. M., *Chem* **2020,** *6*, 1113-1124.

114. Chapman, J. S.; Georgopapadakou, N. H., *Antimicrob. Agents Chemother.* **1988,** *32*, 438-442.

115. Hirai, K.; Aoyama, H.; Irikura, T.; Iyobe, S.; Mitsuhashi, S., *Antimicrob. Agents Chemother.* **1986,** *29*, 535-538.

116. Neves, P.; Berkane, E.; Gameiro, P.; Winterhalter, M.; de Castro, B., *Biophys. Chem.* **2005,** *113*, 123-128.

117. Cárdenas-Youngs, G.-M.; Beltrán, J.-L., *J. Chem. Eng. Data* **2015,** *60*, 3327-3332.

118. Mach, T.; Neves, P.; Spiga, E.; Weingart, H.; Winterhalter, M.; Ruggerone, P.; Ceccarelli, M.; Gameiro, P., *J. Am. Chem. Soc.* **2008,** *130*, 13301-13309.

119. Turel, I., *Coord. Chem. Rev.* **2002,** *232*, 27-47.

120. Farmer, S.; Li, Z.; Hancock, R. E. W., *J. Antimicrob. Chemother.* **1992,** *29*, 27-33.

121. Sánchez, B. M.; Cabarga, M. M.; Navarro, A. S.; Hurlé, A. D.-G., *Int. J. Pharm.* **1994,** *106*, 229-235.

122. Nikaido, H.; Thanassi, D. G., Penetration of lipophilic agents with multiple protonation sites into bacterial cells: tetracyclines and fluoroquinolones as examples. *Antimicrobial agents and chemotherapy* **1993,** *37*, 1393-1399.

123. Aldred, K. J.; McPherson, S. A.; Turnbough Jr, C. L.; Kerns, R. J.; Osheroff, N., *Nucleic acids Res.* **2013,** *41*, 4628-4639.

124. Aldred, K. J.; McPherson, S. A.; Wang, P.; Kerns, R. J.; Graves, D. E.; Turnbough, C. L.; Osheroff, N., *Biochem.* **2012,** *51*, 370-381.

125. Richter, M. F.; Drown, B. S.; Riley, A. P.; Garcia, A.; Shirai, T.; Svec, R. L.; Hergenrother, P. J., *Nature* **2017,** *545*, 299-304.

126. Richter, M. F.; Hergenrother, P. J., *Ann. N.Y. Acad. Sci.* **2019,** *1435*, 18-38.

127. Tanaka, K. S. E.; Houghton, T. J.; Kang, T.; Dietrich, E.; Delorme, D.; Ferreira, S. S.; Caron, L.; Viens, F.; Arhin, F. F.; Sarmiento, I.; Lehoux, D.; Fadhil, I.; Laquerre, K.; Liu, J.; Ostiguy, V.; Poirier, H.; Moeck, G.; Parr, T. R.; Rafai Far, A., *Bioorg. Med. Chem.* **2008,** *16*, 9217-9229.

128. Houghton, T. J.; Tanaka, K. S. E.; Kang, T.; Dietrich, E.; Lafontaine, Y.; Delorme, D.; Ferreira, S. S.; Viens, F.; Arhin, F. F.; Sarmiento, I.; Lehoux, D.; Fadhil, I.; Laquerre, K.; Liu, J.; Ostiguy, V.; Poirier, H.; Moeck, G.; Parr, T. R.; Far, A. R., *J. Med. Chem.* **2008,** *51*, 6955-6969.

129. Yu, X.; Zipp, G. L.; Davidson Iii, G. W. R., *Pharm. Res.* **1994,** *11*, 522-527.

130. Fahey, R. C.; Brown, W. C.; Adams, W. B.; Worsham, M. B., *J. Bacteriol.* **1978,** *133*, 1126.

131. McLaggan, D.; Logan, T. M.; Lynn, D. G.; Epstein, W., *J. Bacteriol.* **1990,** *172*, 3631-3636.

132. Ferguson, G. P.; Booth, I. R., *J. Bacteriol.* **1998,** *180*, 4314-4318.

133. Meister, A., *J. Biol. Chem.* **1988,** *263*, 17205-17208.

134. Böswald, I. Erasmus Report: Inorganic Chemistry. University of Würzburg, 2019.

135. Glanzer, S.; Zangger, K., *J. Am. Chem. Soc.* **2015,** *137*, 5163-5169.

136. Raymond, K. N.; Dertz, E. A.; Kim, S. S., *Proc. Natl. Acad. Sci. USA* **2003,** *100*, 3584-3588.

137. Neumann, W.; Sassone-Corsi, M.; Raffatellu, M.; Nolan, E. M., Esterase-Catalyzed Siderophore Hydrolysis Activates an Enterobactin–Ciprofloxacin Conjugate and Confers Targeted Antibacterial Activity. *J. Am. Chem. Soc.* **2018,** *140*, 5193-5201.

138. Hartmann, A.; Braun, V., *Arch. Microbiol.* **1981,** *130*, 353-356.

139. Madsen, J. L. H.; Johnstone, T. C.; Nolan, E. M., *J. Am. Chem. Soc.* **2015,** *137*, 9117-9127.

140. Endicott, N. P.; Lee, E.; Wencewicz, T. A., *ACS Infect. Dis.* **2017,** *3*, 542-553.

141. Arifin, A. J.; Hannauer, M.; Welch, I.; Heinrichs, D. E., *Microb. Infect.* **2014,** *16*, 967-972.

142. Pandey, A.; Savino, C.; Ahn, S. H.; Yang, Z.; Van Lanen, S. G.; Boros, E., *J. Med. Chem.* **2019,** *62*, 9947-9960.

143. Sadykov, M. R.; Zhang, B.; Halouska, S.; Nelson, J. L.; Kreimer, L. W.; Zhu, Y.; Powers, R.; Somerville, G. A., *J. Biol. Chem.* **2010,** *285*, 36616-36624.

144. Ledala, N.; Zhang, B.; Seravalli, J.; Powers, R.; Somerville, G. A., *J. Bacteriol.* **2014,** *196*, 2178-2189.

145. Wencewicz, T. A.; Long, T. E.; Möllmann, U.; Miller, M. J., *Bioconjugate Chem.* **2013,** *24*, 473-486.

146. Zheng, T. F.; Nolan, E. M., *J. Am. Chem. Soc.* **2014,** *136*, 9677-9691.

147. Bio-rad Chelex 100 and Chelex 20 Chelating Ion Exchange Resin Instruction Manual. http://www.bio-rad.com/webroot/web/pdf/lsr/literature/LIT200.pdf (accessed April 2020).

148. Kadurugamuwa, J. L.; Anwar, H.; Brown, M. R.; Shand, G. H.; Ward, K. H., *J. Clin. Microbiol.* **1987,** *25*, 849-855.

149. Seo, S. W.; Kim, D.; Latif, H.; O'Brien, E. J.; Szubin, R.; Palsson, B. O., *Nat. Commun.* **2014,** *5*, 4910.

150. Eun, Y.-J.; Zhou, M.; Kiekebusch, D.; Schlimpert, S.; Trivedi, R. R.; Bakshi, S.; Zhong, Z.; Wahlig, T. A.; Thanbichler, M.; Weibel, D. B., *J. Am. Chem. Soc.* **2013,** *135*, 9768-9776.

151. WHO, Antibacterial Agents in Clinical Development. (WHO, Geneva, 2019).

152. Humphries, R. M.; Linscott, A. J., *Clin. Microbiol. Rev.* **2015,** *28*, 3-31.

153. Neidhardt, F. C.; Bloch, P. L.; Smith, D. F., *J. Bacteriol.* **1974,** *119*, 736-747.

154. M9 minimal medium (standard). *Cold Spring Harbor Protocols* **2010,** *8*, pdb.rec12295.

155. Sanderson, T. J.; Black, C. M.; Southwell, J. W.; Wilde, E. J.; Pandey, A.; Herman, R.; Thomas, G. H.; Boros, E.; Duhme-Klair, A.-K.; Routledge, A., *ACS Infect. Dis.* **2020,** *6*, 2532-2541.

156. Friedman, E. S.; Bittinger, K.; Esipova, T. V.; Hou, L.; Chau, L.; Jiang, J.; Mesaros, C.; Lund, P. J.; Liang, X.; FitzGerald, G. A.; Goulian, M.; Lee, D.; Garcia, B. A.; Blair, I. A.; Vinogradov, S. A.; Wu, G. D., *PNAS* **2018,** *115*, 4170-4175.

157. Sonnenburg, J. L.; Xu, J.; Leip, D. D.; Chen, C.-H.; Westover, B. P.; Weatherford, J.; Buhler, J. D.; Gordon, J. I., *Science* **2005,** *307*, 1955-1959.

158. Shewaramani, S.; Finn, T. J.; Leahy, S. C.; Kassen, R.; Rainey, P. B.; Moon, C. D., *PLOS Genet.* **2017,** *13*, e1006570.

159. Beauchene, N. A.; Mettert, E. L.; Moore, L. J.; Keleş, S.; Willey, E. R.; Kiley, P. J., *PNAS* **2017,** *114*, 12261-12266.

160. Edmiston Charles, E.; Krepel Candace, J.; Seabrook Gary, R.; Somberg Lewis, R.; Nakeeb, A.; Cambria Robert, A.; Towne Jonathan, B., *Antimicrob. Agents Chemother.* **2004,** *48*, 1012-1016.

161. Soussy, C. J.; Nguyen, J.; Goldstein, F.; Dabernat, H.; Andremont, A.; Leclercq, R.; Drugeon, H.; Cavallo, P.; Chardon, H.; Etienne, J.; Rio, Y.; Courvalin, P., *Clin. Microbiol. Infect.* **2003,** *9*, 997-1005.

162. Zheng, T.; Bullock, J. L.; Nolan, E. M., *J. Am. Chem. Soc.* **2012,** *134*, 18388-18400.

163. Wencewicz, T. A.; Miller, M. J., *J. Med. Chem.* **2013,** *56*, 4044-4052.

164. Ji, C.; Miller, P. A.; Miller, M. J., *J. Am. Chem. Soc.* **2012,** *134*, 9898-9901.

165. Goldberg, J. A.; Nguyen, H.; Kumar, V.; Spencer, E. J.; Hoyer, D.; Marshall, E. K.; Cmolik, A.; O'Shea, M.; Marshall, S. H.; Hujer, A. M.; Hujer, K. M.; Rudin, S. D.; Domitrovic, T. N.; Bethel, C. R.; Papp-Wallace, K. M.; Logan, L. K.; Perez, F.; Jacobs, M. R.; van Duin, D.; Kreiswirth, B. M.; Bonomo, R. A.; Plummer, M. S.; van den Akker, F., *J. Med. Chem.* **2020,** *63*, 5990-6002.

166. Nikaido, H.; Rosenberg, E. Y., *J. Bacteriol.* **1990,** *172*, 1361-1367.

167. Curtis, N. A.; Eisenstadt, R. L.; East, S. J.; Cornford, R. J.; Walker, L. A.; White, A. J., *Antimicrob. Agents Chemother.* **1988,** *32*, 1879-1886.

168. Gensberg, K.; Doyle, E. J.; Perry, D. J.; Smith, A. W., *J. Antimicrob. Chemother.* **1994,** *34*, 697-705.

169. Neumann, W.; Sassone-Corsi, M.; Raffatellu, M.; Nolan, E. M., *J. Am. Chem. Soc.* **2018,** *140*, 5193-5201.

170. Almeida, M.; Boman, A.; Lundstedt, T., *J. Label. Compd. Radiopharm.* **2002,** *45*, 371-377.

171. Thansandote, P.; Hulcoop, D. G.; Langer, M.; Lautens, M., *J. Org. Chem.* **2009,** *74*, 1673-1678.

172. SpectraBase™. https://spectrabase.com/compound/FmHUKluayBy (accessed July 2021).

173. Cheung, C. W.; Surry, D. S.; Buchwald, S. L., *Org. Lett.* **2013,** *15*, 3734-3737.

174. Tornøe, C. W.; Christensen, C.; Meldal, M., *J. Org. Chem.* **2002,** *67*, 3057-3064.

175. Wang, Q.; Chan, T. R.; Hilgraf, R.; Fokin, V. V.; Sharpless, K. B.; Finn, M. G., *J. Amer. Chem. Soc.* **2003,** *125*, 3192-3193.

176. Thirumurugan, P.; Matosiuk, D.; Jozwiak, K., *Chem. Rev.* **2013,** *113*, 4905-4979.

177. McKay, C. S.; Finn, M. G., *Chem. Biol. Rev.* **2014,** *21*, 1075-1101.

178. Mahal, L. K.; Yarema, K. J.; Bertozzi, C. R., *Science* **1997,** *276*, 1125-1128.

179. Veschi, S.; Carradori, S.; De Lellis, L.; Florio, R.; Brocco, D.; Secci, D.; Guglielmi, P.; Spano, M.; Sobolev, A. P.; Cama, A., *J. Enzym. Inhib. Med. Chem.* **2020,** *35*, 1331-1344.

180. Heinisch, L.; Wittmann, S.; Stoiber, T.; Berg, A.; Ankel-Fuchs, D.; Möllmann, U., *J. Med. Chem.* **2002,** *45*, 3032-3040.

181. Oki, N.; Aoki, B.; Kuroki, T.; Matsumoto, M.; Kojima, K.; Nehashi, T., *J. Antibiotic.* **1987,** *40*, 22-28.

182. Ferreira, K.; Hu, H.-Y.; Fetz, V.; Prochnow, H.; Rais, B.; Müller, P. P.; Brönstrup, M., *Angew. Chem. Int. Ed.* **2017,** *56*, 8272-8276.

183. Bergeron, R. J.; McGovern, K. A.; Channing, M. A.; Burton, P. S., *J. Org. Chem.* **1980,** *45*, 1589-1592.

184. Soulere, L.; Viode, C.; Perie, J.; Hoffmann, P., *Chemical and pharmaceutical bulletin* **2002,** *50*, 578-582.

185. Hider, R. C.; Mohd-Nor, A. R.; Silver, J.; Morrison, I. E. G.; Rees, L. V. C., *J. Chem. Soc., Dalton Trans. (1972-2002)* **1981**, 2, 609-622.

186. Harris, W. R.; Raymond, K. N.; Weitl, F. L., *J. Am. Chem. Soc.* **1981,** *103*, 2667-2675.

187. Barden, T. C.; Buckwalter, B. L.; Testa, R. T.; Petersen, P. J.; Lee, V. J., *J. Med. Chem.* **1994,** *37*, 3205-3211.

188. Sleath, P. R.; Noar, J. B.; Eberlein, G. A.; Bruice, T. C., *J. Am. Chem. Soc.* **1985,** *107*, 3328-3338.

189. Corbin, J. L.; Bulen, W. A., *Biochemistry* **1969,** *8*, 757-762.

190. Knosp, O.; von Tigerstrom, M.; Page, W. J., *J. Bacteriol.* **1984,** *159*, 341-347.

191. Moynié, L.; Milenkovic, S.; Mislin, G. L. A.; Gasser, V.; Malloci, G.; Baco, E.; McCaughan, R. P.; Page, M. G. P.; Schalk, I. J.; Ceccarelli, M.; Naismith, J. H., *Nat. Commun.* **2019,** *10*, 3673.

192. McKee, J. A.; Sharma, S. K.; Miller, M. J., *Bioconjugate Chem.* **1991,** *2*, 281-291.

193. Tarapdar, A.; Norris, J. K. S.; Sampson, O.; Mukamolova, G.; Hodgkinson, J. T., *Beilstein J. Org. Chem.* **2018,** *14*, 2646-2650.

194. Diarra, M. S.; Lavoie, M. C.; Jacques, M.; Darwish, I.; Dolence, E. K.; Dolence, J. A.; Ghosh, A.; Ghosh, M.; Miller, M. J.; Malouin, F., *Antimicrob. Agents Chemother.* **1996,** *40*, 2610-2617.

195. Raines, D. J.; Clarke, J. E.; Blagova, E. V.; Dodson, E. J.; Wilson, K. S.; Duhme-Klair, A.-K., *Nat. Catal.* **2018,** *1*, 680-688.

196. Müller, G.; Raymond, K. N., *J. Bacteriol.* **1984,** *160*, 304-312.

197. Page, M. G. P., *Ann. N. Y. Acad. Sci.* **2013,** *1277*, 115-126.

198. Lin, Y.-M.; Ghosh, M.; Miller, P. A.; Möllmann, U.; Miller, M. J., *BioMetals* **2019,** *32*, 425-451.

199. Braun, V.; Pramanik, A.; Gwinner, T.; Koeberle, E.; Bohn, E., *BioMetals* **2009,** *22*, 3-13.

200. Sauer, M.; Hantke, K.; Braun, V., *J. Bacteriol.* **1987,** *169*, 2044-2049.

201. Hantke, K., *Mol. Gen. Genet.* **1983,** *191*, 301-306.

202. Braun, V.; Hantke, K., *Genetics of Bacterial Iron Transport*. CRC Press: 1991.

203. Nelson, M.; Szaniszlo, P. J., *FEMS Microbiol. Lett.* **1992,** *100*, 191-196.

204. Nelson, M.; Carrano, C. J.; Szaniszlo, P. J., *Biometals* **1992,** *5*, 37-46.

205. Nelson, M.; Cooper, C. R.; Crowley, D. E.; Reid, C. P. P.; Szaniszlo, P. J., *J. Plant. Nutr.* **1988,** *11*, 915-924.

206. Ji, C.; Miller, M. J., *Bioorg. Med. Chem.* **2012,** *20*, 3828-3836.

207. Rudd, S. E.; Roselt, P.; Cullinane, C.; Hicks, R. J.; Donnelly, P. S., *Chem. Commun.* **2016,** *52*, 11889-11892.

208. Laurent, Q.; Batchelor, L. K.; Dyson, P. J., *Organometallics* **2018,** *37*, 915-923.

209. Tufano, T. P.; Raymond, K. N., *J. Am. Chem. Soc.* **1981,** *103*, 6617-6624.

210. Mushtaq, S.; Warner, M.; Livermore, D., *J. Antimicrob.Chemother.* **2010,** *65*, 266-270.

211. Page M. G. P.; Dantier, C.; Desarbre, E., *Antimicrob. Agents Chemother.* **2010,** *54*, 2291-2302.

212. Flanagan, M. E.; Brickner, S. J.; Lall, M.; Casavant, J.; Deschenes, L.; Finegan, S. M.; George, D. M.; Granskog, K.; Hardink, J. R.; Huband, M. D.; Hoang, T.; Lamb, L.; Marra, A.; Mitton-Fry, M.; Mueller, J. P.; Mullins, L. M.; Noe, M. C.; O'Donnell, J. P.; Pattavina, D.; Penzien, J. B.; Schuff, B. P.; Sun, J.; Whipple, D. A.; Young, J.; Gootz, T. D., *ACS Med. Chem. Lett.* **2011,** *2*, 385-390.

213. Tomaras A. P.; Crandon J. L.; McPherson C. J.; Banevicius M. A.; Finegan S. M.; Irvine R. L.; Brown M. F.; O'Donnell J. P.; Nicolau D. P., *Antimicrob. Agents Chemother.* **2013,** *57*, 4197-4207.

214. McPherson, C. J.; Aschenbrenner, L. M.; Lacey, B. M.; Fahnoe, K. C.; Lemmon, M. M.; Finegan, S. M.; Tadakamalla, B.; O'Donnell, J. P.; Mueller, J. P.; Tomaras, A. P., *Antimicrob. Agents Chemother.* **2012,** *56*, 6334-6342.

215. Lachowicz, J. I.; Nurchi, V. M.; Crisponi, G.; Jaraquemada-Pelaez, M. G.; Arca, M.; Pintus, A.; Santos, M. A.; Quintanova, C.; Gano, L.; Szewczuk, Z.; Zoroddu, M. A.; Peana, M.; Domínguez-Martín, A.; Choquesillo-Lazarte, D., *Dalton Trans.* **2016,** *45*, 6517-6528.

216. Nurchi, V. M.; Crisponi, G.; Lachowicz, J. I.; Murgia, S.; Pivetta, T.; Remelli, M.; Rescigno, A.; Niclós-Gutíerrez, J.; González-Pérez, J. M.; Domínguez-Martín, A.; Castiñeiras, A.; Szewczuk, Z., *J. Inorg. Biochem.* **2010,** *104*, 560-569.

217. Brown, M. F.; Mitton-Fry, M. J.; Arcari, J. T.; Barham, R.; Casavant, J.; Gerstenberger, B. S.; Han, S.; Hardink, J. R.; Harris, T. M.; Hoang, T.; Huband, M. D.; Lall, M. S.; Lemmon, M. M.; Li, C.; Lin, J.; McCurdy, S. P.; McElroy, E.; McPherson, C.; Marr, E. S.; Mueller, J. P.; Mullins, L.; Nikitenko, A. A.; Noe, M. C.; Penzien, J.; Plummer, M. S.; Schuff, B. P.; Shanmugasundaram, V.; Starr, J. T.; Sun, J.; Tomaras, A.; Young, J. A.; Zaniewski, R. P., *J. Med. Chem.* **2013,** *56*, 5541-5552.

218. Ernst, G.; Akuma, D.; Au, V.; Buchler, I. P.; Byers, S.; Carr, G. V.; Defays, S.; de León, P.; Demaude, T.; DePasquale, M.; Durieu, V.; Huang, Y.; Jigorel, E.; Kimos, M.; Kolobova, A.; Montel, F.; Moureau, F.; Poslusney, M.; Swinnen, D.; Vandergeten, M.-C.; Van houtvin, N.; Wei, H.; White, N.; Wood, M.; Barrow, J. C., *ACS Med. Chem. Lett.* **2019,** *10*, 1573-1578.

219. Ito, A.; Nishikawa, T.; Matsumoto, S.; Yoshizawa, H.; Sato, T.; Nakamura, R.; Tsuji, M.; Yamano, Y., *Antimicrob. Agents Chemother.* **2016,** *60*, 7396-7401.

220. Ghosh, M.; Miller, M. J., *Bioorg. Med. Chem.* **1996,** *4*, 43-48.

221. Moynié, L.; Luscher, A.; Rolo, D.; Pletzer, D.; Tortajada, A.; Weingart, H.; Braun, Y.; Page, M. G. P.; Naismith, J. H.; Köhler, T., *Antimicrob. Agents and Chemother.* **2017,** *61*, e02531-16.

222. van Delden, C.; Page, M. G. P.; Köhler, T., *Antimicrob. Agents and Chemother.* **2013,** *57*, 2095-2102.

223. Chu, H.-s.; Yip, Y.-c.; Chan, K.-c.; Sham, W.-c., *J. Anal. At. Spectrom.* **2006,** *21*, 1068-1071.

224. Dauphas, N.; Pourmand, A.; Teng, F.-Z., *Chemical Geology* **2009,** *267*, 175-184.

225. Sakaitani, M.; Rusnak, F.; Quinn, N. R.; Tu, C.; Frigo, T. B.; Berchtold, G. A.; Walsh, C. T., *Biochemistry* **1990,** *29*, 6789-6798.

226. Völker, T. Metal-Catalysed Chemical Activation for Medical and Biological Applications. Philipps-University Marburg, 2017.

227. Rangama, S.; Lidbury, I. D. E. A.; Holden, J. M.; Borsetto, C.; Murphy, A. R. J.; Hawkey, P. M.; Wellington, E. M. H., *bioRxiv* **2021**, 2021.03.31.437630.

228. Brook, I., *Clin. Microbiol. Infect.* **2004,** *10*, 777-784.

229. https://spectrabase.com/compound/FmHUKluayBy (accessed July 2021).